Localisation in computational geomechanics: a nonlinear micropolar approach

O'HARE, TED,JOSEPH

O'HARE, TED,JOSEPH (2025) *Localisation in computational geomechanics: a nonlinear micropolar approach*, Durham theses, Durham University. Available at Durham E-Theses Online: http://etheses.dur.ac.uk/16144/

Localisation in computational geomechanics: a nonlinear micropolar approach

Ted Joseph O'Hare

Department of Engineering

Durham University, United Kingdom

A thesis presented for the degree of

Doctor of Philosophy

2025

No mud, no lotus.

—Thích Nhất Hạnh

Abstract

The localisation of strain into narrow bands of intense deformations is a pervasive phenomenon in geomechanics. It is closely associated with catastrophic failure – landslides, slope collapses, rock faulting, etc. – and has significant implications for the design, integrity, and risk assessment of geotechnical infrastructure. However, traditional computational modelling techniques cannot capture localised failure in a rigorous or reliable way. Classical continuum theories overlook microstructural effects, including those responsible for triggering and governing localisation processes, and mesh-based approaches like the finite element method typically break down under the large deformations induced by geotechnical failure.

This thesis addresses these challenges by employing the generalised implicit material point method, which discretises the domain using particles to circumvent mesh tangling, and by developing a geometrically-nonlinear elastoplastic micropolar (Cosserat) continuum formulation. This nonlocal theory enriches the classical theory with a field of independent microrotations to represent the relative motion of individual soil particles, as well as internal length scales indicative of particle size. Consequently, localised shear bands emerge naturally and analyses converge to physically meaningful results.

First, strain localisation is introduced as an engineering phenomenon and an analytical subject. This is followed by an outline of the material point method, a classical formulation of which is used to demonstrate its deficiencies in simulating localised failure. To address these shortcomings, a review of existing regularisation approaches is provided, leading to the derivation and implementation of the proposed micropolar continuum – initially for purely hyperelastic material behaviour, before extending the model to elastoplasticity. Numerical examples – encompassing a biaxial test and a column collapse problem – demonstrate the method's capacity to capture complex, evolving failure mechanisms in a robust, convergent, and physically realistic manner. Finally, the analytical consistent linearisation required for the Newton–Raphson solution algorithm is presented in detail in the appendices.

Declaration

This thesis is the result of research carried out at the Department of Engineering, Durham University, United Kingdom. None of its content has been submitted elsewhere for any other degree or qualification. All work presented herein is the original work of the author unless referenced to the contrary in the text. Elements have been disseminated as follows.

Journal articles

- T.J. O'Hare, P.A. Gourgiotis, W.M. Coombs, and C.E. Augarde, "An implicit Material Point Method for micropolar solids undergoing large deformations," *Computer Methods in Applied Mechanics and Engineering*, vol. 419, p. 116668, Feb. 2024.
- T.J. O'Hare, W.M. Coombs, P.A. Gourgiotis, and C.E. Augarde, "An implicit hyperelastoplastic micropolar material point method for shear bands and size effects at finite strains." (Under review.)
- T.J. O'Hare, W.M. Coombs, P.A. Gourgiotis, and C.E. Augarde, "Evolving shear bands in a micropolar material point method." (Under preparation.)

Conference presentations

- "A geometrically-exact Finite Element Method for micropolar continua with finite deformations," *UKACM 2023*, University of Warwick, Coventry, UK, 26 Apr. 2023.
- "Simulation of strain localisation with an elastoplastic micropolar material point method," *UKACM 2024*, Durham University, UK, 12 Apr. 2024.
- "An elasto-plastic finite-deformation micropolar material point method for strain localisation problems," *EMI 2024 IC*, Vienna, Austria, 11 Sep. 2024.
- "Modelling geotechnical failure with an elastoplastic Cosserat material point method," *ALERT Geomaterials*, Aussois, France, 2 Oct. 2024.

The supporting research dataset is published in the Durham University open data repository. DOI: http://doi.org/10.15128/r2kw52j812k.

Acknowledgements

This thesis is the culmination of not only my own efforts, but also the countless seen and unseen contributions of innumerable others over many years. Attempting to express my gratitude to everyone who has helped along the way would be hopelessly futile – but regardless I must try.

First, I gratefully acknowledge the Engineering and Physical Sciences Research Council [grant number EP/T518001/1] and the Department of Engineering, Durham University, who made this work possible. But above all, I am indebted to my brilliant supervisors. Professor Will Coombs, whose intellect, empathy, diligence and optimism gave me the ideal conditions to pursue this research, and to grow both as a scholar and a human being. Professor Charles Augarde, for his patience, sharp eye, and wry wisdom which was always a source of encouragement. And Dr Panos Gourgiotis, whose unflinching zeal for challenging mathematics was such an inspiration, particularly in those dark days of linearisation.

More widely in the Department, I am particularly grateful to Dr Giuliano Pretti for the incisive advice, joy of index notation – and always the welcome reminders of how much worse my problems might be. Thanks are also due to my reviewers, Professor Simon Mathias and Dr Alexandros Petalas, for helping me rationalise my arguments, and to Professor Ashraf Osman, who first encouraged me to consider a PhD. I also thank Rachel Burstow and Sam Rowell, whose MEng research laid valuable groundwork.

This thesis was enhanced by the music of J. S. Bach. For that I am grateful to Nigel Pitceathly, who also instilled in me the importance of being a little obsessive about one's pursuits; indeed, my love of mathematics and mechanics began with Kevin Allen and Neil Berry – a truly precious and enduring gift.

I owe special thanks to all who accompanied me through my doctoral vicissitudes – particularly my friends from Sacred Earth Sangha and the wider Plum Village community, for helping me find the lotus in the mud. But I am indebted to all those who have brightened my life simply through their presence in it (by choice or otherwise) these past few years, especially Henry Bashford, Dr Robert Bird, Dr Robert Bluck, Dr Nathan Gavin, Arielle Loewinger, Dr Matt McCullough, Peter Mitchell, Heather Monro, Takkie Mutsvairo, Tom Parker, Bradley Sims and Sam Sutcliffe. You all deserve so much more than an alphabetical list.

To David, thank you for making these last six months better than I could have ever imagined. And finally, to my parents, Tom and Rachel, whose kindness, generosity and quiet sacrifices shape every day of my life – you are my heroes.

T. J. O'H.
Hebden Bridge, April 2025

Contents

List of Figures

List of Algorithms

Nomenclature

Abbreviations

ALE	arbitrary Lagrangian-Eulerian
AMPLE	*A Material Point Learning Environment*
CEL	coupled Eulerian-Lagrangian
cpGIMPM	contiguous particle GIMPM
DEM	discrete element method
DOF	degree of freedom
EFG	element-free Galerkin
FE	finite-element
FEA	finite element analysis
FEM	finite element method
FLIP	fluid-implicit particle
GIMPM	generalised implicit material point method
KKT	Karush-Kuhn-Tucker
MEMS	micro-electro-mechanical system
MMS	method of manufactured solutions
MPM	material point method
MUSL	modified USL
PDE	partial differential equation
PFEM	particle FEM
PIC	particle-in-cell
SI	International System of Units
slerp	spherical linear interpolation
SPH	smoothed-particle hydrodynamics
StV-K	Saint-Venant-Kirchhoff
uGIMPM	unchanged GIMPM
USF	update-stress-first
USL	update-stress-last

Scalars

α	a Cosserat twist coefficient
α^{DP}	Drucker-Prager friction factor
β	a Cosserat twist coefficient
β^{DP}	Drucker-Prager dilatancy factor
γ	a Cosserat twist coefficient
$\dot{\gamma}^{\mathrm{p}}$	plastic multiplier
γ_g	ghost penalty parameter
ϵ	perturbation
ε^{p}	equivalent plastic strain
θ	extrinsic microrotation angle
ϑ	a microrotation
κ	Cosserat coupling modulus
Λ	hardening force
λ	Lamé parameter
μ	shear modulus
ν	Poisson's ratio
ξ	a local co-ordinate
ρ	mass density
ϱ	viscous-like parameter
ϕ	internal friction angle
φ	intrinsic microrotation angle
χ	internal hardening variable
Ψ	polar ratio
ψ	dilatancy angle

Ω	spatial measure of the physical domain
A	area
a	radius
c	apparent cohesion
d	damage
E	Young's modulus
$e_{(\bullet)}$	norm of error in $(\bullet)$
$\bar{e}$	energy convergence criterion
$\bar{f}$	force convergence criterion
g	gravitational acceleration
H	hardening parameter
h	element size
J	volume ratio
J_2	second invariant of the deviatoric Kirchhoff stress
K	iteration counter
k	yield strength
l_p	GIMPM domain half-length
ℓ	characteristic length
m	mass
N	basis function
n	coupling number
p	hydrostatic pressure
$\bar{p}$	plasticity convergence criterion
$\mathcal{Q}$	real part of a quaternion
q	equivalent von Mises stress
r	heat supply per unit mass
S	weighting function
s	entropy
T	absolute temperature
t	time
v	volume

Tensors and arrays

$\mathbf{0}$	an array of zeros
$\boldsymbol{\Gamma}$	material wryness tensor
$\boldsymbol{\delta}$	Kronecker delta
$\boldsymbol{\epsilon}$	Levi-Civita tensor
$\boldsymbol{\varepsilon}$	logarithmic or incremental strain
$\boldsymbol{\mu}$	Cauchy couple-stress
$\boldsymbol{\nu}$	Kirchhoff couple-stress
$\boldsymbol{\xi}$	local position
$\boldsymbol{\theta}$	extrinsic microrotation Euler vector
$\boldsymbol{\sigma}$	Cauchy stress
$\boldsymbol{\tau}$	Kirchhoff stress
$\boldsymbol{\varphi}$	intrinsic microrotation Euler vector
$\boldsymbol{\Omega}$	micropolar spin tensor
$\boldsymbol{\omega}$	micropolar gyration vector
$\boldsymbol{A}$	acoustic tensor
$\boldsymbol{a}$	spatial tangent modulus
$\boldsymbol{B}$	Biot stress
$\boldsymbol{b}$	left Cauchy-Green strain
$\boldsymbol{C}$	constitutive model Jacobian
$\boldsymbol{D}$	elasticity tensor
$\boldsymbol{\mathcal{D}}$	a tensor derivative
$\boldsymbol{d}$	spatial deformation rate
$\boldsymbol{E}$	material strain tensor
$\boldsymbol{\mathcal{E}}$	derivative of the flow rule exponential map with respect to its argument
$\boldsymbol{e}$	micropolar gyration gradient
$\boldsymbol{F}$	material deformation gradient
$\boldsymbol{f}$	force vector
$\boldsymbol{G}$	spatial strain-displacement matrix
$\boldsymbol{g}$	spatial strain tensor
$\boldsymbol{H}$	intrinsic-extrinsic microrotation vector map
$\boldsymbol{h}$	heat flux vector
$\boldsymbol{I}$	identity tensor
$\boldsymbol{J}$	ghost stabilisation term
$\boldsymbol{K}$	stiffness matrix
$\boldsymbol{k}$	spatial curvature tensor
$\boldsymbol{L}$	fourth-order dyadic stretch
$\boldsymbol{l}$	velocity gradient
$\boldsymbol{m}$	couple-traction
$\boldsymbol{N}$	basis function matrix
$\boldsymbol{n}$	outward normal vector
$\boldsymbol{O}$	origin
$\boldsymbol{P}$	algorithmic Jacobian
$\boldsymbol{p}$	body force per unit volume
$\boldsymbol{Q}$	microrotation tensor
$\boldsymbol{\mathcal{Q}}$	imaginary part of a quaternion
$\boldsymbol{q}$	body couple per unit volume
$\boldsymbol{R}$	macrorotation tensor
$\boldsymbol{r}$	residual
$\boldsymbol{S}$	Biot couple-stress
$\boldsymbol{S}_{vp}$	weighting function matrix
$\boldsymbol{s}$	symmetrised deviatoric Kirchhoff stress
$\boldsymbol{T}$	auxiliary Jacobian
$\boldsymbol{t}$	traction
$\boldsymbol{U}$	material stretch tensor
$\boldsymbol{u}$	displacement or translation
$\boldsymbol{V}$	spatial stretch tensor
$\boldsymbol{v}$	test function

$\boldsymbol{W}$	material micropolar director
$\boldsymbol{w}$	spatial micropolar director
$\boldsymbol{X}$	material position
$\boldsymbol{\mathcal{X}}$	constitutive model unknowns
$\boldsymbol{x}$	spatial position
$\boldsymbol{\mathcal{Y}}$	constitutive model inputs

Subscripts and superscripts

$(\bullet)_0$	original or undeformed
$(\bullet)^+$	positive side
$(\bullet)^-$	negative side
$(\bullet)^*$	perturbed
$(\bullet)^a$	analytical
$(\bullet)_b$	bending
$(\bullet)_D$	Dirichlet
$(\bullet)^{\mathrm{DP}}$	Drucker-Prager
$(\bullet)_E$	element or cell
$(\bullet)^{\mathrm{e}}$	elastic
$(\bullet)^{\mathrm{ext}}$	external
$(\bullet)_g$	ghost
$(\bullet)^h$	numerical
$(\bullet)^{\mathrm{int}}$	internal
$(\bullet)_{\mathrm{lstps}}$	load steps
$(\bullet)_N$	Neumann
$(\bullet)_p$	material point
$(\bullet)^{\mathrm{p}}$	plastic
$(\bullet)^{\mathrm{R}}$	residual
$(\bullet)^{\mathrm{rct}}$	reaction
$(\bullet)^{\mathrm{T}}$	transpose
$(\bullet)_t$	torsion
$(\bullet)_{\mathrm{tol}}$	tolerance
$(\bullet)^{\mathrm{tr}}$	trial
$(\bullet)_v$	nodal

Diacritics

$\widetilde{(\bullet)}$	as computed at the start of a load step/converged value from the previous step
$\dot{(\bullet)}$	time derivative
$\widehat{(\bullet)}$	skew-symmetric second-order representation of an axial vector

Tensor indices

$(\bullet)_{\alpha\beta\gamma}$	material quantities
$(\bullet)_{IJK}$	numerical quantities
$(\bullet)_{ijk}$	spatial quantities
$(\bullet)_{\bar{i}\bar{j}\bar{k}}$	quantities defined in the intermediate configuration

Operators

$\lvert\lvert(\bullet)\rvert\rvert$	L_2-norm
$\nabla(\bullet)$	gradient
$\mathbb{A}(\bullet)$	finite element assembly operator
$\Delta(\bullet)$	change or increment
$\delta(\bullet)$	small change or variation
$\partial(\bullet)$	boundary
$\frac{\mathrm{D}}{\mathrm{D}t}(\bullet)$	material time derivative
$\det(\bullet)$	determinant
$\mathrm{Div}(\bullet)$	divergence with respect to material coordinates
$\mathrm{div}(\bullet)$	divergence with respect to spatial coordinates
$\mathrm{skew}(\bullet)$	skew-symmetric component
$\mathrm{sym}(\bullet)$	symmetric component
$\mathrm{tr}(\bullet)$	trace

Functions

Ξ	motion
χ_p	material point characteristic function
f	yield function
g	plastic potential function
W	Helmholtz free energy function

Other

$C^{(\bullet)}$	continuity class
E	a grid cell
i	imaginary unit
$\mathscr{Q}$	quaternion
$SO(3)$	three-parameter special orthogonal Lie group
$\mathfrak{so}(3)$	three-parameter special orthogonal Lie algebra

CHAPTER 1

Introduction

> "[A] phenomenon occurred incidentally which engrossed [my] whole attention, bearing intimately as it did on the deformation of solid bodies."
>
> —Henri Tresca, on discovering the shear band (June 1878) [1]

These words mark one of the earliest recorded observations in the engineering literature of what is now referred to as *strain localisation*.[1] The excitement they contain is remarkable. Today, Tresca is widely regarded as the father of plasticity, but his legacy extends far beyond the yield criterion which bears his name. Throughout the 1860s and 1870s, he conducted an extensive series of experiments in industrial mechanics, from which he would deduce some of the foundational concepts of material yielding and plastic flow theory [3]. The shear band was observed completely by chance during a set of experiments concerned with the forging of platinum-iridium bars. After being allowed to cool to just below red-hot, a bar was struck by a hammer and, to the onlookers' astonishment, began to glow along two distinct bands. As Tresca would later recall, the

> lines of augmented heat remained luminous for some seconds, and presented the appearance of the two limbs of the letter X. [...] They were the lines of greatest sliding, and also the zones of the greatest development of heat – a perfectly definite manifestation of the principles of thermodynamics [1].

What was observed that day at the *Conservatoire national des arts et métiers* in Paris has

---

[1] The study of discontinuous shear failure arguably dates back to Coulomb in 1776 [2], but Tresca was the first to note the concentration of deformation into narrow failure *zones* rather than along slip *planes* per se.

since become known as an *adiabatic*[2] shear band – a classic phenomenon in ductile metal forming [4]. But the fundamental principle has had a profound impact on our understanding of material failure far beyond metallurgy. It plays a unifying role across multiple disciplines within solid mechanics, with implications extending from geological processes to advanced engineering applications [5]. In earthquake mechanics, shear localisation governs fault rupture dynamics, dictating the onset of seismic slip [6]. In high-speed machining and ballistic impact, it controls chip formation and material fragmentation [7]. In geotechnics – the primary concern of this thesis – it underpins the mechanics of landslides, debris flows, and slope failures [8–10]. From the brittle fracture of metals, then, to the progressive failure of concrete and rock, the localisation of deformations often marks the onset of catastrophic material failure [5]. It therefore presents a critical area of study and, just as it fascinated Tresca over a century and a half ago, it continues to captivate, challenge and surprise researchers today. The reason for this is simple: strain localisation is as difficult to analyse as it is dangerous and ubiquitous. Indeed, as will be revealed (and lamented) over the course of this thesis, it remains one of the most formidable challenges in the field of continuum mechanics. But understanding and predicting strain localisation is not merely an academic pursuit; it is a crucial endeavour with profound implications for engineering safety, structural integrity, and natural hazard mitigation. It is hoped, a little vainly perhaps, that these two-hundred (or so) pages might be a small, positive contribution to that end.

1.1 The nature and significance of strain localisation

What is strain localisation exactly? Simply the concentration of a large amount of deformation into a relatively thin failure zone, rather than being distributed uniformly. It is triggered at the particular point within the material which fails first – often a stress concentration or miniscule weak spot of some kind. A cascade effect then channels all further deformation towards that location, producing a distinct region of intense straining such that the structure is understood to have *bifurcated*.[3] This is why strain localised into the 'X' pattern observed by Tresca, as that was where the shear stress peaked and then initiated yielding – "the lines of greatest sliding".

It is a phenomenon observed in a diverse range of media, including metals [11, 12], granular materials [8, 13–15], glasses [16, 17], ice [18] and even within liquids subjected to high rates of shear loading [19]. It can also occur in a number of distinct modes. As in Tresca's example, concentrated *shear* failure pervades a wide array of ductile materials –

---

[2] This means that the heat generated by plastic dissipation is retained inside the failure zone, cf. *isothermal* shear bands in which the heat is instantly conducted away, preventing localised temperature changes.

[3] In continuum mechanics, bifurcation means two distinct behaviours are present within a structure. Here, it manifests as a discrete failure zone surrounded by an otherwise homogeneous elastic domain.

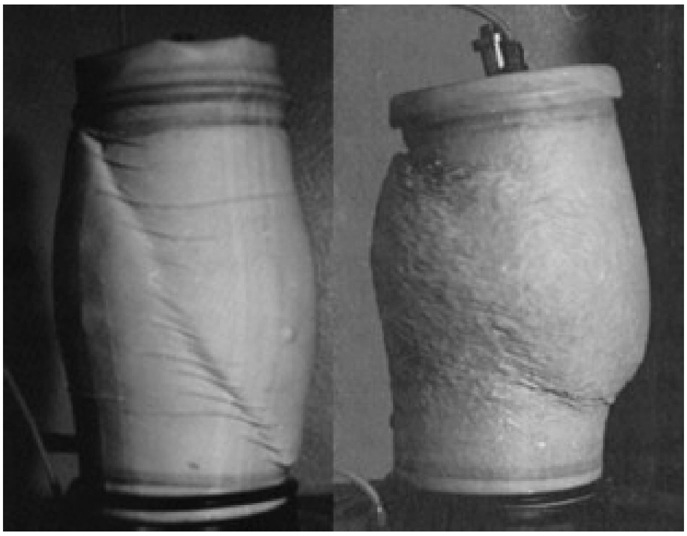

Figure 1.1: Diagonal shear bands observed in triaxial loading of fine (left) and coarse (right) sands, reproduced from [15]. The thickness of the failure zone is strongly tied to particle size.

particularly soils [20], examples of which are shown in Figures 1.1 and 1.2. But *necking*, commonly observed in tensile failure of metals, is also an example of strain localising to a small, finite zone [21], often preceding additional shear banding and, ultimately, fracture. Localised *crushing* and *compaction* are typical failure mechanisms in samples of timber [22] and stone [23] respectively, whereas *kink-banding* is noted in glass- and carbon-fibre reinforced materials and anisotropic rock [24]. Evidence of *dilation* bands in geomaterials has also emerged in just the last few decades [25]. But regardless of the way localisation manifests, it is almost always the result of minute fluctuations or instabilities occurring at the material microscale,[4] which intensify and accumulate under increasing load to induce bifurcation [26]. In granular matter like soils, this might take the form of small changes in the topology of the microstructure: particle assemblies rearranging their composition in order to distribute force, but compromising their structural integrity in the process [15]. Orthotropic materials like wood might experience micro-buckling in the compressive strands, fibres or columns which comprise them, causing a loss of stability [5]. Under dynamic loading, other materials (particularly metals) may experience localised heating due to plastic dissipation, reducing their particle-scale resistance to further deformation – a positive feedback loop responsible for adiabatic shear banding [4].

Strain localisation is therefore a kind of mechanical instability experienced by materials which undergo *softening* – a drop in the amount of force required to sustain a particular level of deformation, or a loss of resistance to any further deformations (see Figure 1.3). If a material begins to soften, then it may deform to a virtually unlimited degree without any

---

[4] Necking is an exception, as it arises due to a reduction in the *macroscopic* cross-sectional area of a specimen at high tensile strains, which leads to a loss of load-bearing capacity past a critical point (even though the true stress may be monotonic).

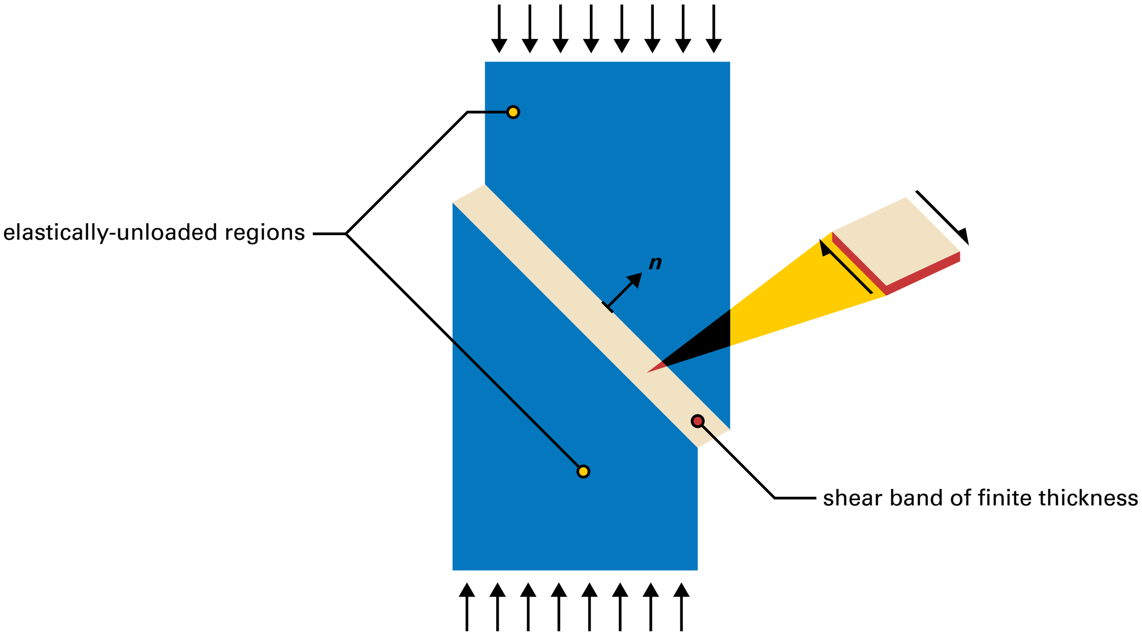

Figure 1.2: An idealised two-dimensional shear band resulting from uniaxial compression of an originally rectangular structure. Material elements in the band undergo simple shearing.

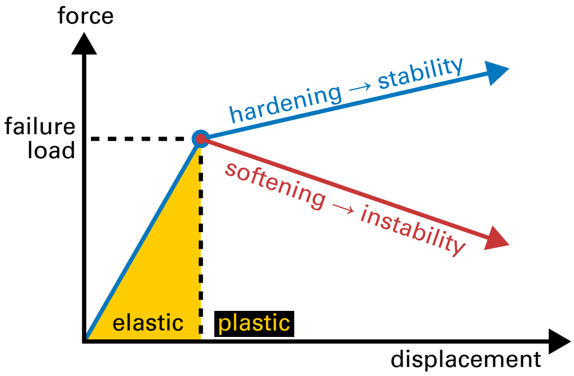

Figure 1.3: Comparison of force-displacement responses for strain-hardening and strain-softening structures. Note that materials exhibiting hardening at the material scale (stress-strain) can still demonstrate softening at the structural scale, leading to instability.

extra force being applied to the system. The dangers associated with this are obvious and immediate. Indeed, localisation is synonymous with sudden structural collapse; ductile landslides, crushing of concrete columns and failure of engineered geotechnical infrastructure (e.g. cuttings, embankments and footings) are salient examples. Being able to predict when, where and how this phenomenon manifests is therefore imperative to protect the stability of natural systems (or react to their instability), and to ensure the safe design of artificial ones. This necessitates engineering models which can reliably and robustly simulate strain localisation in diverse scenarios, involving complex materials, geometries and loading conditions. Ultimately, only computational tools can achieve this level of utility and versatility; as such, they form the principal focus of this thesis.

1.2 Modelling challenges

Despite its practical importance, the mechanics underpinning strain localisation is far from straightforward. Most conventional modes of analysis are (necessarily) rooted in macroscopic modelling paradigms, which neglect the true, discrete nature of real materials. In reality, all physical substances are composed of smaller, discontinuous units, yet to develop workable mechanical models, engineering analysis usually relies on the simplifying assumptions of material homogeneity and continuity. These idealisations have facilitated the development of the classical continuum theories which so powerfully underpin almost all of today's engineering analysis and design. But, in doing so, these models simply cannot predict localisation phenomena as, by definition, they lack the microstructural ingredients described above which govern their formation.

Of course, conventional modelling techniques can be contrived into modelling what might appear to be 'localisation', but the results are inconsistent, inconclusive and not physically meaningful [20, 27]. It is now well known that classical theories can only predict degenerate localisation bands of nil thickness (a mathematical plane), implying a discontinuous failure surface such that no volume actually undergoes yielding. Like crashing a car with no crumple zone, this means no energy can be dissipated, and abrupt, brittle failure ensues. This is clearly inconsistent with reality, in which localisation can be observed to steadily expend plastic work to produce such ductile phenomena as necking, and landslides with long run-outs. In fact, localised failure zones *always* have a finite (i.e. non-zero) size, correlating typically to a length scale associated with the material's microstructure – see Figure 1.1. In geotechnics, this idea was introduced by Roscoe in 1970 [8], when he rejected the traditional notion of the slip plane in favour of invisible *zero-extension lines*, analogous to the neutral axis in flexural analysis. Subsequent experimental evidence has since brought about a consensus that shear failure does not occur discontinuously in geomaterials, but rather is concentrated into narrow regions approximately 10–20 mean particle diameters in thickness [15, 27–30]. Thus without the addition of such an internal length scale to continuum theories it is impossible to use them to predict shear bands of finite thickness or, therefore, to model realistic post-failure material behaviour.

Accordingly, attempting to simulate strain localisation in this way with numerical techniques such as the finite element method leads to troubling results. The analytical failure zone is a discontinuous plane, but because continuum methods do not readily accommodate discontinuities, it instead takes the form of the smallest available discrete unit – a single row of elements in mesh-based techniques. Therefore the size of the localisation band is directly, and solely, determined by the resolution and layout of the mesh, and not by any intrinsic physical properties of the problem under scrutiny. The results are thus completely artificial. This means the rate of plastic dissipation, degree of ductility and residual strength are also entirely mesh dependent, with potentially severe implications when modelling situations where the post-peak behaviour is of particular significance, like simulations of landslides. But the danger lies in the fact that, with many typical choices of mesh size and material parameters, simulations can easily give the *appearance* of realistic strain localisation, when the results are actually devoid of meaning. Perhaps this is why so few analysts of large-deformation geomechanics even acknowledge this pathological deficiency in their modelling, never mind attempt to address it [9, 31].

However, this is not to say that we do not know how to predict localisation in a rigorous, reliable way; in fact the development of techniques for *regularising* the problem of mesh dependency stretches back almost forty years [27]. In short, it requires the inclusion of some characteristic length scale to govern the thickness of the failure zone, preventing the collapse of plastic deformations into a singularity. But how this length is incorporated into the model is a complicated matter, with potentially far-reaching consequences for the validity and tractability of the approach. Some techniques modify the constitutive model (the way in which stresses are related to strains) by introducing strain gradient effects or nonlocal interactions, thereby resisting particularly severe deformation gradients, but often in an artificial manner. Others enhance the richness of the model to explicitly represent microstructural phenomena, e.g. the interparticulate motion and contact of the soil grains. Unfortunately, all come at the expense of convenience and computational cost, and require additional, often non-physical, parameters to be determined or tuned. What is striking, though, is the lack of rigour which is generally adopted in implementing these approaches – namely the widespread reliance by most analysts of strain localisation on linearised *small-strain* formulations, which assume that deformation gradients are *infinitesimal* in magnitude. How can this be reconciled with the very large, complex and nonlinear deformation patterns which are characteristic of strain localisation, especially in geotechnical structures? Put simply, it cannot. In large-deformation scenarios, linear theories do not offer accuracy and are incapable of capturing the true evolution of failure mechanisms; they cannot even guarantee satisfaction of equilibrium. Therefore, to formulate a predictive framework with any hope of promising a useful degree of trustworthiness, restrictive small-strain assumptions must be abandoned and *finite* strains embraced. However, such formulations remain scarce (particularly in numerical implementations) presenting an opportunity to develop a novel, robust computational framework capable of more accurate simulation of strain localisation in geomaterials.

This comes at an exciting time for the study of this important, and pervasive, failure mechanism. New insights derived from high-resolution digital image correlation, X-ray computed tomography and discrete element modelling are unlocking greater understanding of the particle-scale mechanisms that govern failure initiation and progression [30,32,33]. Concurrently, machine learning and data-driven approaches are increasingly being applied to identify hidden patterns in experimental data, potentially offering novel perspectives on the physics of localisation [34–36]. In particular, neural networks and statistical learning models hold promise in uncovering features of strain localisation that may not be evident through conventional analytical techniques. Moreover, interdisciplinary research is expanding the conceptual reach of localisation studies; for instance, analogies have recently been drawn between granular mechanics and epidemiological models, where shear bands are likened to zones of herd immunity – structured yet dissipative states of equilibrium [37,38].

Therefore, in summary, while substantial challenges remain an intrinsic part of the accurate modelling of strain localisation, they also form a compelling opportunity for progress towards a more rigorous and predictive understanding of its formation. To that end, this thesis aims to contribute to the ongoing effort to develop robust, physically-consistent computational models of localised geotechnical failure. Its specific objectives and scope are laid out in the following section.

1.3 Objectives, scope and thesis outline

The principal objective of the research behind this thesis is to develop and validate an advanced computational technique capable of accurately capturing strain localisation in geomaterials. This work must therefore address the following fundamental challenges.

1. *Limitations of classical models:* Strain localisation is a phenomenon governed by microstructural processes which are not accounted for by classical continuum theories. Attempting to use conventional techniques to predict localisation leads to meaningless results which are both unstable and unphysical. An appropriate modification to the approach must be identified and adopted.

2. *Large deformations:* Geotechnical failure processes are marked by severe, heterogeneous deformations, and complex internal and boundary dynamics. This must be taken into account by using a mechanical formulation of an appropriate level of mathematical fidelity, and selecting a sufficiently resilient numerical method with which to implement it.

3. *Computational practicality:* All models, however rich, exist at a particular level of abstraction. The trade-off between realism and tractability must be such that the

method is feasible for large-scale, three-dimensional engineering applications such as slope stability analysis, balancing numerical accuracy with efficiency.

In responding to these points, the remainder of the thesis is structured as follows.

- Chapter 2 (p. 9) reviews numerical methods for large-deformation geotechnics, evaluating their advantages and limitations. The implicit material point method (MPM), stabilised with generalised interpolation basis functions and ghost penalisation, is selected as the computational framework. A conventional formulation is provided to establish a basis for later developments and to illustrate the inadequacy of classical techniques in capturing strain localisation.
- Chapter 3 (p. 41) considers the analytic pathologies of localisation in more depth, and surveys various regularisation strategies. Nonlinear micropolar theory, identified as a rigorous and effective approach for modelling granular materials at finite strains, is adopted. This chapter formulates the theory in a purely elastic setting, details its implementation in the MPM, and verifies it through numerical examples.
- Chapter 4 (p. 111) extends the formulation to incorporate material failure via elastoplasticity. Once implemented in the MPM, the method is applied to localisation problems to assess its robustness and is validated against experimental data.
- Chapter 5 (p. 149) summarises the key findings of the thesis, discusses the limitations of the developed approach, and provides recommendations for future research.

As the development of the continuum formulation and its numerical implementation embodies a significant amount of work alone, the scope of this thesis unfortunately cannot extend to particularly realistic physical problems, or highly advanced empirical or phenomenological constitutive behaviour. These might follow as future extensions of this work.

CHAPTER 2

The material point method

This chapter introduces the numerical method which facilitates the core workings of this thesis, via its history and development, advantages, hindrances and mathematical formulation. A generic algorithm of the implicit type is presented, some stabilisation techniques are outlined, and the chapter concludes with some naïve simulations of strain localisation.

2.1 Introduction

The discipline of computational mechanics can trace its origins to antiquity. Force, and its interaction with matter, have been studied at least since Aristotle occupied himself with the lever in the 3rd Century BCE; the ancient Babylonians were using numerical methods many millennia before al-Khwarizmi, writing in 9th-Century Persia, described the eponymous *algorithm*. What came to be known as *classical* mechanics has its roots in an orchard in Lincolnshire, where Newton formulated his law of universal gravitation – the catalyst of his seminal laws of motion and the *Principia* of 1687 [39]. Although da Vinci made some compelling observations of flexible beams, Jacob Bernoulli was really the first to consider the deformable continuous structure through this lens. Euler then furnished us with applications, and with the tensor Cauchy elevated the theory to generality. Through the contributions of Kirchhoff, Navier, and many others a nascent subdiscipline matured into a field in its own right; *continuum* mechanics was born [40]. But it was the advent of the computer in the 20th Century which would herald some of the most rapid advances in this corner of engineering science. Breaking down a complicated physical problem into discrete elements – each requiring only a few simple instructions to be carried out by a machine – to solve some governing equation would prove to be a brilliantly powerful and transformative ability. As computing resources became more readily accessible to the typical analyst, computational mechanics duly evolved into an integral part of engineering design.

Traditionally, the computational mechanics discipline has been split into two subdomains: the analysis of deformable solids, and the dynamics of fluids. The former, associated with small overall deformations relative to the problem dimensions, naturally favours *Lagrangian* techniques where the motion of the continuum is tracked from its starting position, typically via an attached mesh. Here it is impossible not to mention the ubiquitous finite element method (FEM), now a cornerstone of mechanical, civil and structural engineering, which exemplifies this approach [41]. Conversely, the computational fluid dynamicists produced *Eulerian* techniques, simulating flow through fixed spatial grids by applying conservation laws to finite volumes or examining finite differences [42]. Both approaches have yielded revolutions in their respective fields. But what happens when the subject of the analysis is neither a well-behaved solid, nor a freely-flowing liquid or gas? When the substance under consideration demonstrates such large and complex deformations and boundary dynamics as to invoke tangling of any mesh tracking the material's motion, yet fundamentally cannot be treated as a fluid due to its strongly history-dependent nature? This is precisely the challenge to be confronted in the kinds of geotechnical failure events motivating this thesis. In such cases, neither of the two conventional approaches may be applied without concessions in accuracy or reliability. Consequently, a great deal of work spanning beyond the last half-century has been dedicated to the development of new – hybrid or otherwise – techniques capable of simulating such highly-mobile solid media, without numerical malfunction.

2.1.1 Towards robust simulation of large deformations

Per a recent review article of numerical methods for large-deformation geomechanics [43], techniques fall into two major camps: continuum methods, where the true, granular nature of the material is overlooked and instead continuous field equations are posed, discretised and solved, either transiently or in the steady state, and discontinuum methods, based on discrete inter-particulate contact, reaction forces and friction. Among the first set the pre-eminent example is the FEM, mentioned above. However, its usual Lagrangian mesh-based discretisation means that large deformations, such as those encountered in the post-failure response of geomaterials, quickly lead to a deterioration in performance as the elements become distorted – even inverted – and a remediation strategy must be adopted [9, 41]. A representative example is presented in Figure 2.1.

The arbitrary Lagrangian-Eulerian (ALE) approach [45] to this challenge is to take the malformed mesh, generate a new, regular mesh across the problematic area or volume, and then project all state variables (e.g. stress and strain) from the old integration points onto the new, allowing the simulation to resume with the fresh discretisation. Although ALE formulations represent an immediately appealing, 'common sense' tactic to remedying

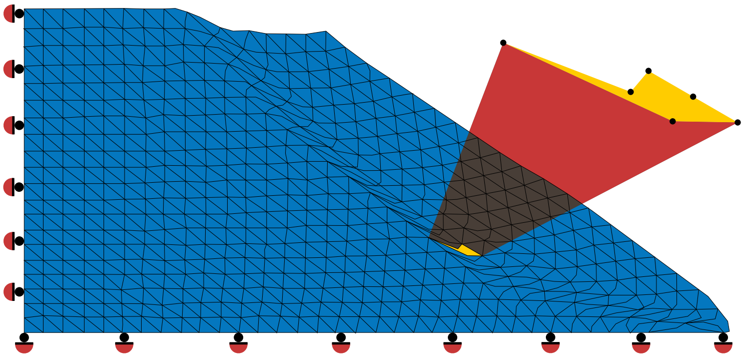

Figure 2.1: Extreme mesh distortion in finite element analysis of a slope stability problem, after [44, Fig. 1.1]. If the simulation is advanced further the highlighted element – originally an equilateral triangle – might soon suffer inversion.

mesh distortion, requiring no changes to the fundamental numerical method, questions immediately arise surrounding how best to remap the historical variables. Augarde et al. [43] name no fewer than four such recovery or interpolation techniques, and furthermore Li and Liu [46] caution that the repeated projection of convective terms (momentum, for example) may lead to numerical diffusion and other artefacts which must be artificially stabilised. Even the remeshing step itself is non-trivial: should the number of elements and nodes be maintained – and their connectivity preserved – or should the new mesh be redrawn completely, as if from new? Again, there is no clear consensus [43]. Altogether, this presents the analyst with a challenging landscape to navigate – and a substantial computational burden if the magnitude of the considered deformations demands frequent remeshing, particularly in three dimensions.

Complementing the ALE framework, the coupled Eulerian-Lagrangian (CEL) method [47,48] has seen a recent proliferation into commercially-available codes (namely Abaqus [49] and LS-DYNA [50]). The method has been applied to problems involving ballistics, hydrodynamics and soft-tissue biomechanics [51], but in geotechnics it is chiefly used for soil-structure interaction (e.g. [52]). Using this application as a model, the soil, which is subject to large deformations, is analysed on an oversized Eulerian mesh which remains stationary through the analysis, and the structure – usually several magnitudes stiffer than the soil and exhibiting much smaller relative deformations – is captured using conventional finite elements (the 'Lagrangian' part). The key component – their interaction (coupling) – is handled with a contact algorithm or constraint equations, with information such as force, velocity and boundary conditions exchanged between the two regions to ensure consistency; for example, the stress within the penetrated Eulerian grid cell drives the reaction force against the interface of the Lagrangian body. However, the approach shares many of the same problems surrounding diffusive advection as the ALE method, and additionally the complexity of setting up and interfacing the two meshes is computationally costly. Sharp interfaces or boundaries also pose a challenge to the Eulerian discretisation, which can struggle with accurate representation and may lead to artificial 'smearing' of interfaces and discontinuities [41, 48]. This is particularly relevant to the work in this thesis, where accurately capturing strain localisation (manifesting as solution discontinuities) is essential.

Another approach to the problem of mesh distortion is to disregard the mesh entirely. Smoothed particle hydrodynamics (SPH) is the original meshless (or meshfree) method, developed in the 1970s for astrophysical fluid mechanics [53, 54] but since adapted for engineering applications, including geomechanics [55]. Rather than discretising into elements, the method uses particles to approximate portions of a continuous medium. Each particle carries a localised 'amount' of continuum properties (e.g. mass, volume, stress), effectively discretising the material without needing a connected mesh. SPH solves the governing equations by considering particles' interactions with their neighbours, achieved by spatially distributing the properties and state variables of each particle via a radially-symmetric kernel function which decays with distance, ensuring each particle only wields influence over a chosen smoothing length. Standard equations (like mass conservation or momentum balance) are then assembled at each particle, incorporating the cumulative effect of nearby particles, and solved as a linear system [56]. Obviously this requires implementation of some kind of search algorithm to determine (at each step of the analysis) which neighbours to include in each particle's set of calculations, running up a substantial computational cost for problems involving a large number of particles [9].

As a meshless method – and pertinent to this work – SPH does offer benefits when modelling strain localisation: without a grid to bias the orientation of the response (see Sections 2.4 and 3.1.1), the localisation zone is free to form in a less artificial manner [57]. However, without some additional regularisation technique, the absence of a mesh per se cannot solve the fundamental problem posed to continuum methods by localised failure, and the solution is still highly discretisation-dependent [58, 59]. Numerical difficulties also arise in sparse regions of the domain, which may be exacerbated by instabilities from under-integration by the point-based scheme used in the standard formulation [9]. The imposition of boundary conditions is typically another challenge to the SPH user, requiring complex and often problem-specific treatment, and poor interpolation of the kernel function near the material's (usually ill-defined) edges can lead to inaccuracies too [56]. Ultimately, these difficulties mean that SPH has seen little uptake in the geotechnical community [43].

Elsewhere, the other particle-based continuum techniques to note here include the element-free Galerkin (EFG) method, the meshless local Petrov-Galerkin (MLPG) method and the particle finite element method (PFEM). Although only the MLPG approach can be considered truly meshless, all three methods abate the problem of mesh distortion by relying on a discretisation into nodes (without fixed connectivity) which carry the field and history variables. In the typical EFG case, moving least squares approximations (or other interpolants, e.g. maximum entropy shape functions [60]) are used to build up an interpolation field across the cloud of nodes, integration of which produces a weak form of the governing equations to be solved for the nodal unknowns [61]. Numerical integration – the step which generally requires use of a mesh – takes place over a node's zone of influence, which does not possess an intrinsic definition but is determined by the resolution and connectivity of the mesh. The inefficiency of this process, particularly in smaller simulations, is widely perceived as a major drawback of the method [43] and, as with SPH, boundary conditions demand special consideration. Nevertheless, EFG methods are still used by researchers today, in disciplines as diverse as computer vision [62] and epidemiology [63].

Introduced by Atluri and Zhu [64], the MLPG method leverages local weak forms of the governing equations, formulated over small subdomains surrounding each node rather than a global domain, to approximate field variables. As the weak forms are solved locally, complex boundary conditions may be handled more flexibly, even admitting the possibility of infinite boundaries [65], and integration of each subdomain takes place locally, without any requirement of a mesh or background cell [46]. However, as with other meshless methods, the MLPG approach faces challenges with boundary representations and manipulation, as well as with computational efficiency, as the construction of local subdomains and integration of weak forms for each node demand significant computational resources, particularly in 3D applications [9]. But despite these challenges, the method has found applications in fields ranging from fracture mechanics to biomechanics [66].

The PFEM uses a FE approach where the nodes are (re-)connected at each step of the simulation, typically via a Delaunay tessellation, to construct a conventional mesh [9]. The method is analogous in many ways to the ALE formulation described earlier, and its similarities with the conventional FEM make the PFEM an attractive choice for researchers working with large deformation geotechnics (e.g. [67,68]). However, the frequent, expensive remeshing required for problems involving rapidly evolving geometries places a restrictive limit on the efficiency of the method; furthermore there is no guarantee, particularly in 3D, that the generated mesh will be of a particularly high quality anyway (in terms of element aspect ratio) or even mass-conserving [69].

Here it would be remiss not to at least mention the last major class of particle-based continuum methods – and the focus of this chapter – the material point method (MPM). But as the MPM is in many ways the destination of this discussion, and as such will be explored at length later, it is useful to first consider the merits of discontinuum methods. Unlike continuum-based approaches, these are tools which abandon the assumption that the behaviour of the body or bodies under consideration can be described by continuous field equations. They therefore require no conjecture on the relationship between displacements, strain and stress, focusing instead on the motion of the discrete particles constituting the material's microstructure. This shift in perspective allows the material behaviour to emerge naturally from particle interactions [43].

Developed from the late 1970s [70] (and initially called the *distinct* element method), the discrete element method (DEM) dominates this genre of numerical technique [43,71]. Although it is now predominantly used as first intended (i.e. for the analysis of geomaterials – see e.g. [72,73]), it can be applied to any problem involving what could be considered a ‘granular assembly’ – crowd dynamics through London Underground stations, for example [74], and the interesting multiphysics challenge of simulating roasting of coffee beans [75]. Particles are governed by a dynamic application of Newton’s laws, are generally modelled as spheres – either perfect or oblate, singular or composite – though non-spherical DEMs have been developed, based on e.g. level-sets [76] or splines [77], and can be rigid or deformable. Contact forces between the particles, including normal and tangential forces, are calculated based on the relative overlap at their contact points (which must be located at each time step), and friction laws are applied to simulate sliding and rolling and to artificially guard against free rotation. This makes the DEM particularly effective in simulating material failure mechanisms such as interparticulate cracking, fragmentation and granular flow, which are difficult to capture using continuum approaches [71]. However, the DEM is computationally expensive for human-scale problems – especially with realistic particle angularity – as the number of particles and their interactions grow significantly with domain size. Therefore, while it can offer valuable insights into fabric evolution at the micro- and mesoscale (which can go on to inform models used in continuum methods), the DEM has limited applicability to large geotechnical failure events like landslides, at least with today’s computational resources [9, 43].

In summary, large deformations represent a significant challenge to any numerical modeller. This discussion has highlighted how there is a great diversity in approaches to dealing with the issue. But a common thread linking these technologies is that each has its own particular set of drawbacks – in terms of expense, inaccuracy or instability. As it would be futile to go in search of proverbial free lunches [78], one must be content to simply minimise the impact of these drawbacks by choosing the most suitable method for the problem at hand. In the context of this thesis, which addresses three-dimensional problems with large physical dimensions, a continuum-based approach is particularly well-suited. It would be convenient to have a method that can readily emulate well-established techniques from the finite element literature and, needless to say, reliability, efficiency and ease of stabilisation are all desirable properties too. As will become clear from the following, it is for these reasons that the MPM was selected.

2.2 Overview of the material point method

This section does not pretend to be in any way comprehensive; for a more detailed examination of the various MPMs which have been developed over the last three decades the reader is referred to the various reviews published with that express aim [79–81]. Instead, the purpose here is simply to refine the scope of this work to (and justify the choice of) the MPM formulation implemented in the rest of this thesis.

2.2.1 Introduction

First developed in the Los Alamos National Laboratory to model fluids [82–86] and plasma [87, 88], the MPM has a long history under its previous guises (the particle-in-cell method, PIC [82–85], and subsequently the fluid-implicit particle method, FLIP [86, 87]) going back to the middle of the last century. But since its genesis in the 1990s [89, 90] as a distinct method for history-dependent materials, it has been used for a wide variety of large-deformation problems across solid mechanics, for example fracture [91], drag anchor installation [92], cardiac mechanics [93], animation of snow [94] and sand [95], and even demystifying historical suspicious deaths [96]. The MPM is perhaps most accurately described as a particle-based continuum method immersed in an unfitted mesh, and is not therefore a meshless method, as some would have it, but nor is it solely mesh-based. Instead drawing ideas from both categories, the MPM leverages advantages from each, and in particular enjoys a large overlap with the FEM – a synergy which was succinctly expressed by Guilkey and Weiss, who summarised the MPM as “a finite element method where the integration points [...] are allowed to move independently of the mesh” [97]. Instead of discretising the domain into elements, these integration points (the *material points*) are used to represent the material body, carrying all state variables such as stress, mass and volume. The material points, which are tracked in a Lagrangian sense, deform through a ‘background’ mesh (or *grid*), which is used solely as a computational device on which to perform a standard finite element calculation. It is always reset or replaced after each load or time step (often the original grid is simply reused throughout an analysis), allowing the material points to undergo large deformations without the problem of mesh tangling. As the grid topology is independent of the deformation, the MPM does not demand the large computational cost needed to remesh from scratch, requiring only an element search to determine the material points populating each grid cell at every step, but this is usually simplified by using a regular Cartesian mesh. Moreover because the same material points are used throughout the simulation, history variables are Lagrangian and do not therefore require repeated projection (as would be performed in e.g. ALE), avoiding the instabilities and diffusion associated with Eulerian advection, and mass is automatically conserved.

Although many diverse formulations have now been developed, a typical MPM implementation is characterised by the following steps, also depicted in Figure 2.2:

1. An element search is conducted to ascertain the relative positions of the material points to the grid. The information held at the material points is mapped to the grid nodes, constructing global matrices and vectors in the same way the Gauss points are used to integrate the governing equations in the FEM.

2. The assembled system is solved for the nodal unknowns, which are then mapped back to the material points. If the problem is nonlinear then repeated remapping, solution and updating may be necessary.

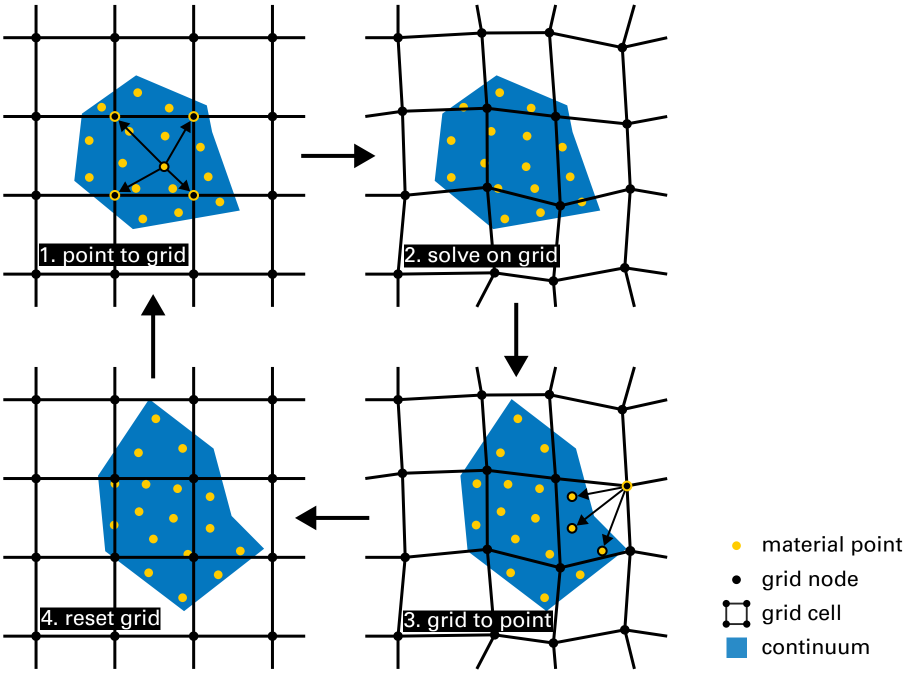

Figure 2.2: The key numerical steps of a material point method. The continuum (blue) is discretised into material points (MPs, yellow) immersed in a computational grid (black).

3. The positions (and all other state and history variables) of the material points are updated accordingly.

4. The grid is reset to its original position, allowing the process to begin again for a new time or load step with a new undistorted mesh.

Each step will be described in more detail in Section 2.3 for the particular formulation of the MPM adopted in this work, and an algorithm is given at the end of Section 2.3.3.

2.2.2 Time integration

How the simulation progresses through time (i.e. how the state of the system is computed in each successive step) depends on the particular choice of time integration scheme. This, in turn, often depends on whether the problem is *dynamic* or *quasi-static* in nature. Dynamic problems explicitly account for inertia, meaning that accelerations play a key role in the system's behaviour. In contrast, quasi-static problems exclude inertial effects, assuming instead that the system is in equilibrium in each step. As time derivatives are no longer involved, quasi-static analysis therefore takes place in dimensionless *pseudo-time*, where steps only reflect an ordering and not specific intervals of time in e.g. seconds.

The first MPM formulation [89] used an *explicit* time integration scheme, in which accelerations are a primary unknown of the system. These determine the velocity and displacement increments for the time step ahead, thereby marching the simulation through time, typically using some kind of forward Euler method. As for the constitutive response, a distinction is drawn between the update-stress-first (USF) and update-stress-last (USL) techniques, which use the material point displacements from the beginning or end of the time step respectively, having implications for the stability and accuracy of the method – see [98]. Specifically, the USF approach is computationally more straightforward to enact, but may introduce inaccuracies as the stress state is not necessarily consistent with the actual deformation at the end of the step. This results in numerical instability and oscillations, particularly in high-deformation scenarios, which may be partially rectified with the USL approach. This adjustment improves stability and accuracy, but numerical artefacts may still arise in large steps when mapping between material points and the grid. To further mitigate these challenges, the modified update-stress-last (MUSL) strategy refines the USL approach by separating velocity and deformation updates from stress updates, creating an intermediate velocity update before stress is calculated at the end of the time step. The stress is updated based on a deformation gradient calculated from this intermediate velocity field, which improves the representation of the deformation path and therefore better aligns the stress state with the actual deformation experienced by each material point.

Although explicit formulations seemingly still dominate the MPM literature [80], they only offer numerical stability when the time-step size is smaller than some value determined by the Courant-Friedrichs-Lewy condition – and often significantly smaller due to other nonlinearities [41]. This can become highly restrictive and inefficient for complex problems requiring a very large number of short time steps. Instead *implicit* time integration may be adopted, where rather than using the state of the system in the previous step to produce an estimate of its next state, an equation describing that state is posed and solved directly. While this demands more computational effort than explicit integration, it guarantees a precise solution (in linear problems, at least) regardless of the size of the step, and is therefore unconditionally stable. Implicit analysis can be employed for dynamic problems (the Newmark-beta method [99], for instance), but it is particularly useful for quasi-statics wherein the forces and displacements to hold the body in static equilibrium are found (often iteratively, in nonlinear problems) for a particular load or displacement level, requiring inversion of a system tangent matrix. As it allows for significantly larger step sizes, implicit MPMs can offer reduced computational effort for problems involving complex material behaviours, such as those commonly observed in large-deformation geotechnics [80]. This is therefore the scheme selected for this work.

The first implicit MPM emerged in 2003 [97], with a semi-implicit[1] formulation following a year later [100]. Although the perceived difficulty associated with analytically deriving the consistent tangent required for implicit solutions may be the cause of the method's limited uptake in the wider MPM community, it is becoming an increasingly popular

---

[1] Semi-implicit time integration entails an explicit treatment of the inertia, while the internal forces are dealt with implicitly. It typically offers greater stability than purely explicit analyses, at the cost of greater computational complexity.

option – particularly among geomechanicians [80]. Current trends seem to be towards implementation of advanced constitutive models, which may be transplanted easily from FEMs (e.g. [101, 102]), as well as more effective stabilisation techniques to offer improved robustness (see elsewhere in this Section 2.2 and in Section 2.3.4).

2.2.3 Material point description and basis functions

One of the most crucial components of any MPM is the way in which information is exchanged between the material points and the grid nodes. Traditionally, this mapping is performed through the use of grid *basis* (or *shape* or *interpolation*) functions, for which a proper mathematical definition will be developed later. For now though, it is sufficient to know that each node has its own basis function, and in summing these functions, an interpolation field of the discrete nodal quantities is built up across the grid cell. This provides the critical mechanism which converts between discrete and continuous problems, allowing an unsolvable field equation to be expressed in terms of a finite linear combination of discrete (nodal) unknowns. This system can then be solved by a machine. Although the basis functions may take one of a large number of diverse forms (forming a research topic in its own right), Lagrange polynomials are the most common type employed across the FEM literature [41] and, consequently, in MPMs too. In the MPM, though, the polynomial order is usually limited to one, as only linear functions are non-negative throughout, guaranteeing that material points cannot generate unphysical negative masses at grid nodes.

Equally fundamental is the continuum representation itself. In the first instance [89], the material points were indeed envisaged as just *points*, defined by a single set of co-ordinates (but still representative of a certain discrete amount of continuum). Although this led to a fairly robust method [80], which in this thesis will henceforth be referred to as the 'standard' MPM, it also resulted in the MPM's most notorious difficulty: the *cell crossing instability*. During the course of a simulation, if a material point crosses a grid cell boundary, then the spatial gradient of the basis function linking the material point to that edge's nodes changes sign. The internal force is mapped to the nodes with these gradients, but the corresponding external forces rely only on the basis function values themselves, which do not change sign. This mismatch creates an abrupt, unphysical oscillation which can introduce significant errors and artefacts into the results.

There are two major ways to tackle the instability: changing the definition of the material point, or adapting the kind of basis functions used. Of course, both have their particular advantages and disadvantages. Among the first set, the most significant development is the generalised implicit material point method (GIMPM) of Bardenhagen and Kober [103], wherein material points are defined explicitly as rectangular or cuboidal domains, perhaps extending into several grid elements. As the entirety of the material point is now unlikely to cross a cell boundary at once, there can be no sudden oscillation in the response, and the stress field remains smooth. Conventionally the GIMPM domains either remain constant (uGIMPM), or are updated by stretching, changing in volume and aspect ratio but remaining rectilinear (cpGIMPM). Although this might not reflect the actual deformations experienced by the material point, and domains may end up overlapping or splitting apart, it greatly simplifies the element search procedure. Furthermore techniques where the domains are additionally rotated and sheared (such as the convected particle domain interpolation MPM [104] and its successor [105]) can result in highly deformed domains – mesh distortion, effectively – the very problem the MPM was designed to avoid [106].

On the other hand, the other most established technique to minimise cell crossing errors is to use B-spline interpolation instead of Lagrange polynomials [107,108]. B-splines are piecewise polynomial functions that offer higher-order continuity and smoother gradients across grid cell boundaries, thereby eliminating the abrupt change in sign described earlier and so avoiding instabilities from cell crossing. However, adoption of B-spline interpolation introduces several challenges. Firstly, the computational cost increases due to the more complex evaluation of higher-order basis functions and their derivatives: B-splines have a wider support than linear functions, meaning that each material point influences more grid nodes, leading to more cumbersome system matrices. Secondly, the extended support can make it difficult to enforce certain boundary conditions directly, often requiring additional techniques like penalty methods or constraint equations. This added complexity can complicate the numerical implementation and potentially affect the robustness of the simulation [80,109].

Therefore, the chosen approach in this work is to use the GIMPM, as implemented implicitly by Charlton et al. [110]. This method provides an attractive balance between the computational simplicity of piecewise linear Lagrange polynomial basis functions and the robustness of the simulation even for very severe deformations, without incurring prohibitive computational costs.

2.2.4 Boundaries

Although far less problematic than in other particle methods including SPH [43], the treatment of boundaries in the MPM is still a persistent challenge. This is because only the *volume* of the continuum is discretised, providing no intrinsic representation of its boundary to be tracked or manipulated. While this allows complex boundary dynamics, self-contact and amalgamation to be captured in a natural way, it can become a hindrance when it is desirable to impose specific behaviours on the edges of the material. The MPM's deficiency in this regard was aptly summarised by Coombs, who lamented that the method's

> greatest advantage, the decoupling of the deformation of the physical material from the computational grid, is also its greatest challenge in terms of robust and efficient engineering computations [111].

Unfortunately this challenge engenders difficulties in terms of both the fundamental numerical stability of the MPM, as well as its tractability with respect to boundary condition imposition.

However, for these issues to be discussed properly it is necessary first to formally introduce boundary conditions themselves, of which there are two kinds generally encountered in solid mechanics.[2] The first, known as the *essential* or *Dirichlet* boundary condition, directly specifies the value of the primary field variable (usually displacement), either fixing it at nil or prescribing some value to apply, perhaps over series of increments. The other kind, the *natural* or *Neumann* boundary condition, can also be applied over a series of load steps, but instead specifies the value of the derivative of the primary field variable, which in solid mechanics corresponds to a traction (force per unit area). The special case is the *traction-free* Neumann boundary condition, which is really the absence of any applied boundary condition at all and implies a free surface with no load applied. For both Dirichlet and Neumann conditions, a further classification into *homogeneous* and *inhomogeneous* is commonly made, which respectively denote fixing the particular quantity at zero, or at some other value.

Imposing boundary conditions is straightforward when there is a computational structure conforming to the material's geometry to allow boundaries to be precisely defined (as provided by the mesh in the FEM). In contrast, the MPM lacks this inherent boundary representation since the grid does not generally conform to the material boundaries, unless they happen to coincide with grid lines. Consequently, boundary conditions may only be applied in the conventional way when the boundary is to remain stationary over a grid line, usually restricting application to homogeneous Dirichlet boundary conditions. However, in many cases, it is in fact perfectly sufficient to set up the analysis so that any fixed boundaries are aligned with the grid, applying loads directly to specific material points to progress the simulation. The loaded material points may either be distributed throughout the continuum to represent body forces like gravity, or along particular edges or surfaces to approximate Neumann boundary conditions, as demonstrated in [112].

Although this rather rugged strategy typically provides an adequate level of accuracy, it is only really effective in fairly simple, idealised problems [80]. In order to deal with more generalised circumstances – and to provide more realistic and useful analyses – many other techniques have been developed for applying non-conforming boundary conditions in the MPM. For example, the *moving mesh* method [113, 114] entails dynamically adjusting the grid (either by individually shifting grid lines or wholesale scaling of the grid) such that there is always a grid line coincident with the surface requiring treatment. This is simple for coplanar Dirichlet boundary conditions, wherein the grid may be updated at the beginning of each new load step with the applied displacement increment from the last step, but is limited to rectilinear boundary shapes and motions. Neumann boundary conditions

---

[2] Excluding *Robin* boundary conditions, which are not widely used and only comprise a linear combination of the other two anyway.

are also a challenge, as they often result in *a priori* unknown boundary deformations which cannot be reflected in a simple translation of the grid line. Instead, non-conforming Neumann boundary conditions generally require some kind of explicit tracking of the moving boundary [115], which may be represented as a collection of zero-volume *dummy* material points, or perhaps as a B-spline for more complex geometries [116], but these struggle with significant boundary distortions and self-contact. More recently, investigations have taken place into imposing Neumann boundary conditions without an explicit boundary representation, instead using a prescribed underlying virtual stress field [117], as well as into the consistency of various imposition techniques [118]. Elsewhere, penalty methods are also commonly used to weakly enforce Dirichlet boundary conditions (e.g. [119]), and there have also been investigations into the use of Lagrange multipliers [120] and level-sets [121], however each of these is accompanied by increased computational cost, algorithmic complexity and, frequently, numerical instabilities.

In addition to the conundrum of rigorous boundary condition application, another problem brought about by the unfitted nature of the mesh is that of the *small cut*. Distinct from, but no less egregious than, the MPM's more widely-debated variational inconsistencies,[3] it represents one of the most significant threats to the stability of the method – a fundamental danger which must be confronted for the numerical formulation to be deemed truly *reliable* [111]. The issue is brought on when a material point only partially intersects a mesh element: potentially a common occurrence in any analysis. If, for example, a grid cell is empty apart from some vanishingly small sliver of a GIMPM domain, then that cell is likely to have a stiffness many magnitudes smaller than that of the bulk of the continuum. This disparity is captured in the *condition number* of the stiffness matrix, which is strictly speaking the ratio between its largest and smallest eigenvalues, and provides a measure of how easy the matrix is to invert. As the small cut becomes ever smaller, the condition number tends to infinity, and the global system can no longer be solved. This effectively kills the simulation.

In explicit MPMs, where it is instead the conditioning of the mass matrix under threat, the small cut issue may be partially mitigated by adopting the MUSL technique described in Section 2.2.2. However, this does not affect construction of the stiffness matrix, and cannot be adapted for implicit MPMs. Therefore, reworking a methodology developed for another unfitted method [122], the so-called *ghost stabilisation* technique was formulated for the MPM by Coombs [111], and is the method adopted in this work. Ghost stabilisation a penalty method which examines gradients in the solution field across grid cells lying around the boundary, and penalises any sharp jumps with respect to some heuristic *ghost penalty*. This manifests as an extra force-like term in the weak statement of equilibrium, and finally as extra terms in the stiffness matrix, preserving its conditioning and allowing

---

[3] For example, the poor (or, in any case, non-exact) quadrature of the polynomial basis, and the loss of continuity and therefore smoothness caused by cell-crossing.

its inversion even for arbitrarily small cuts. The marked increased in stability, in addition to less oscillatory stress and strain fields, elevates the MPM's reliability to a much more dependable level. As Coombs argues [111], this paves the way for the MPM to become the natural choice for analysis of large-deformation problems across geotechnics.

2.2.5 Volumetric locking

Another problem which commonly arises is that of poor numerical integration. In the FEM, the polynomial basis may be integrated exactly when using Gauss-Legendre quadrature, which demands that integration points be located at specific local positions within elements. However, in the MPM, the integration points move independently of the mesh. This independence makes it impossible to maintain the precise Gauss-Legendre positions unless the material points are deliberately initialised that way. Even then, this setup is limited to only a single load step since the remeshing step alters the relative positions between material points and the grid. Although ghost stabilisation goes some way to preventing instabilities arising from severely underpopulated elements with low stiffness (which might result in spurious deformations) a common strategy is to begin the simulation with a large number of material points per grid cell [80]. However, this can result in *volumetric locking* when modelling isochoric (volume-conserving) material behaviours, such as certain types of elastoplasticity, or when Poisson's ratio approaches $\frac{1}{2}$. This is a well-known phenomenon experienced by MPMs, and is typically brought about by point-wise over-enforcement of isochoricity. In a real isochoric material (e.g. an elastomer) the total volume of the body does not change, but the material may deform in ways that involve localised volume changes. But the discrete nature of numerical tools like the MPM means that volume conservation cannot be enforced globally, and must therefore be imposed point-wise, at each material point. Therefore if there are many of these points, motion becomes overly restricted and the continuum locks, demonstrating a non-physical over-stiffness. Regrettably this tends to be exacerbated when modelling complex modes of deformation, such as those observed during strain localisation – especially when attempting to capture the motion with linear basis functions [123].

Fortunately, several stabilisation techniques have been developed to regularise volumetric locking in numerical methods. In the FEM, the most common strategy is to use a lower-order Gauss quadrature scheme than is strictly demanded by the order of the polynomial basis [124]. This process of *reduced integration* uses fewer integration points – and is simple to implement – but cannot be exploited in the MPM, as reduced integration of linear elements results in troublesome zero-energy modes (e.g. hourglassing) and, besides, the whole problem of volumetric locking in the MPM arises from the *increased* number of integration points required. Instead, a more effective approach is perhaps to adopt the $\bar{\boldsymbol{F}}$ approach of de Souza Neto et al. [125], which was adapted by Coombs et al. [126] for the MPM, though inconsistencies in the derived tangent modulus impact the convergence rate and therefore the reliability of the formulation. Conveniently, however, geomaterials – the medium under scrutiny in this thesis – are not in fact isochoric (under drained conditions, at least), but exhibit dilatancy in the plastic regime [127, 128]. Therefore, the difficulty of volumetric locking is not encountered, and ultimately adoption of a stabilisation technique is not required.

2.3 Formulation

The following is a formulation of the version of the MPM implemented in the open-source code AMPLE (*A Material Point Learning Environment*) [129] which is also used and extended in the rest of this thesis. The focus is therefore quasi-static mechanical loading of solids in an elastoplastic finite strain setting, employing implicit time integration and using original definitions of the material points as well as the GIMPM. As the continuum mechanics used here is conventional, scant attention is given to its formulation; for further information the reader is referred to standard textbooks (e.g. [41, 124]) as well as the research articles upon which this section is based [110, 129].

2.3.1 Governing equations

At the heart of finite strain mechanics lies the notion that as the body under consideration deforms, changes in its geometry cannot be ignored. This means that differences between its original (reference) configuration and current, deformed state must be examined explicitly. Consider therefore the Cartesian co-ordinate $\boldsymbol{X}$ of a point in the undeformed *material* body, which is denoted Ω_0. After undergoing some motion Ξ over a period of time t, the point moves to the co-ordinate $\boldsymbol{x}$ located in the deformed *spatial* domain Ω, which is bounded by a surface $\partial\Omega$. In other words,

$$\boldsymbol{x} = \Xi(\boldsymbol{X}, t) \tag{2.1}$$

and $\Xi(\boldsymbol{X}, 0) = \boldsymbol{X}$. These co-ordinates may be connected by the translation vector $\boldsymbol{u}$ through the relation

$$\boldsymbol{x} = \boldsymbol{X} + \boldsymbol{u}. \tag{2.2}$$

Another link is provided by the material deformation gradient tensor

$$\begin{align}
\boldsymbol{F} &= \nabla\Xi(\boldsymbol{X}, t) \tag{2.3}\\
&= \frac{\partial\boldsymbol{x}}{\partial\boldsymbol{X}} \tag{2.4}\\
&= \boldsymbol{I} + \frac{\partial\boldsymbol{u}}{\partial\boldsymbol{X}} \tag{2.5}
\end{align}$$

where $\boldsymbol{I}$ is the second-order identity tensor, which gives rise to a measure of local volume change $J = \det(\boldsymbol{F})$ as the Jacobian determinant. It is assumed that the motion may be broken down into elastic (recoverable) and plastic (irrecoverable) deformations by the

Kröner-Lee decomposition [130, 131]

$$\boldsymbol{F} = \boldsymbol{F}^{\mathrm{e}}\boldsymbol{F}^{\mathrm{p}} \tag{2.6}$$

in which the superscripts $(\bullet)^{\mathrm{e}}$ and $(\bullet)^{\mathrm{p}}$ denote elastic and plastic components respectively. The deformation gradient may then be used in a number of different ways to define various strain tensors. Here the elastic logarithmic (Hencky) strain tensor $\boldsymbol{\varepsilon}^{\mathrm{e}}$ is used, defined as

$$\boldsymbol{\varepsilon}^{\mathrm{e}} = \frac{1}{2}\ln \boldsymbol{b}^{\mathrm{e}} \tag{2.7}$$

where, using $(\bullet)^{\mathrm{T}}$ to denote matrix transpose, $\boldsymbol{b}^{\mathrm{e}} = \boldsymbol{F}^{\mathrm{e}}\left(\boldsymbol{F}^{\mathrm{e}}\right)^{\mathrm{T}}$ is the elastic left Cauchy-Green tensor, also known as the Finger tensor. The Kirchhoff stress is obtained using the fourth-order elasticity tensor $\boldsymbol{D}^{\mathrm{e}}$, derived in a small-strain setting from elastic material properties such as Young's modulus E and Poisson's ratio ν, as

$$\boldsymbol{\tau} = \boldsymbol{D}^{\mathrm{e}} : \boldsymbol{\varepsilon}^{\mathrm{e}}, \tag{2.8}$$

representing the forces acting on a small piece of the deformed body, per unit area of the undeformed body. It is simple to transform into the 'true' Cauchy stress by dividing by the volume change, i.e.

$$\boldsymbol{\sigma} = J^{-1}\boldsymbol{\tau}. \tag{2.9}$$

The Cauchy stress is related to the traction $\boldsymbol{t}$ acting on any surface (defined by an outward normal vector $\boldsymbol{n}$ acting through the point under consideration) in such a way that

$$\boldsymbol{t} = \boldsymbol{\sigma}\boldsymbol{n} \tag{2.10}$$

depends entirely on the value of $\boldsymbol{n}$. Now, by considering the forces and stresses acting on and transmitted by a small element of deformed continuum in static equilibrium, the balance of linear and angular momenta may be expressed as

$$\nabla \cdot \boldsymbol{\sigma} + \boldsymbol{f} = \boldsymbol{0} \tag{2.11}$$

$$\boldsymbol{\sigma}^{\mathrm{T}} = \boldsymbol{\sigma} \tag{2.12}$$

where $\boldsymbol{f}$ is a vector of impressed body forces per unit of deformed volume. In the case of the classical continuum, angular momentum balance is satisfied through the symmetry of the stress tensor, and therefore is not considered further in this chapter. The boundary of the domain is acted upon by Dirichlet and Neumann boundary conditions, such that

$$\boldsymbol{u} = \boldsymbol{u}_D \text{ on } \partial\Omega_D \tag{2.13}$$

$$\boldsymbol{t} = \boldsymbol{t}_N \text{ on } \partial\Omega_N \tag{2.14}$$

where $\boldsymbol{u}_D$ and $\boldsymbol{t}_N$ are prescribed displacements and tractions respectively, and $\partial\Omega = \partial\Omega_D \cup \partial\Omega_N$ but $\partial\Omega_D \cap \partial\Omega_N = 0$. Unless stated to the contrary, it may be assumed that the entirety of the boundary is traction-free.

The governing partial differential equation (PDE), in the form written in (2.11), is continuous and possesses infinitely many degrees of freedom (DOFs). To be solved by a machine it must therefore be cast into a discrete framework with a finite number of DOFs. This is achieved by first rendering it in variational form. The equation is perturbed by some arbitrary *test* function or virtual displacement $\boldsymbol{v}$ (belonging to the space of admissible displacements) and integrated over the (deformed) domain, giving the weak virtual work statement

$$\int_\Omega \boldsymbol{v} \cdot (\nabla \cdot \boldsymbol{\sigma})\,\mathrm{d}\Omega + \int_\Omega \boldsymbol{v} \cdot \boldsymbol{f}\,\mathrm{d}\Omega = 0. \tag{2.15}$$

Now the Gauss-Green theorem (divergence theorem) is exploited to move the derivative from the stress tensor to the test function, where it is easier to manipulate. The theorem states that

$$\int_\Omega \boldsymbol{v} \cdot (\nabla \cdot \boldsymbol{\sigma})\,\mathrm{d}\Omega = \int_{\partial\Omega} \boldsymbol{v} \cdot \boldsymbol{\sigma}\boldsymbol{n}\,\mathrm{d}\partial\Omega - \int_\Omega \nabla\boldsymbol{v} : \boldsymbol{\sigma}\,\mathrm{d}\Omega \tag{2.16}$$

so that, incorporating (2.10) and (2.14), the final variational form reads[4]

$$\int_\Omega \nabla\boldsymbol{v} : \boldsymbol{\sigma}\,\mathrm{d}\Omega = \int_\Omega \boldsymbol{v} \cdot \boldsymbol{f}\,\mathrm{d}\Omega + \int_{\partial\Omega_N} \boldsymbol{v} \cdot \boldsymbol{t}_N\,\mathrm{d}\partial\Omega \tag{2.17}$$

but as AMPLE does not include tractions, the final term will be neglected.

2.3.2 Discretisation and basis functions

The continuum is discretised into a collection of material points which occupy a grid of elements joined at nodes. As in any Bubnov-Galerkin method, the values of the solution (the displacement field $\boldsymbol{u}$) and the test function at each material point are expressed as interpolations of the values held at the grid nodes via a linear combination of basis functions. Using subscripts $(\bullet)_v$ and $(\bullet)_p$ to denote quantities related to nodes (vertices) and material points respectively (following standard MPM convention), this can be written

$$\boldsymbol{u}_p \approx \sum_v S_{vp}\boldsymbol{u}_v = \boldsymbol{u}_p^h \tag{2.18}$$

$$\boldsymbol{v}_p \approx \sum_v S_{vp}\boldsymbol{v}_v = \boldsymbol{v}_p^h \tag{2.19}$$

where S_{vp} is the material point's weighting function (computed from the basis function N_v for each node v) and the superscript $(\bullet)^h$ refers to a numerical approximation.

---

[4] As a non-zero virtual displacement on $\partial\Omega_D$ (i.e. one which perturbs away from the prescribed Dirichlet displacements) would be inadmissible, the boundary term there vanishes, leaving only the Neumann boundary conditions.

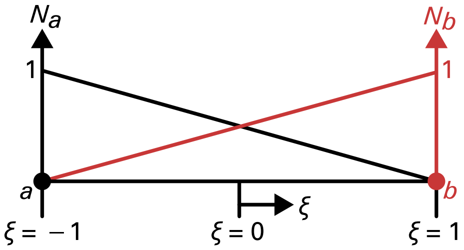

Figure 2.3: One-dimensional linear basis functions for two nodes a and b varying across a single element described by local co-ordinate ξ.

In this work, the form of the basis functions is limited to first-order Lagrange interpolants, which vary linearly (or bilinearly or trilinearly, depending on the dimensionality of the problem) between 1 at the function's 'home' node, and 0 at all other nodes.[5] However, the actual value of the weighting function at the material point varies, depending on whether the standard MPM or the GIMPM is being used. First, though, a local co-ordinate system must be defined for the element. Taking as an example a one-dimensional, two-node element, the single co-ordinate ξ varies between -1 at one extremity (node a) and +1 at the other (node b). Therefore the two basis functions have the form

$$N_v = \frac{1 \pm \xi}{2} \tag{2.20}$$

shown in Figure 2.3. In the case of the standard MPM, the weighting function is just the value of the basis function at the material point ($S_{vp} = N_v|_{\xi=\xi_p}$), calculated by determining the local position of the material point with respect to the element, and substituting the value of ξ in (2.20) – just like in the FEM. This is even simpler if the grid is Cartesian and aligned with the global co-ordinate system as the global position may be used directly: if the material point is at position x_p within an element of size h, then the values of the one-dimensional basis functions are described by

$$S_{vp} = \begin{cases} 1 + \frac{x_p - x_v}{h}, & -h \leq x_p - x_v \leq 0 \\ 1 - \frac{x_p - x_v}{h}, & 0 < x_p - x_v \leq h \end{cases} \tag{2.21}$$

where the node associated with S_{vp} is located at x_v. The spatial gradients are also easy to compute:

$$\nabla_x S_{vp} = \begin{cases} \frac{1}{h}, & -h \leq x_p - x_v \leq 0 \\ -\frac{1}{h}, & 0 < x_p - x_v \leq h, \end{cases} \tag{2.22}$$

but clearly highlighting the abrupt change as the material point passes over a node which precipitates the cell crossing instability.

This changes in the case of the GIMPM. The material point is no longer represented

---

[5] The well-known *Kronecker-delta* property. The second important property of any set of basis functions is that they form a *partition of unity.*

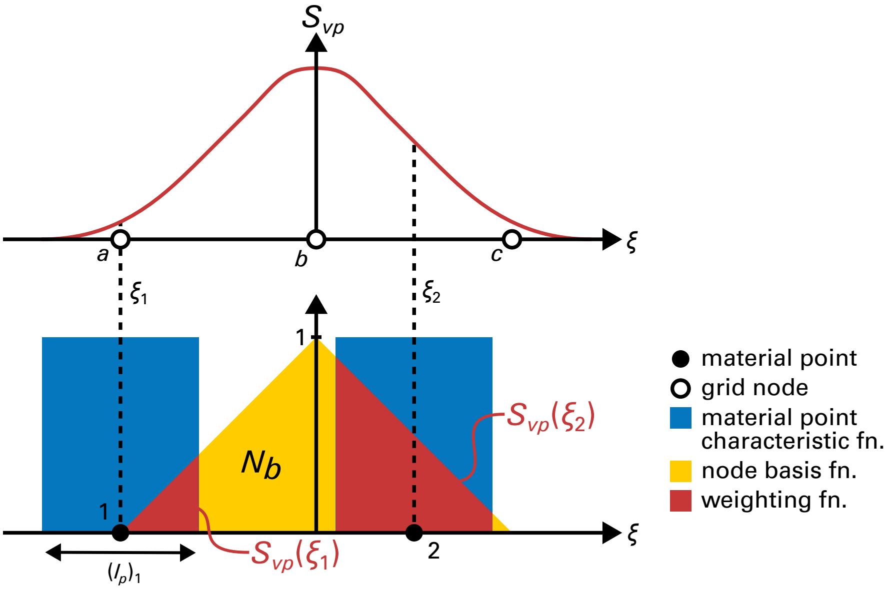

Figure 2.4: Convolution of a triangular node basis function N_b (yellow) with rectangular material point characteristic functions (blue) to produce the GIMPM weighting function S_{vp} (red), adapted from [110, Fig. 1].

by a single point, but by a characteristic function χ_p which, for the sake of simplicity, is limited to a rectangular function with the value 1 within the material point's domain of influence $\Omega_p \subset \Omega$ (of length $2l_p$ in one dimension) and 0 elsewhere.[6] That is,

$$\chi_p(\xi) = \begin{cases} 1, & \xi \in \Omega_p \\ 0 & \text{otherwise.} \end{cases} \tag{2.23}$$

S_{vp} is then the convolution of the node basis function with the characteristic function, expressed as [110]

$$S_{vp}(\xi) = \frac{1}{v_p} \int_{\Omega} \chi_p(\xi) N_v(\xi) \, \mathrm{d}\Omega \tag{2.24}$$

$$= \frac{1}{v_p} \int_{\Omega_p} N_v(\xi) \, \mathrm{d}\Omega \tag{2.25}$$

for the type of characteristic function used, in which v_p is the volume associated with the point. In other words, the weighting function is the integral of the section of the basis function which overlaps with the GIMPM domain, normalised by the material point's volume. This value is represented by the red areas in Figure 2.4 for two different material points located relative to a grid node b. The actual computed value of S_{vp} as a function of the position of a material point is traced out in the upper graph, showing the smooth transition between the two elements and demonstrating the desired continuity in gradient.

---

[6] The standard MPM may be recovered by instead setting the characteristic function to the Dirac delta function.

To account for the varied gradation of the weighting function, it must now be split into five distinct regions rather than two:

$$S_{vp} = \begin{cases} \frac{(h+l_p+x_p-x_v)^2}{4hl_p}, & -h-l_p \leq x_p - x_v \leq -h+l_p \\ 1+\frac{x_p-x_v}{h}, & -h+l_p < x_p - x_v \leq -l_p \\ 1-\frac{(x_p-x_v)^2+l_p^2}{2hl_p}, & -l_p < x_p - x_v \leq l_p \\ 1-\frac{x_p-x_v}{h}, & l_p < x_p - x_v \leq h-l_p \\ \frac{(h+l_p-x_p+x_v)^2}{4hl_p}, & h-l_p < x_p - x_v \leq h+l_p \end{cases} \tag{2.26}$$

and the gradients follow as

$$\nabla_x S_{vp} = \begin{cases} \frac{h+l_p+x_p-x_v}{2hl_p}, & -h-l_p \leq x_p - x_v \leq -h+l_p \\ \frac{1}{h}, & -h+l_p < x_p - x_v \leq -l_p \\ -\frac{x_p-x_v}{hl_p}, & -l_p < x_p - x_v \leq l_p \\ -\frac{1}{h}, & l_p < x_p - x_v \leq h-l_p \\ \frac{h+l_p-x_p+x_v}{2hl_p}, & h-l_p < x_p - x_v \leq h+l_p. \end{cases} \tag{2.27}$$

Therefore if a material point is contained entirely within a single element (the second and fourth cases in (2.26) and (2.27)), then the weighting functions and their derivatives may be computed as in the standard MPM (and, therefore, in the FEM). Practically, only the gradients must be updated throughout the load step; the values of S_{vp} need only be found at the beginning of each step, as although the global positions of the material points change during the course of the step, the elements deform accordingly such that the relative local positioning is unchanged. This is discussed further in [132].

Scaling up the dimensionality of the weighting functions is possible by defining a set for each individual co-ordinate direction and combining them as a Cartesian product, i.e.

$$S_{vp}(\boldsymbol{\xi}_p) = \prod_{i=1}^{n_D} S_{vp}(\xi_p^i), \tag{2.28}$$

using $S_{vp}(\xi_p^i)$ calculated according to (2.21) or (2.26) for each direction i, up to the required number of dimensions n_D. Higher-dimensional gradients are found by substituting the co-ordinate corresponding to the direction of interest into the appropriate formula in (2.22) or (2.27), and multiplying by the weighting function value(s) of the other dimension(s). For example, if a material point is located at $\boldsymbol{\xi}_p = (\xi_p^1, \xi_p^2, \xi_p^3)$ in three-dimensional space, then the value of node v's weighting function and its derivative with respect to the x_1

direction are given by

$$S_{vp} = S_{vp}(\xi_p^1) S_{vp}(\xi_p^2) S_{vp}(\xi_p^3) \tag{2.29}$$

$$\frac{\partial S_{vp}}{\partial x_1} = \left[\nabla_x S_{vp}(\xi_p^1)\right] S_{vp}(\xi_p^2) S_{vp}(\xi_p^3). \tag{2.30}$$

This basis definition provides all the tools required to discretise the variational statement of equilibrium developed earlier. Returning to (2.17), and ignoring tractions, an application of the Galerkin approximation yields

$$\int_\Omega \nabla \boldsymbol{v}^h : \boldsymbol{\sigma}^h \, \mathrm{d}\Omega = \int_\Omega \boldsymbol{v}^h \cdot \boldsymbol{f}^h \, \mathrm{d}\Omega \tag{2.31}$$

or

$$\sum_v \int_\Omega \nabla (S_{vp} \boldsymbol{v}_v) : \boldsymbol{\sigma}^h \, \mathrm{d}\Omega = \sum_v \int_\Omega (S_{vp} \boldsymbol{v}_v) \cdot \boldsymbol{f}^h \, \mathrm{d}\Omega \, , \tag{2.32}$$

by the linearity of operators, since the sum $\sum_v S_{vp} \boldsymbol{v}_v$ is the numerical approximation of the test function calculated per (2.19). As the values of the test function at the nodes are constant, they may be moved outside the integral:

$$\sum_v \boldsymbol{v}_v \cdot \int_\Omega \nabla S_{vp} \cdot \boldsymbol{\sigma}^h \, \mathrm{d}\Omega = \sum_v \boldsymbol{v}_v \cdot \int_\Omega S_{vp} \boldsymbol{f}^h \, \mathrm{d}\Omega \tag{2.33}$$

where they cancel, leaving

$$\sum_v \int_\Omega \nabla S_{vp} \cdot \boldsymbol{\sigma}^h \, \mathrm{d}\Omega = \sum_v \int_\Omega S_{vp} \boldsymbol{f}^h \, \mathrm{d}\Omega \, . \tag{2.34}$$

This is more commonly written

$$\int_\Omega (\nabla \boldsymbol{S}_{vp})^{\mathrm{T}} \boldsymbol{\sigma}^h \, \mathrm{d}\Omega = \int_\Omega (\boldsymbol{S}_{vp})^{\mathrm{T}} \boldsymbol{f}^h \, \mathrm{d}\Omega \tag{2.35}$$

where $\boldsymbol{S}_{vp}$ is a matrix containing the values of the appropriate basis functions with the form

$$\boldsymbol{S}_{vp} = \begin{cases} \begin{bmatrix} S_{1p} & 0 & \cdots & S_{n_v p} & 0 \\ 0 & S_{1p} & \cdots & 0 & S_{n_v p} \end{bmatrix} & \text{in 2D} \\ \\ \begin{bmatrix} S_{1p} & 0 & 0 & \cdots & S_{n_v p} & 0 & 0 \\ 0 & S_{1p} & 0 & \cdots & 0 & S_{n_v p} & 0 \\ 0 & 0 & S_{1p} & \cdots & 0 & 0 & S_{n_v p} \end{bmatrix} & \text{in 3D} \end{cases} \tag{2.36}$$

if a material point is influenced by n_v nodes, and $\nabla \boldsymbol{S}_{vp}$ is its gradient, also known as the *strain-displacement* matrix and denoted $\boldsymbol{G}$ such that $G_{abvj} = \frac{\partial S_{vp}}{\partial x_b} \delta_{aj}$, where δ_{aj} is the Kronecker delta. The next step is to express the stress approximation $\boldsymbol{\sigma}^h$ in terms of the solution field. However, this can only be performed exactly when stress is a linear function of the displacement, which for both geometric and material reasons in this case it is not. Therefore a linearised approximation must be taken instead, and a solution found iteratively.

2.3.3 Nonlinear solution and update procedure

The discretised weak statement of equilibrium (2.35) can be recast in residual form, giving an 'out-of-balance' force $\boldsymbol{f}^{\mathrm{R}}$ to be minimised. This minimisation provides a paradigm for solution of the problem. Focusing now on a single background cell (as denoted by $(\bullet)_E$),

$$\boldsymbol{f}_E^{\mathrm{R}} = \int_E \boldsymbol{G}^{\mathrm{T}} \boldsymbol{\sigma}^h \,\mathrm{d}\Omega - \int_E (\boldsymbol{S}_{vp})^{\mathrm{T}} \boldsymbol{f}^h \,\mathrm{d}\Omega \tag{2.37}$$

$$= \boldsymbol{f}_E^{\mathrm{int}} - \boldsymbol{f}_E^{\mathrm{ext}} \tag{2.38}$$

where $\boldsymbol{f}^{\mathrm{int}}$ and $\boldsymbol{f}^{\mathrm{ext}}$ are internal and external forces which must be balanced for equilibrium – and therefore a solution – to be found. In this work, the chosen nonlinear solution procedure is the Newton-Raphson algorithm, in which the residual equation is repeatedly linearised, solved and updated, until a convergence criterion is met. This algorithm is one of the most popular ways to solve nonlinear boundary value problems across the whole field of numerical analysis, and is attractive for a number of reasons – not least its high rate of asymptotic convergence, which approaches the quadratic in the region of the solution. More information on the Newton-Raphson procedure and its variants is available in many standard texts, including [41, 124].

Assuming that external loads are independent of the deformation, differentiating (2.38) leads to an element stiffness matrix $\boldsymbol{K}_E$ which essentially relates an increment in nodal displacements to the resulting increment in internal force, or

$$\delta \boldsymbol{f}_E^{\mathrm{int}} = \frac{\partial \boldsymbol{f}_E^{\mathrm{int}}}{\partial \boldsymbol{u}_v} \delta \boldsymbol{u}_v = \boldsymbol{K}_E \delta \boldsymbol{u}_v. \tag{2.39}$$

Although the full details of the consistent linearisation of the internal force are beyond the scope of this chapter (but can be found in [110, 133]), it results in

$$\boldsymbol{K}_E = \int_E \boldsymbol{G}^{\mathrm{T}} \boldsymbol{a} \boldsymbol{G} \,\mathrm{d}\Omega \tag{2.40}$$

where

$$a_{ijkl} = \frac{\partial \sigma_{ij}}{\partial F_{K\alpha}} F_{l\alpha} \tag{2.41}$$

(in which the indicial summation convention is employed) is the spatial tangent modulus and incorporates a linearisation of the plasticity algorithm (see [124, 134]). In practice however, (2.40) cannot be integrated exactly and numerical quadrature must be performed using a weighted sum of values from each material point influencing E. Using $\boldsymbol{K}_p$ to represent the stiffness contribution of a single material point, this may be written

$$\boldsymbol{K}_E \approx \sum_p \boldsymbol{G}_p^{\mathrm{T}} \boldsymbol{a}_p \boldsymbol{G}_p v_p = \sum_p \boldsymbol{K}_p. \tag{2.42}$$

The stiffness matrices of individual cells are then assembled together DOF-wise to form a global stiffness matrix

$$\boldsymbol{K} = \underset{\forall E}{\mathbb{A}}(\boldsymbol{K}_E) \tag{2.43}$$

in which $\mathbb{A}(\bullet)$ is the standard finite element assembly operator. But if the nodes influenced by each material point are known beforehand (i.e. from an element search algorithm) then it is not in fact necessary to have to loop over every element, as stiffness contributions from each material point may be built in to the global stiffness matrix directly:

$$\boldsymbol{K} = \underset{\forall p}{\mathbb{A}}(\boldsymbol{K}_p). \tag{2.44}$$

After applying Dirichlet boundary conditions, this matrix is inverted to find the incremental nodal deformations

$$\delta \boldsymbol{u}_K = \boldsymbol{K}^{-1} \boldsymbol{f}_{K-1}^{\mathrm{R}} \tag{2.45}$$

for a Newton-Raphson iteration K which, over the course of a load step, are simply added together so that the total increment is

$$\Delta \boldsymbol{u}_K = \Delta \boldsymbol{u}_{K-1} + \delta \boldsymbol{u}_K \tag{2.46}$$

where the displacement is taken to be zero at the start of a load step, and the reaction forces $\boldsymbol{f}^{\mathrm{rct}}$ required for the Dirichlet boundary conditions are incremented. The displacement increments are used to update the material points, although the change in their positions need not be considered explicitly at this stage; it is sufficient to update only the deformation gradient. This is performed according to the method presented in [110, 132] which, using formula (2.18), states that

$$\Delta \boldsymbol{F}_K = \boldsymbol{I} + \frac{\partial (\Delta \boldsymbol{u}_p)_K}{\partial \widetilde{\boldsymbol{x}}} = \boldsymbol{I} + \sum_v \Delta (\boldsymbol{u}_v)_K \frac{\partial S_{vp}}{\partial \widetilde{\boldsymbol{x}}} \tag{2.47}$$

where $\widetilde{(\bullet)}$ refers to a quantity from the start of the load step so that

$$\boldsymbol{F}_K = \Delta \boldsymbol{F}_K \widetilde{\boldsymbol{F}} \tag{2.48}$$

and $(v_p)_K = \det(\Delta \boldsymbol{F}_K)\widetilde{v}_p$. The updated spatial derivates of the basis functions required to form $\boldsymbol{G}$ may subsequently be expressed

$$\frac{\partial S_{vp}}{\partial \boldsymbol{x}_K} = \frac{\partial S_{vp}}{\partial \widetilde{\boldsymbol{x}}} \frac{\partial \widetilde{\boldsymbol{x}}}{\partial \boldsymbol{x}_K} = \frac{\partial S_{vp}}{\partial \widetilde{\boldsymbol{x}}} (\Delta \boldsymbol{F}_K)^{-1} \tag{2.49}$$

and the stresses are updated accordingly, perhaps using an elastic-predictor/plastic-corrector algorithm, depending on the adopted constitutive model (more details are provided in [110, 129]). This leads to new global internal and external force vectors

$$\boldsymbol{f}_K^{\text{int}} = \underset{\forall p}{\mathbb{A}} \left(\boldsymbol{G}_p^{\text{T}} \boldsymbol{\sigma}_p^h v_p \right)_K \tag{2.50}$$

$$\boldsymbol{f}_K^{\text{ext}} = \underset{\forall p}{\mathbb{A}} \left((S_{vp})^{\text{T}} \boldsymbol{f}_p^h v_p \right)_K \tag{2.51}$$

such that

$$\boldsymbol{f}_K^{\text{R}} = \boldsymbol{f}_K^{\text{int}} - \boldsymbol{f}_K^{\text{ext}}, \tag{2.52}$$

although the external force vector may usually be assumed to remain constant throughout the step. This whole procedure is repeated until $\boldsymbol{f}^{\text{R}}$ is sufficiently minimised; in this thesis the criteria used are the normalised out-of-balance force

$$\bar{f} = \frac{||\boldsymbol{f}^{\text{R}}||}{||\boldsymbol{f}^{\text{ext}} + \boldsymbol{f}^{\text{rct}}||} \tag{2.53}$$

where $||(\bullet)||$ denotes the L_2-norm of $(\bullet)$, and an energy criterion

$$\bar{e} = \boldsymbol{f}^{\text{R}} \cdot \delta \boldsymbol{u} \tag{2.54}$$

so that, unless otherwise stated, convergence is considered to have been reached if $\bar{f} < 10^{-9}$ or $\bar{e} < 10^{-16}$.

A more comprehensive material point update is performed at the end of each load step. First, the (centroids of the) material points are moved to their new positions using displacements mapped with (2.18), i.e.

$$\boldsymbol{x}_p = \widetilde{\boldsymbol{x}}_p + \sum_v S_{vp} \Delta \boldsymbol{u}_v \tag{2.55}$$

and the grid is reset to its original configuration. As indicated earlier, it is also possible when using the GIMPM to update the material points' individual domains. Here the adopted approach is to keep the GIMPM domains rectilinear, but update their half-lengths l_p in each direction according to the corresponding material normal stretch, as proposed by Charlton et al. [110], even though it may result in spurious domain volume changes under simple shear modes [132]. This can be written

$$(l_p)_1 = U_{11} (l_{p_0})_1 \tag{2.56}$$

$$(l_p)_2 = U_{22} (l_{p_0})_2 \tag{2.57}$$

$$(l_p)_3 = U_{33} (l_{p_0})_3 \tag{2.58}$$

where l_{p_0} refers to the material point's original half-length in a particular direction, and (U_{11}, U_{22}, U_{33}) are taken from the leading diagonal of the material stretch tensor $\boldsymbol{U} = \sqrt{\boldsymbol{F}^{\mathrm{T}}\boldsymbol{F}}$. An element search procedure may then be conducted to determine the material points (or parts thereof) which populate each grid cell, and the next load step may commence. A description of the steps making up a typical implicit MPM is provided in Algorithm 1.

2.3.4 Ghost stabilisation

Because the MPM is formulated in a FEM-like framework, but must deviate from the FEM in several ways to achieve its resilience to mesh distortion, the resulting formulation suffers from various instabilities. The most infamous of these – the cell crossing error – is regularised in this thesis by generalised interpolation [103,110], which extends the definition of the material point and modifies the computation of basis functions and their derivatives, as outlined above. Additionally, to guard against the small cut issue which may impact the conditioning of the global system, the second stabilisation technique adopted in this work is ghost penalisation [111,122].

The first step of the ghost stabilisation procedure is to determine which cells constitute the boundary. These are elements that are at least partially populated with material points and are adjacent to elements that are completely empty. The interfaces between the boundary cells and the rest of the continuum – and between each other – then define a set of faces (in three dimensions, or edges in two) to be examined. But to proceed, first a convention must be established: one side of each face is arbitrarily denoted positive, and the other negative. Respective quantities are notated $(\bullet)^+$ and $(\bullet)^-$, and a unit normal vector to the face $\boldsymbol{n}$ is defined such that it always points into the negative element. As developed more fully in [111], the ghost stabilisation term, which is really a measure of the jump in the solution and test function over the interface, for a face ∂E is given by

$$\boldsymbol{J} = \frac{h^3}{3} \int_{\partial E} \boldsymbol{G}_g^{\mathrm{T}} \boldsymbol{n}_g \boldsymbol{n}_g^{\mathrm{T}} \boldsymbol{G}_g \, \mathrm{d}\partial E \tag{2.59}$$

where h is the characteristic size[7] of the face, $\boldsymbol{G}_g = [\boldsymbol{G}^+ \;\; -\boldsymbol{G}^-]$ with $\boldsymbol{G}^+$ and $\boldsymbol{G}^-$ representing the strain-displacement matrices in the positive and negative elements, respectively,

---

[7] The maximum side length, or in two dimensions simply the length of the edge.

Algorithm 1 An implicit material point method, with the Newton-Raphson solution loop on grey.

```
Initialisation:
  Initialise material points with positions $\boldsymbol{x}_p$ and volumes $v_p$.
  Initialise background grid nodes with positions $\boldsymbol{x}_v$.
  Set load step counter $n = 0$ for total number of load steps $n_{\text{lstps}}$.
  Define Newton-Raphson convergence criteria $\bar{f}_{\text{tol}}$ and $\bar{e}_{\text{tol}}$.
while $n \leq n_{\text{lstps}}$ do
    Map material point data to grid nodes
    for each material point $p$ do
        Identify neighbouring grid nodes $v$ influencing $p$.
        for each neighbouring node $v$ do
            Compute weighting function $S_{vp}$ and gradient $\nabla_{\widetilde{\boldsymbol{x}}} S_{vp}$.
        end for
    end for
    while $\bar{f} > \bar{f}_{\text{tol}}$ and $\bar{e} > \bar{e}_{\text{tol}}$ do
        for each material point $p$ do
            Accumulate stiffness matrix: $\boldsymbol{K} \mathrel{+}= \boldsymbol{G}_p^{\text{T}} \boldsymbol{a}_p \boldsymbol{G}_p v_p$
            Accumulate internal force: $\boldsymbol{f}^{\text{int}} \mathrel{+}= \boldsymbol{G}_p^{\text{T}} \boldsymbol{\sigma}_p v_p$
            Accumulate external force: $\boldsymbol{f}^{\text{ext}} \mathrel{+}= \boldsymbol{S}_{vp}^{\text{T}} \boldsymbol{f}_p v_p$
        end for
        Step 2: Solve the global system on the grid nodes
        Out-of-balance force: $\boldsymbol{f}^{\text{R}} = \boldsymbol{f}^{\text{int}} - \boldsymbol{f}^{\text{ext}}$
        Apply boundary conditions.
        Assemble and solve global system: $\delta \boldsymbol{u}_K = \boldsymbol{K}^{-1} \boldsymbol{f}^{\text{R}}$
        Increment nodal displacements: $\Delta \boldsymbol{u}_v \mathrel{+}= \delta \boldsymbol{u}_K$
        Compute $\bar{f}$ and $\bar{e}$.
        Step 3: Update material points
        for each material point $p$ do
            Update deformation gradient: $\boldsymbol{F}_K = \Delta \boldsymbol{F}_K \widetilde{\boldsymbol{F}}$
            Update volume: $v_p = \det(\Delta \boldsymbol{F}_K) \widetilde{v}_p$
            Update weighting function gradients: $\nabla_{\boldsymbol{x}} S_{vp} = \nabla_{\widetilde{\boldsymbol{x}}} S_{vp} (\Delta \boldsymbol{F}_K)^{-1}$
            Compute updated stress $\boldsymbol{\sigma}_p$ using constitutive model.
        end for
    end while
    for each material point $p$ do
        Update position: $\boldsymbol{x}_p \mathrel{+}= \Delta \boldsymbol{u}_p$
    end for
    Step 4: Reset grid
    Reset grid nodes to original positions $\boldsymbol{x}_v$.
    Increment load step: $n \mathrel{+}= 1$
end while
```

and $\boldsymbol{n}_g$ is a matrix formed from components of $\boldsymbol{n}$ such that

$$\boldsymbol{n}_g = \begin{cases} \begin{bmatrix} n_1 & 0 & 0 & n_2 \\ 0 & n_2 & n_1 & 0 \end{bmatrix} & \text{in 2D} \\ \\ \begin{bmatrix} n_1 & 0 & 0 & n_2 & 0 & n_3 \\ 0 & n_2 & 0 & n_1 & n_3 & 0 \\ 0 & 0 & n_3 & 0 & n_2 & n_3 \end{bmatrix} & \text{in 3D.} \end{cases} \tag{2.60}$$

Equation (2.59) is integrated over the face with standard Gauss-Legendre quadrature, leading to an additional stiffness term

$$\boldsymbol{K}_g = \gamma_g \boldsymbol{J} \tag{2.61}$$

which is added into the global stiffness matrix, where γ_g is a user-defined ghost penalty parameter, usually chosen to be some scaling of a relevant elastic modulus of the material. To ensure consistency of the tangent operator, corresponding force terms calculated with

$$\boldsymbol{f}_g = \boldsymbol{K}_g \delta \boldsymbol{u} \tag{2.62}$$

are also added to the global force residual vector $\boldsymbol{f}^R$. By penalising jumps in the displacement solution gradients across faces, the ghost stabilisation technique subtly smooths the solution at domain boundaries. While the actual values of the solution remain largely unchanged, the stress and strain fields become more physically realistic and exhibit natural continuity. This is reflected by the numerical examples provided in [111], which also demonstrate that adequate conditioning of system matrices is maintained such that simulations which previously would fail – seemingly at random – are now able to run to completion. This highlights the effectiveness of ghost stabilisation in transforming the robustness and reliability of MPM simulations.

2.4 Strain localisation in the classical continuum

With an appropriate computational methodology established, the limitations of the continuum framework that motivate this thesis may now be addressed. There are several ways to view the process which leads to strain localisation, and the problems it presents in numerical analysis. A more mathematical perspective will be provided in Chapter 3, but here the problem is introduced with a simple illustrative example. Consider an infinitely wide layer under plane strain conditions. The layer is fixed at the base, and a horizontal displacement is applied to the top such that the layer is under a constant shear stress (Couette flow). To achieve this, the layer is additionally constrained against any vertical

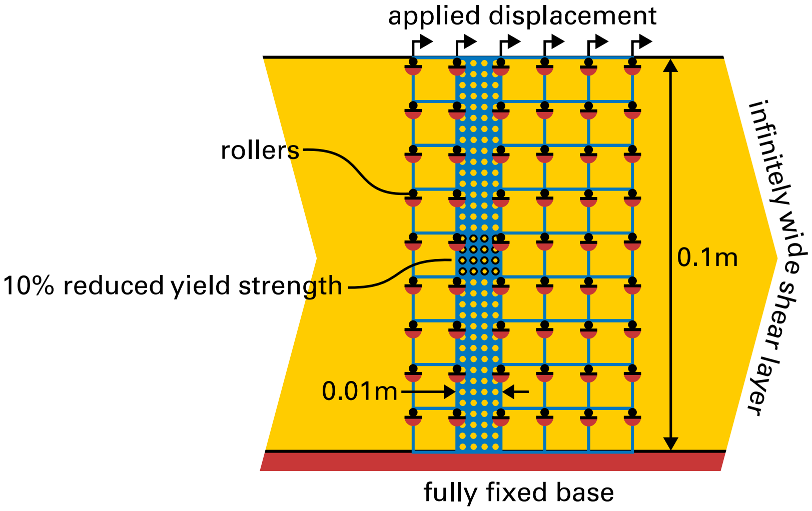

Figure 2.5: Problem setup of the shear layer, showing the coarsest discretisation of 9×5 background grid elements and a representative vertical slice populated by 4^2 generalised interpolation material points per cell.

motion, allowing analysis of a single representative vertical slice, which is discretised into a number of rectangular elements containing generalised interpolation material points. To initiate localisation (a shear band, in this case) one element row must have a slight imperfection,[8] otherwise the entire domain would yield at once, homogeneously. The imperfection may take a geometric form (e.g. a perturbation or reduction in cross section), but here the yield strength in the central row of elements is reduced by a factor of 10%. Failure of the material is governed by a Drucker-Prager constitutive model, incorporating a non-associated flow rule to define the elastoplastic behaviour. Using a tension-positive convention, the yield function f may be written

$$f = \sqrt{3J_2} + \alpha^{\mathrm{DP}} p - k \tag{2.63}$$

where J_2 is the second invariant of the deviatoric Kirchhoff stress tensor $\boldsymbol{s}$, defined as

$$J_2 = \frac{1}{2}\boldsymbol{s} : \boldsymbol{s}, \tag{2.64}$$

where

$$\boldsymbol{s} = \boldsymbol{\tau} - p\boldsymbol{I}. \tag{2.65}$$

Furthermore $p = \frac{1}{3}\mathrm{tr}(\boldsymbol{\tau})$ is the hydrostatic pressure, $\alpha^{\mathrm{DP}} = \frac{6\sin\phi}{3-\sin\phi}$ is the Drucker-Prager alpha parameter calculated from the internal friction angle ϕ, and k is the yield strength

---

[8] Though this may seem artificial and contrived, for the purpose of this illustrative exercise it is a completely adequate, if simplistic, analogue for the natural material heterogeneity which typically induces nucleation of localisation in real media.

of the material. Plastic flow occurs with respect to the plastic potential function

$$g = \sqrt{3J_2} + \beta^{\mathrm{DP}} p \tag{2.66}$$

where $\beta^{\mathrm{DP}} = \frac{6\sin\psi}{3-\sin\psi}$ is the Drucker-Prager beta parameter, related to the dilatancy angle ψ, and is measured with a scalar-valued indication of the accumulated equivalent plastic strain denoted ε^{p}. The constitutive equations are solved according to the standard implicit procedure described in [124, 134], producing a corrected stress and elastic strain for a given trial state.

Figure 2.5 shows the setup of the problem, which is inspired by a similar example (albeit in a small-strain setting with von Mises plasticity) given in [135]. The slice, measuring 0.1m by 0.01m, undergoes a maximum displacement of 0.02m applied at the top nodes. This is implemented using an adaptive routine that adjusts the step size based on convergence: proceeding and doubling the step size if the previous step converged (up to a maximum of the initial displacement increment of $\frac{0.02}{200}$m per step), or returning and halving it if not. For this problem, a fairly large convergence tolerance of $\bar{f}_{\mathrm{tol}} = 10^{-5}$ was used, as untreated strain localisation engenders poor convergence (or even divergence) of the iterative solver [136]. The material has a shear modulus $\mu = 4$GPa, a Poisson's ratio $\nu = 0.25$, a yield strength $k = 100$MPa, and friction and dilatancy angles of $\phi = 8.6°$ and $\psi = 2°$ respectively. Additionally the problem is stabilised with a ghost parameter of $\gamma_g = 10E$, where E is the Young's modulus. Three discretisations of varying refinement are tested: (i) a coarse discretisation (depicted in Figure 2.5) with a background grid of 9×5 cells, (ii) a medium discretisation with 19×10 cells, and (iii) a fine discretisation with 39×20 cells. In each case only the central row of elements has its yield strength reduced.

The corresponding force-displacement curves for the three simulations, shown in Figure 2.6, plot the applied displacement at the top against the horizontal reaction force at the base. While the elastic response is consistent across all cases, the plastic regime reveals a pronounced divergence. Each simulation reaches a similar peak load, but at different applied displacements, and the post-peak softening occurs at markedly different rates, indicating increasingly brittle behaviour with mesh refinement. Only the two coarser discretisations successfully complete the full 0.02m displacement, while the finer mesh halts prematurely, as extreme localised plastic straining precludes the Newton-Raphson algorithm from locating a valid solution. The results do not show any kind of convergence towards a particular solution with mesh refinement, as would be expected in stable numerical analyses, and the solution is instead clearly mesh-dependent. This is confirmed by the results shown in Figure 2.7, which depict the final state of each of the three simulations, and in particular the accumulated equivalent plastic strain ε^{p} of each material point. Hardly any straining is experienced by the regions of the body above or below the localisation zone, with almost all of the deformation concentrated within the single element thickness containing the imperfection. The formation of the shear band is therefore governed completely by the parameters of

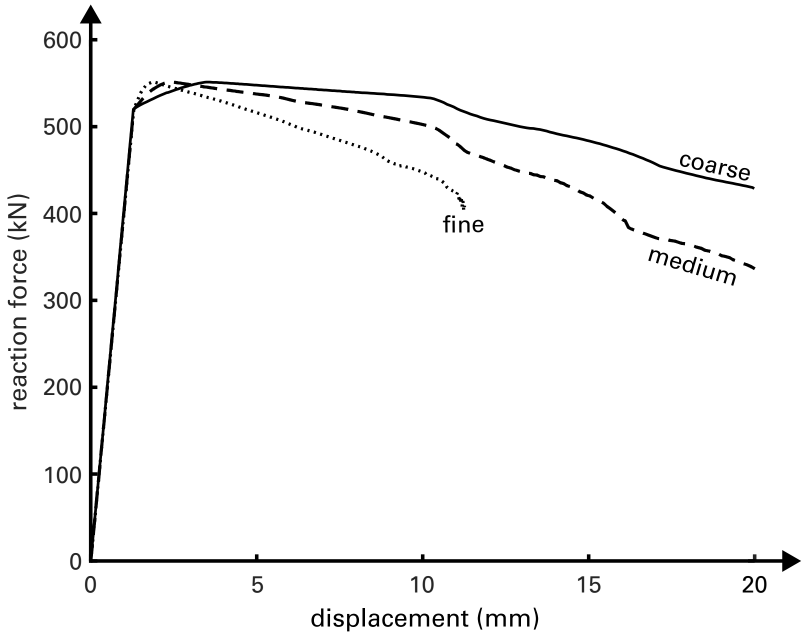

Figure 2.6: Force-displacement curves for the shear layer localisation problem with three levels of discretisation.

the analysis (in particular the size and orientation of the mesh), and convergence towards a true or realistic solution informed by natural underlying phenomena is unattainable. Instead, failure seems to take place on a plane of zero thickness, and plastic dissipation – ideally distributed over a finite region – collapses into an infinitesimal zone. This is entirely unphysical and does not represent real localised failure mechanisms, which occur in finite-sized regions dependent on the scale of the material's constituent microstructure [27]. This effect underscores a significant limitation in the standard continuum model.

Although a more rigorous account will be given in Section 3.1.1, the mesh sensitivity observed in this simulation can be explained from a mechanistic perspective as follows. Initially, the entire domain deforms elastically and uniformly until a yield threshold is reached. Due to the slightly reduced yield strength in the central row of elements, this region yields first, while the rest of the body remains within the elastic regime. The initial yielding initiates instability in the failure zone, inducing structural softening due to the nature of the non-associative elastoplastic constitutive behaviour [137, 138]. Consequently, a virtually unlimited amount of (plastic) deformation becomes available in the localised region, with progressively less force required to sustain it. As a result, the structure's load-bearing capacity diminishes, and the surrounding continuum begins to elastically unload to maintain force equilibrium. All further deformations are then channelled into the single row of imperfect elements, making the width of the shear band directly dependent on the mesh resolution. With finer meshes, achieving the same global deformation necessitates increasingly intense plastic straining within the localised zone, as indicated by the elevated equivalent plastic strain in Figure 2.7. This, in turn, accelerates softening, explaining the

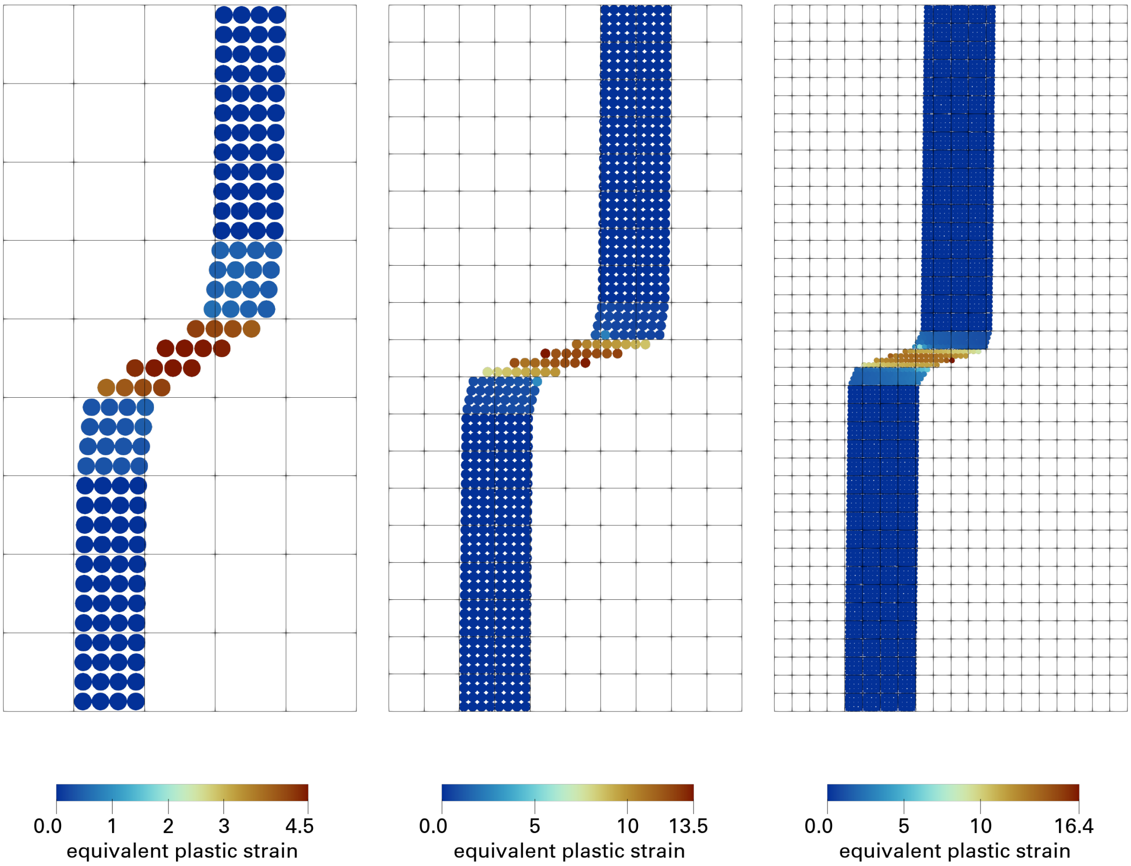

(a) coarse **(b)** medium **(c)** fine

Figure 2.7: Final configurations of each mesh resolution, coloured according to the accumulated equivalent plastic strain at each material point, showing a clear mesh dependency.

marked differences in elastoplastic responses across the three mesh sizes.

As any simulation underpinned by a standard continuum framework demonstrates such mesh dependency, trustworthy (or even meaningful) results of problems involving localised failure can never be obtained. To provide results which are at all useful or reliable it is therefore necessary to find a way to address the fundamental deficiencies in the approach, either by modifying the governing equations or constitutive model, or by applying numerical stabilisation techniques. Generally these involve introduction of some higher-order dependency or complication, for instance a characteristic length or time scale [139], which may or may not be phenomenological. An exploration of such regularisation strategies forms the basis of the beginning of the next chapter.

2.5 Remarks

This chapter has explored some of the challenges associated with large-deformation geotechnical strain localisation problems. Although many numerical methods have been developed to simulate these scenarios, the MPM is particularly well suited to facilitating robust analyses. A synopsis of the adopted numerical formulation has been provided, using the classical continuum approach used almost universally by engineers to model real geotechnical structures and inform decision-making. However, the example of localised failure in a shear layer has demonstrated the danger of applying conventional methodology to the localisation problems which are ubiquitous in geomechanics: the post-peak behaviour is divergent, and depends entirely on the resolution of the discretisation. In order to predict these phenomena in a realistic or meaningful way, then, the approach presented in this chapter must be modified to include a mechanism expressly capable of governing the localisation of plastic deformations.

CHAPTER 3

Nonlinear micropolar elasticity

This chapter begins with an exploration of the numerical issues fomented by strain localisation, and some of the techniques developed to circumvent them. The micropolar approach is selected, developed in a nonlinear hyperelastic form, and implemented in an implicit material point method. Verification and numerical examples follow.

3.1 Introduction

When a solid material fails, plastic deformations of a shearing nature arise, producing permanent changes in shape. In many ductile materials like iron and other crystalline metals, initial plastic straining occurs evenly and continuously throughout the structure. This is the result of work *hardening*, as the already yielded regions only become more resistant and can effectively propagate loading. Materials which *soften*, on the other hand – concrete, rock and soil, for instance – can develop more discontinuous failure patterns: strain localisation, in other words. Often, localisation arises from microstructural changes within the failure zone – intergranular slip, rearrangement and rotation for example [140, 141] – usually instigated by some minute imperfection or weakness. These micromechanical mechanisms lead either to an increased porosity, localised buckling, or rapid reduction in cross-sectional area, resulting in a macroscopic softening of the material and, ultimately, instability.

Clearly, strain localisation is a critical phenomenon in the study of granular materials and in geotechnical engineering. It often plays a crucial role in the structural failure of natural and engineered systems, observed widely in for example ductile landslides, rock faulting and in standard laboratory tests [5]. Understanding and accurately simulating the mechanisms behind strain localisation are therefore essential for predicting realistic failure modes, improving material models, and ensuring the reliable design and analysis of geotechnical infrastructure. It is crucial to note that, although thin, the localisation zone is always of *finite* size (i.e. not of zero thickness), typically corresponding to several multiples of some length scale associated with the material's microstructure, e.g. a soil's mean particle diameter [15, 27, 28]. However, as classical continuum models lack any internal length scale dependency (or indeed any consideration of micromechanical phenomena at all), this cannot be reproduced with conventional numerical approaches. Instead – as demonstrated by the numerical example in Section 2.4 – the size of the failure zone directly depends on the resolution and orientation of the mesh, collapsing onto a mathematical plane of nil or infinitesimal thickness with refinement, and exhibiting unstable post-critical behaviour [123, 139]. This means that, since the constitutive relation is phrased as a stress-strain law (rather than force-displacement), energy dissipation tends to zero, which is physically unreasonable [142]. Moreover the convergence properties of nonlinear solution procedures are also diminished, even leading to divergence [136]. To address these challenges, which occur irrespective of the discretisation method used [58], researchers have developed a broad array of regularisation techniques that in some way modify the standard continuum formulation. The following sections provide a more detailed overview of why exactly these techniques are needed, before continuing on to explore some of the major advancements in the pursuit of these strategies.

3.1.1 Strain localisation as a destabilising mechanism

From a physical standpoint (cf. Section 2.4) the loss of predictive capability of conventional techniques arises because classical continuum models do not account for the microstructural effects limiting the width of localisation zones. But from a more mathematically-grounded perspective, one can think in terms of the conditions which render the governing equations – and, by extension, the numerical method – *well-posed*. A well-posed problem is one in which valid solutions exist, are unique, and depend continuously on the input data (e.g. geometry, material properties, boundary conditions). In other words, does the method dependably supply an appropriate solution to the problem? It is clearly apparent that the conventional approach to strain localisation fails to satisfy these criteria; instead, it produces solutions that vary drastically with changes in the computational mesh. This is because the localisation zone represents a discontinuity in the gradient of the solution field – an entity the governing elliptic PDE (2.11) is not designed to handle.[1] In fact, in regions where localisation occurs, the equations governing the real system's equilibrium are no longer characterised as elliptic; instead they become *hyperbolic* [143] – able to admit discontinuities but, unfortunately, requiring a different mathematical treatment and numerical implementation. The original governing equations are no longer well-posed for the boundary value problem, and hence can no longer stably produce physically-meaningful,

---

[1] Elliptic PDEs typically describe smooth, continuous solutions corresponding to stable equilibrium or steady-state conditions.

objective (i.e. unbiased and mesh-independent) results in numerical simulations. One can therefore conclude that the underlying reason for the instability is a *loss of ellipticity* of the governing rate equilibrium equations.

Focusing now on the causes of this loss, Hill [144] introduced a condition for the onset of discontinuities (bifurcation) in a continuous medium, which is related to the propagation of acceleration waves within the continuum. For the solution field to remain smooth (and therefore for ellipticity to be preserved), disturbances must be able to travel at finite speeds throughout the domain. This information is contained within the acoustic tensor $\boldsymbol{A}$, defined with respect to a normal vector $\boldsymbol{n}$ which points outwards from a potential discontinuity plane within the continuum (see Figure 1.2). It may be written

$$\boldsymbol{A} = \boldsymbol{n} \cdot \boldsymbol{D} \cdot \boldsymbol{n} \tag{3.1}$$

where $\boldsymbol{D} = \frac{\partial \boldsymbol{\sigma}}{\partial \boldsymbol{\varepsilon}}$ is the fourth-order constitutive tensor or tangent operator of an incrementally linear material, and $\dot{\boldsymbol{\varepsilon}}$ and $\dot{\boldsymbol{\sigma}} = \boldsymbol{D} : \dot{\boldsymbol{\varepsilon}}$ are strain and stress rates or increments respectively. The acoustic tensor relates stress rates to velocity discontinuities across a surface normal to $\boldsymbol{n}$, such that its eigenvalues correspond to the squared propagation speeds of infinitesimal disturbances in the material. Positive definiteness of the acoustic tensor therefore implies real wave speeds and, hence, local stability. It follows that when the acoustic tensor becomes singular (i.e. when its determinant vanishes), the deformation field loses its continuity, leaving the possibility of discontinuous strain rates developing. Physically, this is because singularity of the acoustic tensor indicates that the material can no longer sustain stress perturbations in certain directions, leading to bifurcation. Acceleration waves hence become 'trapped' either side of the emergent localisation surface [145]. This marks the onset of strain localisation and structural instability, and the associated loss of ellipticity renders the boundary value problem ill-posed, with mesh dependency ensuing. As pointed out by Hofer et al. [146], although some take this condition as indicative of localisation per se, it only really implies bifurcation, which may manifest in one of a number of diverse modes.[2] But for the purposes of this discussion at least, the loss of strong (Legendre-Hadamard) ellipticity imparted by the singularity of the acoustic tensor is sufficient to be able to explore the relevant regularisation methodology.

Using (3.1) and the properties of positive definite matrices, local material stability is then implied by Drucker's first stability condition [147]

$$\dot{\boldsymbol{\varepsilon}} : \boldsymbol{D} : \dot{\boldsymbol{\varepsilon}} = \dot{\boldsymbol{\sigma}} : \dot{\boldsymbol{\varepsilon}} > 0, \quad \forall \dot{\boldsymbol{\varepsilon}} \neq \boldsymbol{0}. \tag{3.2}$$

Material instability precipitates structural instability so, looking in homogenised terms at

---

[2] The so-called *continuous bifurcation* condition, which explicitly examines jumps in the velocity gradient across possible discontinuities, is preferred for the specific examination of localised failure.

the structure as a whole, the condition may be formulated

$$\int_{\Omega} \dot{\boldsymbol{\sigma}} : \dot{\boldsymbol{\varepsilon}} \, \mathrm{d}\Omega > 0 \tag{3.3}$$

as derived by Hill [148]. That is to say, stability is only guaranteed when the strain energy produced in the continuum is increasing, which is equivalent to saying that the slope of the global force-displacement curve is positive. In the case of strain softening – a phenomenon observed in the constitutive response of a wide range of engineering materials, including sands, rock and pre-cracked concrete [127,143] – where the post-peak elastoplastic behaviour results in a negative gradient (see Figure 2.6), bifurcation is then likely to occur in some form. Overcoming ill-posedness to generate objective results therefore requires some kind of regularisation technique which prevents the acoustic tensor from becoming singular, both during initial material failure and into the softening regime.

Usually, strain softening in continuum models is achieved by some degradation of stiffness or weakening of the material's strength, representing the accumulation of irreversible damage to the internal mechanisms which supply the structural integrity of the material fabric. Therefore before moving to discussing the relevant regularising technologies, it is also worth exploring why the non-associative plasticity models adopted in this work lead to structural softening in the first place, even when they do not explicitly incorporate softening effects [137]. In classical associative models, the plastic strain increment direction is aligned with the gradient of the yield surface, which maximises the rate of energy dissipation based on Drucker's postulate [147,149]

$$\dot{\boldsymbol{\sigma}} : \dot{\boldsymbol{\varepsilon}}^{\mathrm{p}} \geq 0 \quad \forall \delta \boldsymbol{\sigma} \tag{3.4}$$

where $\dot{\boldsymbol{\varepsilon}}^{\mathrm{p}}$ is the plastic strain rate. The postulate demands any increment in applied loads should not lead to a decrease in the work done by the external forces on the system. Instead it suggests that a stable material will always resist further deformation in a way that does not reduce the energy absorbed by the material, thereby avoiding strain softening and instability. This assumption legitimately underpins a family of isochoric or work hardening elastoplastic constitutive models promoting stable, predictable and realistic material behaviour for e.g. metals, but it significantly overestimates the degree of volumetric plastic straining when applied to frictional materials [127,128]. Non-associated flow rules, on the other hand, in which the plastic potential function (which defines the flow direction) differs from the yield surface, can be chosen such that the resulting dilatancy aligns more closely with experimental evidence [150]. However, this represents a violation of Drucker's postulate, leading to inefficiency and instability in the way energy is dissipated due to the mismatch in direction between the applied stress and plastic strain increment. Accordingly, the structure is less able to resist applied loads, often manifesting as softening in the structural response.

It is also important to note the other conditions which lead to ill-posedness of the governing rate equilibrium equations. Two are named by de Borst et al. [143], both of which explicitly address the stability of wave propagation in a material under deformation. The *boundary-complementing* condition precludes the emergence of stationary free-surface waves (Rayleigh waves) which may grow unbounded, and the similar *interfacial-complementing* condition excludes the emergence of stationary waves on material interfaces (Stoneley waves) [151,152]. Both relate to unstable and unphysical oscillations in the absence of proper dissipation or damping. Furthermore, the Baker-Ericksen inequalities also protect against loss of ellipticity by enforcing the monotonicity of constitutive relationships – a generalised constraint which encompasses the problems associated with strain softening [153]. However, while violation of any of these conditions might indirectly induce localisation, the critical mechanism remains the loss of Legendre-Hadamard ellipticity indicated by singularity of the acoustic tensor [143]. Therefore any regularisation technique must focus principally on the maintenance of a smooth, continuous deformation field in the face of localised material failure.

3.2 Regularisation techniques

There is a significant body of research addressing the fundamental pathology of mesh dependency in classical continuum approaches. Though a great variety of regularisation techniques have been developed, typically they always enrich the continuum description or constitutive model by in some way incorporating a characteristic length scale. This provides a mechanism for the continuum behaviour to include microstructural phenomena. Naturally, each class of technique exists relative to various purposes and intentions. Some are grounded in thermodynamics and phenomenology – more difficult to understand and implement, but providing rigour and, perhaps, the tantalising prize of clearer insight into the aetiologies of strain localisation. Others follow more intuitive, rugged or simplistic approaches to produce reliable and expedient numerical ‘fixes’. The following is an exploration of the three primary categories of regularisation methods: nonlocal and gradient-enhanced models, generalised continuum theories, and viscoplasticity, as well as their MPM implementations.

3.2.1 Nonlocal and gradient models

In classical plasticity models, the yield function depends on both the current stress state and some collection of internal variables. In the case of isotropic hardening or softening, the sole necessary internal variable is a scalar denoting the accumulated plastic strain, which may be defined

$$\gamma^{\mathrm{p}} = \int \dot{\gamma}^{\mathrm{p}} \, \mathrm{d}t \,, \tag{3.5}$$

where $\dot{\gamma}^{\mathrm{p}}$ is the plastic multiplier, governing the magnitude of plastic straining experienced at a material point.[3] The yield function is then

$$f = f(\boldsymbol{\sigma}, \gamma^{\mathrm{p}}) \tag{3.6}$$

and the γ^{p} dependency may be formulated in any number of ways to reproduce certain work-hardening or strain-softening behaviours. Bažant and Lin [154] proposed an artificial averaging of $\dot{\gamma}$ over a distance $||\boldsymbol{x}' - \boldsymbol{x}||$, such that

$$\dot{\check{\gamma}}^{\mathrm{p}} = \frac{1}{\Omega_r(\boldsymbol{x})} \int_{\Omega} S(||\boldsymbol{x}' - \boldsymbol{x}||)\dot{\gamma}^{\mathrm{p}}(\boldsymbol{x}')\,\mathrm{d}\Omega \tag{3.7}$$

where $\Omega_r(\boldsymbol{x}) = \int S(||\boldsymbol{x}' - \boldsymbol{x}||)\,\mathrm{d}\Omega$ and S is a weighting function (e.g. Gaussian) that defines the spatial influence of neighbouring points. This is placed into the yield function so that

$$f = f(\boldsymbol{\sigma}, \check{\gamma}^{\mathrm{p}}) \tag{3.8}$$

is *nonlocal*. The result is that the elastoplastic behaviour no longer relies only on the deformation and loading history of the specific material *point* under scrutiny, but on the averaged or smoothed strain field surrounding it. This prevents excessive softening at a single location, instead distributing the deformation over a finite region and so avoiding discontinuous, zero-thickness localisation. Nonlocal regularisation is therefore an effective way of preserving ellipticity when a material softens, but raises two important questions, which in some way concern all higher-order continuum theories. The first relates to the selection of the smoothing distance (or internal length), and the second to the proper formulation of the nonlocal boundary conditions. As nonlocal plastic strain does not directly constitute a measurable physical phenomenon (i.e. one which could be observed in a laboratory)[4] there is often no obvious way to address these challenges. Usually a heuristic approach is taken, which calibrates the material-specific internal length and weighting function to match experimental results, but as a numerical 'fix' this does not necessarily provide much insight into the fundamental microstructural mechanisms which lead to finite-sized localisation zones. Instead it only ensures that localisation occurs in a region of approximately the appropriate thickness, and is otherwise superficial. As for the boundaries, the lack of neighbouring material points at the edges of the domain can distort the nonlocal averaging process. If the formulation is not adapted to account for this, non-physical behaviour such as excessive softening or unrealistic strain distributions may emerge [156].

---

[3] The direction of plastic flow is determined by the gradient with respect to stress of the plastic potential function, which may or may not coincide with the yield function – see above.

[4] The approach is viewed by some as a phenomenological representation of microstructural interactions, such as grain boundary effects, dislocation interactions, or crack bridging, which contribute to the finite size of localisation zones [155].

Another disadvantage to nonlocal models is the challenge presented by the integral (3.7). Elastoplastic behaviour is governed by the following constraints:

$$f \leq 0, \qquad \dot{\gamma}^{\mathrm{p}} \geq 0, \qquad f\dot{\gamma}^{\mathrm{p}} = 0 \tag{3.9}$$

which are known as the Karush-Kuhn-Tucker (KKT) conditions. Therefore when plastic flow is occurring (i.e. when $\dot{\gamma}^{\mathrm{p}} > 0$), the consistency condition becomes $\dot{f} = 0$, which due to the dependency on (3.7) turns into an integro-differential equation which cannot be solved locally. Its solution requires an iterative process in each load step, involving quadrature via a discretisation into finite weighted sums, which significantly increases computational complexity and cost [143]. Further information on nonlocal methods of the integral or *strong* type in the context of strain softening is provided in [157].

In contrast to integral-based nonlocal methods, gradient-enhanced models introduce regularisation through spatial derivatives of kinematic quantities or internal variables – typically strain or damage. For instance, an elastic strain-gradient constitutive model might be phrased

$$\dot{\boldsymbol{\sigma}} = \boldsymbol{D} : \left(\dot{\boldsymbol{\varepsilon}} - \ell^2 \nabla^2 \dot{\boldsymbol{\varepsilon}}\right), \tag{3.10}$$

illustrating how an internal length ℓ is embedded into the constitutive equations for dimensional consistency. These methods are classified as *weakly* nonlocal, as they do not explicitly consider neighbouring particles. The gradient dependency alone provides a sufficient *sense* of the deformation occurring around the point in question for a nonlocal regularisation to take place when employing gradient plasticity models. A seminal example is the theory proposed by Aifantis [158], which alters the plastic flow rule to incorporate the Laplacian of the accumulated plastic strain. In its simplest form this can be written

$$\dot{\boldsymbol{\sigma}} = \dot{\boldsymbol{\sigma}}(\dot{\boldsymbol{\varepsilon}}, \gamma^{\mathrm{p}}, \nabla^2 \gamma^{\mathrm{p}}). \tag{3.11}$$

Again, the internal length scale appears in the constitutive model as a coefficient of the higher-order term. This length scale governs how rapidly gradients in plastic strain can develop, thereby setting a finite width for localisation bands [159, 160]. Additionally, the inclusion of the gradient term requires the presence of a conjugate forcing term, leading to the concept of *microstresses* as in the theory of Fleck and Hutchinson [161], as well as specific boundary conditions. However, neither of these necessarily possesses an observable physical basis.

From a numerical perspective, compared to more elaborate higher-order or integral-type models, this approach can be implemented with only moderate modifications to standard codes. Typically a coupled system of equations must be posed to solve for the higher-order strains, requiring a C^1-continuous numerical basis. This complicates finite element implementations, though one workaround is to introduce an implicit coupling between the classical and gradient terms to retain a conventional C^0-continuous finite element space [162]. However, a more fundamental controversy of gradient plasticity models is that many of the most widely used formulations cannot be reconciled with the principles of continuum thermodynamics [163]. Without a rigorous derivation, they may violate the second law of thermodynamics or fail to provide a consistent definition of free energy and dissipation. This is problematic, especially when considering challenging failure processes like strain localisation in which the rate at which mechanical work is dissipated is crucial. Therefore, gradient plasticity models remain subject to ongoing discussions about theoretical soundness [164]. Of course, thermodynamically-consistent gradient theories have been developed [163], but given the poor phenomenology of the involved quantities, the degree of aetiological insight they can provide remains to be seen. Nevertheless, their appeal and utility mean that they are likely the most popular regularisation tool employed for objective strain localisation analyses [21, 159, 160, 165–167].

3.2.2 Generalised continuum theories

The regularisation techniques presented so far have altered the way the continuum description is used to form constitutive models, but none has ventured so far as to modify the description of the continuum itself. In contrast, a generalised continuum theory is one which admits the existence of additional fields to the configuration space, typically to represent motion of the elements which constitute the material's microstructure. In an engineering context it is usually sufficient to ignore the discrete nature of real materials, making the so-called *continuum assumption* and homogenising particulate interactions into a traction in the sense of Cauchy. But many important phenomena cannot be predicted by such simplistic models, including realistic strain localisation, as has been demonstrated. This is also the case when the overall size of the structure is small enough to approach its own microstructural scale, when salient *size effects* in terms of stiffness, hardness and toughness are observed [168–170]. Although they retain the familiar continuum framework, generalised continuum theories address this deficiency by explicitly incorporating additional DOFs, alongside higher-order gradients such that they are considered nonlocal in a weak sense, and microstructural material properties (e.g. internal lengths) typically appear in their constitutive laws. They are therefore naturally capable of capturing size effects, which crucially in geomaterials manifest in the relationship between shear band thickness and particle size [8, 13, 155].

Couple-stress theory

The simplest example of a generalised continuum theory[5] is the couple-stress theory of Voigt [172], Toupin [173], Mindlin [174–177] and Koiter [178], which posits that the continuum can transmit moments in addition to forces, thereby supporting angular momentum

---

[5] Excluding the classical theory of continuum mechanics, which may be recovered as a special case of all generalised theories [171].

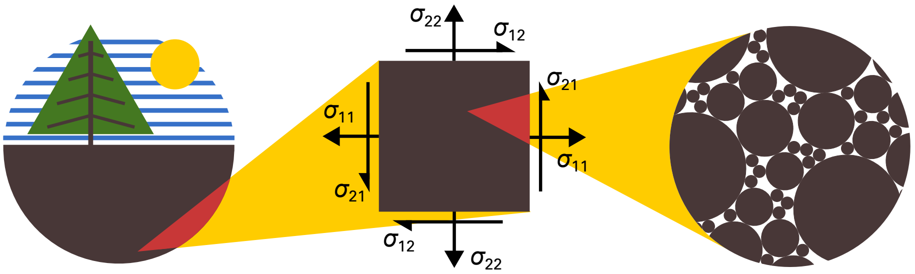

(i) macroscale (ii) continuum scale (iii) microscale

Figure 3.1: The three scales under consideration when using a generalised continuum theory. Although the microstructure is not modelled explicitly, the continuum behaviour is adapted to incorporate homogenised microstructural phenomena.

flux. For the classical continuum, Boltzmann had decreed that torques could not exist at the material point scale, effectively mandating symmetry of the stress tensor (the Boltzmann axiom[6]) [180]. Therefore couple-stress theory, and all theories involving couples, are described as *non-Boltzmann*, and may be contrasted with the conventional *Cauchy-Boltzmann* mechanical formulation. The couple-stresses (couples, moments or torques per unit area) introduced by the theory are directly linked to the gradient of the local rotation $\boldsymbol{R}$ (curvature) of the continuum, obtained from a polar decomposition of the deformation gradient $\boldsymbol{F} = \boldsymbol{R}\boldsymbol{U}$, or the skew-symmetric part of the displacement gradient tensor in small-strain formulations. They also affect the balance of angular momentum, now expressed[7]

$$\nabla \cdot \underset{3}{\boldsymbol{\mu}} + \underset{2}{\boldsymbol{q}} + \boldsymbol{\sigma}^{\mathrm{T}} = \boldsymbol{\sigma}, \tag{3.12}$$

cf. (2.12), where $\underset{3}{\boldsymbol{\mu}}$ represents skew-symmetric third-order Cauchy couple-stress, and $\underset{2}{\boldsymbol{q}}$ is a skew-symmetric second-order tensor of body couples, which act rather like an applied body force only they impress a moment per unit of volume. The presence of couples in this equation means shear stresses are no longer required to be self-equilibrating, thus the Cauchy stress tensor $\boldsymbol{\sigma}$ is generally asymmetric and the Boltzmann axiom is violated. This can be visualised using Mohr's circle, which is depicted in Figure 3.2.

Furthermore couple-stress theory is endowed with internal length scales, as constants with the dimensions of length emerge from the quotient of the couple-stresses and curvature. Localisation zones of a finite size are therefore made possible, enforced by the angular momentum balance equation which resists sharp rotation gradients. Intuitively the existence of couples is not obvious, as their effects are barely discernible in the elastic deformations of most materials. But this deception is completely specious, as couples (or their effects) have repeatedly been observed experimentally. For instance, the micromechanical findings of Fleck et al. [21] show a pronounced length-scale dependency in the elastoplastic regime, and

---

[6] Established and so-named not by Boltzmann but by Hamel [179, p. 326].

[7] The underset numbers are used here to distinguish these quantities from their lower-order, non-skew-symmetric counterparts to be introduced later in this chapter.

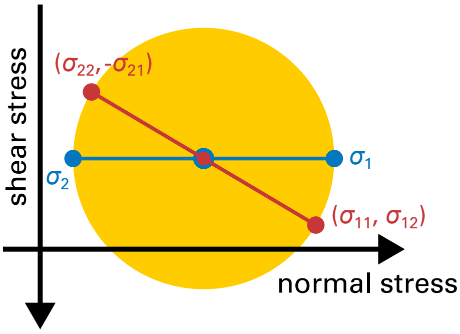

Figure 3.2: A stress Mohr's circle for a two-dimensional non-Boltzmann continuum, after [185, Fig. A6]. The principal stresses σ_1 and σ_2 do not generally lie on the normal stress axis.

Bardet and Vardoulakis [181] demonstrated a clear stress tensor asymmetry in small volumes of granular material. Moreover it is generally agreed that internal couples arise in granular assemblies by direct consequence of the arbitrary angularity of grain shapes [27, 182–184]. Typically this means they become interlocked with multiple points of contact so that,

> the grains having finite dimensions, the forces they exchange raise moments with respect to their centres of mass; the resultants of this moments on the relevant grain, serve, in the discrete picture, the same role as the skew-symmetric part of the Cauchy stress tensor [182].

Couple-stresses are therefore a way of representing the flux of the force stress asymmetry, which must be propagated and conserved to balance the internal angular momentum of the body.

Couple-stress theory has been employed in a variety of ways, including for the analysis of fracture [186], contact [187] and stress concentrations [175], usually to investigate any size effects therein. It has also been widely implemented within numerical schemes, of which the FEM of Oden et al. [188] was the first, but more recently for example an isogeometric boundary element method [189] has appeared. Application to the shear band problem [190] leads to mesh-independent results, making it completely sufficient to regularise the associated loss of ellipticity in most scenarios [191, 192]. But, like all models, couple-stress theory is still a simplification which makes certain assumptions. In particular, it does not account for the specific deformation of microstructural elements, assuming instead that the macroscale deformation gradient $\boldsymbol{F}$ accurately describes the motion of all parts of the structure at every scale. While this may be reasonably accepted for certain polycrystalline materials like metals, the same cannot be said for those which are granular, cellular or colloidal in composition [193]. These materials exhibit behaviours like intergranular slip, and volume and shape change of microelements, which cannot be captured by single homogenised kinematic field. Such micromechanical phenomena are directly responsible for precipitating strain localisation in geomaterials [13, 15, 140, 141], so a more faithful (and, hence, insightful) analysis can only really be achieved by a more complex model capable of capturing more realistically the motion at the microscale. It is for this reason that a phenomenologically richer theory than couple-stress theory, with the potential of shedding more light on the relevant microstructural processes, was ultimately selected.

Micropolar theory

Further generalisation has taken place in various directions and to several degrees of complexity. A strain-gradient theory like those described in Section 3.2.1 can be obtained, for instance, by modifying the gradient dependency in couple-stress theory to include the macroscopic strain tensor. The most prominent example, though, is the *micropolar* continuum [194], of which there will be more discussion later. Micropolar (or *Cosserat*) theory explicitly enriches the continuum with an additional field of independent rotations. The couple-stresses are now conjugate to the gradient of these rotations; if they are constrained so as to follow the macrorotation $\boldsymbol{R}$ of the continuum, the couple-stress theory described above is recovered. But since the new rotation field is generally independent of (but not wholly decoupled from) the macrorotation, it is commonly interpreted as the rigid relative motion of discrete elements making up the material's microstructure and is thus referred to as *microrotation*.[8] Therefore micropolar models are potentially better equipped to illuminate the relationship between granular rotations and continuum-level behaviours like strain localisation. This has made micropolar theory a popular choice for modelling strain localisation in granular media, with a substantial body of literature supporting its application [27, 184, 195–197]. However, micropolar theory does introduce its own modelling difficulties: accurately capturing the independent microrotation field can be numerically challenging, particularly in three dimensions (see Section 3.4) and, even in the simplest of elastic cases, at least two additional material parameters are required: an internal length ℓ, and a coupling modulus κ to determine the degree of independence of the microrotation field (see Section 3.3.7). Although they do have physical significance, their determination is far from straightforward [198, 199], forming the subject of continued academic debate [200, 201].

The presence of κ (also known as the modulus of local rotational stiffness, Cosserat shear modulus and modulus of torsional rigidity) is chiefly what distinguishes micropolar theory from the simpler couple-stress theory. Conceptually, one may think of it as characterising a microscopic rotational spring attached to the microstructure at one end, and anchored to the surrounding macrocontinuum at the other. When this spring is *infinitely* stiff ($\kappa \to \infty$), the rotation of the microstructure must match the macroscopic rotation prescribed by the global displacement field. By contrast, if the spring has *finite* stiffness, then local, independent microrotations become possible.[9] The phenomenological problem here is

---

[8] To be clear, microrotations in micropolar theory are still a homogenised, continuous field and thus do not explicitly represent discrete particulate motions. This does not invalidate their phenomenology.

[9] Part of the process of reducing the linearised micropolar theory to the classical Cauchy-Boltzmann model involves setting $\kappa = 0$, rendering microrotations irrelevant to the mechanical response. For a full

that while such independent microrotations have been observed in post-failure conditions (where they manifest as plastic spin of soil grains), the question remains whether these rotations play any significant role during elastic loading of soils. Indeed, some claim that measurements of decoupled rotations under purely elastic conditions have been of the order of experimental precision, thereby calling into question the necessity of incorporating micropolar theory in the elastic regime [197]. This raises the possibility that the micropolar approach might amount to an *over-regularisation* – in other words, it could unintentionally alter the material response in regimes where the classical theory is already valid. Naturally, the key requirement for any regularisation scheme is that it should *only* address specific deficiencies (such as ill-posedness and pathological mesh dependence) without unduly altering predictions in situations where conventional theory is completely adequate. Thus, if micropolar theory were to produce large deviations from classical predictions under well-posed conditions, that would be a strong indication that the formulation is invalid or inappropriate. Accordingly, a comparison between the elastic loading of the classical specimen in Section 2.4 and the micropolar model developed over the following pages is attempted as part of its verification in Section 4.4. It must be emphasised, however, that micropolar theory is not an arbitrary numerical regularisation; its formulation arises from rigorous variational and thermodynamical principles rooted in physical considerations of real materials. There is, in fact, no fundamental reason to deny the possibility of small, local microrotations – even under elastic conditions – in granular materials. Future advances in experimental techniques, such as high-resolution X-ray computed tomography, may eventually confirm their presence. Consequently, micropolar theory, unlike some other regularisation approaches, should not be dismissed as producing spurious artefacts simply because it allows for non-classical phenomena. On the contrary, such phenomena may prove to be valuable for understanding how and why geotechnical structures fail – insights that simpler models would, by definition, miss. The significance of the coupling modulus κ and the phenomenology of its concomitant independent microrotation field is treated in more detail in Section 3.3.7. However, it suffices here to note that all known materials for which complete sets of elastic micropolar parameters have been experimentally derived exhibit a significant, but finite, κ [203]. Although these available data sets do not yet include purely granular materials, their finite κ values suggest that local independent microrotations are not unphysical in the elastic regime. Ultimately, this strengthens the case for micropolar theory as a tool that, while it regularises the field equations, does so in a physically justifiable way.

But how is it that the introduction of an independent microrotation field can preserve the ellipticity of the governing rate-equilibrium equations into the strain-softening regime? Recall that ellipticity is lost when acceleration waves travelling in the medium are stopped from propagating by some discontinuity, coinciding with singularity of the acoustic tensor

---

reduction other parameters must also be controlled – see [202].

$\boldsymbol{A}$. In micropolar theory, the acoustic tensor must be augmented so as to incorporate microrotational wave modes. More specifically, while for the nonpolar continuum $\boldsymbol{A}$ depends only on the fourth-order constitutive tensor $\boldsymbol{D} = \frac{\partial \boldsymbol{\sigma}}{\partial \boldsymbol{\varepsilon}}$ linking classical incremental stresses to strains (see (3.1)), the micropolar acoustic tensor $\check{\boldsymbol{A}}$ also depends on the tangent operators interlinking these quantities with incremental couple-stresses $\dot{\boldsymbol{\mu}}$ and curvatures $\dot{\boldsymbol{k}}$. A full derivation is provided in e.g. [204, 205], culminating in the block matrix

$$\check{\boldsymbol{A}} = \begin{bmatrix} \boldsymbol{A}^{\sigma\varepsilon} & \boldsymbol{A}^{\sigma\kappa} \\ \boldsymbol{A}^{\mu\varepsilon} & \boldsymbol{A}^{\mu\kappa} \end{bmatrix} = \begin{bmatrix} \boldsymbol{n}\cdot\frac{\partial \boldsymbol{\sigma}}{\partial \boldsymbol{\varepsilon}}\cdot\boldsymbol{n} & \boldsymbol{n}\cdot\frac{\partial \boldsymbol{\sigma}}{\partial \boldsymbol{k}}\cdot\boldsymbol{n} \\ \boldsymbol{n}\cdot\frac{\partial \boldsymbol{\mu}}{\partial \boldsymbol{\varepsilon}}\cdot\boldsymbol{n} & \boldsymbol{n}\cdot\frac{\partial \boldsymbol{\mu}}{\partial \boldsymbol{k}}\cdot\boldsymbol{n} \end{bmatrix}, \tag{3.13}$$

where $\boldsymbol{A}^{\sigma\varepsilon} = \boldsymbol{A}$ and

$$\begin{Bmatrix} \dot{\boldsymbol{\sigma}} \\ \dot{\boldsymbol{\mu}} \end{Bmatrix} = \begin{bmatrix} \frac{\partial \boldsymbol{\sigma}}{\partial \boldsymbol{\varepsilon}} & \frac{\partial \boldsymbol{\sigma}}{\partial \boldsymbol{k}} \\ \frac{\partial \boldsymbol{\mu}}{\partial \boldsymbol{\varepsilon}} & \frac{\partial \boldsymbol{\mu}}{\partial \boldsymbol{k}} \end{bmatrix} \begin{Bmatrix} \dot{\boldsymbol{\varepsilon}} \\ \dot{\boldsymbol{k}} \end{Bmatrix}. \tag{3.14}$$

The formation of discontinuous surfaces in a micropolar medium occurs when the generalised acoustic tensor (3.13) becomes singular. Hence the strong ellipticity condition becomes

$$\det\left(\check{\boldsymbol{A}}\right) > 0 \tag{3.15}$$

so that bifurcation now depends on the coupling between classical stresses and curvature rates and couple-stresses and strain rates and, therefore, on ℓ and κ. When these two quantities are greater than zero (i.e. as long as the model is nonlocal), infinitely steep rotation gradients are precluded and discontinuities cannot emerge. As shown in [204], this is because the lowest eigenvalue of $\check{\boldsymbol{A}}$ is prevented from becoming negative when this coupling exists, guaranteeing (3.15) is fulfilled. Essentially, the micropolar continuum's extra stiffness against rotational gradients keeps wave speeds from collapsing to zero, thereby preserving the positivity of the generalised acoustic tensor (and thus preserving ellipticity) even though the classical part of the tensor may soften. Moreover in the converse (local, nonpolar) case that $\ell = 0$ or the microrotations are constrained, the two fields are decoupled and the model loses its ability to prevent loss of ellipticity. Interestingly, it is possible for $\check{\boldsymbol{A}}$ to become singular in extreme examples, typically involving very high degrees of material anisotropy. This phenomenon is discussed by Gourgiotis and Bigoni [191, 192] in relation to couple-stress elasticity, where it may lead to instances of stress channelling, faulting and wrinkling – deformation modes which cannot be captured by classical models.

Microstretch and micromorphic theories

A generalised continuum may be considered to have an additional microcontinuum embedded at every location within it, characterised in terms of kinematics by a microdeformation tensor [206]. For the micropolar continuum, this quantity is the microrotation tensor. But generalisation does not, of course, end with micropolar theory. As its name suggests, *microstretch* or *microstrain* theory is produced if the tensor captures independent isotropic

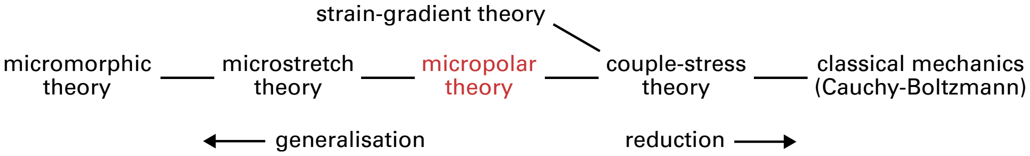

Figure 3.3: A family of generalised continuum theories. Each theory may be recovered as a special case of its left-hand neighbour.

expansion and contraction (termed *breathing*) relative to the surrounding macrocontinuum, in addition to rotations. The microstretch continuum therefore has four DOFs associated with the microcontinuum, in addition to the three translations of the classical macrocontinuum. Micropolar theory can be reproduced by constraining microstretch theory which, in turn, is a special case of *micromorphic* theory, developed by Mindlin in the 1960s [176] – a relationship depicted in Figure 3.3. This highly generalised model enlarges the microdeformation space to include nine non-classical DOFs (three microrotations, three microstretches and three microshears, making twelve total DOFs) such that it can capture advanced multiscale material behaviour in a rigorous, systematic and objective manner. From a practical standpoint, both continuum theories find application in systems where the local substructure undergoes significant inhomogeneous or higher-order deformations, including [206, 207]:

- Biological tissues, in which the microdeformation tensor may track the motion of individual cells, e.g. corpuscles in blood;
- Bubbly and porous fluids, turbulent flow fields, and deformable or pressure-filled suspensions;
- Metamaterials and architected lattices, whose mechanical response can exploit microscale rotation, stretching, or shearing;
- Composites and molecular-scale systems.

Despite their potential for capturing rich micromechanical effects, microstretch and micromorphic theories engender substantial challenges in practice. The principal drawback lies in their constitutive complexity: a more refined material description inevitably entails a greater number of parameters, each of which must be calibrated to reflect real physical behaviour. Experimental identification of these parameters, or their link to first principles or atomistic models, is far from trivial [207, 208]. Consequently, neither theory is widely employed in conventional engineering applications. Elastoplastic formulations are similarly scarce and do not seem to share a unified methodological foundation [164, 209–211], although the inherent regularising properties of micromorphic theories have been demonstrated both theoretically [212] and numerically [213].

Within the context of this thesis, the primary micromechanical features of most geomaterials can be captured by micropolar theory's allowance for rigid particle rotations, without the need for additional microstretching or microshearing modes. Indeed, for granular media in particular, the introduction of those extra modes would be unphysical, and their application is not advised [206]. Consequently, both microstretch and micromorphic theory represent unnecessary complications for the purposes of the present work.

3.2.3 Viscoplasticity

The last genre of regularisation technique which has seen wide use in geotechnics is the introduction of viscosity to the continuum description. Where nonlocal methods introduce a characteristic *length*, viscous models include a characteristic *time* scale. It is for this reason that such methods are considered *time-dependent*, and thus are capable of modelling mechanical processes which depend on the rate at which loading is applied to and propagated through the system [139]. This is in contrast to classical (rate-independent) models, in which the same mechanical response is produced regardless of how fast loading occurs. The primary objective of viscous regularisation is to introduce a time-dependent damping or resistance term into the constitutive model or governing equations of the system. This term is usually analogous to a viscous damping force that acts on the material, which helps to smooth out the solution around potential bifurcation surfaces, preventing discontinuities or singularities and, therefore, mesh dependency. As such, viscous regularisation has been applied to both quasi-static and dynamic analyses of localisation problems [214–216].

Viscosity is of course a natural phenomenon observed in geomaterials at all scales, for example in creeping landslides, solid-fluid regime changes, microinertial effects during rapid loading, and processes within the earth's mantle governed by thermo-hydro-chemo-mechanical changes. Although viscous regularisation may therefore seem an appealing way to overcome ill-posedness, in practice it is much more complicated. As noted in e.g. [217, 218], viscous media are not automatically immune to the loss of ellipticity, and rate dependency can only restore well-posedness when implemented in specific ways. In viscoplasticity, this effect is typically implemented by modifying the plastic flow rule to incorporate rate sensitivity, as was first conceived by Perzyna [219]. In particular, the plastic multiplier $\dot{\gamma}^{\mathrm{p}}$ is usually redefined so that it resembles

$$\dot{\gamma}^{\mathrm{p}} = \varrho g, \tag{3.16}$$

where ϱ is a viscosity-like parameter containing the inverse of the characteristic time scale and g is the plastic potential function (or *overstress*). In other words, the plastic strain rate does not depend on incremental quantities but on constitutive properties of the model. The plastic potential is derived (often semi-empirically, incorporating scalings and power laws) and incorporated into the KKT conditions (3.9) such that irrecoverable deformations may arise when the stress state does not lie on the yield surface f, allowing for the possibility of creep. This effectively 'smears' the transition from elastic to inelastic behaviour, as the rate at which the yield surface is approached alters the magnitude of plastic straining.

This implies that abrupt changes in stress or strain cannot occur instantaneously within an infinitely small region, as the rate-dependent viscous resistance prevents the failure zone from localising onto a singular plane. This smearing effect maintains the stability of the analysis and reduces the pathological mesh dependence. However, this is only the case for dynamic analyses, and viscous regularisation cannot be achieved in quasi-statics where inertial effects are not inherent [216]. Instead, quasi-static viscoplasticity can only *slow down* the rate at which discontinuous bifurcation occurs and, even sometimes in dynamic analysis, rate-dependency only gives the *appearance* of mesh objectivity when simulations are curtailed before the system reaches a steady state [218]. In light of this, viscous regularisation is not pursued in this work.

3.2.4 In the material point method

There have been few extensions of the MPM to include higher-order theories. The first instance, using nonlocal plasticity of the integral (strong) type, emerged in 2012 [220], and a weakly nonlocal version appeared in 2017 [221]. Meanwhile, Charlton [133, 222, Ch. 5] implemented gradient plasticity within an implicit GIMPM, managing to model mesh-objective strain localisation in a numerically robust fashion. This was followed by another integral-type model to simulate quasi-brittle damage of particle grains [223], an implementation of Johnson-Cook damage in a Total Lagrangian[10] MPM [224], and a recent application of a strongly nonlocal elastoplastic constitutive model for brittle soils to the GIMPM [225]. A handful of rate-dependent MPMs have been developed for the purpose of simulating viscoelastic fluids [226–228], which therefore have no applicability to localised failure, with several extensions to plasticity too [229–232]. Micropolar theory has also been implemented within the MPM, but usually again only to model elastic deformations – see the explicit formulation of Ma and Sun [233], and the implicit implementation upon which this chapter is based [112] and its associated conference papers [234, 235]. The recent work of Neuner's group has culminated in an implicit inelastic micropolar B-spline MPM which also incorporates a nonlocal gradient damage model, for the purpose of modelling localised failure and fracture in cohesive-frictional materials such as stone and concrete [102]. However, this highly advanced formulation suffers from numerical issues, particularly at the physical domain boundaries where spurious deformations emerge as a result of the large support required by B-spline basis functions (see Section 2.2.4 in this thesis). An opportunity is thereby presented to develop an implicit micropolar MPM stabilised with a combination of generalised interpolation and ghost penalisation, and without the supernumerary complication of gradient damage. Indeed, geometrically-nonlinear micropolar theory has never hitherto been used to analyse strain localisation in

---

[10] This means all deformations are referred back to the material frame, where the governing equations are solved. As this requires the maintenance of the original geometry, Total Lagrangian MPMs are essentially nothing more than badly-integrated FEMs [W.M. Coombs, personal communication (2025)].

soils, nevermind in the MPM. This task forms the remainder of this thesis.

3.3 Continuum formulation

What has come to be known as micropolar theory has its origins in the 1909 treatise *Théorie des corps déformables* [*Theory of deformable bodies*] [194] by the Cosserat brothers, Eugène and François. It is for this reason that the theory is also known as *Cosserat* theory, though in the present work the more descriptive *micropolar* is preferred.[11] The brothers were eminent scions of a wealthy industrial family, famed for producing luxury corduroy and velvet textiles in Amiens, northern France [236]. François, the elder, trained as a civil engineer in Paris, and in 1895 was appointed a chief engineer designing tunnels and bridges for the French railway. Conversely, Eugène remained in academia following his scientific training, and joined the science faculty at the University of Toulouse as a professor of differential geometry [237]. Their collaboration spanned a fruitful period of thirteen years, during which time they published several papers on the foundations of mechanics, culminating in the treatise of 1909. It is thought that François, whose genius has been compared to that of Poincaré and Einstein [236], was the primary innovator, as his untimely death in 1914 marked the cessation of any further outputs on elasticity. By this time, Eugène had already been appointed Director of the Toulouse Observatory (a position he held until his own death in 1931) and his focus thereafter shifted away from mechanics [180]. Their ambitious plans, to unify the mathematical theories of elasticity, heat and electromagnetism, never materialised. But the Cosserat brothers were pioneers: they had, for the first time, connected geometry (namely Lie theory) to physics – a feat for which they are not widely credited. It is unsure whether they even realised it themselves [236].

Traditional analysis of deformable bodies considers a continuum of infinitesimal points which are allowed to translate. A profound new idea was introduced by Duhem [238]: a body can be regarded as a collection of not only points but also *directions associated with the points*. The proposal of these vectors, called *directors*, planted the seed which would lead to the workings of the Cosserat brothers. Indeed, their first co-written paper opens by remarking

> how powerful an instrument of discovery the moving reference triad has been in the theory of surfaces [...] and one can see that [its] introduction to the mechanics of rigid solids is no less fortuitous. We proposed to extend the use of this triad to the study of deformable bodies, and we have thus been led, by several important enquiries, to results which appear to us novel [239].[12]

---

[11] A cursory survey of Google Scholar indicates that *micropolar* is used more frequently by applied mathematicians and fluid dynamicists, while *Cosserat* is favoured by those working in soft robotics and by some geotechnicians.

[12] My translation.

(a) **(b)** **(c)**

Figure 3.4: **(a)** François Cosserat (1852-1914), **(b)** Eugène Cosserat (1866-1931) and **(c)** the Cosserat cat (trans. *Pussy Cat reigns over the most beautiful corduroy in the world*).

This represents the most crucial of the Cosserats' advancements. Succeeding where Lord Kelvin and Helmholtz had failed [180], they attached a set of rigid orthogonal directors (the *triad*,[13] not unlike axes) to each point in the deformable medium [194, p. 122], such that each point takes on an orientation and the medium may be considered *polar*. It therefore makes sense to speak of the rotation of each point, which acts much like an infinitesimal rigid body, representing an independent additional kinematic field (see Figure 3.5). They examined in turn rods, shells and three-dimensional continua, applying principles of differential geometry and imposing the invariance of a kind of generalised strain energy under Euclidean transformations – a methodology which they named *l'action euclidienne* [Euclidean action] [240]. The balance laws were achieved [194, p. 137], incorporating couples applied to and transmitted by the medium, impressively without any consideration of static equilibrium in the sense of Newton. But, disappointingly for the modern interpreter, no mention is made of constitutive equations. In fact, the treatise's hundreds of pages of relentlessly abstract derivations (written in a time before tensor calculus had been properly formalised) are unpunctuated by applications or practical considerations, reflecting the mathematical intentions of the Cosserats' work. This may go some way towards explaining why it was largely forgotten about (beside a single exploratory monograph by Sudria [241]) until the theory was investigated as part of a broader theoretical movement interested in non-classical continua some fifty years later, when it was linked to newly-discovered liquid crystals [236].

The revived interest led to the essential developments made by Cowin [171], Ericksen and Truesdell [243], Eringen [244–247], Kafadar and Eringen [248], Mindlin [174–177, 249], Neuber [250], Nowacki [251], Schaefer [180, 252], Toupin [253], Truesdell and Noll [254] and Truesdell and Toupin [255]. Together they systematically formulated the foundations of micropolar theory, transforming it from a mere mathematical curiosity to the rigorous continuum framework used today, albeit in a restricted linearised form. Notably it was

---

[13] *Trièdre* originally, also translated as *triade*, *trihedron* or *cross*.

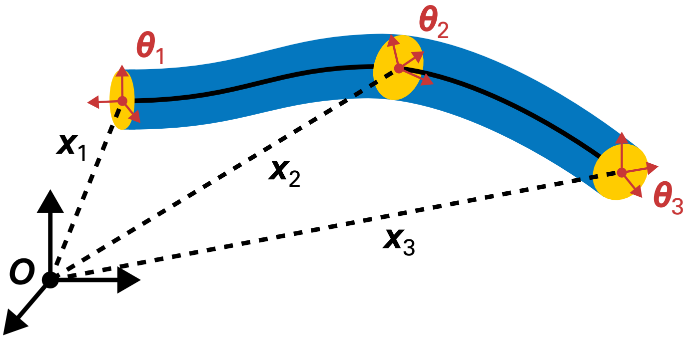

Figure 3.5: A Cosserat rod, equivalent to a generalised Timoshenko beam [242]. Each point along the rod not only has a position $\boldsymbol{x}$ but also rotates to an orientation $\boldsymbol{\theta}$ denoted by each red triad.

Eringen who formally introduced the notion of microinertia, and first styled the theory *micropolar*. The connection between micropolar theory and strain localisation was then made in 1987 by Mühlhaus and Vardoulakis [27], around the time that the first numerical implementations of the linearised theory were being developed [135, 195, 196, 256]. Since then, micropolar FEMs have been developed for a variety of purposes, including plane problems and patch tests [257], torsion [258], the Saint-Venant effect [259], three-dimensional bending [260], size effects [261], isoparametric studies [262] and, of course, mesh-objective shear bands [128, 135, 196, 263–266]. Recently, micropolar theory has been implemented with SPH [59] and peridynamics [267] too. However, each of these makes use of only the linearised, small-strain formulation of micropolar theory, limited in accuracy to the domain of infinitesimal deformations. The intense deformation gradients[14] which develop during strain localisation processes suggest that infinitesimal theories should not be used, if a physically-consistent description is the goal. Hence, following the theoretical workings of Eringen [206, 246, 247], Steinmann [269], Sansour [209, 270] and Neff [197] (among others), geometrically-nonlinear implementations also began to emerge. Initially, both Grammenoudis and Tsakmakis [271] and Bauer et al. [272] considered large displacements, but made small-strain assumptions in order to use constitutive models from the linear theory. Then Ramezani et al. [273] developed and conducted studies of various hyperelastic models, but these were limited to plane problems. Therefore the first truly geometrically-exact three-dimensional formulations are those of Bauer et al. [274, 275] which respectively consider hyperelasticity and hyperelastoplasticity – the latter in the context of metal plasticity and necking. Further implementations of purely *geometric* nonlinearity were established by Erdelj et al. [276], as well as by Ma and Sun [233] and O'Hare et al. [112] for the MPM. Neuner and his collaborators have also combined geometrically-exact micropolar elastoplasticity with a gradient-enhanced continuum damage model in both the FEM [277, 278] and, latterly, the MPM [102].

---

[14] For instance, Amirrahmat et al. [268] observed grain rotations in excess of 40° inside a shear band produced during triaxial testing of sand.

Contemporary micropolar research is not limited to the discipline of geomechanics. The nature of the micropolar medium means it lends itself to any application involving rigid motion of the material's substructure. For example, Lakes and coworkers have used micropolar theory extensively to model cellular biological materials, and in particular human bone [198, 279]; a key size effect exerted by osteons over structural stiffness has been perceived as a resounding validation of the theory. Elsewhere, the rise of the *Cosserat robot* has led to an application of one-dimensional micropolar theory (see Figure 3.5) to the field of soft (continuum) robotics [280, 281]. Here the framework offers increased flexibility in the available modes of deformation, as each element of the robot can not only move in a translational sense, but can also rotate to a desired angle or curvature. Micropolar fluid dynamics has also become a field of particular note, concerned with rigid polar particles suspended in a surrounding fluid matrix [282, 283]. A key application has been to the analysis of ferromagnetic fluids, where an applied electromagnetic field may invoke a body couple acting on magnetic dipoles held by the fluid, causing them to rotate. This in turn might lead to stresses and mechanical work such that the piezoelectric effect is captured naturally [206]. Other work has focused on removing some of the barriers to more widespread use of micropolar theory, for example block preconditioning in computational implementations [284], and addressing the difficulty of consistent linearisation [285, 286].

The rest of this section entails a mathematical formulation of a nonlinear hyperelastic micropolar continuum, including an exploration and justification of the specific constitutive model adopted. Its subsequent implementation in an implicit MPM (for which a full account of the consistent linearisation is provided in Appendix A) is verified with the method of manufactured solutions (MMS), and tested with several numerical experiments. An elastoplastic extension of the model will follow in Chapter 4.

3.3.1 Kinematics

With reference to Figure 3.6, consider a micropolar continuum undergoing a nonlinear deformation Ξ over a time t from its reference volume Ω_0 to its spatial configuration $\Omega = \Xi(\Omega_0, t)$. The continuum is embedded in three-dimensional Euclidean space, described by an orthogonal (Cartesian) right-handed co-ordinate system $\boldsymbol{X}_{\alpha,\alpha\in\{1,2,3\}}$ referred to some fixed origin $\boldsymbol{O}$. Material elements of the continuum, described by a position vector $\boldsymbol{X} \in \Omega_0$, hence undergo a motion to arrive at a spatial position $\boldsymbol{x} \in \Omega$, viz.

$$\boldsymbol{x} = \Xi(\boldsymbol{X}, t) \tag{2.1}$$

and $\Xi(\boldsymbol{X}, 0) = \boldsymbol{X}$. As with the classical continuum described in Section 2.3, the two states are connected by both a translation vector $\boldsymbol{u}$, defined

$$\boldsymbol{x} = \boldsymbol{X} + \boldsymbol{u}, \tag{2.2}$$

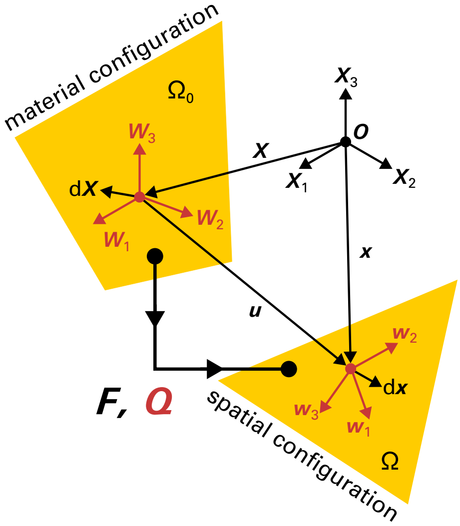

Figure 3.6: The finite strain kinematics of a micropolar continuum, with the microrotational objects depicted in red.

and a deformation gradient tensor providing the elemental mapping $\mathrm{d}\boldsymbol{x} = \boldsymbol{F}\,\mathrm{d}\boldsymbol{X}$ such that

$$\begin{aligned} \boldsymbol{F} &= \nabla \Xi \tag{2.3} \\ &= \frac{\partial \boldsymbol{x}}{\partial \boldsymbol{X}} \tag{2.4} \\ &= \boldsymbol{I} + \frac{\partial \boldsymbol{u}}{\partial \boldsymbol{X}} \tag{2.5} \end{aligned}$$

and $J = \det(\boldsymbol{F})$ is the local volume change ratio so $\mathrm{d}\Omega = J\,\mathrm{d}\Omega_0$.

In a micropolar continuum, each material element is additionally defined by an attached orthonormal triad of rigid directors $\boldsymbol{W}_{\alpha,\alpha\in\{1,2,3\}}$ aligned with the coordinate axes of the space. They are related to their spatial counterparts $\boldsymbol{w}_{\alpha,\alpha\in\{1,2,3\}}$ through the relation

$$\boldsymbol{w}_\alpha = \boldsymbol{Q}\boldsymbol{W}_\alpha \tag{3.17}$$

such that

$$\boldsymbol{Q} = \sum_{\alpha=1}^{3} \boldsymbol{w}_\alpha \otimes \boldsymbol{W}_\alpha. \tag{3.18}$$

This makes $\boldsymbol{Q}$ a special orthogonal transformation called the *microrotation tensor*, which is completely independent from the mapping Ξ and, therefore, the deformation gradient and translation field. It belongs to the set of rigid three-dimensional transformations such that a formal designation $\boldsymbol{Q} \in SO(3)$ can be made, denoting $\underline{\text{s}}$pecial $\underline{\text{o}}$rthogonal Lie[15] groups with three parameters (e.g. angles). This identifies the transformation as a

---

[15] Earlier it was noted that the Cosserats were the first to unify physics with geometry, which they accomplished via Lie theory, and likely unknowingly. However, this connection is not related to the presence of rotations in their theory, but rather to the skew-symmetry of the angular momentum balance equation

finite three-dimensional rotation, and means it must obey certain well-known conditions to preserve the length, orthogonality and handedness of the triad: namely the orthonormality condition

$$\boldsymbol{Q}\boldsymbol{Q}^{\mathrm{T}} = \boldsymbol{Q}^{\mathrm{T}}\boldsymbol{Q} = \boldsymbol{I} \tag{3.19}$$

from which follow the additional properties

$$\boldsymbol{Q}^{\mathrm{T}} = \boldsymbol{Q}^{-1} \tag{3.20}$$

and

$$\det(\boldsymbol{Q}) = 1. \tag{3.21}$$

Specifically, the determinant of the microrotation tensor must be $+1$ (rather than -1) to preserve the handedness or orientation of the system, avoiding mirror-image reflections. This stipulation is the distinction between *special* and merely *proper* orthogonal transformations.

The addition of these independent orthogonal transformations to the configuration space means that three-dimensional motion is now described by six DOFs, rather than the conventional three of a nonpolar continuum. To be clear, deformation occurs by two distinct mechanisms:

1. Classical macrodeformation, consisting of some combination of a translation $\boldsymbol{u}$ which carries a particle from position $\boldsymbol{X}$ to $\boldsymbol{x}$, a macrorotation and a macrostretch – all encoded within the deformation gradient tensor $\boldsymbol{F}$; and

2. Rigid microrotation $\boldsymbol{Q}$ of the micropolar triad attached to the particle,

requiring three DOFs each. As the motion as a whole results from a product composite of these modes, the state of any intermediate configurations depends on the order in which they are applied [244]. In general, however, this does not affect the final state.

Via Euler's rotation theorem [287], any number of sequential rotations are equivalent to a single rotation around some particular fixed axis. The rotation occurs entirely in the plane to which the axis is normal – see Figure 3.7 for a visualisation. Therefore the rotation may be parametrised completely by a vector denoting this axis, and an angle of rotation defined with a right-hand screw rule. If however the angle is allowed further to define the *length* of the vector, then the transformation may be described by a set of just three independent parameters. To that end, let the rotation effected by $\boldsymbol{Q}$ (i.e. the transformation rotating each $\boldsymbol{W}_\alpha$ into $\boldsymbol{w}_\alpha$) be parametrised by a microrotation angle θ about a microrotation vector $\boldsymbol{\theta}$, where $\theta = ||\boldsymbol{\theta}||$. The axis is invariant to its corresponding

---

(3.12) in hyperstress space. It is more closely tied to Lie's original motivations for his work in group theory: to model continuous symmetries of differential equations. This intersection is described in [236] in French.

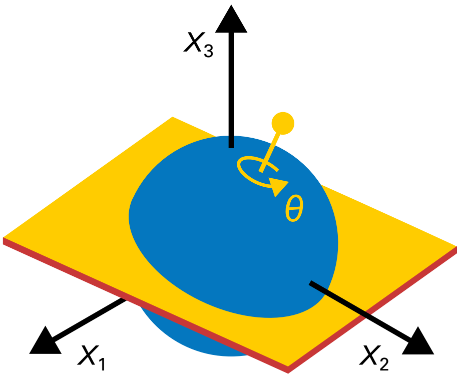

Figure 3.7: A rotation of a sphere by an angle θ on a plane.

orthogonal transformation, fulfilling the eigenequation

$$\boldsymbol{Q}\boldsymbol{\theta} = \boldsymbol{\theta} \tag{3.22}$$

such that the microrotation vector is the only real eigenvector of the microrotation tensor. The quantity $\boldsymbol{\theta}$ will later be classified as the *extrinsic* microrotation vector as it refers to rotation relative to the fixed material triad, cf. the *intrinsic* microrotation vector which describes incremental rotations relative to the moving spatial triad. As might be inferred from Figure 3.7, the set of all possible microrotation vectors (i.e. those pointing in any direction from the origin with length $0 \leq \theta \leq \pi$) defines a solid sphere of radius π.[16] This satisfying topological interpretation of an algebraic system is what qualifies rotations as a Lie group (every example of which has an associated smooth, differentiable manifold, not just $SO(3)$). It is important to note that while $\boldsymbol{\theta}$ is an Euler *vector*, apart from in special cases its contents are not the well-known Euler *angles* (e.g. yaw, pitch and roll) used in aeronautics, navigation and geodesy.

Any tensor which is skew-symmetric in any two of its indices (e.g. $A_{ij} = -A_{ji}$) has, by definition, the same number of DOFs as a tensor of one order fewer. Therefore a skew-symmetric second-order tensor $\widehat{\boldsymbol{\theta}}$ populated entirely by $\boldsymbol{\theta}$ can be written

$$\widehat{\boldsymbol{\theta}} = -\boldsymbol{\epsilon}\boldsymbol{\theta} = \begin{bmatrix} 0 & -\theta_3 & \theta_2 \\ \theta_3 & 0 & -\theta_1 \\ -\theta_2 & \theta_1 & 0 \end{bmatrix} \tag{3.23}$$

such that $\widehat{\boldsymbol{\theta}}\boldsymbol{v} = \boldsymbol{\theta} \times \boldsymbol{v}$ for any vector $\boldsymbol{v}$. The vector $\boldsymbol{\theta}$ is known as the *axial* vector of the corresponding skew-symmetric tensor $\widehat{\boldsymbol{\theta}}$; henceforth this notation is always used to indicate

---

[16] Rotations between π and 2π radians must be redefined as the equivalent rotation in the opposite direction, i.e. relative to the inverted axis $-\boldsymbol{\theta}$. Antipodes of the sphere are equivalent.

this operation. In index notation it is equivalently

$$\widehat{\theta}_{ij} = -\epsilon_{ijk}\theta_k, \tag{3.24}$$

and the third-order Levi-Civita (or *permutation* or *alternating*) tensor, represented by $\boldsymbol{\epsilon}$, is defined

$$\epsilon_{ijk} = \begin{cases} 1, & \{i,j,k\} = \{1,2,3\},\ \{2,3,1\} \text{ or } \{3,1,2\} \\ -1, & \{i,j,k\} = \{3,2,1\},\ \{1,3,2\} \text{ or } \{2,1,3\} \\ 0, & i=j,\ j=k \text{ or } k=i. \end{cases} \tag{3.25}$$

In other words, it supplies the value of positive unity for even permutations of its indices, negative for odd, and zero otherwise. The inverse operation is achieved by taking

$$\boldsymbol{\theta} = -\frac{1}{2}\boldsymbol{\epsilon} : \widehat{\boldsymbol{\theta}}, \qquad \theta_i = -\frac{1}{2}\epsilon_{ijk}\widehat{\theta}_{jk} = \frac{1}{2}\epsilon_{jik}\widehat{\theta}_{jk}. \tag{3.26}$$

As a skew-symmetric tensor $\widehat{\boldsymbol{\theta}} = -\widehat{\boldsymbol{\theta}}^{\mathrm{T}}$ is classified as a Lie *algebra*, i.e. $\widehat{\boldsymbol{\varphi}} \in \mathfrak{so}(3)$. As shown in Figure 3.8, a Lie algebra is formally a local chart of the $SO(3)$ manifold, and may therefore be mapped to become a corresponding Lie group $\boldsymbol{Q}$. In the case of infinitesimal rotations, this mapping is simply

$$\boldsymbol{Q} \approx \boldsymbol{I} + \widehat{\boldsymbol{\theta}} \tag{3.27}$$

which demonstrates how a Lie algebra constructed from the total Euler vector $\boldsymbol{\theta}$ is a linearisation (i.e. a truncated Taylor series) of a Lie group at the reference orientation $\boldsymbol{Q} = \boldsymbol{I}$ where $\boldsymbol{\theta} = \boldsymbol{0}$. However, for finite rotations a simple additive formula will not suffice,[17] and the canonical exponential map

$$\boldsymbol{Q} = \exp\left(\widehat{\boldsymbol{\theta}}\right) = \sum_{n=0}^{\infty} \frac{1}{n!}\widehat{\boldsymbol{\theta}}^n \tag{3.28}$$

must be used instead. In practice the equivalent but rather more conveniently phrased Euler-Rodrigues formula

$$\boldsymbol{Q} = \boldsymbol{I} + \frac{\sin\theta}{\theta}\widehat{\boldsymbol{\theta}} + \frac{1-\cos\theta}{\theta^2}\widehat{\boldsymbol{\theta}}^2, \tag{3.29}$$

derived elegantly in closed form by Argyris [288], might be preferred. Indeed there are myriad ways to represent and manipulate elements of the rotation group and its algebras. Beyond the orthogonal tensor, (Euler) axis-angle and Rodrigues vector formalisms demonstrated above, these include spectral eigendecomposition, Euler angles and Cayley-Klein parameters. Later an alternative rotation formalism based on quaternions will be developed for use in the numerical algorithm.

To illustrate some of the finite rotation machinery established so far, consider a

---

[17] This is because each successive rotation is defined relative to a new reference frame.

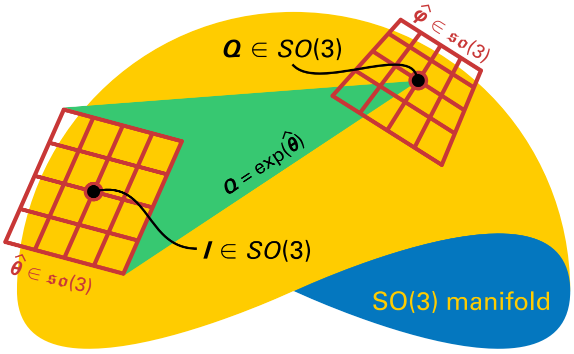

Figure 3.8: Lie algebras constructed from rotation vectors form local linearised charts of the nonlinear Lie group manifold. The intrinsic microrotation vector $\boldsymbol{\varphi}$, which measures superposed or spatial rotation increments, will be defined later in Section 3.4.1.

microrotation ϑ around the X_3 axis (i.e. in the X_1–X_2 plane). The microrotation vector and associated skew-symmetric tensor are then

$$\boldsymbol{\theta} = \begin{Bmatrix} 0 \\ 0 \\ \vartheta \end{Bmatrix} \quad \longleftrightarrow \quad \widehat{\boldsymbol{\theta}} = \begin{bmatrix} 0 & -\vartheta & 0 \\ \vartheta & 0 & 0 \\ 0 & 0 & 0 \end{bmatrix} \tag{3.30}$$

and application of (3.29) generates

$$\boldsymbol{Q} = \begin{bmatrix} \cos\vartheta & -\sin\vartheta & 0 \\ \sin\vartheta & \cos\vartheta & 0 \\ 0 & 0 & 1 \end{bmatrix} \tag{3.31}$$

which is recognisable as a two-dimensional rotation matrix. Furthermore the transpose of this matrix is clearly the inverse transformation $\vartheta \to -\vartheta$. If it is assumed that ϑ is infinitesimal, a small angle approximation leads to

$$\boldsymbol{Q} \approx \begin{bmatrix} 1 & -\vartheta & 0 \\ \vartheta & 1 & 0 \\ 0 & 0 & 1 \end{bmatrix} = \begin{bmatrix} 1 & 0 & 0 \\ 0 & 1 & 0 \\ 0 & 0 & 1 \end{bmatrix} + \begin{bmatrix} 0 & -\vartheta & 0 \\ \vartheta & 0 & 0 \\ 0 & 0 & 0 \end{bmatrix} \tag{3.32}$$

which is exactly (3.27).

The parametrisation of three-dimensional finite rotations is far from trivial, presenting difficulties from both an intellectual and numerical perspective. Their multiplicative, nonlinear and periodic structure can be challenging and especial care is advised, particularly when the rotation axis does not remain fixed. So far only a relatively simplistic overview of the key relationships has been outlined, but the topic will be revisited at greater depth and breadth in relation to its numerical treatment in Section 3.4. A limpid and comprehensive investigation is also provided in [289] in relation to classical (i.e. constrained or non-independent) finite rotations, and further information specifically on the Lie groups $SO(3)$

and algebras and $\mathfrak{so}(3)$ can be found in e.g. [290].

3.3.2 Deformation measures

To examine the strain developing in the continuum, the portion of the deformation accounted for by the microrotation alone must be separated out. This is achieved by the multiplicative decomposition [269]

$$\boldsymbol{F} = \boldsymbol{QU} = \boldsymbol{VQ} \tag{3.33}$$

where $\boldsymbol{U}$ and $\boldsymbol{V}$ are respectively material (right) and spatial (left) stretch tensors, inspired by the right and left Cauchy-Green deformation tensors of classical mechanics. However, this is not the polar decomposition which is conventionally performed on the deformation gradient to produce the macrorotation $\boldsymbol{R}$, so both stretches are generally non-symmetric. Therefore they do not represent stretch in the conventional sense, but rather all deformation which is distinct from the independent microrotation field, which will likely include additional rotation or shearing. If however the deformation *is* wholly accounted for by microrotations (i.e. if $\boldsymbol{F} = \boldsymbol{Q}$), each stretch tensor simply becomes the identity tensor $\boldsymbol{I}$. Therefore a measure of the material strain $\boldsymbol{E}$ is given by the divergence of $\boldsymbol{U}$ away from $\boldsymbol{I}$, or

$$\boldsymbol{E} = \boldsymbol{U} - \boldsymbol{I} = \boldsymbol{Q}^{\mathrm{T}}\boldsymbol{F} - \boldsymbol{I}, \tag{3.34}$$

referred to by some as the *first Cosserat deformation measure* [247], which vanishes in the undeformed state. Equally a spatial measure $\boldsymbol{g}$ can be written

$$\boldsymbol{g} = \boldsymbol{I} - \boldsymbol{V}^{-1} = \boldsymbol{I} - \boldsymbol{QF}^{-1}, \tag{3.35}$$

related to its counterpart through

$$\boldsymbol{g} = \boldsymbol{QEF}^{-1}, \qquad\qquad \boldsymbol{E} = \boldsymbol{Q}^{\mathrm{T}}\boldsymbol{gF} \tag{3.36}$$

which also define, respectively, micropolar push-forward and pull-back operations. Note that the micropolar stretch tensors coincide with the classical stretch tensors in the case of identical microrotation and macrorotation, i.e. when $\boldsymbol{Q}^{\mathrm{T}}\boldsymbol{R} = \boldsymbol{I}$.

A measure of the microrotational curvature is a little less straightforward to establish. A simple gradient of the microrotation vector might be the most obvious candidate but, given that $\boldsymbol{\theta}$ is not strictly a true vector but instead a *pseudovector*,[18] this measure is not invariant to superposed Galilean transformations and therefore cannot be pursued in a finite strain setting. Equally, the gradient of the microrotation tensor could be taken, but the resulting third-order tensor would not be particularly amenable to useful or intuitive

---

[18] This is linked to the fact that $\boldsymbol{\theta}$ does not obey standard vectorial transformation rules; its incrementation cannot be achieved by a simple concatenation of two subsequent rotations (the parallelogram rule). This is because, unlike the translation vector $\boldsymbol{u}$, Euler vectors do not exist in Euclidean space but on a sphere.

interpretations of its contents (e.g. bending or torsional curvatures) or then to standard constitutive modelling. Hence a less obvious route is taken, beginning with a differentiation of the orthonormality condition (3.19) to produce the parallel statements

$$\frac{\partial}{\partial \boldsymbol{X}}(\boldsymbol{Q}\boldsymbol{Q}^{\mathrm{T}}) = \frac{\partial \boldsymbol{Q}}{\partial \boldsymbol{X}}\boldsymbol{Q}^{\mathrm{T}} + \boldsymbol{Q}\frac{\partial \boldsymbol{Q}^{\mathrm{T}}}{\partial \boldsymbol{X}} = \boldsymbol{0} \tag{3.37}$$

and

$$\frac{\partial}{\partial \boldsymbol{X}}(\boldsymbol{Q}^{\mathrm{T}}\boldsymbol{Q}) = \frac{\partial \boldsymbol{Q}^{\mathrm{T}}}{\partial \boldsymbol{X}}\boldsymbol{Q} + \boldsymbol{Q}^{\mathrm{T}}\frac{\partial \boldsymbol{Q}}{\partial \boldsymbol{X}} = \boldsymbol{0}, \tag{3.38}$$

which may be rearranged to become

$$\frac{\partial \boldsymbol{Q}}{\partial \boldsymbol{X}}\boldsymbol{Q}^{\mathrm{T}} = -\boldsymbol{Q}\frac{\partial \boldsymbol{Q}^{\mathrm{T}}}{\partial \boldsymbol{X}}, \qquad \frac{\partial \boldsymbol{Q}^{\mathrm{T}}}{\partial \boldsymbol{X}}\boldsymbol{Q} = -\boldsymbol{Q}^{\mathrm{T}}\frac{\partial \boldsymbol{Q}}{\partial \boldsymbol{X}}. \tag{3.39}$$

Evidently, each term is skew-symmetric and thus can be reduced down to a more desirable second-order tensor, leaving an apparently free choice between the four options. However, each has a slightly different geometric interpretation, and it has been shown that the most 'natural' is in fact the final one, in an intuitive geometrical sense [205, 291]. This is also the formula used most widely in the literature. Rewriting it as a second-order tensor by extracting its axial components with the Levi-Civita tensor gives the second Cosserat deformation measure

$$\boldsymbol{\Gamma} = -\frac{1}{2}\boldsymbol{\epsilon} : \boldsymbol{Q}^{\mathrm{T}}\frac{\partial \boldsymbol{Q}}{\partial \boldsymbol{X}} \tag{3.40}$$

known as the *wryness* tensor. In index notation it is written

$$\Gamma_{\alpha\beta} = -\frac{1}{2}\epsilon_{\alpha\gamma\delta}Q_{i\gamma}\frac{\partial Q_{i\delta}}{\partial X_\beta} \tag{3.41}$$

and it can also be considered an array of three axial vectors;

$$\boldsymbol{Q}^{\mathrm{T}}\frac{\partial \boldsymbol{Q}}{\partial X_\beta} = \widehat{\boldsymbol{\Gamma}}_{\cdot\beta} \tag{3.42}$$

if $\boldsymbol{\Gamma}_{\cdot\beta}$ represents the β^{th} column of $\boldsymbol{\Gamma}$, which may be elaborated as

$$\boldsymbol{\Gamma}_{\cdot\beta} = \frac{\sin\theta}{\theta}\frac{\partial \boldsymbol{\theta}}{\partial X_\beta} + \frac{1-\cos\theta}{\theta^2}\frac{\partial \boldsymbol{\theta}}{\partial X_\beta} \times \boldsymbol{\theta} + \left(\frac{1}{\theta^2} - \frac{\sin\theta}{\theta^3}\right)\left(\boldsymbol{\theta}\cdot\frac{\partial \boldsymbol{\theta}}{\partial X_\beta}\right)\boldsymbol{\theta} \tag{3.43}$$

in terms of the microrotation axis and angle [292]. As $\boldsymbol{\Gamma}$ is a material tensor, a rotation-forward produces the related spatial left curvature tensor [269, 274]

$$\boldsymbol{k} = \boldsymbol{Q}\boldsymbol{\Gamma}\boldsymbol{Q}^{\mathrm{T}} \tag{3.44}$$

by the same operation which links $\boldsymbol{U}$ and $\boldsymbol{V}$, cf. (3.33). In this work, however, only the material strain and wryness measures will be used; for proof of their objectivity see [269]. This is to simplify the derivation of the constitutive model, as frame invariance is automatically guaranteed if the stress and strain measures are both defined in the material frame [124]. Otherwise, fulfilling the principle of material objectivity requires the determination of objective stress rates and material time derivatives, which in the micropolar continuum is by no means a simple task. That said, constitutive models defined entirely in the spatial frame have been developed – see for example [273–275].

3.3.3 Deformation rates

To derive an incremental rate-independent hyperelastic constitutive model, it is necessary to examine infinitesimal changes in (or rates of) the deformation measures so they may be linked energetically to changes in the resulting stresses and couple-stresses. This section follows the standard procedures laid out for the micropolar continuum by e.g. [269, 274, 293] to that end. Using $(\dot{\bullet})$ to denote a derivative with respect to time, the velocity gradient $\boldsymbol{l}$ is defined as usual, viz.

$$\boldsymbol{l} = \frac{\partial \dot{\boldsymbol{u}}}{\partial \boldsymbol{x}} = \dot{\boldsymbol{F}}\boldsymbol{F}^{-1}. \tag{3.45}$$

The angular velocity of the micropolar triad is found by differentiating (3.17), giving

$$\begin{aligned} \dot{\boldsymbol{w}}_\alpha &= \dot{\boldsymbol{Q}}\boldsymbol{W}_\alpha && (3.46)\\ &= \dot{\boldsymbol{Q}}\boldsymbol{Q}^{\mathrm{T}}\boldsymbol{w}_\alpha && (3.47) \end{aligned}$$

so that the micropolar spin $\boldsymbol{\Omega}$ is defined

$$\boldsymbol{\Omega} = \dot{\boldsymbol{Q}}\boldsymbol{Q}^{\mathrm{T}} \in \mathfrak{so}(3). \tag{3.48}$$

The proof that $\boldsymbol{\Omega} \in \mathfrak{so}(3)$ (that the spin tensor is skew symmetric, in other words) is trivial: the time derivative of the orthogonality constraint (3.19) is

$$\frac{\partial}{\partial t}(\boldsymbol{Q}\boldsymbol{Q}^{\mathrm{T}}) = \dot{\boldsymbol{Q}}\boldsymbol{Q}^{\mathrm{T}} + \boldsymbol{Q}\dot{\boldsymbol{Q}}^{\mathrm{T}} = \boldsymbol{0} \quad \longleftrightarrow \quad \dot{\boldsymbol{Q}}\boldsymbol{Q}^{\mathrm{T}} = -(\dot{\boldsymbol{Q}}\boldsymbol{Q}^{\mathrm{T}})^{\mathrm{T}}. \tag{3.49}$$

From this property it follows that the micropolar gyration vector $\boldsymbol{\omega}$ is the axial vector of the spin tensor, i.e. $\boldsymbol{\Omega} = \widehat{\boldsymbol{\omega}}$. The spatial deformation rate $\boldsymbol{d}$ is then the difference between the velocity gradient and the micropolar spin, i.e.

$$\boldsymbol{d} = \boldsymbol{l} - \boldsymbol{\Omega} = \boldsymbol{l} + \boldsymbol{\Omega}^{\mathrm{T}} = \dot{\boldsymbol{F}}\boldsymbol{F}^{-1} + \boldsymbol{Q}\dot{\boldsymbol{Q}}^{\mathrm{T}} \tag{3.50}$$

and an additional deformation rate tensor $\boldsymbol{e}$ accounting for curvature results from taking the micropolar gyration gradient

$$\boldsymbol{e} = \frac{\partial \boldsymbol{\omega}}{\partial \boldsymbol{x}}. \tag{3.51}$$

Manipulation of $\boldsymbol{d}$ to incorporate the material strain rate

$$\dot{\boldsymbol{E}} = \dot{\boldsymbol{U}} = \dot{\boldsymbol{Q}}^{\mathrm{T}}\boldsymbol{F} + \boldsymbol{Q}^{\mathrm{T}}\dot{\boldsymbol{F}} \tag{3.52}$$

leads to

$$\boldsymbol{d} = \boldsymbol{Q}\boldsymbol{Q}^{\mathrm{T}}\dot{\boldsymbol{F}}\boldsymbol{F}^{-1} + \boldsymbol{Q}\dot{\boldsymbol{Q}}^{\mathrm{T}}\boldsymbol{F}\boldsymbol{F}^{-1} \tag{3.53}$$

$$= \boldsymbol{Q}(\boldsymbol{Q}^{\mathrm{T}}\dot{\boldsymbol{F}} + \dot{\boldsymbol{Q}}^{\mathrm{T}}\boldsymbol{F})\boldsymbol{F}^{-1} \tag{3.54}$$

$$= \boldsymbol{Q}\dot{\boldsymbol{E}}\boldsymbol{F}^{-1}. \tag{3.55}$$

Meanwhile, switching briefly to index notation to simplify operations, differentiation of the wryness tensor gives

$$\dot{\Gamma}_{\alpha\beta} = -\frac{1}{2}\epsilon_{\alpha\gamma\delta}\left(Q_{i\gamma}\frac{\partial Q_{i\delta}}{\partial X_\beta}\right)^{\cdot} \tag{3.56}$$

$$= -\frac{1}{2}\epsilon_{\alpha\gamma\delta}\left(\dot{Q}_{i\gamma}\frac{\partial Q_{i\delta}}{\partial X_\beta} + Q_{i\gamma}\frac{\partial \dot{Q}_{i\delta}}{\partial X_\beta}\right) \tag{3.57}$$

$$= -\frac{1}{2}\epsilon_{\alpha\gamma\delta}\left(\Omega_{ij}Q_{j\gamma}\frac{\partial Q_{i\delta}}{\partial X_\beta} + Q_{i\gamma}\frac{\partial(\Omega_{ij}Q_{j\delta})}{\partial X_\beta}\right) \tag{3.58}$$

$$= -\frac{1}{2}\epsilon_{\alpha\gamma\delta}\left(\Omega_{ij}Q_{j\gamma}\frac{\partial Q_{i\delta}}{\partial X_\beta} + Q_{i\gamma}\frac{\partial \Omega_{ij}}{\partial X_\beta}Q_{j\delta} + Q_{i\gamma}\Omega_{ij}\frac{\partial Q_{j\delta}}{\partial X_\beta}\right). \tag{3.59}$$

Since $\Omega_{ij} = -\Omega_{ji}$, a reversal of the free indices i and j in the final term yields

$$\dot{\Gamma}_{\alpha\beta} = -\frac{1}{2}\epsilon_{\alpha\gamma\delta}\left(\Omega_{ij}Q_{j\gamma}\frac{\partial Q_{i\delta}}{\partial X_\beta} + Q_{i\gamma}\frac{\partial \Omega_{ij}}{\partial X_\beta}Q_{j\delta} + Q_{j\gamma}\Omega_{ji}\frac{\partial Q_{i\delta}}{\partial X_\beta}\right) \tag{3.60}$$

$$= -\frac{1}{2}\epsilon_{\alpha\gamma\delta}Q_{i\gamma}\frac{\partial \Omega_{ij}}{\partial X_\beta}Q_{j\delta} \tag{3.61}$$

into which may be substituted $\Omega_{ij} = -\epsilon_{ijk}\omega_k$ for

$$\dot{\Gamma}_{\alpha\beta} = \frac{1}{2}\epsilon_{\alpha\gamma\delta}Q_{i\gamma}Q_{j\delta}\epsilon_{ijk}\frac{\partial \omega_k}{\partial X_\beta}. \tag{3.62}$$

The properties of the Levi-Civita tensor and of orthogonal tensors may then be used to manipulate this expression into its final form:

$$\dot{\Gamma}_{\alpha\beta} = Q_{k\alpha}\frac{\partial \omega_k}{\partial X_\beta} \tag{3.63}$$

or

$$\dot{\boldsymbol{\Gamma}} = \boldsymbol{Q}^{\mathrm{T}}\frac{\partial \boldsymbol{\omega}}{\partial \boldsymbol{X}} = \boldsymbol{Q}^{\mathrm{T}}\frac{\partial \boldsymbol{\omega}}{\partial \boldsymbol{x}}\boldsymbol{F}. \tag{3.64}$$

Therefore the spatial micropolar gyration gradient is simply

$$\boldsymbol{e} = \boldsymbol{Q}\dot{\boldsymbol{\Gamma}}\boldsymbol{F}^{-1}. \tag{3.65}$$

Note the similarity between (3.36) and the final expressions for $\boldsymbol{d}$ and $\boldsymbol{e}$.

3.3.4 Stress and couple-stress

Although the primary application of micropolar theory is to problems involving prominent microstructural phenomena, its mathematical basis is still that of a *continuum.* Therefore the continuum assumption still holds, and it is assumed that analysis takes place at a sufficiently large scale to consider the transfer of momentum through the body as continuous, rather than as the synthesis of discrete interparticulate interactions. It follows that Cauchy's theorem can be applied to the flux of both linear and angular momentum through any given plane in the deformed body, defined by a normal vector $\boldsymbol{n}$. Respectively this defines a (force) traction $\boldsymbol{t}$ and couple-traction $\boldsymbol{m}$ which are related to the Cauchy or true stress $\boldsymbol{\sigma}$ and couple-stress $\boldsymbol{\mu}$ by the linear mappings

$$\boldsymbol{t} = \boldsymbol{\sigma}\boldsymbol{n} \tag{3.66}$$

and

$$\boldsymbol{m} = \boldsymbol{\mu}\boldsymbol{n} \tag{3.67}$$

which follow from the static equilibrium of an infinitesimal tetrahedron.[19] Note that this definition differs from that given in e.g. [269] and subsequent works by the presence of a transpose. While this reflects only a minor difference in convention, the general asymmetry of the stress tensors in micropolar theory means its consequences are potentially drastic if not properly acknowledged. The adopted convention is demonstrated graphically in Figure 3.9, showing the Cauchy stresses and couple-stresses acting on an infinitesimal (but still larger in scale than that of the microstructure) micropolar cube.

If the Cauchy stresses represent forces and couples acting on an infinitesimal cross section $\mathrm{d}A$ of the deformed continuum, then their corresponding Kirchhoff stresses represent those same forces and couples distributed over an elemental, undeformed area $\mathrm{d}A_0$ (i.e. acting in the same direction). Conversion takes place by weighting the Cauchy stresses by the determinant of the Jacobian transformation so that

$$\boldsymbol{\tau} = J\boldsymbol{\sigma} \tag{3.68}$$

is the Kirchhoff stress and

$$\boldsymbol{\nu} = J\boldsymbol{\mu} \tag{3.69}$$

---

[19] The proof is omitted here as it is found in many standard works e.g. [245]

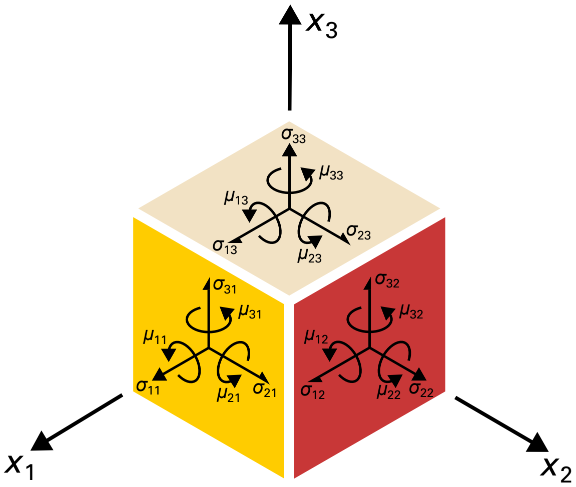

Figure 3.9: Cauchy stresses $\boldsymbol{\sigma}$ and couple-stresses $\boldsymbol{\mu}$ acting on a small element of micropolar continuum.

is the Kirchhoff couple-stress. As the Kirchhoff stresses are still defined with respect to directions defined in the deformed configuration, like the Cauchy stresses they are fully spatial. The two measures only differ in terms of magnitude.

The last species of stress used in this thesis is a fully *material* measure known as the Biot stress. The Biot (force) stress $\boldsymbol{B}$ and couple-stress $\boldsymbol{S}$ are achieved through a micropolar pull-back of each Kirchhoff stress, giving

$$\boldsymbol{B} = \boldsymbol{Q}^{\mathrm{T}}\boldsymbol{\tau}\boldsymbol{F}^{-\mathrm{T}} = J\boldsymbol{Q}^{\mathrm{T}}\boldsymbol{\sigma}\boldsymbol{F}^{-\mathrm{T}} \tag{3.70}$$

and

$$\boldsymbol{S} = \boldsymbol{Q}^{\mathrm{T}}\boldsymbol{\nu}\boldsymbol{F}^{-\mathrm{T}} = J\boldsymbol{Q}^{\mathrm{T}}\boldsymbol{\mu}\boldsymbol{F}^{-\mathrm{T}}. \tag{3.71}$$

These stresses are useful for the derivation of materially-framed objective constitutive relationships as detailed in Section 3.3.6.

3.3.5 Balance equations

Microrotations have no effect on the change in mass or volume of the body. Therefore the continuity equation may be derived by exactly the same procedure used in the classical continuum: by requiring that the total mass m is conserved. If the mass density is denoted ρ, then

$$\mathrm{d}m_0 = \rho_0\,\mathrm{d}\Omega_0 \tag{3.72}$$

must equal

$$\mathrm{d}m = \rho\,\mathrm{d}\Omega\,, \tag{3.73}$$

giving the standard result

$$J = \frac{\rho_0}{\rho} \tag{3.74}$$

since

$$\mathrm{d}\Omega = J\,\mathrm{d}\Omega_0\,. \tag{3.75}$$

The conservation of mass is stated

$$\frac{\mathrm{D}}{\mathrm{D}t}\int_{\Omega_0}\mathrm{d}m_0 = \frac{\mathrm{D}}{\mathrm{D}t}\int_{\Omega}\mathrm{d}m = 0 \tag{3.76}$$

where $\frac{\mathrm{D}}{\mathrm{D}t}(\bullet)$ denotes a material time derivative and hence, given $\dot{J} = J\,\mathrm{tr}(\boldsymbol{l})$,

$$\dot{\rho} + \rho\,\mathrm{tr}(\boldsymbol{l}) = 0. \tag{3.77}$$

Next the balance of linear momentum is considered. Cauchy's (first) momentum equation is achieved by balancing changes in linear momentum with applied external loads (tractions and body forces). In the spatial frame, this is expressed

$$\frac{\mathrm{D}}{\mathrm{D}t}\int_{\Omega}\dot{\boldsymbol{x}}\,\mathrm{d}m = \int_{\partial\Omega}\boldsymbol{t}\,\mathrm{d}A + \int_{\Omega}\boldsymbol{p}\,\mathrm{d}\Omega \tag{3.78}$$

where $\boldsymbol{p}$ is a vector of body forces per unit volume. This may be rewritted using (3.66) and (3.72)–(3.75) to become

$$\frac{\mathrm{D}}{\mathrm{D}t}\int_{\Omega_0}\rho_0\dot{\boldsymbol{x}}\,\mathrm{d}\Omega_0 = \int_{\partial\Omega}\boldsymbol{\sigma}\boldsymbol{n}\,\mathrm{d}A + \int_{\Omega}\boldsymbol{p}\,\mathrm{d}\Omega \tag{3.79}$$

so that the left-hand side may be evaluated, as the integrand is now defined fully in the reference frame. This yields

$$\int_{\Omega_0}\rho_0\ddot{\boldsymbol{x}}\,\mathrm{d}\Omega_0 = \int_{\Omega}\rho\ddot{\boldsymbol{x}}\,\mathrm{d}\Omega = \int_{\partial\Omega}\boldsymbol{\sigma}\boldsymbol{n}\,\mathrm{d}A + \int_{\Omega}\boldsymbol{p}\,\mathrm{d}\Omega\,. \tag{3.80}$$

Application of the Reynolds transport theorem and the Gauss-Green theorem then leads to the first Cauchy momentum equation

$$\rho\ddot{\boldsymbol{x}} = \mathrm{div}\,\boldsymbol{\sigma} + \boldsymbol{p}. \tag{3.81}$$

This is reduced to the strong form of static translational equilibrium by neglecting the inertia term, such that

$$\mathrm{div}\,\boldsymbol{\sigma} + \boldsymbol{p} = \boldsymbol{0}, \qquad \frac{\partial\sigma_{ij}}{\partial x_j} + p_i = 0. \tag{3.82}$$

The balance of angular momentum begets similar equilibrium statements. Their derivation entails the same procedure followed in response to the balance of linear momentum, so only the final result is provided here, viz.

$$\operatorname{div} \boldsymbol{\mu} - \boldsymbol{\epsilon} : \boldsymbol{\sigma} + \boldsymbol{q} = \boldsymbol{0}, \qquad \frac{\partial \mu_{ij}}{\partial x_j} - \epsilon_{ijk}\sigma_{jk} + q_i = 0 \tag{3.83}$$

is the strong statement of static rotational equilibrium, where $\boldsymbol{q}$ is a vector of body couples per unit volume. A complete account of its derivation is available in e.g. [269].

For completeness, the equilibrium statements can also be expressed in the material frame in terms of the Biot stresses. By applying pull-back operations, these are [294]

$$\operatorname{Div}(\boldsymbol{QB}) + J\boldsymbol{p} = \boldsymbol{0} \tag{3.84}$$

and

$$\operatorname{Div}(\boldsymbol{QS}) - \boldsymbol{\epsilon} : (\boldsymbol{QBF}^{\mathrm{T}}) + J\boldsymbol{q} = \boldsymbol{0}, \tag{3.85}$$

where $\operatorname{Div}(\cdot)$ denotes the divergence taken with respect to material coordinates.

3.3.6 Hyperelastic thermodynamical setting

For a constitutive model to be considered thermodynamically *consistent*, it cannot spontaneously generate or lose energy. Energy conservation statements must therefore be posed so that stresses are linked to strains in an energetically and entropically non-dissipative manner. This is a procedure which was first set out by Coleman and Noll [295] for the classical continuum, but has now become *de rigueur* across continuum mechanics to systematically validate mathematical formulations of dissipative material processes. An account of the generalised framework is given in many standard texts, e.g. [124].

The first two laws of thermodynamics state respectively that

1. the change in total energy of a system is equal to the sum of the mechanical work done on the system and the heat transferred into it (i.e. energy is conserved); and
2. a thermodynamical process cannot produce negative entropy.

In a continuum setting, the first law can be written in terms of the specific energy e held per unit mass of the undeformed body:

$$\rho_0 \dot{e} = \boldsymbol{\tau} : \boldsymbol{d} + \boldsymbol{\nu} : \boldsymbol{e} + \rho_0 r - J\nabla \cdot \boldsymbol{h} \tag{3.86}$$

in which r is a heat source per unit mass and $\boldsymbol{h}$ is the heat flux vector. Additionally, the terms $\boldsymbol{\tau} : \boldsymbol{d}$ and $\boldsymbol{\nu} : \boldsymbol{e}$ represent the mechanical work rate per unit of volume impressed upon the system by the stress and couple-stress respectively. As for the second law, using s to denote entropy and T for the absolute temperature, the inequality

$$\rho_0 \dot{s} \geq \frac{\rho_0 r}{T} - \frac{J\nabla \cdot \boldsymbol{h}}{T} \tag{3.87}$$

states the principle of non-negative entropy change. Here the Helmholtz free energy function W is introduced, which indicates the amount of 'useful' energy stored per unit mass of the system (i.e. that which has not been dissipated through entropy production). It is defined

$$W = e - Ts \tag{3.88}$$

such that the time derivative of the specific energy may be written

$$\dot{e} = \dot{W} + \dot{T}s + T\dot{s}. \tag{3.89}$$

Substituting this into the first law yields

$$\rho_0(\dot{W} + \dot{T}s + T\dot{s}) = \boldsymbol{\tau} : \boldsymbol{d} + \boldsymbol{\nu} : \boldsymbol{e} + \rho_0 r - J\nabla \cdot \boldsymbol{h} \tag{3.90}$$

which when rearranged becomes

$$\rho_0\dot{W} = \boldsymbol{\tau} : \boldsymbol{d} + \boldsymbol{\nu} : \boldsymbol{e} + \rho_0 r - J\nabla \cdot \boldsymbol{h} - \rho_0 T\dot{s} - \rho_0\dot{T}s. \tag{3.91}$$

For an elastic material, to be consistent with the idea that deformations are fully recoverable it is assumed that internal dissipation does not take place. It is further assumed that in the purely mechanical processes under consideration here that heat conduction effects are negligible, meaning $r = 0$ and $\boldsymbol{h} = \boldsymbol{0}$. Therefore entropy remains constant, and (3.87) simplifies into the equality

$$\rho_0 T\dot{s} = 0. \tag{3.92}$$

This result, combined with the additional assumption that the material is isothermal (i.e. $\dot{T} = 0$), reduces (3.91) to

$$\rho_0\dot{W} = \boldsymbol{\tau} : \boldsymbol{d} + \boldsymbol{\nu} : \boldsymbol{e}. \tag{3.93}$$

From this it can be inferred that all mechanical work done on the body is stored as internal free energy. No energy is lost as heat or internal dissipation. Although this holds for elastic materials, this principle will be revisited in the following chapter in Section 4.2.2, where it will be reformulated as an inequality to allow for plastic deformation.

The conservation statement (3.93) is now in a sufficiently refined format to be usefully combined with the deformation rate tensors derived in Section 3.3.3, to wit

$$\begin{align} \rho_0\dot{W} &= \boldsymbol{\tau} : (\boldsymbol{l} - \boldsymbol{\Omega}) + \boldsymbol{\nu} : \frac{\partial \boldsymbol{\omega}}{\partial \boldsymbol{x}} \tag{3.94} \\ &= \boldsymbol{\tau} : \boldsymbol{Q}\dot{\boldsymbol{E}}\boldsymbol{F}^{-1} + \boldsymbol{\nu} : \boldsymbol{Q}\dot{\boldsymbol{\Gamma}}\boldsymbol{F}^{-1}. \tag{3.95} \end{align}$$

For the constitutive model to be considered *objective* (and indeed *hyperelastic* or *Green* elastic), the free energy of the system must only depend on the strain and wryness which has developed in the body, and not on any additional internal state variables. In other words

$$W = W(\boldsymbol{E}, \boldsymbol{\Gamma}) \tag{3.96}$$

so, by the chain rule,

$$\dot{W} = \frac{\partial W}{\partial \boldsymbol{E}} : \dot{\boldsymbol{E}} + \frac{\partial W}{\partial \boldsymbol{\Gamma}} : \dot{\boldsymbol{\Gamma}}. \tag{3.97}$$

At this point it is not yet necessary to define the specific form of the free energy function, but only to require that it vanish when $\boldsymbol{E} = \boldsymbol{\Gamma} = \boldsymbol{0}$. Combining (3.95) with (3.97) makes

$$\rho_0 \frac{\partial W}{\partial \boldsymbol{E}} : \dot{\boldsymbol{E}} + \rho_0 \frac{\partial W}{\partial \boldsymbol{\Gamma}} : \dot{\boldsymbol{\Gamma}} = \boldsymbol{\tau} : \boldsymbol{Q}\dot{\boldsymbol{E}}\boldsymbol{F}^{-1} + \boldsymbol{\nu} : \boldsymbol{Q}\dot{\boldsymbol{\Gamma}}\boldsymbol{F}^{-1} \tag{3.98}$$

and standard operations of tensor algebra lead to

$$\rho_0 \frac{\partial W}{\partial \boldsymbol{E}} : \dot{\boldsymbol{E}} + \rho_0 \frac{\partial W}{\partial \boldsymbol{\Gamma}} : \dot{\boldsymbol{\Gamma}} = \boldsymbol{Q}^{\mathrm{T}}\boldsymbol{\tau}\boldsymbol{F}^{-\mathrm{T}} : \dot{\boldsymbol{E}} + \boldsymbol{Q}^{\mathrm{T}}\boldsymbol{\nu}\boldsymbol{F}^{-\mathrm{T}} : \dot{\boldsymbol{\Gamma}}. \tag{3.99}$$

From this follow

$$\rho_0 \frac{\partial W}{\partial \boldsymbol{E}} = \boldsymbol{Q}^{\mathrm{T}}\boldsymbol{\tau}\boldsymbol{F}^{-\mathrm{T}} \tag{3.100}$$

and

$$\rho_0 \frac{\partial W}{\partial \boldsymbol{\Gamma}} = \boldsymbol{Q}^{\mathrm{T}}\boldsymbol{\nu}\boldsymbol{F}^{-\mathrm{T}} \tag{3.101}$$

for non-trivial cases, which are identified as the Biot stresses derived earlier. Hence

$$\boldsymbol{B} = \rho_0 \frac{\partial W}{\partial \boldsymbol{E}} \tag{3.102}$$

and

$$\boldsymbol{S} = \rho_0 \frac{\partial W}{\partial \boldsymbol{\Gamma}} \tag{3.103}$$

and W can then be devised to suit the particular material or modelling needs.

3.3.7 Constitutive equations

According to Truesdell, constitutive equations represent the heart of continuum mechanics [255]. It is here that more profound insight into the physical nature of engineering materials begins; it could be argued that the rest has been mere abstractions of geometry and thermodynamics to facilitate the proper *usage* of a constitutive model. Several hyperelastic constitutive models have been developed in the context of the nonlinear micropolar continuum, including the Neo-Hookean [273, 274] and Mooney-Rivlin formulations [273]. However, while soils exhibit nonlinear elastic behaviour [296], their dominant inelastic deformations (driven by plasticity and damage accumulation) are the primary concern in failure processes. Given that elastic strains contribute only a small fraction of the total deformation, differences between these simple hyperelastic models therefore become negligible in this context. Although a more empirically-grounded hyperelastic model (such as those proposed for the classical continuum in [296]) could be formulated for the nonlinear micropolar continuum, this lies beyond the scope of this thesis. Moreover, the practical benefits of such an approach would likely be limited. As such, the Saint-Venant-Kirchhoff (StV-K) model is adopted in this work due to its simplicity, ease of computational implementation, and analytical tractability. Its limitations and instabilities in capturing large elastic strains stemming from its linear stress-strain relationship [297] are of little consequence here.

The classical formulation of the StV-K hyperelastic free energy assumes that the energy potential function is a homogeneous quadratic function of the material Green strain. Extension to the micropolar continuum is straightforward: the free energy is instead quadratic in both the material strain tensor $E_{\alpha\beta}$ and the wryness tensor $\Gamma_{\alpha\beta}$. That is,

$$\rho_0 W = \frac{1}{2} E_{\alpha\beta} D_{\alpha\beta\gamma\delta} E_{\gamma\delta} + \frac{1}{2} \Gamma_{\alpha\beta} \check{D}_{\alpha\beta\gamma\delta} \Gamma_{\gamma\delta} + E_{\alpha\beta} \breve{D}_{\alpha\beta\gamma\delta} \Gamma_{\gamma\delta} \tag{3.104}$$

where $\boldsymbol{D}$, $\check{\boldsymbol{D}}$ and $\breve{\boldsymbol{D}}$ are fourth-order elasticity tensors which encode the material's elastic response, and the factors of a half have been introduced arbitrarily for notational clarity later. Of the three constitutive tensors, $\boldsymbol{D}$ and $\check{\boldsymbol{D}}$ must possess major symmetry ($D_{\alpha\beta\gamma\delta} = D_{\gamma\delta\alpha\beta}$), but none can be assumed to have minor symmetry ($D_{\alpha\beta\gamma\delta} \neq D_{\beta\alpha\delta\gamma}$) given the general asymmetry of the strain and wryness tensors. This means that of the original $3 \times 3^4 = 243$ material parameters in this most general of cases, only 171 are independent. Nevertheless, it would still clearly be deeply impractical – arrogant even – to propose an engineering model with such an enormity of free variables. Thus to make the model tractable, simplifications must be introduced based on the physical nature of the material.

The first assumption is that the material is *centrosymmetric*. Centrosymmetric materials are simply those which possess symmetry with respect to some centre point, such that the mechanical response at any point is invariant under inversion of the coordinate system. In other words, for a transformation $\boldsymbol{X} \to -\boldsymbol{X}$ there must be no consequence in terms of the mechanical work developed, i.e.

$$W(\Xi(\boldsymbol{X}, t)) = W(\Xi(-\boldsymbol{X}, t)). \tag{3.105}$$

Centrosymmetry (cf. chirality of crystalline structure for example) means certain specific behaviours like the piezoelectric effect cannot be exhibited. This is because when centrosymmetric molecules become stressed, their ions move symmetrically and cannot create a net dipole moment [298]. But this is not of concern in the mechanical modelling of geomaterials, where centrosymmetry may be reasonably assumed. Coordinate inversion leaves the strain measure $\boldsymbol{E} \to \boldsymbol{E}$ completely unaffected, but produces a change in sign of the wryness tensor $\boldsymbol{\Gamma} \to -\boldsymbol{\Gamma}$ due to the 'skewness' entailed by its composition from three axial pseudovectors – see (3.42). Therefore the first two terms in (3.104) are inert to such a transformation, but the final term remains invariant only if $\check{\boldsymbol{D}}$ vanishes. This leaves

$$\rho_0 W = \frac{1}{2} E_{\alpha\beta} D_{\alpha\beta\gamma\delta} E_{\gamma\delta} + \frac{1}{2} \Gamma_{\alpha\beta} \check{D}_{\alpha\beta\gamma\delta} \Gamma_{\gamma\delta} \tag{3.106}$$

which is also consistent with the idea that microrotation represents a fully independent kinematical field, as the energetic contribution of the strain is now decoupled from that of the wryness: $W = W(\boldsymbol{E}) + W(\boldsymbol{\Gamma})$.

Following (3.102), an expression for the Biot stress may be found by differentiating (3.106) with respect to strain:

$$\begin{aligned} B_{\mu\theta} &= \rho_0 \frac{\partial W}{\partial E_{\mu\theta}} && (3.107) \\ &= \frac{1}{2} \frac{\partial}{\partial E_{\mu\theta}} \left(E_{\alpha\beta} D_{\alpha\beta\gamma\delta} E_{\gamma\delta} \right) && (3.108) \\ &= \frac{1}{2} \left(\frac{\partial E_{\alpha\beta}}{\partial E_{\mu\theta}} D_{\alpha\beta\gamma\delta} E_{\gamma\delta} + E_{\alpha\beta} D_{\alpha\beta\gamma\delta} \frac{\partial E_{\gamma\delta}}{\partial E_{\mu\theta}} \right) && (3.109) \\ &= \frac{1}{2} \left(\delta_{\alpha\mu} \delta_{\theta\beta} D_{\alpha\beta\gamma\delta} E_{\gamma\delta} + E_{\alpha\beta} D_{\alpha\beta\gamma\delta} \delta_{\gamma\mu} \delta_{\theta\delta} \right) && (3.110) \\ &= \frac{1}{2} \left(D_{\mu\theta\gamma\delta} E_{\gamma\delta} + E_{\alpha\beta} D_{\alpha\beta\mu\theta} \right) && (3.111) \end{aligned}$$

and, by the major symmetry of the elasticity tensor,

$$\begin{aligned} B_{\mu\theta} &= \frac{1}{2} \left(D_{\mu\theta\gamma\delta} E_{\gamma\delta} + E_{\alpha\beta} D_{\mu\theta\alpha\beta} \right) && (3.112) \\ &= D_{\mu\theta\gamma\delta} E_{\gamma\delta}, && (3.113) \end{aligned}$$

or

$$\boldsymbol{B} = \boldsymbol{D} : \boldsymbol{E}. \tag{3.114}$$

A similar result is obtained for the couple-stress by following the equivalent procedure with (3.103), giving

$$\boldsymbol{S} = \check{\boldsymbol{D}} : \boldsymbol{\Gamma}. \tag{3.115}$$

Hence the material model can be considered *Hookean.* Finally, the Cauchy stresses may be expressed in terms of the strain and wryness tensors as follows:

$$\boldsymbol{\sigma} = J^{-1} \boldsymbol{Q} \boldsymbol{D} : \boldsymbol{E} \boldsymbol{F}^{\mathrm{T}} \tag{3.116}$$

$$\boldsymbol{\mu} = J^{-1} \boldsymbol{Q} \check{\boldsymbol{D}} : \boldsymbol{\Gamma} \boldsymbol{F}^{\mathrm{T}}. \tag{3.117}$$

Attention may now turn to the form taken by the two fourth-order elasticity tensors. In particular, the remaining 72 independent coefficients can be significantly reduced by assuming that the material is isotropic in addition to centrosymmetric. Isotropic tensors (i.e. those possessing the same components in all rotated coordinate systems) have a general form based on a linear, homogeneous combination of products of Kronecker deltas which represent the invariants of the system. This can be expressed

$$D_{\alpha\beta\gamma\delta} = \lambda\delta_{\alpha\beta}\delta_{\gamma\delta} + (\mu+\kappa)\delta_{\alpha\gamma}\delta_{\beta\delta} + (\mu-\kappa)\delta_{\alpha\delta}\delta_{\beta\gamma} \tag{3.118}$$

$$\check{D}_{\alpha\beta\gamma\delta} = \alpha\delta_{\alpha\beta}\delta_{\gamma\delta} + (\gamma+\beta)\delta_{\alpha\gamma}\delta_{\beta\delta} + (\gamma-\beta)\delta_{\alpha\delta}\delta_{\beta\gamma} \tag{3.119}$$

which means that the constitutive response now depends on only six independent parameters. Hence

$$\boldsymbol{B} = \lambda\,\mathrm{tr}(\boldsymbol{E})\boldsymbol{I} + (\mu+\kappa)\boldsymbol{E} + (\mu-\kappa)\boldsymbol{E}^{\mathrm{T}} \tag{3.120}$$

$$\boldsymbol{S} = \alpha\,\mathrm{tr}(\boldsymbol{\Gamma})\boldsymbol{I} + (\gamma+\beta)\boldsymbol{\Gamma} + (\gamma-\beta)\boldsymbol{\Gamma}^{\mathrm{T}} \tag{3.121}$$

which is equivalent to

$$\boldsymbol{B} = \lambda\,\mathrm{tr}(\boldsymbol{E})\boldsymbol{I} + 2\mu\,\mathrm{sym}(\boldsymbol{E}) + 2\kappa\,\mathrm{skew}(\boldsymbol{E}) \tag{3.122}$$

$$\boldsymbol{S} = \alpha\,\mathrm{tr}(\boldsymbol{\Gamma})\boldsymbol{I} + 2\gamma\,\mathrm{sym}(\boldsymbol{\Gamma}) + 2\beta\,\mathrm{skew}(\boldsymbol{\Gamma}) \tag{3.123}$$

if $\mathrm{sym}(\bullet) = \frac{1}{2}\left((\bullet) + (\bullet)^{\mathrm{T}}\right)$ and $\mathrm{skew}(\bullet) = \frac{1}{2}\left((\bullet) - (\bullet)^{\mathrm{T}}\right)$ represent symmetric and skew-symmetric components respectively. The free energy (3.106) can be expressed directly in terms of strain energy and curvature energy

$$W(\boldsymbol{E}) = \frac{\lambda}{2}\,\mathrm{tr}(\boldsymbol{E})^2 + (\mu+\kappa)\boldsymbol{E} : \boldsymbol{E} + (\mu-\kappa)\boldsymbol{E} : \boldsymbol{E}^{\mathrm{T}} \tag{3.124}$$

$$W(\boldsymbol{\Gamma}) = \frac{\alpha}{2}\,\mathrm{tr}(\boldsymbol{\Gamma})^2 + (\gamma+\beta)\boldsymbol{\Gamma} : \boldsymbol{\Gamma} + (\gamma-\beta)\boldsymbol{\Gamma} : \boldsymbol{\Gamma}^{\mathrm{T}} \tag{3.125}$$

and $W = W(\boldsymbol{E}) + W(\boldsymbol{\Gamma})$. Both free energy components are usually subject to local positivity and uniform convexity constraints, separately [299].

These equations are neatly analogous to the Hookean stress-strain laws used in classical linearised formulations of micropolar theory, for which there exists a large corpus of research. Note that the exact way in which the stresses are related to the strains by the six parameters varies across the literature, and conversion is often necessary; in the words of Neff, *notation is a nightmare* [300] and care is advised. The particular phrasing of the equations used here matches the format recommended in Hassanpour and Heppler's systematic review of the linear isotropic parameters [203], and is similar – though not identical – to that of O'Hare et al. [112], but differs from the other most highly favoured format used by e.g. Neff [197, 301].[20] The alternative formulation instead places distinct dependencies on the

---

[20] Discarding the popular notation of Eringen [244] which confusingly uses the symbol μ to refer to a quantity which is *not* the classical Lamé shear modulus – the source of widespread misunderstanding and erroneous conclusions, including by Eringen himself [203, 302].

wryness tensor and its transpose, viz.

$$\boldsymbol{S} = \alpha\,\mathrm{tr}(\boldsymbol{\Gamma})\boldsymbol{I} + \widehat{\gamma}\boldsymbol{\Gamma} + \widehat{\beta}\boldsymbol{\Gamma}^{\mathrm{T}}. \tag{3.126}$$

The parameters are linked as follows:

$$\gamma = \frac{1}{2}(\widehat{\gamma} + \widehat{\beta}) \tag{3.127}$$

$$\beta = \frac{1}{2}(\widehat{\gamma} - \widehat{\beta}). \tag{3.128}$$

The two parameters λ and μ can quickly be identified as the conventional Lamé parameters of classical elasticity. Indeed, when the continuum is behaving classically and $\boldsymbol{E} = \boldsymbol{E}^{\mathrm{T}}$, the Biot stress becomes invariant to the parameter κ. This coefficient is the Cosserat coupling modulus mentioned in Section 3.2.2, and controls the symmetry of the Biot stress tensor. When $\kappa = 0$ it renders $\boldsymbol{B}$ fully symmetric, but this does *not* mean that the Cauchy stress is symmetric as a result; asymmetry may arise during the push-forward operation. In infinitesimal formulations of micropolar theory, however, a vanishing Cosserat couple modulus does lead to a symmetric Cauchy stress tensor and, therefore, to disappearing couple-stresses and decoupling of the translation field from the microrotations. This in turns means there is no curvature energy generated in the continuum, which contradicts the uniform positivity of the free energy function. Therefore to retain nonlocal behaviour in the linearised theory, $\kappa = 0$ is inadmissible. But the higher-order coupling between stress and microrotations in the geometrically exact formulations means that only the more lax constraint $\kappa \geq 0$ is required for the model still to be micropolar and physically consistent. This is discussed further in [301]. It is also noteworthy that couple-stress theory is recovered as a special case of micropolar theory (at least in its linearised form) when $\kappa \to \infty$ [302]. This has the effect of fully constraining the microrotation field to the macrorotation field, but this result cannot be readily implemented numerically and thus is only really of analytic interest.

The physical basis of κ is still controversial, and its interpretation varies depending on the application. For example, when using the micropolar model as a continuum homogenisation of an assembly of rigid spheres (e.g. an idealised sand), the coupling modulus represents the *sliding stiffness* of the spheres at their contact points. Interparticulate rotation is generally regarded as a dissipative, frictional process [13], but is conjectured to incorporate an elastic component too which is accounted for by this parameter [303]. In contrast, if only the regularising properties of micropolar theory as a localisation band-limiter are of interest, then to a particularly blithe analyst κ (and, to a degree, all four new coefficients) only represent numerical tuning parameters and their physical meaning can be neglected. This approach is perhaps a little blunt, as micropolar theory still regularises ill-posedness when the parameters are chosen to be materially representative; this is the the template attempted in setting up the numerical experiments which appear later in this thesis. As for materials which are feasibly envisaged as completely continuous solids (i.e. those without voids), but perhaps possessing a microstructural configuration amenable to size effects, Neff concludes that only $\kappa = 0$ can be physically consistent [301]. Therefore, given the granular nature of the materials under scrutiny in this thesis, a coupling modulus $\kappa > 0$ is to be selected.

Turning now to the second constitutive equation, the three novel parameters α, γ and β each link couple-stresses to curvatures, and are referred to as *Cosserat twist coefficients*. Couple-stresses (moments per unit area) have the SI units $\mathrm{Pa} \cdot \mathrm{m}$, whereas curvatures (rotations per unit length) use m^{-1}. Therefore the constitutive parameters must be defined according to $\mathrm{Pa} \cdot \mathrm{m}^2$ – the units of a classical elastic modulus multiplied by the square of a length. The parameters cannot be size dependent, otherwise smaller test specimens would deliver results completely incongruous with those of larger ones. Therefore this length must be indicative of some *internal* scale associated with the particular material, related to e.g. the microstructure. Size effects emerge naturally by immediate consequence. Although the exact physical meaning of these parameters is the subject of continued conjecture, often they are determined through experimental testing of a series of specimens with varying slenderness. These results are then compared with analytical solutions of micropolar elasticity to determine e.g. characteristic length scales. For example, the pure torsion of a sample with a prescribed torque applied at either end was considered from a theoretical perspective in [304–306], and was extended to various materials including foams and bone in e.g. [198, 199, 304, 305, 307]. However, the size effect observed in the stiffness appears to be unbounded, hence the derived micropolar constants depend strongly on the relative size of the smallest sample tested, which is clearly unphysical and represents a flaw in this methodology of investigation (which is known as the *method of size effects*) [301]. The internal length scales of micropolar theory (and other generalised continuum theories) can also be determined by analytical homogenisation of heterogeneous materials – see the accounts provided in [200, 308–310]. Additionally, other researchers take a more intuitive approach, and simply infer that the length scales directly denote a representative dimension of the microstructural assembly – for example the radius of a single particle [27, 184]. This approach is particularly amenable to numerical regularisation scenarios where only the size of the resulting localisation zone is of importance (see e.g. [128, 311]), but limits mesh resolution to a size comparable to the characteristic length scale. Even simpler is the two-dimensional case, where specification of just two additional parameters is required (the coupling modulus and a single twist coefficient or length scale).

These differing interpretations have led to pronounced disagreements across the field, and no single reading has gained acceptance even within the micropolar community, never mind beyond it [301]. Furthermore, despite the sustained academic interest yielding significant advancements in the conceptualisation of these parameters, complete sets (fully detailed, analysed and cited in [203]) have so far only been derived for a handful of materials, viz.

- composite aluminium shot in an epoxy matrix
- graphite grade H237
- human bone
- polystyrene foam
- polyurethane foam
- syntactic foam
- polymethacrylimade foam grades WF51, WF110 and WF300.

This is perceived as a major barrier to uptake (or even acceptance) of the theory across engineering science more widely. Vardoulakis, a pioneer of micropolar regularisation of strain localisation, was a prominent experimentalist who was for many years at the forefront of developing innovative techniques to determine these parameters for geomaterials, some of which are described in [184]. Unfortunately progress has stagnated following his tragic and untimely death in 2009, which represented an immeasurable loss of expertise and leadership within the community [312].

The six coefficients listed earlier are often related to a set of engineering parameters, which might offer a less abstracted degree of insight into the material they describe. The Lamé parameters can be converted to any other two classical elastic moduli as usual. For example, the formulae for Young's modulus and Poisson's ratio read

$$E = \frac{\mu(3\lambda + 2\mu)}{\lambda + \mu} \tag{3.129}$$

$$\nu = \frac{\lambda}{2(\lambda + \mu)}. \tag{3.130}$$

Additionally a *polar ratio* Ψ is introduced, alongside characteristic lengths for both bending ℓ_b and torsion ℓ_t, as well as a coupling number n. These are defined [200, 203]

$$\Psi = \frac{2\gamma}{2\gamma + \alpha} \tag{3.131}$$

$$\ell_b = \sqrt{\frac{\gamma + \beta}{4\mu}} \tag{3.132}$$

$$\ell_t = \sqrt{\frac{\gamma}{\mu}} \tag{3.133}$$

$$n = \sqrt{\frac{\kappa}{\mu + \kappa}}. \tag{3.134}$$

The polar ratio relates torsional curvatures in a similar manner to how Poisson's ratio connects transverse and longitudinal strains. Meanwhile the two characteristic length scales control the intensity of size effects in their respective modes of deformation. Finally, the coupling number (not to be confused with the coupling modulus κ) determines the degree of first-order coupling between displacements and microrotations: when $n = 0$ at small deformations the two fields are coupled and the model reverts to couple-stress theory. The inverse relations read

$$\kappa = \frac{n^2}{1 - n^2}\mu \tag{3.135}$$

$$\alpha = 2\gamma\left(\frac{1}{\Psi} - 1\right) \tag{3.136}$$

$$\gamma = \ell_t^2\mu \tag{3.137}$$

$$\beta = 4\ell_b^2\mu - \gamma. \tag{3.138}$$

In plane strain – where torsion cannot exist and Γ is traceless – the parameters α and ℓ_t are of no consequence. Hence the elastic response depends only on the choice of coupling modulus (or number) and characteristic length in bending, in addition to the two parameters of classical elasticity. By contrast, the case frequently considered for the three-dimensional micropolar continuum is that which sets $\alpha = 0$ and $\beta = \gamma$ (i.e. $\ell_t = \sqrt{2}\ell_b$), which guarantees a pointwise positive-definite free energy [313]. This condition is sufficient but not necessary for non-negativity of the free energy function; other relationships between the parameters may be construed to attain certain other constitutive qualities [299, 313].

The principle of bounded stiffness

The way that the micropolar continuum is able to predict size effects in bending and torsion means that, for some sets of parameters, stiffness tends to infinity for increasingly slender structures. This is utterly unphysical, apart from perhaps for some specially contrived orthotropic material which is effectively rigid in one direction [198]. While this has the potential to be solved by further generalisation of the theory to include additional microstructural DOFs (e.g. microstretch), such overcomplication can be avoided through more careful selection of material parameters. In particular, this is done by applying the *principle of bounded stiffness* of Neff et al. [313]. This corresponds to the weakest possible, so-called *conformal* constraint on the curvature energy, requiring that only the work that depends on the deviatoric part of the symmetric component of $\boldsymbol{\Gamma}$ be strictly positive, with all other components having no energetic consequence [314]. The principle establishes that size effects demonstrated by a micropolar continuum should be limited, independent of the dimensions of the structure, such that the elastic response is singularity free. It is also consistent with the notion that the mechanical properties of the continuum should not exceed those of the smallest reasonable specimen that the micropolar model could be used to represent (e.g. a single lattice cell or representative elementary volume of soil), as illustrated in Figure 3.10. Although in practice it is unlikely that many simulations (certainly in this thesis) will approach such a miniature scale, the principle of bounded stiffness provides a

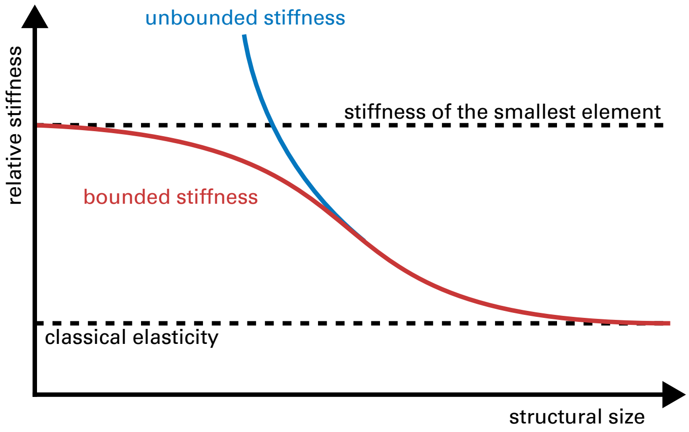

Figure 3.10: The principle of bounded stiffness provides a physically-motivated, singularity-free constitutive response. As the size of the structure approaches ℓ, it may only become as stiff as its smallest constituent microelement.

convenient way to reduce the number of independent additional micropolar parameters in a physically-motivated manner, without risking ill-posedness [299]. Furthermore a precedent for its application to the geometrically-nonlinear micropolar continuum lies in the oeuvre of Neuner and co-workers [102, 277, 278]. Therefore this approach will be adopted for the geomechanical simulations demonstrated in Chapter 4.

For the stiffness to be bounded so, the Biot couple-stress depends only on the deviatoric part of the symmetrised wryness tensor, i.e.

$$\boldsymbol{S} = \boldsymbol{S}\left(\frac{1}{2}(\boldsymbol{\Gamma} + \boldsymbol{\Gamma}^{\mathrm{T}}) - \frac{1}{3}\,\mathrm{tr}(\boldsymbol{\Gamma})\boldsymbol{I}\right), \tag{3.139}$$

and must be invariant to all other curvature components. A short process of deduction and computation results in [314]

$$\beta = 0 \tag{3.140}$$

$$\Psi = \frac{3}{2} \tag{3.141}$$

such that

$$\gamma = 4\ell_b^2\mu = \ell_t^2\mu \tag{3.142}$$

$$\alpha = -\frac{2}{3}\gamma \tag{3.143}$$

$$\ell_t = 2\ell_b. \tag{3.144}$$

Therefore to fulfil the principle of bounded stiffness only two non-classical elastic coefficients must be determined: the coupling modulus and a characteristic length.

3.4 Numerical implementation

Application of the same methodology used in Section 2.3 to the equations of static linear and angular momentum balance (3.82) and (3.83) leaves the discrete Galerkin forms of equilibrium

$$\int_\Omega \boldsymbol{G}^{\mathrm{T}} \boldsymbol{\sigma}^h \, \mathrm{d}\Omega = \int_\Omega \boldsymbol{S}_{vp}^{\mathrm{T}} \boldsymbol{p}^h \, \mathrm{d}\Omega \tag{3.145}$$

and

$$\int_\Omega \left(\boldsymbol{G}^{\mathrm{T}} \boldsymbol{\mu}^h + \boldsymbol{S}_{vp}^{\mathrm{T}} \boldsymbol{\epsilon} : \boldsymbol{\sigma}^h \right) \mathrm{d}\Omega = \int_\Omega \boldsymbol{S}_{vp}^{\mathrm{T}} \boldsymbol{q}^h \, \mathrm{d}\Omega \,, \tag{3.146}$$

complemented by the boundary conditions

$$\boldsymbol{u} = \boldsymbol{u}_D \text{ on } \partial\Omega_D^u \tag{3.147}$$

$$\boldsymbol{\theta} = \boldsymbol{\theta}_D \text{ on } \partial\Omega_D^\theta \tag{3.148}$$

$$\boldsymbol{t} = \boldsymbol{t}_N \text{ on } \partial\Omega_N^t \tag{3.149}$$

$$\boldsymbol{m} = \boldsymbol{m}_N \text{ on } \partial\Omega_N^m, \tag{3.150}$$

where $\partial\Omega = \partial\Omega_D^u \cup \partial\Omega_N^t = \partial\Omega_D^\theta \cup \partial\Omega_N^m$ and $\partial\Omega_D^u \cap \partial\Omega_N^t = \partial\Omega_D^\theta \cap \partial\Omega_N^m = 0$. As before, these equations are assembled and solved numerically on the computational grid according to a Newton-Raphson algorithm. However, before detailing the specifics of the solution procedure, the exact form of the primary field variables (the unknowns for which the algorithm will solve) must first be established. While this is usually obvious – displacement, for example, in classical quasi-statics – in the case of rotations several distinct possibilities present themselves to be discerned. This section, therefore, begins with an examination of the numerical treatment of finite rotations – arguably the most significant distinction between the classical formulation of Chapter 2 and that of a micropolar continuum. Indeed, a careful consideration of their intricate analytical properties is crucial, given their typically thorny nature. Let us begin by recalling some of the characteristics of finite rotations delineated in Section 3.3.1:

- A finite rotation is a transformation constrained by certain properties. Specifically, it cannot alter an object's shape, size, chirality or position.

- Finite rotations are *multiplicative* rather than *additive* due to their moving reference frame. It cannot be assumed that sequential rotations can simply be added together to represent the equivalent total rotation.

- While *finite* rotations demand the more stringent $SO(3)$ representation, *infinitesimal* rotations take the skew-symmetric form $\mathfrak{so}(3)$, typically represented as a vector of three angles or components.

- There is no single 'correct' way to represent rotations algebraically, and many different *formalisms* have been developed and refined over several centuries.

Rotations are a mapping between one three-dimensional vector and another. Recalling (3.17), therefore the smallest enclosing Euclidean space of the rotation group is that of second-order (nine-valued) tensors $\boldsymbol{Q}$ which describe this transformation. But this does not mean rotations cannot be parametrised by spaces of narrower dimensionality, as long as they are either non-Euclidean or accept a degree of limitation. It has previously been stated that any rotation (or sequence of rotations) in three dimensions can be expressed as a single rotation about an axis, equivalent to a vector $\boldsymbol{\theta}$ with an assigned handedness [287]. The set of all possible rotation vectors therefore forms a three-dimensional hypersphere in the nine-dimensional tensor space, where the L_2-norm $\theta = ||\boldsymbol{\theta}||$ corresponds to the rotation angle [289]. Since only two coordinates are needed to specify any location on a sphere (e.g. latitude and longitude), and the rotation angle provides a third, one might initially conclude that just three parameters are sufficient to fully describe any rotation. However, this reasoning is a little naïve. The hairy ball theorem [315] states that a continuous, non-degenerate vector field cannot exist on a spherical surface, leading to unavoidable singularities in any three-parameter representation or coordinate chart; what meaning does longitude have at the north and south poles? This loss of a DOF is more generally known as *gimbal lock* and is usually associated with Euler angles, but it can be shown that no rotation formalism with only three independent parameters can avoid degeneracy. Therefore the Euler vector $\boldsymbol{\theta}$ is an unsuitable basis for a robust numerical formulation, and another candidate must be identified instead.

In the final developed algorithm, as explained below, this takes the form of a quaternion representation updated with intrinsic rotation increments. While quaternions neatly resolve the issue of singularities, their introduction comes at the cost of added abstraction, requiring careful implementation and interpretation. In general, in fact, the treatment of rotations is notoriously challenging, and it is not controversial to describe them as tricky. They are difficult to understand and to work with, especially when transitioning from infinitesimal transformations, but also very rewarding. Indeed, there is a cold but striking elegance to their elusive, and surprising, nature. Perhaps this is why they have intrigued us for so many hundreds of years.

> *Beauty is the first test: there is no permanent place in*
> *the world for ugly mathematics.*
>
> —G.H. Hardy, *A Mathematician's Apology* (1941)

3.4.1 Intrinsic rotations

Since micropolar triads rotate via

$$\boldsymbol{w}_\alpha = \boldsymbol{Q}\boldsymbol{W}_\alpha, \tag{3.17}$$

then the concatenation of an incremental rotation must have the form

$$\boldsymbol{Q}_K = \Delta\boldsymbol{Q}\boldsymbol{Q}_{K-1}. \tag{3.151}$$

It follows that the superposed rotation increment $\Delta\boldsymbol{Q}$ is a finite rotation in its own right, measured relative to the triad directors oriented according to $\boldsymbol{Q}_{K-1}$. The transformation corresponds to a spatial rotation vector $\Delta\boldsymbol{\varphi}$ known as a *spin* or *intrinsic* rotation, which always occurs relative to the moving spatial triad $\boldsymbol{w}_\alpha$. Specifically, it defines another Euler rotation axis, such that the vector represents a normal to a new, relative plane of rotation and the magnitude is the rotation angle $\Delta\varphi = ||\Delta\boldsymbol{\varphi}||$. Intrinsic or *spin* rotations are contrasted with the extrinsic or *total* rotation vector $\boldsymbol{\theta}$ defined previously, which instead refers to a rotation relative to the fixed material triad $\boldsymbol{W}_\alpha$. However, there is no such thing as a *total* intrinsic rotation vector; intrinsic rotations only ever manifest as an *increment*. Intrinsic rotations represent a primary field variable, and it is for these variations which the numerical algorithm will solve in each sequential step of the nonlinear solution scheme; a depiction is provided in Figure 3.11. Equally important to note is that the total rotation *cannot* be updated using the incremental spin rotation directly, i.e.

$$\boldsymbol{\theta}_K \neq \boldsymbol{\theta}_{K-1} + \Delta\boldsymbol{\varphi}, \tag{3.152}$$

and a multiplicative update must be used instead, to respect the nonlinearity of the microrotation field. That said, the spin rotation increment can be exchanged for its material equivalent (providing a linear increment in the total rotation vector $\Delta\boldsymbol{\theta}$) via the map $\boldsymbol{H}$, defined [316]

$$\boldsymbol{H} = \boldsymbol{I} + \frac{1-\cos\Delta\varphi}{\Delta\varphi^2}\widehat{\Delta\boldsymbol{\varphi}} + \frac{\Delta\varphi - \sin\Delta\varphi}{\Delta\varphi^3}\widehat{\Delta\boldsymbol{\varphi}}^2 \tag{3.153}$$

such that $\Delta\boldsymbol{\theta} = \boldsymbol{H}\Delta\boldsymbol{\varphi}$.

Conversion between the intrinsic microrotation vector increment $\Delta\boldsymbol{\varphi}$ and the microrotation tensor increment $\Delta\boldsymbol{Q}$ is achieved as with any other mapping between $\mathfrak{so}(3)$ and $SO(3)$. Concisely,

$$\Delta\boldsymbol{Q} = \exp\left(\widehat{\Delta\boldsymbol{\varphi}}\right) \tag{3.154}$$

where $\widehat{\Delta\boldsymbol{\varphi}} = -\boldsymbol{\epsilon}\cdot\Delta\boldsymbol{\varphi}$ is a skew-symmetric second-order tensor populated by intrinsic rotation angles $\Delta\boldsymbol{\varphi}$. Hence the first variation (linearisation) of the microrotation tensor in the direction of a superposed intrinsic rotation increment $\delta\boldsymbol{\varphi}$ can be obtained by taking its Gateaux derivative (see e.g. [317] for further details). The perturbed microrotation is defined as

$$\boldsymbol{Q}^* = \exp\left(\epsilon\widehat{\delta\boldsymbol{\varphi}}\right)\boldsymbol{Q}, \tag{3.155}$$

where ϵ is a small scalar parameter. Then the Gateaux derivative of $\boldsymbol{Q}$ in the direction $\delta\boldsymbol{\varphi}$

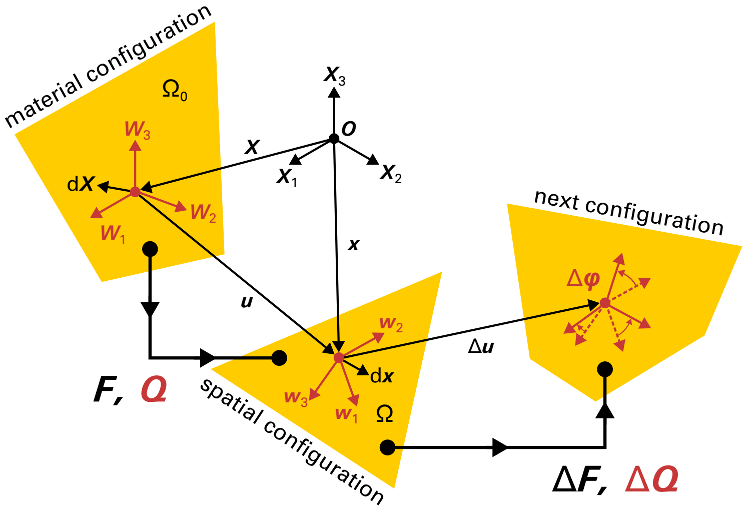

Figure 3.11: The nonlinear solution scheme delivers increments in the translation and intrinsic microrotation vector in each iteration. Mappings lead to changes in the deformation gradient and microrotation tensor which update the state of the domain. Cf. Figure 3.6.

is given by

$$
\begin{aligned}
\delta \boldsymbol{Q} &= \left.\frac{\mathrm{d}\boldsymbol{Q}^*}{\mathrm{d}\epsilon}\right|_{\epsilon\to 0} && (3.156)\\
&= \left.\frac{\mathrm{d}}{\mathrm{d}\epsilon}\left(\exp\left(\epsilon\widehat{\delta\boldsymbol{\varphi}}\right)\boldsymbol{Q}\right)\right|_{\epsilon\to 0} && (3.157)\\
&= \left.\widehat{\delta\boldsymbol{\varphi}}\exp\left(\epsilon\widehat{\delta\boldsymbol{\varphi}}\right)\boldsymbol{Q}\right|_{\epsilon\to 0} && (3.158)\\
&= \widehat{\delta\boldsymbol{\varphi}}\boldsymbol{Q}, && (3.159)
\end{aligned}
$$

which in index notation is equivalently

$$\delta Q_{m\theta} = -\epsilon_{mnj}\delta\varphi_j Q_{n\theta} = \epsilon_{mjn}\delta\varphi_j Q_{n\theta}. \tag{3.160}$$

Since the variation of $\boldsymbol{Q}$ depends entirely on $\delta\boldsymbol{\varphi}$, and the mapping $\delta\boldsymbol{\varphi} \to \delta\boldsymbol{Q}$ is linear (owing to the smoothness of the matrix exponential and the linear nature of the Lie algebra), this variation can be identified with the total differential of $\boldsymbol{Q}$ with respect to the intrinsic microrotation vector, or

$$\delta Q_{m\theta} = \frac{\partial Q_{m\theta}}{\partial\varphi_j}\delta\varphi_j. \tag{3.161}$$

Thus the partial derivative is

$$\frac{\partial Q_{m\theta}}{\partial\varphi_j} = \epsilon_{mjn}Q_{n\theta}. \tag{3.162}$$

The simplicity of this result strengthens the case for using a parametrisation based on intrinsic rotations. Although others (e.g. [274, 275]) have instead proposed a numerical scheme utilising only the extrinsic rotation vector, not only does it risk gimbal lock but its variations are also much more complex and lengthy to derive. For example, differentiation of the Euler-Rodrigues formula (3.29) with respect to the rotation vector is non-trivial, not least because of the singularities it suffers due to loss of axis direction when passing through whole revolutions; a demonstration of these discontinuities is indicated in Section 3.5.3. Moreover the trigonometry involved exacerbates the analytical challenge of consistent linearisation as well as the computational cost required for evaluation of the tangent. Further discussion of the distinction between these rotation formalisms is available in [318].

3.4.2 Interpolation of rotational quantities

The previous section established intrinsic rotation vectors as a primary field variable of the system. This means that the nonlinear solution algorithm (which will be described fully later) delivers a nodal increment $\delta\boldsymbol{\varphi}_v$ in each iteration, which must be mapped to the material points in order to update the microrotation field. Unfortunately the interpolation of rotation parameters is not a trivial exercise [292]. Unlike translation vectors which lie in Euclidean space and can reasonably be broken down into additive contributions, finite $SO(3)$ rotations exist on a 3-sphere (a curved non-Euclidean manifold) and cannot simply be added together. Regrettably conventional interpolation with Lagrange polynomials (see Section 2.3.2) is based on this very principle. Therefore any rotation vector or tensor produced through standard linear interpolation techniques is likely to contain inadequacies in some regard, as uniform rotation in three-dimensional space cannot be captured in this way.[21]

For example, one might attempt to convert $\delta\boldsymbol{\varphi}_v$ directly into the corresponding microrotation tensor $\delta\boldsymbol{Q}_v$ at the nodes. However, this would require interpolating nine separate tensor components, and the resulting matrix would no longer remain an element of $SO(3)$, thus losing its defining property as a proper orthogonal transformation. Because such a procedure renders the interpolated tensor physically meaningless, there is little precedent for it in the literature [319]. In practice, linear interpolation is usually applied to $\delta\boldsymbol{\varphi}$ or $\delta\boldsymbol{\theta}$ (depending on the chosen parametrisation), and the rotation tensor is reconstructed at the integration points [112, 271, 274, 276]. Although this approach cannot rigorously capture variations in rotation fields because of the inherent limitations of linear interpolation, it still produces a tensor in $SO(3)$, allowing the micropolar model to function as designed. However, over the course of a simulation, the poor interpolation becomes iteratively embedded into microrotation tensor, leading to a path-dependent response [316]. In fully mesh-based schemes such as the FEM, this path dependency can be circumvented by storing and updating the rotation tensor at the nodes themselves, meaning no interpolated history needs to be repeatedly recycled [292]. Unfortunately, in the MPM, the computational mesh is re-established at each time step, forcing Lagrangian variables to remain at the

---

[21] Imagine a straight line between two orientations on the $SO(3)$ manifold, and a number of integration points positioned along this line. If the points are evenly spaced, then the rotation will speed up around the centre of the line. A rigorous rotational interpolation instead follows a curved or spherical path.

material points and thereby making repeated interpolation – and hence path dependency – inevitable. But this is potentially a relatively minor issue compared to the path-dependent integration issues already engendered by MPM analyses, and as such is unlikely to diminish the accuracy of the formulation by any significant degree.

The pursuit of more rigorous methods to interpolate finite rotations has led to the development of several techniques worth mentioning here. In particular, spherical linear interpolation (slerp, first described by Shoemake [320] for quaternions – see Section 3.4.3) constructs a shortest-path great-circle arc (geodesic) between two orientations, allowing for a more consistent interpolation based on a principle of constant angular velocity along the $SO(3)$ manifold (a *torque-minimal* path). However, this is usually used for *temporal* interpolation between two orientations (in computer graphics applications, typically) and extensions to multidimensional spatial interpolation come with an array of challenges. In particular, slerp is *non-commutative*, so the order in which the interpolants are applied has an effect [321]; in an 8-noded hexahedral grid cell there would be $8! = 40320$ ways of constructing the interpolation and therefore 40320 different results. Slerping the rotational trial function space in order to discretise the weak forms would also require a special Petrov-Galerkin formulation, complicating the linearisation significantly and leading to a more cumbersome consistent tangent [316], not to mention the considerable computational expense required to execute the trigonometric interpolants. A more relaxed alternative to slerp is normalised linear interpolation, which is computationally less intensive but slightly less rigorous. This method entails separating each nodal Euler vector into a normalised vector and rotation angle (the classical axis-angle representation), linearly interpolating each of the four values, re-normalising the resultant vector, before finally converting it back into an Euler vector. While this is now commutative, it does not represent a constant velocity operation [321]. Although other methods exist, based on e.g. Runge-Kutta integration [322] and logarithms [321], ultimately it would appear that none is universally advantageous or, indeed, widely adopted.

Therefore, given that the implementation is likely only ever to deal with small increments in the intrinsic microrotation vector, the chosen approach is simply to use conventional linear interpolation on this vector directly.[22] The arc-lengths over which interpolation is to take place are likely to be so short that the $SO(3)$ manifold would closely resemble Euclidean space anyway, making non-spherical interpolation a reasonable approximation of the 'true' variation, which follows a curved path. This also simplifies the numerical formulation, as both primary field variables (translations and rotations) are interpolated identically, using the same basis functions; that is

$$\delta\boldsymbol{\varphi}_p \approx \sum_v S_{vp}\delta\boldsymbol{\varphi}_v, \tag{3.163}$$

---

[22] This is also by far the most commonly adopted approach in the literature [271, 274–276, 278].

cf. (2.18). This increment can then be mapped to become $SO(3)$ in order to update the microrotation tensor stored at the material points.

As a final remark on the conundrum of rigorous rotational interpolation, consider briefly the case of plane deformations. Here, rotations are constrained such that they may only occur around the normal to the plane. Therefore the rotational parameters degenerate to a single scalar: the rotation angle. Since the reference frame no longer moves, concatenation may be achieved by simple addition of consecutive angles, and linear interpolation is fully legitimate. Ultimately this means that a proper verification of any numerical implementation of finite rotations must examine the much more complex and nonlinear case of non-planar rotations, as examples where the rotation axis remains fixed represent a trivial special case and will not suffice.[23] This is attempted in Section 3.5.4.

3.4.3 Quaternions

Although proper orthogonal second-order tensors are the most common way to manipulate elements of $SO(3)$, they are by no means the only available formalism. In fact it does not matter how they are represented, as long as the format preserves the definitional Lie group properties listed previously. However, each formalism has its own particular characteristics. Although the microrotation tensor $\boldsymbol{Q}$ is appealingly intuitive, updating it via

$$\boldsymbol{Q}_K = \exp\left(\widehat{\delta\boldsymbol{\varphi}}\right)\boldsymbol{Q}_{K-1} \tag{3.164}$$

can invoke poor conditioning when the total rotation angle passes through $\theta = 2n\pi,\ \forall\, n \in \mathbb{Z}$. This corresponds to orientations passing through whole revolutions, where the direction of the Euler vector becomes indeterminate. Therefore discontinuities can arise, producing nonsensical and artificial results as will be demonstrated in Section 3.5.3, particularly when numerical imprecision is a factor, and gimbal lock can withhold access to certain rotation axes.

Instead, the implemented rotation update algorithm uses a *quaternion* representation of $SO(3)$. Quaternions are an extension of complex numbers to multiple dimensions, and have the general hypercomplex form

$$\mathscr{Q} = \mathcal{Q} + \boldsymbol{\mathcal{Q}} i = \mathcal{Q} + (\mathcal{Q}_1, \mathcal{Q}_2, \mathcal{Q}_3) i \tag{3.165}$$

where $\mathcal{Q}$ is a real scalar, $\boldsymbol{\mathcal{Q}} \in \mathbb{R}^3$ and i is the (generalised) imaginary unit.[24] When used to

---

[23] I am grateful to an anonymous reviewer for raising this point.

[24] This is a simplification of the proper Hamiltonian description of a quaternion, in which each component of the vector $\boldsymbol{\mathcal{Q}}$ corresponds to different, orthogonal hyper-imaginary number. They are often denoted i, j, k and are subject to the relations $i^2 = j^2 = k^2 = -1$, $ij = (-ji) = k$, $jk = (-kj) = i$ and $ki = (-ik) = j$. These properties endow quaternions with their useful multiplicative characteristics which allow them to embody rotations, but with a little abuse of notation they can also be sufficiently notated with standard operations of vector arithmetic.

parametrise rotations, they offer greater stability and efficiency in comparison to rotation tensors [318]. Not only are they more concise, but they additionally lack the degeneracy associated with other formalisms, guaranteeing a smooth, singularity-free update path. Their composition from four parameters, rather than three, also prevents them from succumbing to gimbal lock. From a topological perspective, quaternions naturally form a 3-sphere, providing a neat double-cover of the rotation group space. Unidimensional spherical interpolation between quaternions is also appealingly straightforward [320], but this is not attempted here as its multidimensional extension is not.

How can such a mathematical structure represent a rotation? This comes down to the manner in which quaternions are multiplied. Firstly, only unit quaternions (*versors*) are used, i.e.

$$||\mathscr{Q}|| = \sqrt{\mathcal{Q}^2 + ||\boldsymbol{\mathcal{Q}}||^2} = 1, \tag{3.166}$$

which corresponds to the property $\det \boldsymbol{Q} = 1$ in rotation tensors. This ensures polar triad directors remain the same size, no matter the number of rotations they undergo. The product of two sequential quaternions $\mathscr{Q}_1$ and $\mathscr{Q}_2$ uses both the dot product and the cross product, and is written

$$\mathscr{Q}_2\mathscr{Q}_1 = (\mathcal{Q}_2\mathcal{Q}_1 - \boldsymbol{\mathcal{Q}}_2 \cdot \boldsymbol{\mathcal{Q}}_1) + (\mathcal{Q}_2\boldsymbol{\mathcal{Q}}_1 + \mathcal{Q}_1\boldsymbol{\mathcal{Q}}_2 + \boldsymbol{\mathcal{Q}}_2 \times \boldsymbol{\mathcal{Q}}_1)i \tag{3.167}$$

which, like matrix multiplication, is not associative. The key actor in this equation is the cross product. As Shoemake explains,

> quaternions multiply with a cross product because rotations confound axes. To illustrate, place a book in front of you, face up, with the top farthest away. Use this orientation as a reference. Now hold the sides and flip in toward you onto its face, rotating 180 degrees around a left-to-right axis, y. Then, keeping it face down, spin it clockwise 180 degrees around an up-down z axis. Two rotations around two perpendicular axes; yet the total change in orientation must be, according to Euler, a single rotation. Indeed, if you hold the ends of the spine and flip the book 180 degrees around this third, outward-pointing, x axis, you should restore the original orientation. As quaternions this is – anticipating developments ahead – $\{0 + (0, 1, 0)i\}$ times $\{0 + (0, 0, 1)i\}$ equals $\{0 + (1, 0, 0)i\}$; the cross product is essential [320].

The rotation matrix $\boldsymbol{Q}$ equivalent to a quaternion may be written [289]

$$\boldsymbol{Q} = (2\mathcal{Q}^2 - 1)\boldsymbol{I} + 2\boldsymbol{\mathcal{Q}} \otimes \boldsymbol{\mathcal{Q}} + 2\mathcal{Q}\widehat{\boldsymbol{\mathcal{Q}}} \tag{3.168}$$

from which it follows that the reference quaternion (corresponding to $\boldsymbol{Q} = \boldsymbol{I}$) is

$$\mathscr{Q}^0 = 1 + \mathbf{0}i. \tag{3.169}$$

As $\mathscr{Q} = \delta\mathscr{Q}\mathscr{Q}^0$ a quaternion increment $\delta\mathscr{Q}$ must then be [276, 323, 324]

$$\delta\mathscr{Q} = \delta\mathcal{Q} + \delta\boldsymbol{\mathcal{Q}}i = \cos\frac{\delta\varphi}{2} + \frac{\delta\boldsymbol{\varphi}}{\delta\varphi}\sin\frac{\delta\varphi}{2}i \tag{3.170}$$

in terms of the incremental spin vector, which fully elucidates Shoemake's example above. Due to the symmetry of the sine and cosine functions, each unique rotation corresponds to two distinct locations (antipodes) on the quaternion hypersphere – the *double-cover* alluded to earlier. The parametrical machinery could therefore be reformulated entirely in terms of a quaternion *hemisphere* instead such that $0 \leq \varphi \leq 2\pi$ rather than $-2\pi \leq \varphi \leq 2\pi$ [289]. But the introduction of a discontinuity at $\varphi = 0$ could be potentially problematic in terms of the nonlinear solver, which is likely to supply small values of φ in both clockwise and anticlockwise directions. Therefore, the slightly more ambiguous – but also more flexible and descriptive – quaternion sphere is retained.

A complete rotational formulation has now been developed. The associated primary field variable comprises intrinsic microrotation vectors $\boldsymbol{\varphi}$ such that the nonlinear solution will be formulated in terms of incremental translations $\delta\boldsymbol{u}_v$ and superposed spin rotations $\delta\boldsymbol{\varphi}_v$. The intrinsic rotations are mapped from the nodes to the material points in the conventional manner for the sake of simplicity; there they are converted into quaternion increments in order to update the stored quantities. The microrotation tensor $\boldsymbol{Q}$ to be used in the continuum mechanics model follows from (3.168) and, although it is not actually used anywhere in the formulation, the equivalent total rotation vector $\boldsymbol{\theta}$ can be generated (e.g. for post-processing) by taking the axial components of the matrix logarithm of $\boldsymbol{Q}$.[25] However, as this is an expensive computation to perform and only delivers $-\pi \leq \theta_i \leq \pi$, the vector may be obtained directly from the quaternion as

$$\boldsymbol{\theta} = \frac{2\arccos\mathcal{Q}}{\sqrt{1-\mathcal{Q}^2}}\boldsymbol{\mathcal{Q}} \tag{3.171}$$

which widens the interval to $-2\pi \leq \theta_i \leq 2\pi$, but is clearly unstable at $\mathcal{Q} \approx 1$, recovering the indeterminacy of the extrinsic rotation vector at whole revolutions. The inverse map can be achieved through e.g. Spurrier's algorithm [325].

3.4.4 Nonlinear solution

Recall the weak statements of equilibrium

$$\int_\Omega \boldsymbol{G}^{\mathrm{T}}\boldsymbol{\sigma}^h \,\mathrm{d}\Omega = \int_\Omega \boldsymbol{S}_{vp}^{\mathrm{T}}\boldsymbol{p}^h \,\mathrm{d}\Omega \tag{3.145}$$

and

$$\int_\Omega \left(\boldsymbol{G}^{\mathrm{T}}\boldsymbol{\mu}^h + \boldsymbol{S}_{vp}^{\mathrm{T}}\boldsymbol{\epsilon} : \boldsymbol{\sigma}^h\right) \mathrm{d}\Omega = \int_\Omega \boldsymbol{S}_{vp}^{\mathrm{T}}\boldsymbol{q}^h \,\mathrm{d}\Omega\,, \tag{3.146}$$

---

[25] The inverse of (3.28), in other words.

in which the left-hand sides represent the internal force $\boldsymbol{p}^{\text{int}}$ and couple $\boldsymbol{q}^{\text{int}}$ vectors respectively, while the right-hand sides are the body force $\boldsymbol{p}^{\text{ext}}$ and couple $\boldsymbol{q}^{\text{ext}}$. The Newton-Raphson algorithm iteratively solves these two equations in terms of translation $\boldsymbol{u}^h$ and intrinsic microrotation vector $\boldsymbol{\varphi}^h$. The consistent tangent to each equation with respect to increments in both primary fields must therefore be found in each iteration. Essentially this means four sub-tangents are required, defined

$$\delta\boldsymbol{p}^{\text{int}} = \boldsymbol{K}^{pu}\delta\boldsymbol{u} + \boldsymbol{K}^{p\varphi}\delta\boldsymbol{\varphi} \tag{3.172}$$

$$\delta\boldsymbol{q}^{\text{int}} = \boldsymbol{K}^{qu}\delta\boldsymbol{u} + \boldsymbol{K}^{q\varphi}\delta\boldsymbol{\varphi} \tag{3.173}$$

so that, if the external loads are not configuration-dependent follower loads,

$$\begin{Bmatrix} \boldsymbol{p}^{\text{R}} \\ \boldsymbol{q}^{\text{R}} \end{Bmatrix} = \begin{bmatrix} \boldsymbol{K}^{pu} & \boldsymbol{K}^{p\varphi} \\ \boldsymbol{K}^{qu} & \boldsymbol{K}^{q\varphi} \end{bmatrix} \begin{Bmatrix} \delta\boldsymbol{u} \\ \delta\boldsymbol{\varphi} \end{Bmatrix} = \begin{Bmatrix} \boldsymbol{0} \\ \boldsymbol{0} \end{Bmatrix} \tag{3.174}$$

must be solved iteratively and monolithically, where $(\bullet)^{\text{R}} = (\bullet)^{\text{int}} - (\bullet)^{\text{ext}}$ is a residual. Ghost stabilisation can be applied as before to this tangent stiffness matrix, but only the two submatrices on the main diagonal require treatment for the conditioning of $\boldsymbol{K}$ to be guaranteed. Respectively, then, the matrices corresponding to $\boldsymbol{K}^{pu}$ and $\boldsymbol{K}^{q\varphi}$ are scaled by ghost parameters γ_{g1} and γ_{g2}.

The analytical consistent linearisation of (3.145) and (3.146) is intricate and lengthy, but uses the relations already derived in this chapter and does not otherwise depart from conventional tensor calculus and algebra. The derivation is given in full in Appendix A, but for a single grid cell E the submatrices read

$$\boldsymbol{K}_E^{pu} = \int_E \boldsymbol{G}^{\text{T}} : \boldsymbol{a}_1 : \boldsymbol{G}\,\mathrm{d}\Omega \tag{3.175}$$

$$\boldsymbol{K}_E^{p\varphi} = \int_E \boldsymbol{G}^{\text{T}} : \boldsymbol{a}_2 : \check{\boldsymbol{G}}\,\mathrm{d}\Omega \tag{3.176}$$

$$\boldsymbol{K}_E^{qu} = \int_E \check{\boldsymbol{G}}^{\text{T}} : \boldsymbol{a}_2^{\text{T}} : \boldsymbol{G}\,\mathrm{d}\Omega = \left(\boldsymbol{K}_E^{p\varphi}\right)^{\text{T}} \tag{3.177}$$

$$\boldsymbol{K}_E^{q\varphi} = \int_E \left(\check{\boldsymbol{G}}^{\text{T}} : \boldsymbol{a}_2 : \check{\boldsymbol{G}} + \boldsymbol{G}^{\text{T}} : \left(\boldsymbol{a}_3 : \boldsymbol{G} + \boldsymbol{a}_4 : \check{\boldsymbol{G}}\right)\right)\mathrm{d}\Omega \tag{3.178}$$

where, using index notation in a Cartesian frame,

$$(a_1)_{ijkl} = J^{-1} Q_{i\alpha} F_{j\beta} D_{\alpha\beta\gamma\delta} Q_{k\gamma} F_{l\delta} \tag{3.179}$$

$$(a_2)_{ijkl} = (a_1)_{ijkl} + \delta_{il}\sigma_{kj} \tag{3.180}$$

$$(a_3)_{ijkl} = J^{-1} Q_{i\alpha} F_{j\beta} \check{D}_{\alpha\beta\gamma\delta} Q_{k\gamma} F_{l\delta} \tag{3.181}$$

$$(a_4)_{ijkl} = \delta_{il}\mu_{kj} \tag{3.182}$$

and

$$G_{klJn} = \frac{\partial (S_{vp})_J}{\partial x_l}\delta_{kn} \tag{3.183}$$

$$\check{G}_{klJn} = \epsilon_{kln}(S_{vp})_J, \tag{3.184}$$

leading to tangent stiffnesses K^{ab}_{ImJn} representing a linearisation of the m^{th} component of a quantity a at node I, with respect to an increment in the n^{th} component of quantity b at node J.

As with the classical formulation of AMPLE, the solution is advanced by extracting the solution vector $\left\{ \begin{smallmatrix} \delta \boldsymbol{u} \\ \delta \boldsymbol{\varphi} \end{smallmatrix} \right\}$ each time, mapping the increments to the material points, and updating the kinematics and stress fields. The Newton-Raphson algorithm is halted according to the same convergence criteria as before (see Section 2.3.3).

3.4.5 Update procedure

The solution vector is separated into incremental nodal translations $\delta \boldsymbol{u}_v$ and rotations $\delta \boldsymbol{\varphi}_v$, which are mapped via the weighting functions to the material points to become $\delta \boldsymbol{u}_p$ and $\delta \boldsymbol{\varphi}_p$ respectively. The new position of each material point is obtained simply by adding $\delta \boldsymbol{u}_p$ to its previous position, but note that this computation is only required at the end of each load step, using the total translation $\Delta \boldsymbol{u}_p = \sum \delta \boldsymbol{u}_p$ accumulated throughout the step. On the other hand, the nonlinear nature of the microrotation field requires the micropolar orientations to be updated after each individual iteration of the Newton-Raphson scheme. This is achieved by first converting $\delta \boldsymbol{\varphi}_p$ into the equivalent quaternion with (3.170), multiplying the previous orientation quaternion stored at the material point with (3.167), and converting the new orientation into tensorial format via (3.168).

As the deformation gradient depends wholly on the displacement field, there is no change in its update procedure from the steps detailed in Section 2.3.3. It follows that the weighting function gradients are updated in precisely the same manner too. Once these are obtained, the updated wryness tensor for each Newton-Raphson iteration K results from the formula

$$\boldsymbol{\Gamma}_K = \boldsymbol{\Gamma}_{K-1} + \boldsymbol{Q}^{\mathrm{T}} \boldsymbol{H} \frac{\partial (\delta \boldsymbol{\varphi})}{\partial \boldsymbol{x}} \boldsymbol{F}, \tag{3.185}$$

as derived by Erdelj et al. [276], using the mapping $\boldsymbol{H}$ defined in (3.153). Two things are striking about this equation: firstly its brevity, given the prickly character of the principles and fields with which it is defined, but secondly the revelation that the wryness tensor decomposes *additively* [270]. This is an appealing property which will be exploited in the elastoplastic formulation of Chapter 4 when splitting the deformation into elastic and plastic components.

The stress and couple-stress update is performed according to the steps derived in the formulation of the constitutive model in Section 3.3. The procedure is given in Algorithm 2. From these the internal force and couple may be obtained, which are integrated and assembled to form the global system of equations to be fed into the Newton-Raphson algorithm.

Algorithm 2 Procedure for updating stress and couple-stress at the material points in Newton-Raphson iteration K.

```
1: Nodes to material points
   (a) Extract translation and microrotation vector increments from the solution vector.
   (b) Map to material points using standard or GIMPM weighting functions and their derivatives computed at the start of the step to obtain $\delta\boldsymbol{u}_p$, $\delta\boldsymbol{\varphi}_p$, $\frac{\partial(\delta\boldsymbol{u}_p)}{\partial\widetilde{\boldsymbol{x}}}$ and $\frac{\partial(\delta\boldsymbol{\varphi}_p)}{\partial\widetilde{\boldsymbol{x}}}$.
2: Kinematic update
   (a) Update deformation gradient: $\boldsymbol{F}_K = \Delta\boldsymbol{F}_K\widetilde{\boldsymbol{F}}$.
   (b) Update volume: $(v_p)_K = \det(\Delta\boldsymbol{F}_K)\widetilde{v}_p$.
   (c) Update gradients: $\frac{\partial(\bullet)}{\partial\boldsymbol{x}_K} = \frac{\partial(\bullet)}{\partial\widetilde{\boldsymbol{x}}}(\Delta\boldsymbol{F}_K)^{-1}$.
   (d) Update quaternion using (3.170) and (3.167), and calculate the microrotation tensor with (3.168).
   (e) Optionally compute the corresponding microrotation vector with (3.171).
3: Stress update
   (a) Calculate material strain and wryness from (3.34) and (3.185) respectively.
   (b) Obtain Biot stress and couple-stress with constitutive laws (3.122) and (3.123).
   (c) Push forward for spatial Cauchy stress and couple-stress:
       $\boldsymbol{\sigma} = J^{-1}\boldsymbol{QBF}^{\mathrm{T}} \quad \text{and} \quad \boldsymbol{\mu} = J^{-1}\boldsymbol{QSF}^{\mathrm{T}}.$
```

3.5 Numerical examples

The terms *verification* and *validation* are sometimes used interchangeably. However, they serve distinct purposes and should not be conflated. Verification refers to the process of ensuring that a model has been implemented correctly according to the specification of its own design. To paraphrase Boehm [326], *are we building it right*? For instance, a particular model may be constructed from a specified set of governing PDEs. Verification would entail demonstrating that the numerical solution to these PDEs is sufficiently accurate and well behaved (i.e. stable, consistent, and convergent), adhering to the mathematical assumptions made in its formulation. Techniques with this purpose might involve comparing computed solutions against known analytical solutions, and performing convergence studies to ensure that the accuracy of the solution improves at the correct rate as the discretisation is refined.

Validation, on the other hand, determines whether the model is appropriate for its intended real-world application. In other words, *are we building the right thing*? While verification ensures that the numerical solution is correct with respect to the chosen governing equations, validation examines whether these equations, the selected parameters, and the underlying assumptions correctly capture the physics or phenomena of interest. A model is therefore said to be validated if it reliably predicts outcomes observed in the physical world. In computational mechanics, this often involves comparing simulation results against experimental data: if the numerical predictions closely match the empirical observations, the model can be considered validated, at least within the context of those comparisons.

These two processes are complementary and both are crucial for establishing confidence in a model. Without verification, a model may be internally inconsistent, producing misleading or unreliable results even if it seems to align with external data in certain cases. Without validation, a perfectly verified model is pointless if its underlying formulation fails to represent the target physical system accurately. Further information on 'V&V' in the context of numerical methods can be found in e.g. [327, 328].

In this section several numerical examples are presented – each designed either to test or demonstrate a particular feature of the derived method or continuum model underpinning it. However, since a purely *elastic* model cannot be used to simulate localised failure, the implementation cannot yet be validated against the kind of real-world problems motivating this thesis, and as such its general applicability is unfortunately a little limited. The example problems given here therefore only represent a *verification* of this initial 'stepping stone'; validation of the full elastoplastic formulation will come in the Chapter 4.[26]

3.5.1 Method of manufactured solutions

Verification of numerical techniques typically begins by designing a simple model problem and determining its analytical solution. By comparing the numerical solution to this known analytical benchmark, the performance, accuracy, and reliability of the method can be assessed in a systematic, well-established manner. Then, as parameters of the simulation (e.g. the step size or order of the polynomial basis) are modified, observing the corresponding change in the resultant numerical error can provide insight into the robustness and convergence properties of the method. Classic examples of this approach are the plane cantilever of Timoshenko and Goodier [329, 330] used to verify formulations of linear elastostatics, and Charlton et al.'s [110] one-dimensional compression of a ponderous column at finite strains. However, as the complexity of the governing equations increases, deriving closed-form solutions quickly becomes a formidable challenge. After all, is this not the principal motivation for developing numerical methods in the first place? Indeed there are no existing analytic benchmark problems for nonlinear micropolar theory in the literature, likely due to its mathematical complexity. Some closed-form solutions describing the geometrically-nonlinear response of a micropolar cantilever are given in [276, 331], but the derivation makes an unfortunate but necessary assumption which renders the result inexact. This problem therefore cannot be used for convergence studies. Furthermore, it requires application of a non-conforming Neumann boundary condition, which is not trivial in the MPM (see Section 2.2).

---

[26] Although the size effects predicted by even an elastic micropolar continuum might provide a paradigm for validation, in practice empirical size effects only really become measurable in the elastoplastic regime.

Faced with this difficulty, a more flexible approach is provided by the *method of manufactured solutions* (MMS) [327]. Instead of working backwards from a complex formulation to an elusive analytical solution, it can be far easier to *start* with a deliberately-chosen elegant solution – often one that is entirely artificial – defined on a simple geometry. The prescribed solution is then substituted into the governing equations and constitutive relationships to deduce the forcing terms and boundary conditions that must accompany it. This is the most challenging, error-prone step, but in practice symbolic computing packages can be used rather than relying on hand calculations. By 'manufacturing' both the solution and the problem conditions in a self-consistent manner, the analytical outcome is known precisely. Subsequently, the numerical method can be tested against these contrived conditions to verify its correctness. It is important to note that as the machinery linking the problem setup and its solution are the same in the MMS as they would be in a more conventional model problem, it provides an equally rigorous verification, even if the problem itself is not physically motivated. In fact, it may even be more rigorous: the method's simplicity and elegance allow for greater confidence in the precision of any analytical workings.

To that end, consider a unit cube domain defined along rectangular coordinate axes $[X_1, X_2, X_3] \in [0, 1]$, on which the arbitrary displacement-rotation field

$$u_1 = u_2 = u_3 = \theta_1 = \theta_2 = \theta_3 = \frac{1}{30}\sin(2\pi X_1)\sin(2\pi X_2)\sin(2\pi X_3) \tag{3.186}$$

is imposed. This particular solution was selected as it vanishes on the boundaries of the domain, making the boundary conditions trivial, and is infinitely differentiable. The scaling factor of $\frac{1}{30}$ is introduced for the sake of numerical stability; without it, the deformation field could produce kinematically inadmissible configurations, such as material points penetrating the constrained boundaries. For simplicity, all components of both the translation vector $\boldsymbol{u}$ and total rotation vector $\boldsymbol{\theta}$ are defined by the same formula. Consequently, however, the rotation axis is constant throughout the domain, parallel to $(1, 1, 1)^{\mathrm{T}}$, and only the angle (the vector's magnitude) possesses spatial variability. Verification of the formulation's ability to capture fully nonlinear finite rotations takes place in Section 3.5.4.

The domain is discretised into a uniform grid of tri-linear hexahedral elements, each containing 2^3 material points. Rather than positioning the material points evenly, they are placed as Gauss-Legendre integration points: $\xi = \pm\frac{1}{\sqrt{3}}$ for each coordinate direction. Additionally, neither the GIMPM nor ghost stabilisation is employed, and the applied load is introduced in a single increment. Under these conditions, the methodology effectively reduces to a classical FEM. This is because the key MPM-related complications – such as cell-crossing of material points, mesh resetting, and the associated numerical integration errors – are absent. Effectively this isolates the core formulation's behaviour, allowing for a more direct verification of its convergence properties, coercivity, and stability which might otherwise be obfuscated by numerical or variational inconsistencies.

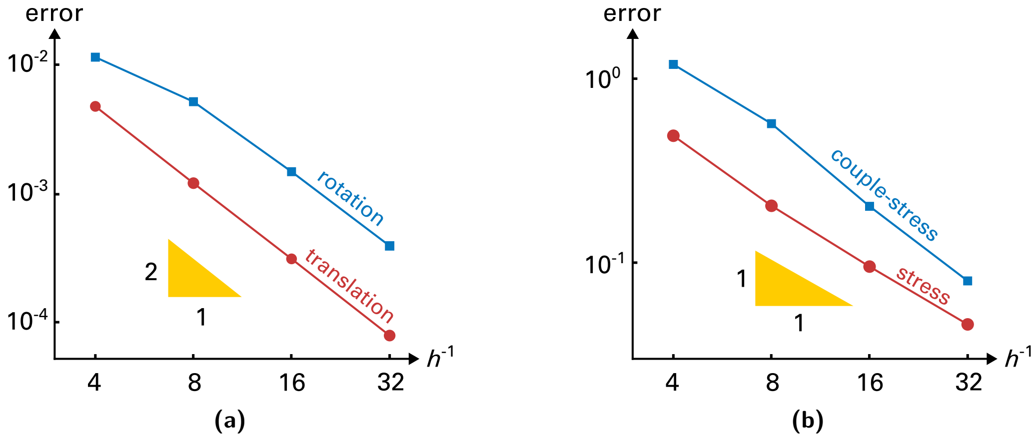

Figure 3.12: MMS convergence with mesh refinement of **(a)** translation and rotation and **(b)** Cauchy stress and couple-stress, on log-log plots.

The coarsest mesh in this study uses a discretisation into 4^3 elements, which halve in size each time for a total of four tests. Homogeneous Dirichlet displacement and rotation boundary conditions are applied over all six sides of the domain, and the requisite body forces and couples are applied at each material point.[27] Although the chosen elastic parameters have no substantive significance in this test, the selected values are $\lambda = 15\,\mathrm{GPa}$, $\mu = 10\,\mathrm{GPa}$, $\kappa = \frac{\mu}{3}$, $\alpha = 0$ and $\gamma = \beta = 50\,\mathrm{N}$. The convergence tolerances used are $\bar{f}_{\mathrm{tol}} = 1 \times 10^{-9}$ and $\bar{e}_{\mathrm{tol}} = 1 \times 10^{-16}$, and both conditions are required to be fulfilled for the Newton-Raphson search to conclude. The numerical error e in the translation and rotation, and stress and couple-stress, is quantified with

$$e_{\boldsymbol{u}} = \int_\Omega ||\boldsymbol{u}^h - \boldsymbol{u}^a||\,\mathrm{d}\Omega\,, \qquad e_{\boldsymbol{\theta}} = \int_\Omega ||\boldsymbol{\theta}^h - \boldsymbol{\theta}^a||\,\mathrm{d}\Omega\,, \tag{3.187}$$

$$e_{\boldsymbol{\sigma}} = \int_\Omega \frac{||\boldsymbol{\sigma}^h - \boldsymbol{\sigma}^a||}{||\boldsymbol{\sigma}^a||}\,\mathrm{d}\Omega\,, \qquad e_{\boldsymbol{\mu}} = \int_\Omega \frac{||\boldsymbol{\mu}^h - \boldsymbol{\mu}^a||}{||\boldsymbol{\mu}^a||}\,\mathrm{d}\Omega \tag{3.188}$$

where $(\bullet)^a$ denotes an analytical solution. The results are shown plotted on log-log scales in Figure 3.12.

For the error in the primary field variables, a quadratic rate of decay is exhibited in both translation and rotation: the expected result for linear elements. The convergence of the Cauchy stress is linear, as it depends on the gradient of the translation field, and the couple-stress error decays at a supralinear rate such that it begins to converge towards the stress results. The higher relative value of the rotation and couple-stresses with respect to their counterparts is likely due to the fact that rotation represents a higher-order quantity than translations, placing couple-stress at the second-derivative level with respect to the displacement (or displacement-like) fields. Such second-derivative-like quantities are more sensitive to mesh refinement because linear elements do not provide direct polynomial basis

---

[27] The analytical expressions for the body force and couple were produced using MATLAB's Symbolic Math Toolbox. They are much too long to provide here.

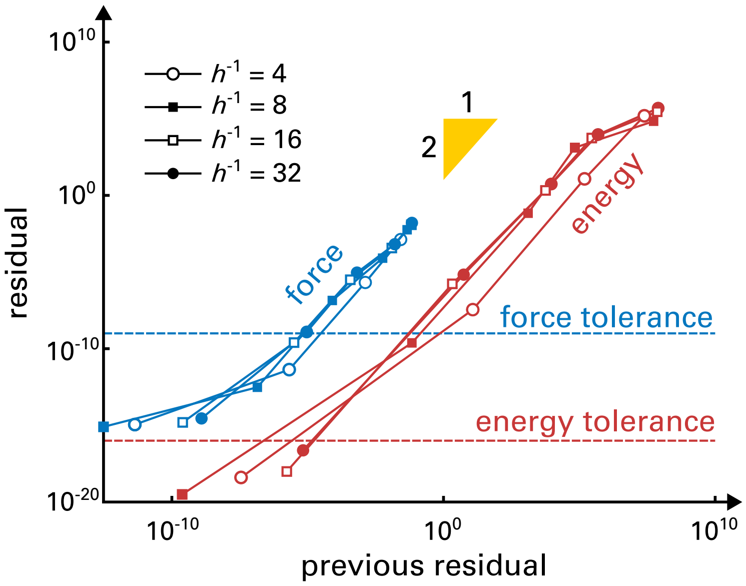

Figure 3.13: The Newton-Raphson convergence for the MMS problem in terms of both the normalised force and energy on a log-log plot.

functions that can represent second derivatives smoothly. Initially, this leads to higher errors. But as the mesh is refined, the piecewise-linear approximations to the rotation field become more smooth and can represent the continuous spatial variation more closely. This improved resolution of the rotation field results in a better approximation to its gradient. Consequently, the couple-stress converges more rapidly once a certain mesh resolution threshold is passed. This manifests as the supralinear 'catch-up' phase in the convergence rate of the couple-stress error.[28] From these results it is clear that the method supplies numerical solutions that are consistent with the governing equations, in a manner which is stable, convergent and in accordance with the nonlinear framework laid out in Section 3.3.

The progression of the force and energy residuals $\bar{f}$ and $\bar{e}$ is depicted in Figure 3.13 for the four levels of discretisation. In the region of the solution, and before the solution is hampered by machine precision, asymptotically quadratic convergence is exhibited in both quantities. This is a well-known quality of the Newton-Raphson algorithm, mentioned earlier in Section 2.3, and verifies that the tangent is correct and consistent with the residual equations.

3.5.2 Two-dimensional bending

The formulation has now been rigorously verified for scenarios involving uniaxial rotations. To further illustrate the capabilities and characteristics of the underlying continuum model

---

[28] In [112] I postulated that this phenomenon arises from the poor-quality interpolation of the rotations – an effect which is known to diminish on finer meshes [316]. In reality this is unlikely to be the case here given that only the rotation angle (and not the axis) varies across the domain, which linear interpolation should have no problem recovering.

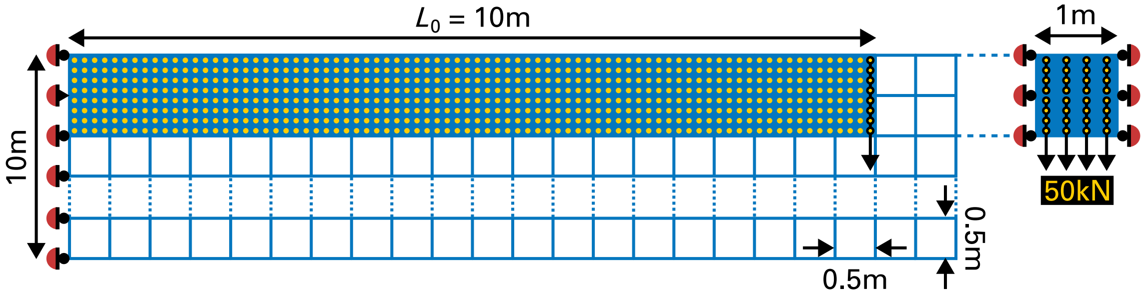

Figure 3.14: Setup of the plane strain cantilever beam problem.

– beyond the specific numerical qualities already tested – this numerical experiment presents a canonical example to highlight its inherent size-dependent behaviour. Although it does not examine a particular aspect of the numerical scheme itself, it offers an instructive demonstration of one of the model's most iconic and physically meaningful properties: the emergence of size effects in structural response.

Consider a cantilever beam lying in the plane which is constrained against any out-of-plane translation or rotation (plane strain conditions). The beam has an initial length L_0 of 10 m, and has a square cross section measuring 1 m × 1 m. It is subject to an end load of 50 kN acting in a direction which is initially perpendicular to the axis of the beam, applied uniformly to the final layer of material points in fifty equal steps to approximate an inhomogeneous Neumann boundary condition. The elastic material parameters satisfy the pointwise-positive free energy condition (see Section 3.3.7), and are chosen to give two different characteristic bending lengths but are otherwise arbitrary. They are: $\lambda = \frac{10}{3}$MPa, $\mu = 5\,\text{MPa}$, $\kappa = \frac{\mu}{3}$, $\alpha = 0\,\text{N}$ and $\gamma = \beta =$ (a) 100 kN or (b) 10 MN. From (3.132), the corresponding bending lengths are $\ell_b =$ (a) 0.1 m and (b) 1 m. Interpreting ℓ_b as a measure of the inherent microstructural length scale, these two cases can be seen as examining beams whose macroscopic dimensions approach the size of their underlying microstructure. Such conditions are relevant to various contemporary applications, for instance MEMS (micro-electro-mechanical systems), where size effects become pronounced and can significantly influence design and performance via the Hall-Petch effect or similar [21,168,169]. As shown in Figure 3.14, the beam is discretised into $20 \times 2 \times 1 = 40$ three-dimensional elements, each populated by 4^3 GIMPM elements which are evenly spaced along each coordinate direction. The boundary conditions enforce zero rotations along the beam's root and a pinned constraint along its central axis, while the remainder of the left-hand boundary of the domain is supported on rollers to prevent horizontal motion. These conditions ensure that the beam deformation primarily occurs under bending so that microrotation gradients are allowed to develop fully. Convergence in each load step is deemed to have been achieved when either $\bar{f} < 1 \times 10^{-9}$ or $\bar{e} < 1 \times 10^{-16}$. Ghost stabilisation is not applied.

Figure 3.15 displays the final deformed configurations for both beams, along with representative stress fields. For the beam with the smaller bending length (a), the structural scale is large compared to the microstructural length scale, and the response is closer to

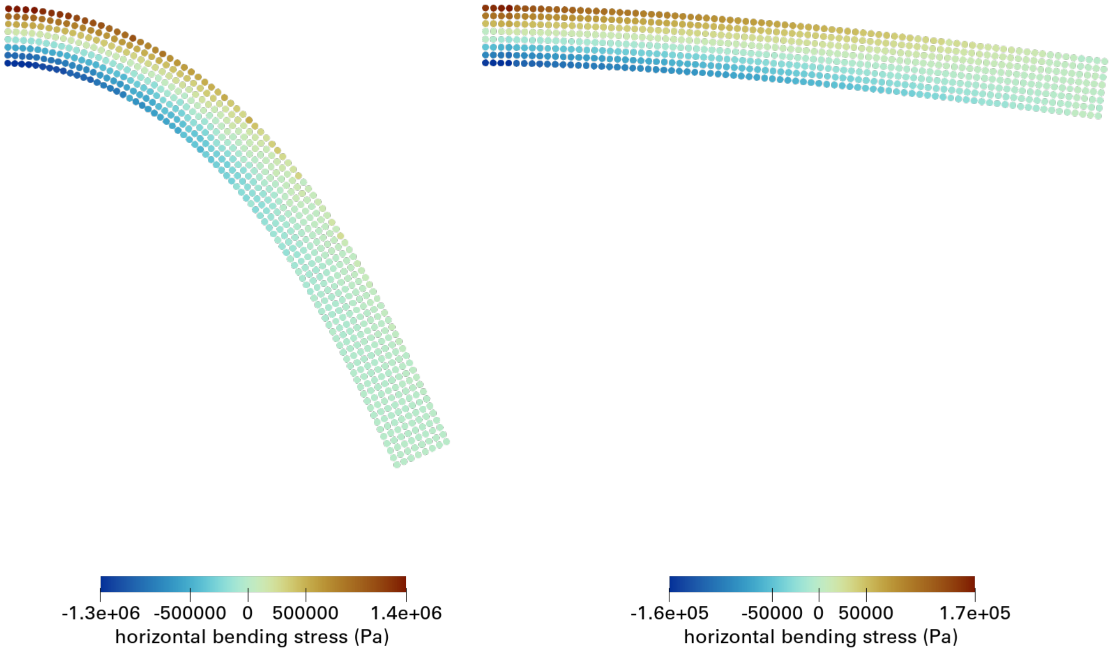

(a) **(b)**

Figure 3.15: The final configurations of the beam possessing **(a)** $L_0 = 100\ell_b$ and **(b)** $L_0 = 10\ell_b$, coloured according to bending stress (horizontal normal Cauchy stress).

classical behaviour where size effects are negligible. In contrast, beam (b) behaves as if it is microscopically even smaller, meaning that its overall dimension is closer to that of its microstructural length scale. In this regime, pronounced size effects emerge, manifesting as an increased structural stiffness and a differing internal stress field.

The force-displacement curves shown in Figure 3.16 further quantify these effects. Beam (a) with the smaller bending length – which can be viewed as a structure composed of more, but smaller, microstructural units – exhibits a significantly less stiff response, as expected. The magnitude of the deformation is able to reach such a high degree that the beam's deformation pattern evolves from bending to axial tension, leading to an apparent stiffening in the structural response as the test progresses. Meanwhile, beam (b) exhibits a much higher stiffness and final displacement such that its principal mode of deformation does not transition away from bending, and its mechanical response is essentially linear.

From a physical perspective, the essence of this phenomenon is that the mechanical response cannot be fully described by a classical continuum model if the characteristic structural length shrinks to approach the inherent material length scale. Instead, additional rotational degrees of freedom, couple stresses, and internal length scale-dependent material parameters become significant [21, 170]. This leads directly to the observed stiffening effect as the structural size decreases relative to the microstructure.

While this example does not test specific convergence properties or any other aspects of the numerics, it showcases micropolar theory's distinctive ability to predict size-dependent

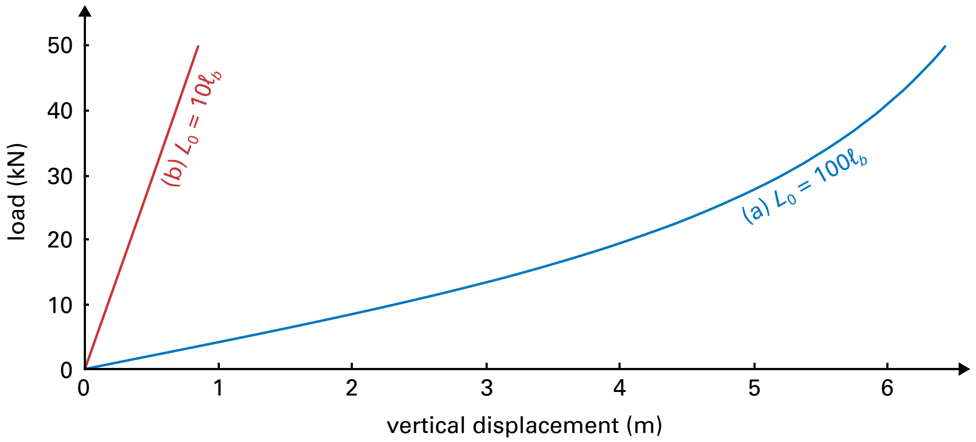

Figure 3.16: Applied end load against vertical deflection of the tip centroid for both beams.

mechanical behaviour. Although elastic size effects are difficult to measure experimentally due to the required precision in the testing apparatus – and have little consequence for strain localisation problems – this phenomenon is likely to become increasingly relevant during the perennial industrial shift towards miniaturisation. Therefore the development of robust numerical tools is essential for designing and analysing micro- to nanoscale structures where classical continuum assumptions do not suffice [193].

3.5.3 Torsion

For the moment, the model has been verified only for use in problems involving a single, static rotation axis. However, this does not limit analysis to simple planar problems; uniaxial torsion, which cannot exist in two dimensions, is one such example. This is the problem presented here, in order to test the formulation's resilience at very large rotations where the angle of twist approaches and then exceeds a whole revolution. In Section 3.4 it was explained how certain parametrisations of microrotation can lose objectivity when $\theta \approx 2\pi$, but that the quaternion formalism is a way of avoiding this problem. This example is designed to verify this property of the derived method.

With reference to Figure 3.17, consider a $5\,\mathrm{m} \times 1\,\mathrm{m} \times 1\,\mathrm{m}$ shaft acted upon by an end moment of $8\,\mathrm{GN\,m}$, applied in fifty equal increments in the same manner as to the cantilever beams in the preceding section. In other words, the total moment is divided equally among the final layer of sixty-four material points closest to the tip of the shaft. The shaft is discretised into three-dimensional cuboidal elements measuring $0.25\,\mathrm{m} \times 0.25\,\mathrm{m} \times 0.25\,\mathrm{m}$ each, occupied by 2^3 GIMPM material points, embedded within a grid measuring $5.5\,\mathrm{m} \times 1.5\,\mathrm{m} \times 1.5\,\mathrm{m}$, and ghost stabilisation is not applied. The entire root of the shift is fixed: homogeneous Dirichlet boundary conditions are applied in both translation and rotation; the tip of the shaft is totally free. The elastic constants are the same as case (b) in Section 3.5.2, viz. $\lambda = \frac{10}{3}\mathrm{MPa}$, $\mu = 5\,\mathrm{MPa}$, $\kappa = \frac{\mu}{3}$, $\alpha = 0\,\mathrm{N}$ and $\gamma = \beta = 10\,\mathrm{MN}$. They correspond to a characteristic torsion length $\ell_t = \sqrt{2}\mathrm{m}$, from

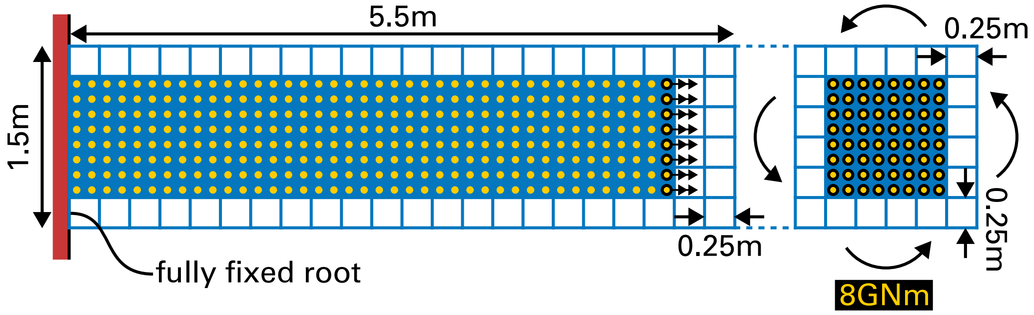

Figure 3.17: Setup of the uniaxial torsion problem, using double arrowheads to denote an applied couple with a right-hand screw rule.

(3.133).

The specimen is depicted in Figure 3.18 throughout its entire deformation at intervals of ten load steps. As the rotation occurs around a single, fixed axis (the longitudinal axis of the shaft), then the Euler microrotation vector $\boldsymbol{\theta}$ is parametrised by a single scalar: the angle of twist. Furthermore, as the axis is aligned with a coordinate direction, then two of the components of the vector should be always nil, with the angle given by the remaining component directly.[29] The value of this component at each material point is shown in Figure 3.18, computed from the quaternion using (3.171). All three components are shown scattered in Figure 3.19 for every material point as a function of its location in the fully deformed cantilever, in addition to the mean value of the rotation angle across each longitudinal layer of material points.

As the angle of twist approaches and passes through 2π (the limit of its formal definition), there is no sudden discontinuity or artefact in its deformation field visible in Figure 3.18f. This and the lack of any ill conditioning of the system implies the absence of any singularity at this point in the kinematic update procedure. The intrinsic rotation vector incrementation of the quaternion basis is therefore working as intended, and it can be concluded that the formulation is robust even for very large rotations.

But this is not to say the rotation vector singularity does not appear in the results shown. In fact it emerges in a very striking way. However, it manifests only as a result of the manner in which the rotation angle is *depicted*, rather than due to any deficiency in the formulation itself. At a complete revolution the direction of the Euler vector becomes indeterminate, because a rotation of 2π is equivalent to no rotation at all. Therefore in the region of $\theta = 2\pi$ (approximately 4 m along the shaft) the components of the vector shown in Figure 3.19 show spurious values indicating a wide array of rotation axes, when really the axis of torsion remains fixed throughout. This artefact can also be observed in Figure 3.18f, where some of the material points surrounding the point at which θ_1 jumps from 2π to -2π show completely different values instead. But beyond this problematic area – towards the shaft's tip – the solution returns to the expected result. These material points

---

[29] This angle is also an Euler angle in this special case.

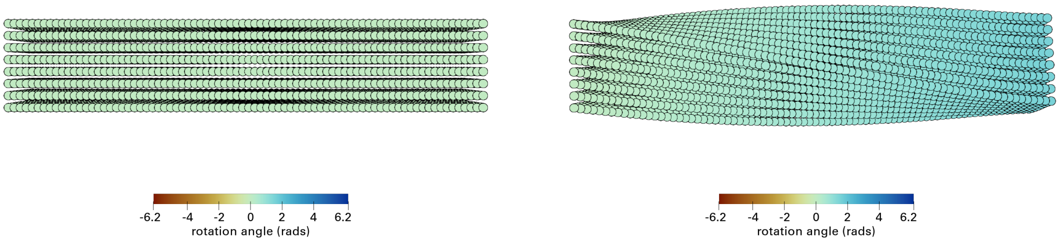

(a) initial configuration **(b)** load step 10

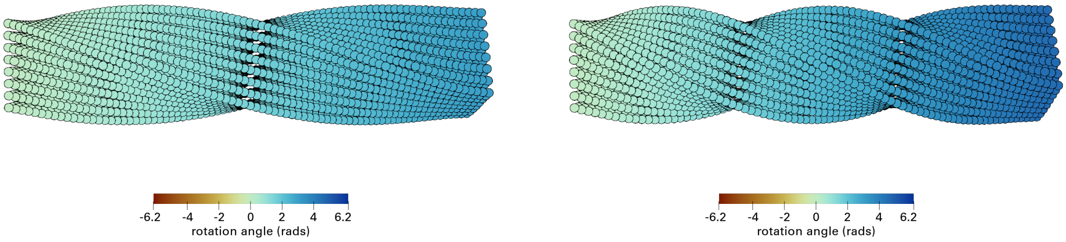

(c) load step 20 **(d)** load step 30

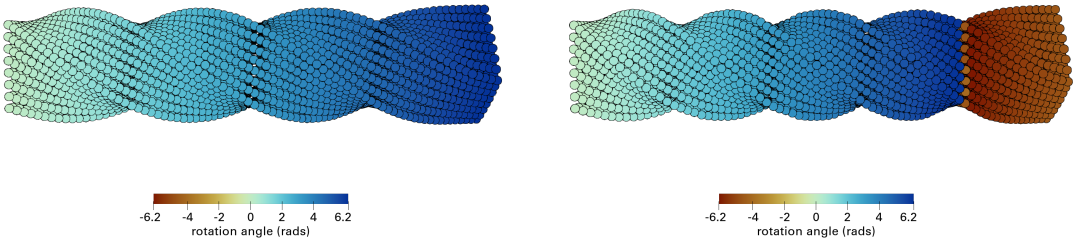

(e) load step 40 **(f)** load step 50 (final configuration)

Figure 3.18: The cantilever shaft under torsion, coloured according to the angle of micro-rotation around the shaft's longitudinal axis at each material point. These results can be observed in GIF format here.

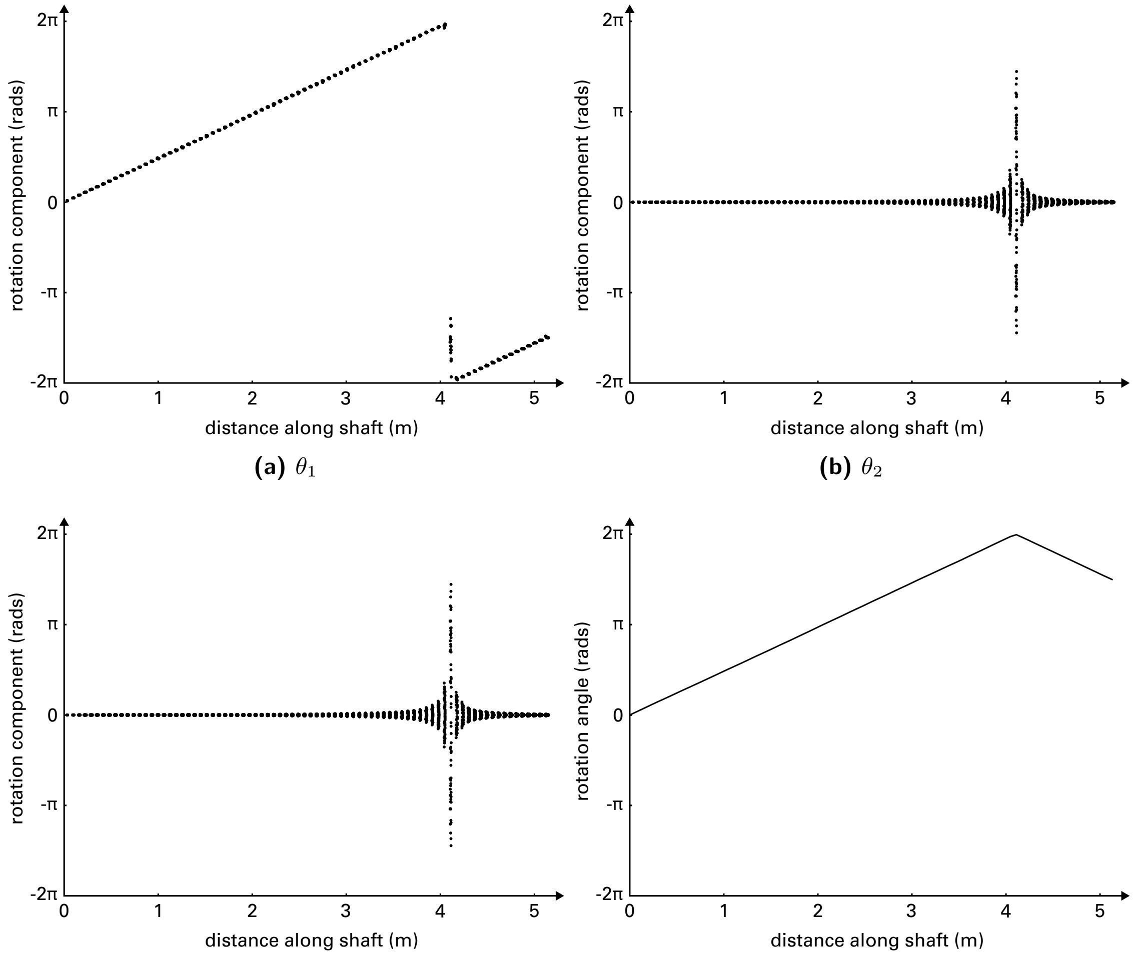

(a) θ_1 **(b)** θ_2

(c) θ_3 **(d)** θ

Figure 3.19: The vector components of $\boldsymbol{\theta}$ at each material point throughout the deformed cantilever shaft (Figure 3.18f) and the total rotation angle θ averaged over each cross section. Note that a Poynting effect has led the shaft to extend beyond its original length of 5 m.

had, in their loading history, passed through a complete revolution but clearly did not suffer any enduring numerical instability as a result. Therefore there is no problem with the underlying formulation which underpins the kinematic update algorithm and internal force and couple calculation. If, however, the formulation *had* used the Euler vector as its basis instead of quaternions, then the spurious values would be input to the model, inevitably leading to errors, instabilities and divergence away from any actual physical behaviour. But in this formulation, the Euler vector is computed as an output for graphical purposes only, and such problems are avoided.

3.5.4 Three-dimensional bending

In every numerical example presented so far the axis of rotation has remained constant. This limits the scope of the verification, because in these scenarios the rotation parameters degenerate to a single scalar which could be captured by a simple linearised version of the formulation. For the geometrically-exact model to be verified fully, it must also be tested with genuinely three-dimensional finite rotations, where the rotation axis varies both spatially and temporally. Although initially designed for classical beam analysis, the 45° curved cantilever of Bathe and Bolourchi [332] provides such a benchmark, and has previously been explored within a nonlinear micropolar context [276]. As depicted in Figure 3.20, the cantilever's central axis is constructed by subtending a 45° circular arc in the X_1–X_2 plane at a radius of $100\,\mathrm{m}$. This forms one eighth of a full circular ring. The arch has a square cross section measuring $1\,\mathrm{m} \times 1\,\mathrm{m}$, and is fully fixed (in translation and rotation) at one end, and has a uniform load of $600\,\mathrm{N}$ pulling in the X_3-direction applied in fifteen equal steps to the other end. For the closest possible comparison with the analytical results of [332], the same elastic parameters are used as derived in [276]: $\lambda = 0\,\mathrm{Pa}$, $\mu = 5\,\mathrm{MPa}$, $\kappa = 50\,501.5\,\mathrm{Pa}$, $\alpha = 0\,\mathrm{N}$, $\gamma = 12.5\,\mathrm{kN}$ and $\beta = 37.5\,\mathrm{kN}$. These correspond to $E = 10\,\mathrm{MPa}$, $\nu = 0$, $n = 0.1$, $\Psi = 1$ and $\ell_b = \ell_t = 0.05\,\mathrm{m}$. However, as Bathe and Bolourchi's original analytical solution assumes a classical nonlinear mechanical formulation, it must be emphasised that exact agreement cannot be achieved, regardless of how closely the parameters are tuned. This is due to size effects and independent microrotations in micropolar theory which are not present in classical models. Additionally, the initialisation of this problem in the MPM is not particularly straightforward, and the regularity and orthogonality of the background grid means a slightly imprecise discretisation must be employed. This is shown in Figure 3.21. A regular Cartesian background grid with hexahedral elements of dimension h^3 is generated first, and each cell is initially seeded with a set of uniformly spaced standard material points. Any points which lie outside the extremities of the curved arch are subsequently discarded to leave the final computational domain. The end loading is achieved in the same manner as the previous examples: by applying it as an equivalent set of point forces on the plane of material point closest to the free end of the cantilever. Ghost stabilisation is not applied. Figure 3.22 depicts both

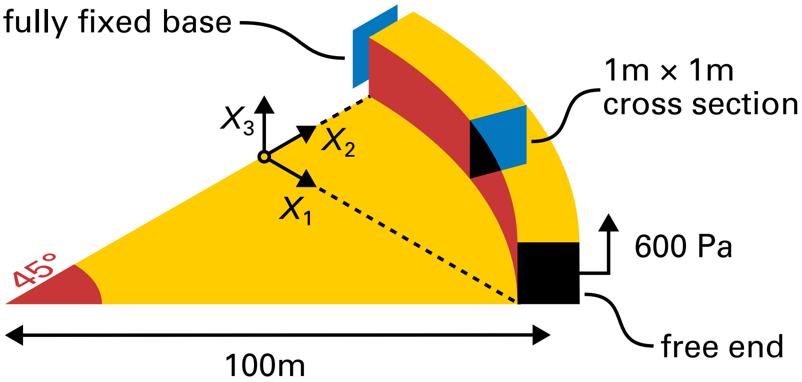

Figure 3.20: Setup of the 45° curved cantilever. The end loading of 600 Pa is distributed uniformly over the free end. Not to scale.

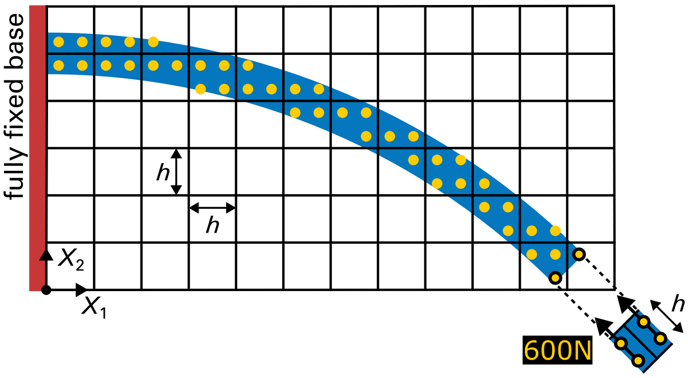

Figure 3.21: Illustrative MPM discretisation of the 45° curved cantilever with 2^3 material points per cell. The actual discretisations used in this study are of much higher resolution. Not to scale.

the undeformed and deformed configurations for the finest mesh resolution used, coloured according to the out-of-plane displacement component u_3.

To compare against the analytical predictions of [332], the displacement at the free end of the arch is computed as an average over the plane of material points nearest the tip (the same material points to which the load is applied). The classical solution cited in [276] for the beam's free end displacement is $\boldsymbol{u}^{\mathrm{T}} = [-23.30, 13.64, 53.21]\,\mathrm{m}$, which is used to compute error norms $e_{\boldsymbol{u}}$ as defined in (3.187). Figure 3.23 plots $e_{\boldsymbol{u}}$ against the inverse element size h^{-1} for three different grid refinement levels with 4^3 points per cell, as well as for an additional three different material point densities at a fixed cell size of $h = 1\,\mathrm{m}$. The results indicate an h-convergence rate between one and two, demonstrating that the present formulation can indeed handle large, three-dimensional rotations. It is reiterated here that perpetual convergence towards the 'true' solution is impossible in this study, given the necessary differences in setup and in the formulation of the model. Therefore the verisimilitude of any conclusions drawn from these results cannot be taken as absolute, so the precise convergence rate is not of significant interest. The supralinear trend alone

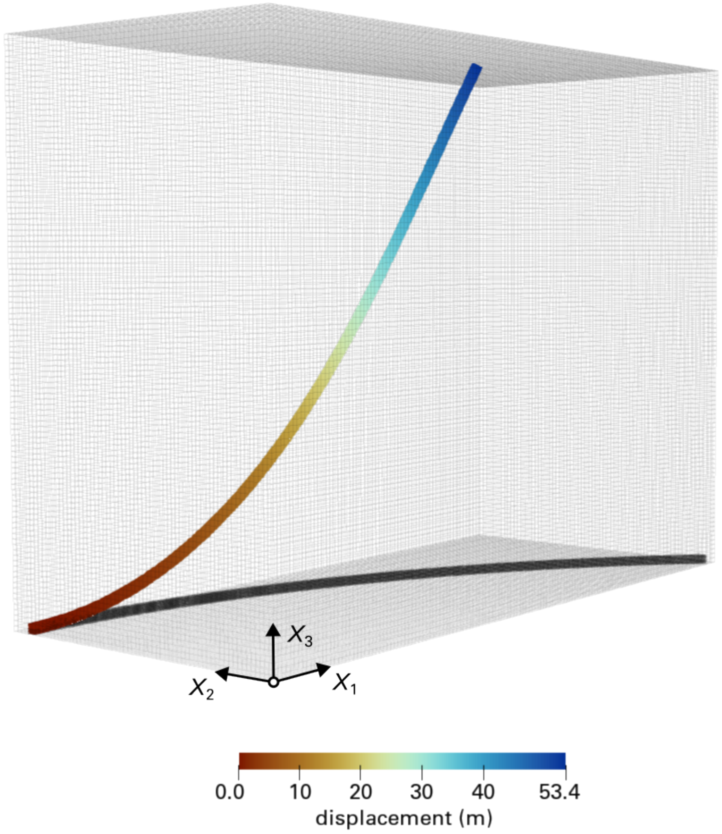

Figure 3.22: Undeformed and final configurations in the example where $h = 0.5\,\mathrm{m}$ with 4^3 material points per cell, coloured according to u_3.

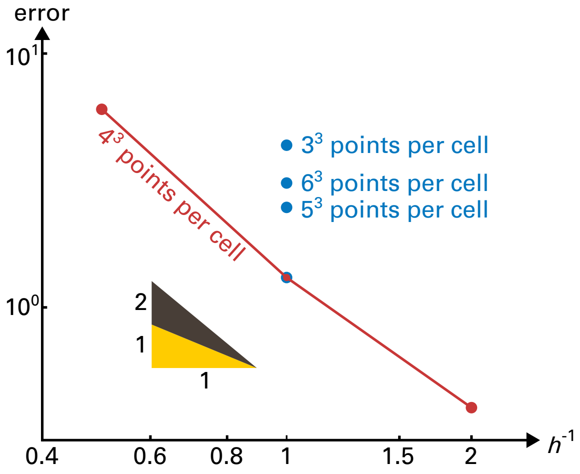

Figure 3.23: Convergence with mesh refinement and material point densification on a log-log plot.

provides a sufficient verification of the method's nonlinear finite rotation framework.

A noteworthy observation is the existence of a 'sweet spot' at 4^3 material points per cell for $h = 1\,\text{m}$. Reducing this to 3^3 significantly degrades accuracy, likely due to under-integration effects and insufficient resolution of both displacements and microrotations. Conversely, an increase to 5^3 or 6^3 does not improve accuracy either; instead, it introduces over-stiff behaviour as the density of material points per cell increases. This occurs because as integration quality improves, the scheme approaches true Gaussian quadrature and more accurately captures the system's stiffness. However, discrete numerical models inherently exhibit greater stiffness than the continuous structures they approximate, as their motion is constrained to a finite number of degrees of freedom, unlike the infinite degrees of freedom possessed by real systems. Consequently, increasing the material point density amplifies this over-stiff response. In contrast, using 4^3 material points per cell introduces some numerical under-integration, similar to reduced integration in conventional FEMs. Paradoxically, this leads to a more realistic structural response, as it mitigates excessive stiffness. Carefully selecting the material point density is therefore crucial for achieving optimal performance.

This phenomenon is explored further in [112], where this benchmark problem is used both to validate the model's three-dimensional rotational capabilities and to facilitate direct comparisons with the FEM. Interestingly, for a similar element size, the MPM produces results nearly an order of magnitude closer to the analytical solution than the equivalent FEA. As mentioned above, this is attributed to the intrinsic over-stiffness of finite elements, which is alleviated in the MPM by the effective under-integration caused by partially filled grid cells. Nevertheless, the MPM's more complex domain construction and higher computational cost at equivalent mesh resolutions remain practical considerations. For a detailed comparison, interested readers are referred to [112].

3.6 Remarks

This chapter began with a dissection of the key drivers of the instability this thesis aims to tackle: the loss of strong ellipticity brought about by strain softening. It was discussed that bifurcation occurs when the acoustic tensor becomes singular, preventing strain waves from being propagated and instead allowing deformations to localise onto an inadmissible singular plane. Further it was explained that the system can remain well posed if the continuum model includes some kind of resistance against sharp variations in plastic deformations, measured with respect to an internal length scale. This insight forms the basis of the many kinds of regularisation techniques which have been developed for strain localisation. For granular materials, micropolar theory emerged as the most suitable and rigorous candidate, chiefly because of its inclusion of independent microrotations.

In this chapter, the focus remained on a purely *elastic* variant of the micropolar framework. The simplest possible hyperelastic, geometrically-exact model was derived, establishing the fundamental kinematic, thermodynamic, and constitutive principles that will guide the forthcoming elastoplastic extension. Key aspects of the numerical implementation were also verified, notably the ability to handle large, nonlinear rotations in a smooth and objective manner. Since Chapter 4 will concentrate on modifying the constitutive model alone rather than the overall formulation, a further comprehensive suite of verification problems is unnecessary. The next chapter begins immediately with a discussion of some of the constitutive choices available in a finite strain micropolar elastoplastic formulation, before moving onto the proposed continuum model, its MPM implementation, and numerical examples.

CHAPTER 4

Micropolar elastoplasticity

Here the elastic micropolar continuum model developed in Chapter 3 is extended to include material failure within a hyperelastoplastic framework. Particular attention is given to the implementation of the elastoplastic constitutive equations, which are solved implicitly. The shear layer test from Chapter 2 is revisited, and geotechnical numerical examples are used to validate the proposed model.

4.1 Elastic-plastic split

As micropolar theory sits within a conventional continuum framework, many of the same ideas developed for classical plasticity can be used without much modification. For instance, it holds that although elastic and plastic strains usually develop concurrently, in rate-independent models their ordering does not affect the final state. One can therefore pretend that the elastic and plastic deformations are completely separated in time, and occur in series. This leads to the well-known Kröner-Lee decomposition [130,131] of the deformation gradient into multiplicative elastic and plastic components, written

$$\boldsymbol{F} = \boldsymbol{F}^{\mathrm{e}}\boldsymbol{F}^{\mathrm{p}}, \tag{2.6}$$

such that a fictitious stress-free intermediary configuration containing only plastic deformations is defined implicitly. The question then arises of how this concept might be extended to the micropolar continuum. Here two distinct schools of thought have emerged regarding the decomposition of the micropolar kinematical quantities. Steinmann [269], Bauer et al. [275], de Borst [135] and others explicitly decompose both the microrotations and the wryness/curvature tensor into elastic and plastic parts. While this presents no problems in a small-strain setting – where trivial, additive residual equations can be posed – it is impossible to find enough equations in finite strain formulations to balance the large number of unknowns. This can be overcome in principle, but only by two specific formulations of the elastoplastic residual equations which render the splits of the deformation gradient and microrotation tensors implicit, such that either the elastic or plastic *strain* can be solved for directly (rather than their two constituent components separately), thereby eliminating one set of unknowns. However, because the exact splits remain undefined, only one of the two formulations is viable in practice: the materially-framed model only delivers the *plastic* strain and not its elastic counterpart, meaning there is no way to determine the corresponding stress state. Consequently only the spatial model can be pursued – see its finite element implementation by Bauer et al. [275]. But many important quantities – such as the spatial plastic strain, the plastic microrotations and the plastic deformation gradient – are left indeterminate or implicit in this approach. Therefore although the phenomenology of this direct decomposition of the microrotations might be superficially appealing, it cannot be implemented in a way that would appear to be adequately fruitful – what is the point of making an explicit split if the split cannot be known explicitly? There is also no way to enact it in a materially-framed formulation, rendering it incompatible with the specific Saint-Venant-Kirchhoff (StV-K) constitutive model developed in Chapter 3.

An alternative is to decompose only the wryness tensor (along with the deformation gradient), leaving the orientation of the micropolar triads in the stress-free intermediate configuration undefined. There is a strong precedent for this choice in the literature [102, 270, 277, 278], resting on several arguments. Firstly, the smaller set of unknown variables introduced by this simpler split means that all elastic and plastic components can be ascertained explicitly. This provides much greater flexibility in terms of the formulation of the residual equations, and a free choice over the quantities and frame with or in which they are defined. However, this split is not taken for convenience alone; more importantly, it also corrects a phenomenological flaw. Microrotations represent *rigid* – thus non-dissipative – motions of the microstructure, and they do not possess a conjugate stress term; it is only their *gradient* that interacts with couple-stresses to dissipate energy. As in the classical continuum, where one never decomposes the displacement vector (only its gradient), attaching a dissipative mechanism to microrotations themselves would be physically unreasonable. Therefore although clear evidence of independent plastic spins of microstructural grains has been established [333], linking this phenomenon to microrotations directly is meretricious. Instead it is important to realise that particle slip is a phenomenon that occurs at the *interface* of particles, and not within them. Hence it is not their rotation per se which expends energy but their frictional *relative* motion, which is nonlocal with respect to an internal length scale corresponding to a particle diameter. As Neuner et al. write,

> for the micropolar continuum plastic material behaviour does not occur within a macroelement, but rather in between neighbouring macroelements, and

> consquently, inelastic material behaviour is observed in the gradient of the [microrotation] field [278].

While this argument has been rationalised in terms of concrete-type materials, it is equally valid in the context of purely granular media. It simply means that any significant post-failure, seemingly 'plastic' microrotations follow solely from plastic wryness flow. Sansour [270] further argues that because microrotations are a fundamental kinematic variable underpinning the configuration space, they cannot be decomposed directly. Instead they provide a definition of the space itself, and as such cannot be seen as either 'elastic' or 'plastic' – concepts they transcend.

Therefore it only remains to determine how to decompose the wryness tensor. In the literature, the universal approach is to take an additive split, i.e.

$$\boldsymbol{\Gamma} = \boldsymbol{\Gamma}^{\mathrm{e}} + \boldsymbol{\Gamma}^{\mathrm{p}}. \tag{4.1}$$

This is because wryness does not possess a multiplicative structure; instead, as demonstrated by (3.185), it is innately additive. This is also substantiated by Sansour [270], who reasoned that an additive split is appropriate due to the tensor's composition from three independent vectors (see (3.42)) all defined in the reference configuration. And besides, as a higher-order quantity, wryness does not require the same rigorous treatment as the deformation gradient anyway, which is itself only a first-order mapping:

$$\mathrm{d}\boldsymbol{x} = \boldsymbol{F}\,\mathrm{d}\boldsymbol{X} + \boldsymbol{\mathcal{O}}(||\,\mathrm{d}\boldsymbol{X}||^2) \tag{4.2}$$

and the microrotation tensor, as a constituent component of $\boldsymbol{F}$, is of the same order. The wryness tensor, as the *gradient* of the microrotation, is therefore a second-order quantity, so an additive split is completely acceptable – regardless of the above reasoning – for the same order of accuracy to be preserved.

Although this particular choice of elastic-plastic split introduces nuances in terms of the exact configuration (fictitious or otherwise) in which the various quantities are defined, as long as thermodynamic consistency is achieved there are no consequences for the general validity of the model – see the discussion in [212, 278]. Therefore one can rewrite the material stretch tensor $\boldsymbol{U}$ as

$$\boldsymbol{U} = \boldsymbol{Q}^{\mathrm{T}}\boldsymbol{F} = \boldsymbol{Q}^{\mathrm{T}}\boldsymbol{F}^{\mathrm{e}}\boldsymbol{F}^{p} \tag{4.3}$$

to produce a natural expression for the elastic material stretch

$$\boldsymbol{U}^{\mathrm{e}} = \boldsymbol{Q}^{\mathrm{T}}\boldsymbol{F}^{\mathrm{e}} = \boldsymbol{U}(\boldsymbol{F}^{p})^{-1} \tag{4.4}$$

and strain

$$\boldsymbol{E}^{\mathrm{e}} = \boldsymbol{U}^{\mathrm{e}} - \boldsymbol{I}. \tag{4.5}$$

These quantities are defined between the reference and stress-free configurations, whereas the elastic and plastic wryness tensors both remain defined in the material frame. An alternative, consistently-framed split was proposed in [278], but this is not pursued here in order to avoid potentially supererogatory complication of what is already admittedly a cumbersome constitutive model.

4.2 Continuum formulation

A complete formulation is not provided here; the continuum model from Chapter 3 is simply extended by introducing elastic-plastic splits to the relevant quantities, and deriving hence. The entire framework follows the same thermodynamical methodology laid out for the hyperelastic model, culminating in constitutive equations which include a set of plastic flow rules describing the inelastic evolution of the strain and wryness.

4.2.1 Deformation rates

As in classical mechanics, the Kröner-Lee decomposition (2.6) leads to an additive split of the velocity gradient

$$\begin{aligned}\boldsymbol{l} &= \dot{\boldsymbol{F}}\boldsymbol{F}^{-1} && (4.6)\\ &= \left(\dot{\boldsymbol{F}}^{\mathrm{e}}\boldsymbol{F}^{\mathrm{p}} + \boldsymbol{F}^{\mathrm{e}}\dot{\boldsymbol{F}}^{\mathrm{p}}\right)(\boldsymbol{F}^{\mathrm{p}})^{-1}(\boldsymbol{F}^{\mathrm{e}})^{-1} && (4.7)\\ &= \boldsymbol{l}^{\mathrm{e}} + \boldsymbol{F}^{\mathrm{e}}\boldsymbol{l}^{\mathrm{p}}(\boldsymbol{F}^{\mathrm{e}})^{-1}, && (4.8)\end{aligned}$$

where $\boldsymbol{l}^{\mathrm{e}} = \dot{\boldsymbol{F}}^{\mathrm{e}}(\boldsymbol{F}^{\mathrm{e}})^{-1}$ and, likewise, $\boldsymbol{l}^{\mathrm{p}} = \dot{\boldsymbol{F}}^{\mathrm{p}}(\boldsymbol{F}^{\mathrm{p}})^{-1}$. The micropolar spin $\boldsymbol{\Omega}$ remains unchanged, so the spatial deformation rate becomes

$$\begin{aligned}\boldsymbol{d} &= \boldsymbol{l} - \boldsymbol{\Omega} && (4.9)\\ &= \boldsymbol{l}^{\mathrm{e}} + \boldsymbol{F}^{\mathrm{e}}\boldsymbol{l}^{\mathrm{p}}(\boldsymbol{F}^{\mathrm{e}})^{-1} - \dot{\boldsymbol{Q}}\boldsymbol{Q}^{\mathrm{T}} && (4.10)\\ &= \boldsymbol{Q}\dot{\boldsymbol{E}}^{\mathrm{e}}(\boldsymbol{F}^{\mathrm{e}})^{-1} + \boldsymbol{F}^{\mathrm{e}}\boldsymbol{l}^{\mathrm{p}}(\boldsymbol{F}^{\mathrm{e}})^{-1} && (4.11)\end{aligned}$$

since $\dot{\boldsymbol{E}}^{\mathrm{e}} = \dot{\overline{\boldsymbol{Q}^{\mathrm{T}}}}\boldsymbol{F}^{\mathrm{e}} + \boldsymbol{Q}^{\mathrm{T}}\dot{\boldsymbol{F}}^{\mathrm{e}}$. As for the spatial micropolar gyration gradient $\boldsymbol{e}$, the time derivative of (4.1) means that

$$\boldsymbol{e} = \boldsymbol{Q}\dot{\boldsymbol{\Gamma}}\boldsymbol{F}^{-1} = \boldsymbol{Q}\left(\dot{\boldsymbol{\Gamma}}^{\mathrm{e}} + \dot{\boldsymbol{\Gamma}}^{\mathrm{p}}\right)\boldsymbol{F}^{-1}. \tag{4.12}$$

4.2.2 Hyperelastoplastic thermodynamical setting

Recall from Section 3.3.6 the general forms of the first

$$\rho_0\dot{e} = \boldsymbol{\tau} : \boldsymbol{d} + \boldsymbol{\nu} : \boldsymbol{e} + \rho_0 r - J\nabla\cdot\boldsymbol{h} \tag{3.86}$$

and second

$$\rho_0 \dot{s} \geq \frac{\rho_0 r}{T} - \frac{J\nabla \cdot \boldsymbol{h}}{T} \tag{3.87}$$

laws of thermodynamics phrased in terms of local continuum quantities. The continuum is again assumed to be isothermal, which eliminates the heat source r and flux $\boldsymbol{h}$ and means $\dot{T} = 0$. However, unlike in an elastic body, entropy s cannot now be assumed to remain constant; in hyperplasticity entropy production is the thermodynamically-sound mechanism through which plastic dissipation is allowed to occur. Therefore the above laws reduce to

$$\rho_0 \dot{e} = \boldsymbol{\tau} : \boldsymbol{d} + \boldsymbol{\nu} : \boldsymbol{e} \tag{4.13}$$

and

$$\rho_0 T\dot{s} \geq 0 \tag{4.14}$$

respectively. Here, the Helmholtz free energy function W is reintroduced

$$W = e - Ts \tag{3.88}$$

alongside its time derivative $\dot{W}$ such that

$$\dot{e} = \dot{W} + \dot{T}s + T\dot{s} = \dot{W} + T\dot{s}. \tag{4.15}$$

Substituting this into (4.13) and combining with (4.14) produces

$$\rho_0 T\dot{s} = \boldsymbol{\tau} : \boldsymbol{d} + \boldsymbol{\nu} : \boldsymbol{e} - \rho_0 \dot{W} \geq 0 \tag{4.16}$$

which is otherwise known as the *Clausius-Duhem* (or *dissipation*) inequality.[1]

While structural softening can arise solely from the use non-associated flow rules alone (see Section 2.4 and Section 3.1.1), this formulation retains the possibility of internal hardening and softening at the material point level. However, only linear and isotropic hardening are considered – the simplest possible case. Therefore the free energy of the system is split into an elastic part W^{e} which, as with the elastic formulation, is attached solely to the amount of (elastic) deformation which has developed in it, and a plastic part W^{p} which quantifies contributions from hardening. This is written

$$W = W^{\mathrm{e}}(\boldsymbol{E}^{\mathrm{e}}, \boldsymbol{\Gamma}^{\mathrm{e}}) + W^{\mathrm{p}}(\chi), \tag{4.17}$$

where χ is an internal hardening variable conjugate to a thermodynamical hardening force $\Lambda = H\chi$, and H is a constitutive parameter determining the degree of hardening (if

---

[1] Actually this form of the inequality, i.e. ignoring heat effects, is strictly called the *Clausius-Planck* inequality.

positive) or softening (if negative). This means that

$$\dot{W} = \frac{\partial W^{\mathrm{e}}}{\partial \boldsymbol{E}^{\mathrm{e}}} : \dot{\boldsymbol{E}}^{\mathrm{e}} + \frac{\partial W^{\mathrm{e}}}{\partial \boldsymbol{\Gamma}^{\mathrm{e}}} : \dot{\boldsymbol{\Gamma}}^{\mathrm{e}} + \frac{\partial W^{\mathrm{p}}}{\partial \chi} \dot{\chi}, \tag{4.18}$$

which can be substituted along with (4.11) and (4.12) into the Clausius-Duhem inequality (4.16) to yield

$$\begin{aligned}
\rho_0 T \dot{s} = {} & \boldsymbol{\tau} : \left(\boldsymbol{Q} \dot{\boldsymbol{E}}^{\mathrm{e}} (\boldsymbol{F}^{\mathrm{e}})^{-1} + \boldsymbol{F}^{\mathrm{e}} \boldsymbol{l}^{\mathrm{p}} (\boldsymbol{F}^{\mathrm{e}})^{-1} \right) + \boldsymbol{\nu} : \left(\boldsymbol{Q} \left(\dot{\boldsymbol{\Gamma}}^{\mathrm{e}} + \dot{\boldsymbol{\Gamma}}^{\mathrm{p}} \right) \boldsymbol{F}^{-1} \right) \\
& - \rho_0 \left(\frac{\partial W^{\mathrm{e}}}{\partial \boldsymbol{E}^{\mathrm{e}}} : \dot{\boldsymbol{E}}^{\mathrm{e}} + \frac{\partial W^{\mathrm{e}}}{\partial \boldsymbol{\Gamma}^{\mathrm{e}}} : \dot{\boldsymbol{\Gamma}}^{\mathrm{e}} + \frac{\partial W^{\mathrm{p}}}{\partial \chi} \dot{\chi} \right) \qquad (4.19) \\
= {} & \boldsymbol{Q}^{\mathrm{T}} \boldsymbol{\tau} (\boldsymbol{F}^{\mathrm{e}})^{-\mathrm{T}} : \dot{\boldsymbol{E}}^{\mathrm{e}} + \boldsymbol{Q}^{\mathrm{T}} \boldsymbol{\nu} \boldsymbol{F}^{-1} : \dot{\boldsymbol{\Gamma}}^{\mathrm{e}} + \boldsymbol{\tau} : \boldsymbol{F}^{\mathrm{e}} \boldsymbol{l}^{\mathrm{p}} (\boldsymbol{F}^{\mathrm{e}})^{-1} \\
& + \boldsymbol{\nu} : \boldsymbol{Q} \dot{\boldsymbol{\Gamma}}^{\mathrm{p}} \boldsymbol{F}^{-1} - \rho_0 \frac{\partial W^{\mathrm{e}}}{\partial \boldsymbol{E}^{\mathrm{e}}} : \dot{\boldsymbol{E}}^{\mathrm{e}} - \rho_0 \frac{\partial W^{\mathrm{e}}}{\partial \boldsymbol{\Gamma}^{\mathrm{e}}} : \dot{\boldsymbol{\Gamma}}^{\mathrm{e}} - \rho_0 \frac{\partial W^{\mathrm{p}}}{\partial \chi} \dot{\chi} \geq 0. \qquad (4.20)
\end{aligned}$$

As set out in the Coleman-Noll procedure [295], the inequality must hold, i.e. dissipation occurs, regardless of the level or rate of elastic loading, so

$$\rho_0 \frac{\partial W^{\mathrm{e}}}{\partial \boldsymbol{E}^{\mathrm{e}}} = \boldsymbol{Q}^{\mathrm{T}} \boldsymbol{\tau} (\boldsymbol{F}^{\mathrm{e}})^{-\mathrm{T}} = \boldsymbol{B} \tag{4.21}$$

and

$$\rho_0 \frac{\partial W^{\mathrm{e}}}{\partial \boldsymbol{\Gamma}^{\mathrm{e}}} = \boldsymbol{Q}^{\mathrm{T}} \boldsymbol{\nu} \boldsymbol{F}^{-\mathrm{T}} = \boldsymbol{S}, \tag{4.22}$$

leaving

$$\boldsymbol{\tau} : \boldsymbol{F}^{\mathrm{e}} \boldsymbol{l}^{\mathrm{p}} (\boldsymbol{F}^{\mathrm{e}})^{-1} + \boldsymbol{\nu} : \boldsymbol{Q} \dot{\boldsymbol{\Gamma}}^{\mathrm{p}} \boldsymbol{F}^{-1} - \rho_0 \frac{\partial W^{\mathrm{p}}}{\partial \chi} \dot{\chi} \geq 0. \tag{4.23}$$

This is the final reduced form of the Clausius-Duhem inequality, which directly generates the plastic flow rules constrained by certain consistency conditions in relation to a yield function f and flow potential g.

4.2.3 Constitutive equations

There is no change in the elastic component of the constitutive model, which remains StV-K. Therefore the same fourth-order elastic constitutive tensors are used to determine the Biot stress $\boldsymbol{B}$ and couple-stress $\boldsymbol{S}$ from the elastic strain and wryness measures respectively, i.e.

$$\boldsymbol{B} = \boldsymbol{D} : \boldsymbol{E}^{\mathrm{e}} \tag{4.24}$$

and

$$\boldsymbol{S} = \check{\boldsymbol{D}} : \boldsymbol{\Gamma}^{\mathrm{e}}. \tag{4.25}$$

The push-forward operation differs slightly, but only for the Cauchy stress which, following (4.21), is now

$$\boldsymbol{\sigma} = J^{-1} \boldsymbol{Q} \boldsymbol{B} (\boldsymbol{F}^{\mathrm{e}})^{\mathrm{T}} \tag{4.26}$$

and, for completeness,

$$\boldsymbol{\mu} = J^{-1}\boldsymbol{Q}\boldsymbol{S}\boldsymbol{F}^{\mathrm{T}} \tag{4.27}$$

is the Cauchy couple-stress which retains its prior definition.

As for the equations governing the evolution of plastic deformation, certain constitutive assumptions must be made first. In particular, plastic flow must occur with respect to a potential which preserves non-negativity of the dissipation statement (4.23). In associative plasticity models, where the flow potential coincides with the yield function, this is accomplished through their automatic enforcement of the principle of maximum plastic dissipation. This is a consequence of Drucker's postulate (recall (3.4)) which demands that the plastic strain rate be maximised, subject to the yield constraints. In other words, among all admissible plastic strain increments that do not violate the yield surface, the actual increment is the one that maximises the plastic work. Assuming the yield surface is convex in stress space, this increment must therefore take place in a direction which is normal to the yield surface, or

$$\dot{\boldsymbol{\varepsilon}}^{\mathrm{p}} \propto \frac{\partial f}{\partial \boldsymbol{\sigma}} \tag{4.28}$$

for a linearised classical continuum. This is a standard result of associative plasticity also known as the normality rule [149]. However, plastic dissipation obviously does not have to be maximised for it to be non-negative or for (4.23) to be fulfilled. This is fortuitous, as non-associated flow rules which violate Drucker's postulate are the subject of this thesis. Instead, it is simply incumbent to prove that, for the particular flow potential $g \neq f$, a non-negative amount of plastic work is predicted for all stress states lying on the yield surface $f = 0$. This is an arduous process, and is usually neglected by positing that thermodynamic consistency is still achieved by simply selecting g to be equivalent to f in *shape*, but defined according to a more conservative set of material parameters [334]. This reasoning is invoked here to define a flow potential which differs from the yield function only in that it employs the dilatancy angle $\psi \geq 0$ in place of the internal friction angle $\phi \geq \psi$, to better approximate the real behaviour of geomaterials [127, 150]. Therefore the flow rules satisfying (4.23) are

$$\boldsymbol{F}^{\mathrm{e}}\boldsymbol{l}^{\mathrm{p}}(\boldsymbol{F}^{\mathrm{e}})^{-1} = \dot{\gamma}^{\mathrm{p}}\frac{\partial g}{\partial \boldsymbol{\tau}}, \tag{4.29}$$

$$\boldsymbol{Q}\dot{\boldsymbol{\Gamma}}^{\mathrm{p}}\boldsymbol{F}^{-1} = \dot{\gamma}^{\mathrm{p}}\frac{\partial g}{\partial \boldsymbol{\nu}} \tag{4.30}$$

and

$$\dot{\chi} = -\dot{\gamma}^{\mathrm{p}}\frac{\partial g}{\partial \Lambda} \tag{4.31}$$

where $g = g(\boldsymbol{\tau}, \boldsymbol{\nu})$ is a convex scalar-valued function and $\dot{\gamma}^{\mathrm{p}}$ is the plastic multiplier, subject to the KKT conditions

$$f \leq 0, \qquad \dot{\gamma}^{\mathrm{p}} \geq 0, \qquad f\dot{\gamma}^{\mathrm{p}} = 0. \tag{3.9}$$

4.2.4 Yield function and plastic potential

Classically, yield functions are defined according to *invariants* of the stress tensor. This is because yielding in isotropic media occurs irrespective of the orientation of the system. For instance, the von Mises yield function is written

$$f = \sqrt{3J_2} - (k + \Lambda) \tag{4.32}$$

in which $J_2 = \frac{1}{2}\boldsymbol{s} : \boldsymbol{s}$ is the second invariant of the Kirchhoff stress deviator $\boldsymbol{s} = \boldsymbol{\tau} - p\boldsymbol{I}$, where $p = \frac{1}{3}\mathrm{tr}(\boldsymbol{\tau})$ is the hydrostatic pressure, and k is the initial yield limit. By depending on J_2 alone, the onset of plasticity occurs only as a result of shearing and is independent of the hydrostatic component of the stress, making it applicable to ductile materials like metals. The Drucker-Prager yield condition generalises (4.32) by explicitly introducing a pressure term, rendering it suitable for frictional (i.e. pressure-sensitive) materials such as drained geomaterials. It is written

$$f = \sqrt{3J_2} + \alpha^{\mathrm{DP}} p - (k + \Lambda) \tag{4.39}$$

where α^{DP} is a frictional coefficient which controls the degree of pressure dependency. The corresponding plastic potential function which is commonly paired with this yield criterion differs only in that the hydrostatic pressure coefficient is instead a dilatancy factor β^{DP}, to capture more realistic volumetric behaviour. That is,

$$g = \sqrt{3J_2} + \beta^{\mathrm{DP}} p - \Lambda \tag{4.33}$$

where the constant k has also been removed, as only the gradient of g is ever used in practice. The formulae for the two parameters α^{DP} and β^{DP} are

$$\alpha^{\mathrm{DP}} = \frac{6\sin\phi}{3 - \sin\phi} \tag{4.34}$$

and

$$\beta^{\mathrm{DP}} = \frac{6\sin\psi}{3 - \sin\psi}. \tag{4.35}$$

Additionally, k is related to the cohesion c of the material through

$$k = \frac{6c\cos\phi}{3 - \sin\phi}, \tag{4.36}$$

i.e. the more cohesive a material is, the more tensile loading it can resist before yielding. The particular form of these three relationships means that, in this case, the Drucker-Prager yield surface is a smooth cone circumscribing the equivalent (but non-smooth) Mohr-Coulomb yield surface in principal stress space. A depiction of f, g and the material parameters ϕ, ψ and k is given in Figure 4.1.

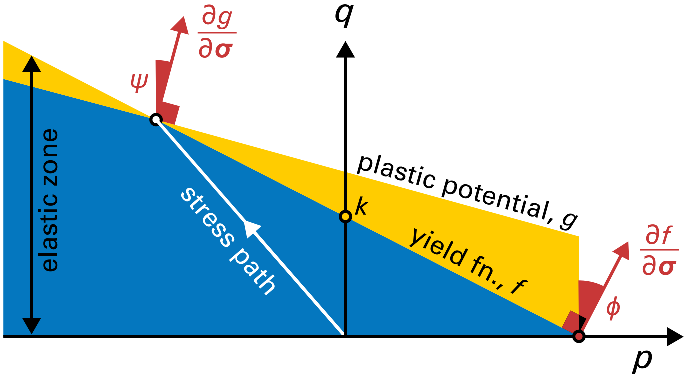

Figure 4.1: A non-associated Drucker-Prager yield criterion f and plastic potential function g in p–q space, where p is the hydrostatic pressure and q is the von Mises stress. Plastic flow occurs normal to the plastic potential function, and not the yield function itself.

To adapt such well-established models of classical plasticity to the micropolar continuum, the usual approach is to supplant the von Mises stress $\sqrt{3J_2}$ with a generalised quantity q which also includes couples [27, 135, 269, 275, 335–337]. This is because, like shear stresses, couple-stresses are intrinsically distortive in nature. The use of a generalised stress invariant means that yielding is described by a single, unified yield surface which takes into account the combined effect of both the conventional stress and the couple-stress. First, the deviatoric stress is adapted to remove the skew-symmetric component of the micropolar Kirchhoff stress, expressed

$$\boldsymbol{s} = \mathrm{sym}(\boldsymbol{\tau}) - p\boldsymbol{I}. \tag{4.37}$$

This leads to the equivalent von Mises stress

$$q = \sqrt{\frac{3}{2}\left(\boldsymbol{s} : \boldsymbol{s} + \frac{1}{(\ell^{\mathrm{P}})^2}\boldsymbol{\nu} : \boldsymbol{\nu}\right)}, \tag{4.38}$$

where ℓ^{P} is a plastic characteristic length, such that

$$f = q + \alpha^{\mathrm{DP}} p - (k + \Lambda) \tag{4.39}$$

and

$$g = q + \beta^{\mathrm{DP}} p - \Lambda. \tag{4.40}$$

Although further coefficients and terms are sometimes introduced, particularly when analysing plane problems (e.g. [135, 143, 333, 338]), the form of the generalised invariant q given above reduces to the classical von Mises stress in the case of vanishing couple-stresses and is therefore a perfectly reasonable choice. It also coincides with the form given in [269, 278], and the one used (but not consistently written) in [275].

4.3 Numerical implementation

The numerical evolution of the elastoplastic constitutive equations is considered through use of an operator split, where an elastic trial state is posed and, if necessary, returned to the yield surface by a plastic mapping. That is, the kinematic increments from the previously converged state suggested by each Newton-Raphson iteration are always presumed to be entirely elastic. If this leads to a stress state lying within the yield surface (i.e. $f < 0$) then $\dot{\gamma}^{\mathrm{p}} = 0$ and no further action must be taken. The ansatz is accepted and the nonlinear solver may proceed. On the other hand, if the yield limit has indeed been exceeded, then plastic flow must occur in accordance with the elastoplastic constitutive equations developed above. In this formulation these are resolved with an additional implicit nonlinear solution algorithm, which takes place at the material point level within each global Newton-Raphson step. This section follows the discretisation and integration of the flow rules in pseudo-time, which allow for the construction of elastoplastic residual equations which are minimised to determine the local constitutive state. The constitutive model is then inserted into the wider numerical scheme developed in Chapter 3, with the addition of tracking history-dependent material quantities.

4.3.1 Elastic trial state

A load step begins with quantities determined by the global Newton-Raphson search in the previous load step, denoted $\widetilde{(\bullet)}$. The solver in iteration K within the load step proposes new total values for the kinematic variables such that an increment in the deformation gradient is written

$$\Delta \boldsymbol{F}_K = \boldsymbol{F}_K \widetilde{\boldsymbol{F}}^{-1}. \tag{4.41}$$

The elastic trial strain is produced by assuming that this increment is entirely elastic, i.e. that

$$(\boldsymbol{F}^{\mathrm{e}})^{\mathrm{tr}} = \Delta \boldsymbol{F}_K \widetilde{\boldsymbol{F}^{\mathrm{e}}} = \boldsymbol{F}_K \widetilde{\boldsymbol{F}^{\mathrm{p}}}^{-1} \tag{4.42}$$

so

$$(\boldsymbol{E}^{\mathrm{e}})^{\mathrm{tr}} = \boldsymbol{Q}^{\mathrm{T}} (\boldsymbol{F}^{\mathrm{e}})^{\mathrm{tr}} - \boldsymbol{I}, \tag{4.43}$$

where $(\bullet)^{\mathrm{tr}}$ refers to the trial state in iteration K. Similarly, the trial elastic wryness is simply the difference between the proposed total wryness tensor $\boldsymbol{\Gamma}_K$ and the last converged plastic wryness, written

$$(\boldsymbol{\Gamma}^{\mathrm{e}})^{\mathrm{tr}} = \boldsymbol{\Gamma}_K - \widetilde{\boldsymbol{\Gamma}^{\mathrm{p}}}. \tag{4.44}$$

Furthermore, as no further plastic flow is presumed to take place, the trial hardening parameter simply carries over from the previous load step, i.e.

$$\chi^{\mathrm{tr}} = \widetilde{\chi}. \tag{4.45}$$

The trial measures are then used to determine a corresponding stress state. If this stress state exceeds the yield surface (by some small user-defined tolerance, in practice), then the plastic flow rules are invoked to produce an admissible constitutive state. This process is known as the *plastic corrector*, and while several methods have been developed for classical plasticity, a generalised backward Euler scheme is employed here [124]. This is chiefly because, as an implicit algorithm, it offers accuracy and stability even for large time steps, whereas explicit techniques (even advanced schemes e.g. Runge-Kutta with error control) do not guarantee an admissible constitutive state at the end of the step [339]. Furthermore, many of the less generalised methods – particularly those with geometrical motivations like radial return mappings – do not possess sufficient flexibility to admit non-associated flow rules and generalised stress invariants at finite strains.

4.3.2 Plastic flow rules

Henceforth the subscript $(\bullet)_K$ is neglected for notational convenience. The first flow rule (4.29) can be rewritten as

$$\dot{\boldsymbol{F}}^{\mathrm{p}} = \dot{\gamma}^{\mathrm{p}} \boldsymbol{F}^{\mathrm{p}} \boldsymbol{F}^{-1} \frac{\partial g}{\partial \boldsymbol{\tau}} \boldsymbol{F} \tag{4.46}$$

which may be discretised by means of an exponential map [124] to make

$$\boldsymbol{F}^{\mathrm{p}} = \widetilde{\boldsymbol{F}^{\mathrm{p}}} \exp\left(\Delta\gamma^{\mathrm{p}} \boldsymbol{F}^{-1} \frac{\partial g}{\partial \boldsymbol{\tau}} \boldsymbol{F}\right) = \widetilde{\boldsymbol{F}^{\mathrm{p}}} \boldsymbol{F}^{-1} \exp\left(\Delta\gamma^{\mathrm{p}} \frac{\partial g}{\partial \boldsymbol{\tau}}\right) \boldsymbol{F}. \tag{4.47}$$

Given that $\boldsymbol{U}^{\mathrm{e}} = \boldsymbol{Q}^{\mathrm{T}} \boldsymbol{F} (\boldsymbol{F}^{\mathrm{p}})^{-1}$ and $(\boldsymbol{F}^{\mathrm{e}})^{\mathrm{tr}} = \boldsymbol{F} \widetilde{\boldsymbol{F}^{\mathrm{p}}}^{-1}$, this expression is equivalently

$$\boldsymbol{U}^{\mathrm{e}} = \boldsymbol{Q}^{\mathrm{T}} \exp\left(-\Delta\gamma^{\mathrm{p}} \frac{\partial g}{\partial \boldsymbol{\tau}}\right) (\boldsymbol{F}^{\mathrm{e}})^{\mathrm{tr}}. \tag{4.48}$$

The exponential term can be computed by taking an infinite series according to (3.28), or by its eigendecomposition – see e.g. [124]. As for the plastic wryness flow, (4.30) becomes

$$\Delta\boldsymbol{\Gamma}^{\mathrm{p}} = \Delta\gamma^{\mathrm{p}} \boldsymbol{Q}^{\mathrm{T}} \frac{\partial g}{\partial \boldsymbol{\nu}} \boldsymbol{F} \tag{4.49}$$

so that, following (4.1),

$$\begin{aligned} \boldsymbol{\Gamma} &= \boldsymbol{\Gamma}^{\mathrm{e}} + \left(\widetilde{\boldsymbol{\Gamma}^{\mathrm{p}}} + \Delta\boldsymbol{\Gamma}^{\mathrm{p}}\right) && (4.50) \\ &= \boldsymbol{\Gamma}^{\mathrm{e}} + \widetilde{\boldsymbol{\Gamma}^{\mathrm{p}}} + \Delta\gamma^{\mathrm{p}} \boldsymbol{Q}^{\mathrm{T}} \frac{\partial g}{\partial \boldsymbol{\nu}} \boldsymbol{F}. && (4.51) \end{aligned}$$

Alternatively, as the plastic wryness increment is also the difference between the trial elastic wryness and its final value, it may be expressed

$$(\boldsymbol{\Gamma}^{\mathrm{e}})^{\mathrm{tr}} = \boldsymbol{\Gamma}^{\mathrm{e}} + \Delta\gamma^{\mathrm{p}} \boldsymbol{Q}^{\mathrm{T}} \frac{\partial g}{\partial \boldsymbol{\nu}} \boldsymbol{F}. \tag{4.52}$$

Thirdly, the hardening flow rule is simply

$$\chi = \widetilde{\chi} - \Delta\gamma^{\mathrm{p}} \frac{\partial g}{\partial \Lambda}. \tag{4.53}$$

As derived in Appendix B, the flow vectors are

$$\frac{\partial g}{\partial \boldsymbol{\tau}} = \frac{3\boldsymbol{s}}{2q} + \frac{1}{3}\beta^{\mathrm{DP}}\boldsymbol{I}, \tag{4.54}$$

which is symmetric,

$$\frac{\partial g}{\partial \boldsymbol{\nu}} = \frac{3\boldsymbol{\nu}}{2(\ell^{\mathrm{p}})^2 q}, \tag{4.55}$$

and

$$\frac{\partial g}{\partial \Lambda} = -1. \tag{4.56}$$

Along with the yield function itself, the discretised flow rules are rearranged to form residual equations which are solved numerically.

4.3.3 Solution of the local nonlinear problem

In total four residual equations are posed, viz.

$$\begin{aligned}
\boldsymbol{r}^{U} &= \boldsymbol{U}^{\mathrm{e}} - \boldsymbol{Q}^{\mathrm{T}} \exp\left(-\Delta\gamma^{\mathrm{p}} \frac{\partial g}{\partial \boldsymbol{\tau}}\right) (\boldsymbol{F}^{\mathrm{e}})^{\mathrm{tr}} = \boldsymbol{0} && (4.57)\\
\boldsymbol{r}^{\Gamma} &= \boldsymbol{\Gamma}^{\mathrm{e}} + \Delta\gamma^{\mathrm{p}} \boldsymbol{Q}^{\mathrm{T}} \frac{\partial g}{\partial \boldsymbol{\nu}} \boldsymbol{F} - (\boldsymbol{\Gamma}^{\mathrm{e}})^{\mathrm{tr}} = \boldsymbol{0} && (4.58)\\
r^{\chi} &= \chi - \widetilde{\chi} - \Delta\gamma^{\mathrm{p}} = 0 && (4.59)\\
f &= 0, && (4.60)
\end{aligned}$$

where an admissible constitutive state is only achieved when all equations are equal to zero, i.e. at convergence. The specific form of (4.60) depends on the yield function and hardening rule chosen to represent the particular material to be modelled. In this work, for instance, a Drucker-Prager failure criterion is employed in conjunction with linear isotropic hardening, so

$$f = q - \alpha^{\mathrm{DP}} p - (k + \Lambda). \tag{4.39}$$

The solution of the four nonlinear residual equations takes place simultaneously, by iteratively linearising them with respect to a set of unknowns $\boldsymbol{\mathcal{X}}$, which here are selected to be the elastic stretch $\boldsymbol{U}^{\mathrm{e}}$, the elastic wryness $\boldsymbol{\Gamma}^{\mathrm{e}}$, the internal hardening variable χ and the plastic multiplier $\Delta\gamma^{\mathrm{p}}$, i.e.

$$\boldsymbol{\mathcal{X}} = \{\boldsymbol{U}^{\mathrm{e}}, \boldsymbol{\Gamma}^{\mathrm{e}}, \chi, \Delta\gamma^{\mathrm{p}}\}, \tag{4.61}$$

solving for the increments in these quantities, and updating the residuals until a convergence criterion is met. In other words, a Newton-Raphson search is conducted, which in each local iteration can be expressed as a truncated Taylor expansion:

$$\underbrace{\begin{Bmatrix} \boldsymbol{r}^U \\ \boldsymbol{r}^\Gamma \\ r^\chi \\ f \end{Bmatrix}}_{\boldsymbol{r}} + \underbrace{\begin{bmatrix} \frac{\partial \boldsymbol{r}^U}{\partial \boldsymbol{U}^\mathrm{e}} & \frac{\partial \boldsymbol{r}^U}{\partial \boldsymbol{\Gamma}^\mathrm{e}} & \boldsymbol{0} & \frac{\partial \boldsymbol{r}^U}{\partial \Delta\gamma^\mathrm{p}} \\ \frac{\partial \boldsymbol{r}^\Gamma}{\partial \boldsymbol{U}^\mathrm{e}} & \frac{\partial \boldsymbol{r}^\Gamma}{\partial \boldsymbol{\Gamma}^\mathrm{e}} & \boldsymbol{0} & \frac{\partial \boldsymbol{r}^\Gamma}{\partial \Delta\gamma^\mathrm{p}} \\ \boldsymbol{0} & \boldsymbol{0} & \frac{\partial r^\chi}{\partial \chi} & \frac{\partial r^\chi}{\partial \Delta\gamma^\mathrm{p}} \\ \frac{\partial f}{\partial \boldsymbol{U}^\mathrm{e}} & \frac{\partial f}{\partial \boldsymbol{\Gamma}^\mathrm{e}} & \frac{\partial f}{\partial \chi} & 0 \end{bmatrix}}_{\boldsymbol{C}} \underbrace{\begin{Bmatrix} \Delta \boldsymbol{U}^\mathrm{e} \\ \Delta \boldsymbol{\Gamma}^\mathrm{e} \\ \Delta\chi \\ \Delta\Delta\gamma^\mathrm{p} \end{Bmatrix}}_{\Delta\boldsymbol{\mathcal{X}}} = \begin{Bmatrix} \boldsymbol{0} \\ \boldsymbol{0} \\ 0 \\ 0 \end{Bmatrix}, \tag{4.62}$$

for which the full analytical linearisation of the residuals $\boldsymbol{r}$ making up the Jacobian $\boldsymbol{C} = \frac{\partial \boldsymbol{r}}{\partial \boldsymbol{\mathcal{X}}}$ is provided in Appendix B. Once the increments in the unknowns $\Delta\boldsymbol{\mathcal{X}}$ are found by performing

$$\Delta\boldsymbol{\mathcal{X}} = -\boldsymbol{C}^{-1}\boldsymbol{r}, \tag{4.63}$$

the corresponding stress state and plastic flows are computed in order to update the three residuals. The entire procedure is detailed in Algorithm 3. Here, the convergence criterion is twofold, due to the difference in magnitude between the first three residuals and the yield function. Namely, the implicit solver concludes when $\bar{p} < \bar{p}_\mathrm{tol}$ and $f < k\bar{p}_\mathrm{tol}$, where

$$\bar{p} = \sqrt{||\boldsymbol{r}^U||^2 + ||\boldsymbol{r}^\Gamma||^2 + (r^\chi)^2} \tag{4.64}$$

and $\bar{p}_\mathrm{tol}$ is a user-defined parameter, in this work chosen to be 10^{-9} unless stated otherwise.

4.3.4 Solution of the global nonlinear problem

Solution of the spatially-discretised weak forms takes place according to the same procedure as for the nonlinear elastic micropolar formulation. However, the calculation of the consistent tangent differs significantly in order to take into account the nonlinear solution of the material point-level constitutive state. In other words, it must include a linearisation of the local Newton-Raphson procedure such that it may be considered *algorithmically consistent.* A way of finding the derivatives of the outputs of the constitutive model solver $\boldsymbol{\mathcal{X}} = \boldsymbol{\mathcal{X}}(\boldsymbol{\mathcal{Y}})$ with respect to its inputs $\boldsymbol{\mathcal{Y}}$ – the total, trial and previously-converged variables which are posited at the beginning of the iteration – is therefore needed. A sufficient set of input variables $\boldsymbol{\mathcal{Y}}$ here is

$$\boldsymbol{\mathcal{Y}} = \{\boldsymbol{F}, \boldsymbol{Q}, (\boldsymbol{F}^\mathrm{e})^\mathrm{tr}, (\boldsymbol{\Gamma}^\mathrm{e})^\mathrm{tr}, \widetilde{\chi}\} \tag{4.65}$$

and an algorithmic Jacobian $\boldsymbol{P}$ filled with useful derivates $\frac{\partial \boldsymbol{\mathcal{X}}}{\partial \boldsymbol{\mathcal{Y}}}$ is the objective. This Jacobian can be produced by inserting $\boldsymbol{C}$ into a chain rule. But first it is important to note that, at convergence, not only is $\boldsymbol{r} = \boldsymbol{r}(\boldsymbol{\mathcal{X}}(\boldsymbol{\mathcal{Y}}), \boldsymbol{\mathcal{Y}})$ minimised – it is also *stationary.*

Algorithm 3 Elastic predictor and plastic corrector at a material point within global Newton-Raphson iteration k.

```
1: Elastic predictor
2: Obtain the new total deformation gradient $\boldsymbol{F}$, microrotation tensor $\boldsymbol{Q}$ and wryness $\boldsymbol{\Gamma}$, and deformation gradient increment $\Delta\boldsymbol{F}$, and recall the previously converged elastic deformation gradient $\widetilde{\boldsymbol{F}^{\mathrm{e}}}$, plastic wryness $\widetilde{\boldsymbol{\Gamma}^{\mathrm{p}}}$ and hardening variable $\widetilde{\chi}$.
3: Compute the trial elastic deformation gradient $(\boldsymbol{F}^{\mathrm{e}})^{\mathrm{tr}} = \Delta\boldsymbol{F}\widetilde{\boldsymbol{F}^{\mathrm{e}}}$ and trial elastic strain $(\boldsymbol{E}^{\mathrm{e}})^{\mathrm{tr}} = \boldsymbol{Q}^{\mathrm{T}}(\boldsymbol{F}^{\mathrm{e}})^{\mathrm{tr}} - \boldsymbol{I}$.
4: Compute the trial elastic wryness $(\boldsymbol{\Gamma}^{\mathrm{e}})^{\mathrm{tr}} = \boldsymbol{\Gamma} - \widetilde{\boldsymbol{\Gamma}^{\mathrm{p}}}$.
5: Set $\boldsymbol{F}^{\mathrm{e}} \leftarrow (\boldsymbol{F}^{\mathrm{e}})^{\mathrm{tr}}$, $\boldsymbol{E}^{\mathrm{e}} \leftarrow (\boldsymbol{E}^{\mathrm{e}})^{\mathrm{tr}}$ and $\boldsymbol{\Gamma}^{\mathrm{e}} \leftarrow (\boldsymbol{\Gamma}^{\mathrm{e}})^{\mathrm{tr}}$.
6: Determine the corresponding Kirchhoff stress $\boldsymbol{\tau} = \boldsymbol{Q}\boldsymbol{D} : \boldsymbol{E}^{\mathrm{e}}(\boldsymbol{F}^{\mathrm{e}})^{\mathrm{T}}$ and couple-stress $\boldsymbol{\nu} = \boldsymbol{Q}\check{\boldsymbol{D}} : \boldsymbol{\Gamma}^{\mathrm{e}}\boldsymbol{F}^{\mathrm{T}}$.
7: Compute the hydrostatic pressure $p = \frac{1}{3}\mathrm{tr}(\boldsymbol{\tau})$, deviatoric stress $\boldsymbol{s} = \boldsymbol{\tau} - p\boldsymbol{I}$, von Mises stress $q = \sqrt{\frac{3}{2}\left(\boldsymbol{s} : \boldsymbol{s} + \frac{1}{(\ell^{\mathrm{p}})^2}\boldsymbol{\nu} : \boldsymbol{\nu}\right)}$, hardening force $\Lambda = H\chi$ and yield function $f = q + \alpha^{\mathrm{DP}}p - (k + \Lambda)$.
8: if $f > k\bar{p}_{\mathrm{tol}}$ then
9:     Plastic corrector
10:    Compute additional residuals $\boldsymbol{r}^{U}$, $\boldsymbol{r}^{\Gamma}$ and $r^{\chi}$ with (4.57)–(4.59).
11:    while $\bar{p} > \bar{p}_{\mathrm{tol}}$ and $f > k\bar{p}_{\mathrm{tol}}$ do
12:        Construct the Jacobian and solve (4.62).
13:        Increment unknowns: $\boldsymbol{U}^{\mathrm{e}}$ += $\Delta\boldsymbol{U}^{\mathrm{e}}$, $\boldsymbol{\Gamma}^{\mathrm{e}}$ += $\Delta\boldsymbol{\Gamma}^{\mathrm{e}}$, $\chi$ += $\Delta\chi$ and $\Delta\gamma^{\mathrm{p}}$ += $\Delta\Delta\gamma^{\mathrm{p}}$.
14:        Compute elastic deformation gradient $\boldsymbol{F}^{\mathrm{e}} = \boldsymbol{Q}\boldsymbol{U}^{\mathrm{e}}$ and strain $\boldsymbol{E}^{\mathrm{e}} = \boldsymbol{U}^{\mathrm{e}} - \boldsymbol{I}$.
15:        Repeat steps 6, 7 and 10.
16:    end while
17: end if
18: Proceed to compute the consistent tangent and internal force and couple.
```

Hence there is no variation in $\boldsymbol{r}$ at this point, so one can write

$$\delta\boldsymbol{r} = \frac{\partial\boldsymbol{r}}{\partial\boldsymbol{\mathcal{X}}}\delta\boldsymbol{\mathcal{X}} + \frac{\partial\boldsymbol{r}}{\partial\boldsymbol{\mathcal{Y}}}\delta\boldsymbol{\mathcal{Y}} = \mathbf{0}. \tag{4.66}$$

Dividing by $\delta\boldsymbol{\mathcal{Y}}$ and rearranging leads to

$$\frac{\partial\boldsymbol{r}}{\partial\boldsymbol{\mathcal{X}}}\frac{\partial\boldsymbol{\mathcal{X}}}{\partial\boldsymbol{\mathcal{Y}}} = -\frac{\partial\boldsymbol{r}}{\partial\boldsymbol{\mathcal{Y}}}, \tag{4.67}$$

or

$$\boldsymbol{C}\boldsymbol{P} = -\boldsymbol{T} \tag{4.68}$$

$$\hookrightarrow \boldsymbol{P} = -\boldsymbol{C}^{-1}\boldsymbol{T}. \tag{4.69}$$

Therefore to find $\boldsymbol{P}$, it only remains to compute the auxiliary Jacobian $\boldsymbol{T} = \frac{\partial\boldsymbol{r}}{\partial\boldsymbol{\mathcal{Y}}}$. The analytical derivation of this matrix is provided in Appendix C, and is constructed according to

$$\boldsymbol{T} = \begin{bmatrix} \frac{\partial\boldsymbol{r}^U}{\partial\boldsymbol{F}} & \frac{\partial\boldsymbol{r}^U}{\partial\boldsymbol{Q}} & \frac{\partial\boldsymbol{r}^U}{\partial(\boldsymbol{F}^{\mathrm{e}})^{\mathrm{tr}}} & \mathbf{0} & \mathbf{0} \\ \frac{\partial\boldsymbol{r}^\Gamma}{\partial\boldsymbol{F}} & \frac{\partial\boldsymbol{r}^\Gamma}{\partial\boldsymbol{Q}} & \mathbf{0} & \frac{\partial\boldsymbol{r}^\Gamma}{\partial(\boldsymbol{\Gamma}^{\mathrm{e}})^{\mathrm{tr}}} & \mathbf{0} \\ \mathbf{0} & \mathbf{0} & \mathbf{0} & \mathbf{0} & \frac{\partial r^\chi}{\partial\widetilde{\chi}} \\ \frac{\partial f}{\partial\boldsymbol{F}} & \frac{\partial f}{\partial\boldsymbol{Q}} & \mathbf{0} & \mathbf{0} & 0 \end{bmatrix}. \tag{4.70}$$

The Jacobian $\boldsymbol{P}$ then follows as

$$\boldsymbol{P} = \begin{bmatrix} \frac{\partial\boldsymbol{U}^{\mathrm{e}}}{\partial\boldsymbol{F}} & \frac{\partial\boldsymbol{U}^{\mathrm{e}}}{\partial\boldsymbol{Q}} & \frac{\partial\boldsymbol{U}^{\mathrm{e}}}{\partial(\boldsymbol{F}^{\mathrm{e}})^{\mathrm{tr}}} & \frac{\partial\boldsymbol{U}^{\mathrm{e}}}{\partial(\boldsymbol{\Gamma}^{\mathrm{e}})^{\mathrm{tr}}} & \frac{\partial\boldsymbol{U}^{\mathrm{e}}}{\partial\widetilde{\chi}} \\ \frac{\partial\boldsymbol{\Gamma}^{\mathrm{e}}}{\partial\boldsymbol{F}} & \frac{\partial\boldsymbol{\Gamma}^{\mathrm{e}}}{\partial\boldsymbol{Q}} & \frac{\partial\boldsymbol{\Gamma}^{\mathrm{e}}}{\partial(\boldsymbol{F}^{\mathrm{e}})^{\mathrm{tr}}} & \frac{\partial\boldsymbol{\Gamma}^{\mathrm{e}}}{\partial(\boldsymbol{\Gamma}^{\mathrm{e}})^{\mathrm{tr}}} & \frac{\partial\boldsymbol{\Gamma}^{\mathrm{e}}}{\partial\widetilde{\chi}} \\ \frac{\partial\chi}{\partial\boldsymbol{F}} & \frac{\partial\chi}{\partial\boldsymbol{Q}} & \frac{\partial\chi}{\partial(\boldsymbol{F}^{\mathrm{e}})^{\mathrm{tr}}} & \frac{\partial\chi}{\partial(\boldsymbol{\Gamma}^{\mathrm{e}})^{\mathrm{tr}}} & \frac{\partial\chi}{\partial\widetilde{\chi}} \\ \frac{\partial\Delta\gamma^{\mathrm{p}}}{\partial\boldsymbol{F}} & \frac{\partial\Delta\gamma^{\mathrm{p}}}{\partial\boldsymbol{Q}} & \frac{\partial\Delta\gamma^{\mathrm{p}}}{\partial(\boldsymbol{F}^{\mathrm{e}})^{\mathrm{tr}}} & \frac{\partial\Delta\gamma^{\mathrm{p}}}{\partial(\boldsymbol{\Gamma}^{\mathrm{e}})^{\mathrm{tr}}} & \frac{\partial\Delta\gamma^{\mathrm{p}}}{\partial\widetilde{\chi}} \end{bmatrix}, \tag{4.71}$$

elements of which are used as necessary in the algorithmically-consistent linearisation of the global elastoplastic problem detailed in Appendix D. Considering a single background cell E, the derived expressions for the tangent stiffness matrices are

$$\boldsymbol{K}_E^{pu} = \int_E \boldsymbol{G}^{\mathrm{T}} : \boldsymbol{a}_1 : \boldsymbol{G}\,\mathrm{d}\Omega \tag{4.72}$$

$$\boldsymbol{K}_E^{p\varphi} = \int_E \boldsymbol{G}^{\mathrm{T}} : \big(\boldsymbol{a}_2 : \breve{\boldsymbol{G}} + \boldsymbol{a}_3 : \boldsymbol{G}\big)\,\mathrm{d}\Omega \tag{4.73}$$

$$\boldsymbol{K}_E^{qu} = \int_E \big(\boldsymbol{G}^{\mathrm{T}} : \boldsymbol{a}_4 : +\breve{\boldsymbol{G}}^{\mathrm{T}} : \boldsymbol{a}_5\big)\,\boldsymbol{G}\,\mathrm{d}\Omega \tag{4.74}$$

$$\boldsymbol{K}_E^{q\varphi} = \int_E \big(\boldsymbol{G}^{\mathrm{T}} : \big(\boldsymbol{a}_6 : \boldsymbol{G} + \boldsymbol{a}_7 : \breve{\boldsymbol{G}}\big) + \breve{\boldsymbol{G}}^{\mathrm{T}} : \big(\boldsymbol{a}_3 : \boldsymbol{G} + \boldsymbol{a}_2 : \breve{\boldsymbol{G}}\big)\big)\,\mathrm{d}\Omega\,, \tag{4.75}$$

where the tangent moduli are defined differently to their purely elastic counterparts given in Chapter 3. They are now

$$(a_1)_{ijkl} = J^{-1}\left(L^{\mathrm{e}}_{ij\alpha\bar{l}}D_{\alpha\bar{l}\psi\bar{b}} + Q_{i\alpha}B_{\alpha\bar{b}}Q_{j\psi}\right)\left(\frac{\partial U^{\mathrm{e}}_{\psi\bar{b}}}{\partial F_{k\theta}}F_{l\theta} + \frac{\partial U^{\mathrm{e}}_{\psi\bar{b}}}{\partial (F^{\mathrm{e}})^{\mathrm{tr}}_{k\bar{i}}}(F^{\mathrm{e}})^{\mathrm{tr}}_{l\bar{i}}\right) - \sigma_{il}\delta_{jk} \tag{4.76}$$

$$(a_2)_{ijkl} = J^{-1}\left(L^{\mathrm{e}}_{ij\alpha\bar{l}}D_{\alpha\bar{l}\gamma\bar{k}} + Q_{i\alpha}B_{\alpha\bar{k}}Q_{j\gamma}\right)\frac{\partial U^{\mathrm{e}}_{\gamma\bar{k}}}{\partial Q_{l\theta}}Q_{k\theta} + \sigma_{kj}\delta_{il} + \sigma_{ik}\delta_{jl} \tag{4.77}$$

$$(a_3)_{ijkl} = J^{-1}\left(L^{\mathrm{e}}_{ij\alpha\bar{l}}D_{\alpha\bar{l}\gamma\bar{k}} + Q_{i\alpha}B_{\alpha\bar{k}}Q_{j\gamma}\right)\frac{\partial U^{\mathrm{e}}_{\gamma\bar{k}}}{\partial (\Gamma^{\mathrm{e}})^{\mathrm{tr}}_{\theta\pi}}L_{kl\theta\pi} \tag{4.78}$$

$$(a_4)_{ijkl} = J^{-1}L_{ij\alpha\beta}\check{D}_{\alpha\beta\gamma\delta}\left(\frac{\partial \Gamma^{\mathrm{e}}_{\gamma\delta}}{\partial F_{k\theta}}F_{l\theta} + \frac{\partial \Gamma^{\mathrm{e}}_{\gamma\delta}}{\partial (F^{\mathrm{e}})^{\mathrm{tr}}_{k\bar{i}}}(F^{\mathrm{e}})^{\mathrm{tr}}_{l\bar{i}}\right) \tag{4.79}$$

$$(a_5)_{ijkl} = (a_1)_{ijkl} + \sigma_{il}\delta_{jk} \tag{4.80}$$

$$(a_6)_{ijkl} = J^{-1}L_{ij\alpha\beta}\check{D}_{\alpha\beta\gamma\delta}\frac{\partial \Gamma^{\mathrm{e}}_{\gamma\delta}}{\partial (\Gamma^{\mathrm{e}})^{\mathrm{tr}}_{\psi\pi}}L_{kl\psi\pi} \tag{4.81}$$

$$(a_7)_{ijkl} = J^{-1}L_{ij\alpha\beta}\check{D}_{\alpha\beta\gamma\delta}\frac{\partial \Gamma^{\mathrm{e}}_{\gamma\delta}}{\partial Q_{l\theta}}Q_{k\theta} + \mu_{kj}\delta_{il}, \tag{4.82}$$

where

$$L_{kl\theta\pi} = Q_{k\theta}F_{l\pi} \tag{4.83}$$

and

$$L^{\mathrm{e}}_{ij\alpha\bar{l}} = Q_{i\alpha}F^{\mathrm{e}}_{j\bar{l}}. \tag{4.84}$$

If the particular material point under scrutiny lies within the yield surface (i.e. in the elastic regime), then these same tangent moduli may be used by substituting the following derivatives:

$$\frac{\partial U^{\mathrm{e}}_{\psi\bar{b}}}{\partial Q_{m\theta}} = \delta_{\theta\psi}(F^{\mathrm{e}})^{\mathrm{tr}}_{m\bar{b}} \tag{4.85}$$

$$\frac{\partial U^{\mathrm{e}}_{\psi\bar{b}}}{\partial (F^{\mathrm{e}})^{\mathrm{tr}}_{m\bar{i}}} = Q_{m\psi}\delta_{\bar{i}\bar{b}} \tag{4.86}$$

$$\frac{\partial \Gamma^{\mathrm{e}}_{\gamma\delta}}{\partial (\Gamma^{\mathrm{e}})^{\mathrm{tr}}_{\psi\pi}} = \delta_{\gamma\psi}\delta_{\pi\delta}, \tag{4.87}$$

and setting all other components of $\boldsymbol{P}$ to zero.

4.4 Strain localisation in the micropolar continuum

A full numerical implementation of the finite strain elastoplastic micropolar continuum has now been developed. It must now therefore be verified. This is achieved by returning to the simple one-dimensional shear layer problem attempted in Chapter 2, which was used to highlight the inherent inability of the classical continuum to simulate strain localisation

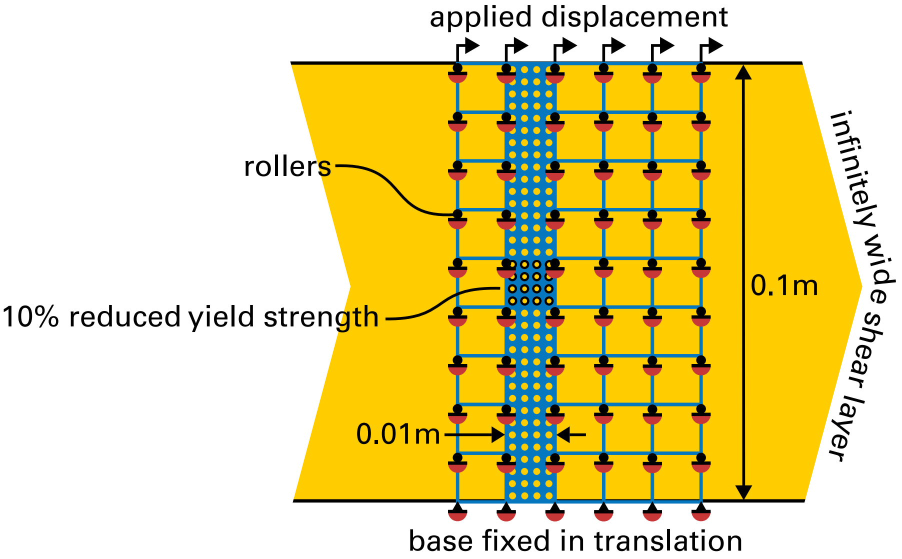

Figure 4.2: The setup of the micropolar shear layer problem, showing the coarsest discretisation used.

in an acceptable way. The same problem dimensions and discretisations are used, as shown in Figure 4.2: a slice measuring 0.01 m × 0.1 m is divided into (i) 9 × 1, (ii) 19 × 2 and (iii) 39 × 4 cells, each containing 4^3 generalised interpolation material points (as the formulation is three-dimensional, the domain is also one grid cell thick in the out-of-plane direction). To render the problem one-dimensional, all kinematics are constrained except horizontal translation and in-plane microrotation, and only the translation is fixed at the bottom of the slice in order to emulate the classical problem, leaving microrotations free[2] (homogeneous Neumann). Meanwhile a horizontal translation of 0.02 m is applied at the top of the layer in 200 equal steps. To induce localisation, the yield strength of the central element (or row of elements) is degraded by a factor of 10%. The conventional material constants are kept the same: the Lamé parameters $\lambda = \mu = 4\,\mathrm{GPa}$, the friction angle $\phi = 8.6°$, dilatancy $\psi = 2°$ and yield strength $k = 100\,\mathrm{MPa}$, while the additional micropolar parameters are selected in order to most effectively demonstrate their regularising properties, namely the Cosserat coupling modulus $\kappa = \frac{\mu}{10}$ and internal lengths $\ell_b = \ell^{\mathrm{p}} = 5\,\mathrm{mm}$. By invoking the principle of bounded stiffness (see Section 3.3.7) the other elastic micropolar parameters are $\alpha = -\frac{8\mu\ell_b^2}{3}$, $\gamma = 4\mu\ell_b^2$ and $\beta = 0$, though α and β only have an effect in three-dimensional problems. The problem is also stabilised with ghost parameters $\gamma_{g1} = \frac{\lambda}{100}$ and $\gamma_{g2} = \frac{\gamma}{100}$, and the Newton-Raphson convergence criteria are $\bar{f}_{\mathrm{tol}} = 10^{-9}$, $\bar{e}_{\mathrm{tol}} = 10^{-14}$ and $\bar{p}_{\mathrm{tol}} = 10^{-9}$.

The force-displacement response of the three discretisations tested are shown in Figure 4.3, along with the results from Chapter 2 for comparison. In the elastic regime, there is no discernable difference between the two models. This indicates that the introduction

---

[2] If microrotations are constrained at the top and bottom of the slice, then the resulting inhomogeneous deformation field would induce localisation at the centre of the layer *without* the need of an imperfection – see [135].

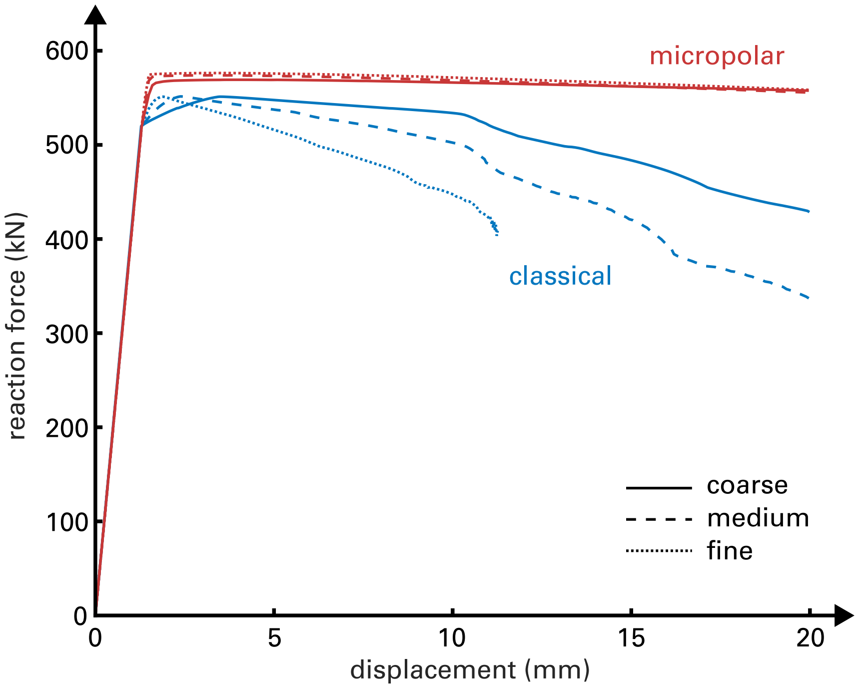

Figure 4.3: Force-displacement curves for the shear layer problem across three discretisation levels, in both the classical and micropolar continua.

of micropolar theory does not lead to an over-regularisation of the problem (a concern initially raised in Section 3.2.2). Instead, initial yielding appears to occur at exactly the same displacement and load level, but the micropolar response produces a higher failure load which in the more refined tests almost coincides with the extension of the elastic loading branch. This apparent discrepancy is a consequence of the imperfection introduced in the central row of elements. In the classical case, plastic deformations are almost entirely confined to the imperfect material, while in the micropolar model, the nonlocal resistance to sharp rotation gradients causes the failure zone to extend into the surrounding intact material (see Figure 4.4). Hence the structure is able to reach the true specified yield limit of the material and is unaffected by the artificial imperfection, which now serves its intended purpose of inducing localisation without altering the overall mechanical behaviour. Already it is clear that the micropolar formulation provides a more physically meaningful response, as it captures the real or intended material behaviour without being excessively influenced by numerical artefacts.

In the plastic regime itself, the differences between the two models become far more pronounced. The classical model gives strikingly different results across the three levels of discretisation, with a significant, mesh-dependent degree of softening, despite the absence of explicit strain-softening in the constitutive model. The micropolar results are much more consistent, however, and in fact barely differ at all across the three mesh sizes. The rate of softening, although sufficient for strain localisation to occur, is minimal and stands in contrast with the artificial brittleness predicted by the classical model. The final state of

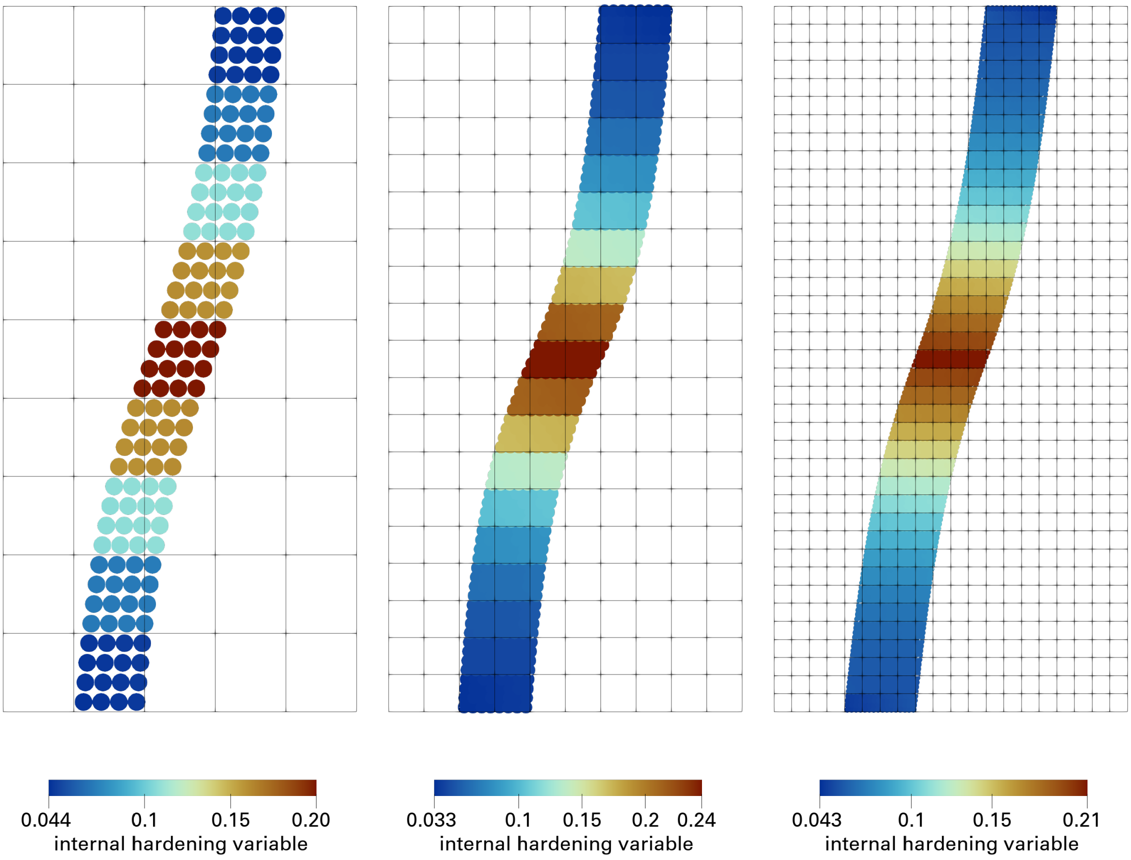

(a) coarse **(b)** medium **(c)** fine

Figure 4.4: Final configurations of each mesh resolution, coloured according to the internal hardening variable χ, cf. Figure 2.7. The localisation zone is continuous and independent of the mesh.

each simulation is depicted in Figure 4.4, showing each material point coloured according the internal hardening variable[3] χ as a scalar measure of the degree of accumulated plastic straining, similar to ε^{p} used in Chapter 2. Again, there is very little difference across the three results. The deformations throughout each slice are continuous, rather than the crooked, unphysical localisation pattern predicted by the classical model (see Figure 2.7). The size of the failure zone appears to be roughly constant across the three discretisation levels, and is therefore mesh-*independent*, culminating in a similar magnitude of plastic straining at the centre of each shear band. By comparison, the ultimate plastic strain in each of the classical examples differed considerably: the most refined test developed almost four times as much plastic strain as the coarsest, in approximately half the applied displacement. Therefore the micropolar formulation regularises the problem precisely as intended: it dependably delivers consistent simulations of strain localisation, where the

---

[3] The material is still perfectly-plastic as the hardening modulus H is set to nil, thus the evolution of χ has no effect on the yield function.

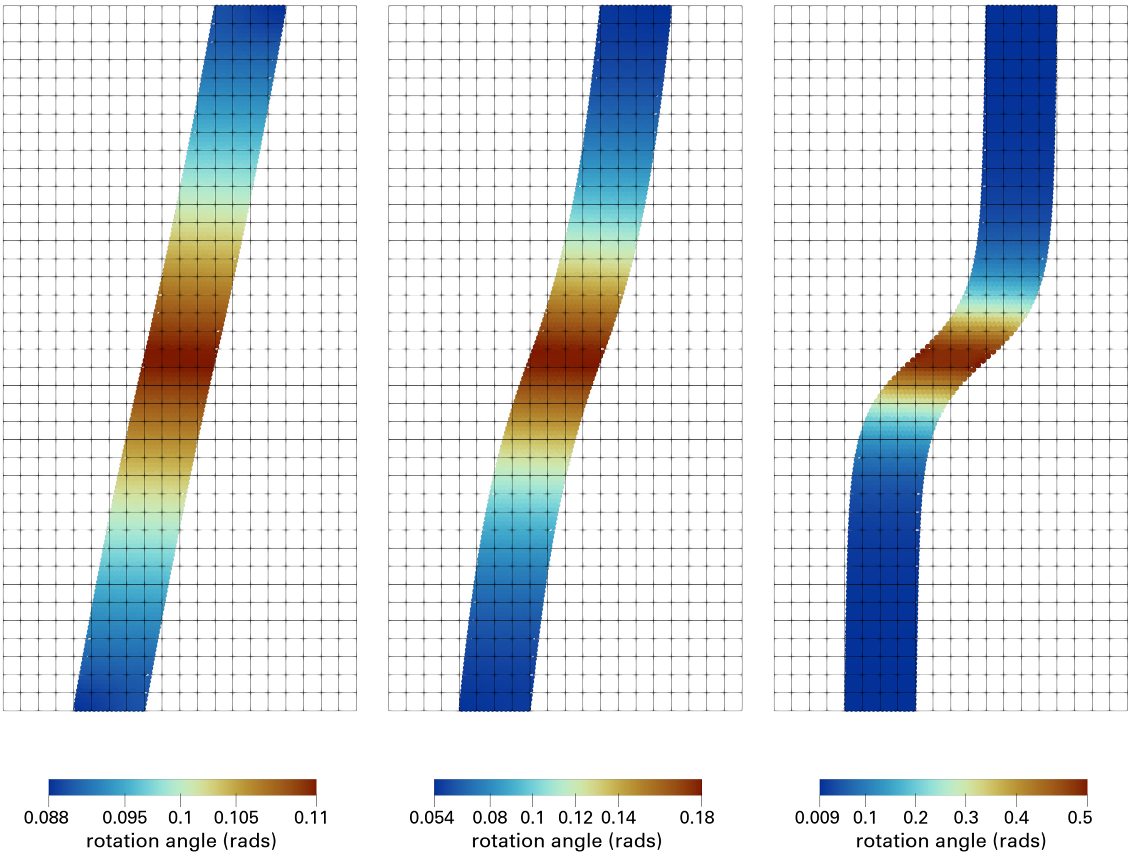

(a) $\ell = 10\,\mathrm{mm}$ **(b)** $\ell = 5\,\mathrm{mm}$ **(c)** $\ell = 2.5\,\mathrm{mm}$

Figure 4.5: Shear bands for three different internal length scales $\ell_b = \ell^\mathrm{p}$ on the finest discretisation used, coloured according to the in-plane microrotation. For scale, each background cell is $2.56\,\mathrm{mm}$ tall.

mechanical response is controlled not by extrinsic numerical factors like mesh size, but instead by parameters which are rooted in reality, such as the internal length scales.

This relationship is highlighted in Figure 4.5, which shows the effect of modifying the bending and plastic lengths $\ell_b = \ell^\mathrm{p}$ on the thickness of the shear band. Via the resistance they provide to rotation gradients, the internal lengths clearly provide direct control over the size of the failure zone. With $\ell = 10\,\mathrm{mm}$, this resistance is so great that the structure is barely allowed to localise, resulting in a highly diffuse shear band where the overall deformation pattern more closely resembles homogeneous shearing. On the other hand, when $\ell = 2.5\,\mathrm{mm}$ the penalisation to curvature is significantly reduced, such that a thinner and much more distinct (but still smooth and continuous) shear band emerges. Given the correspondence between particle size and shear band thickness in real geomaterials [15, 28–30], this natural link between material parameters and failure zone size is a crucial validation of the micropolar approach, and demonstrates that the model can simulate strain localisation in a physically-consistent way – a critical aspect of its

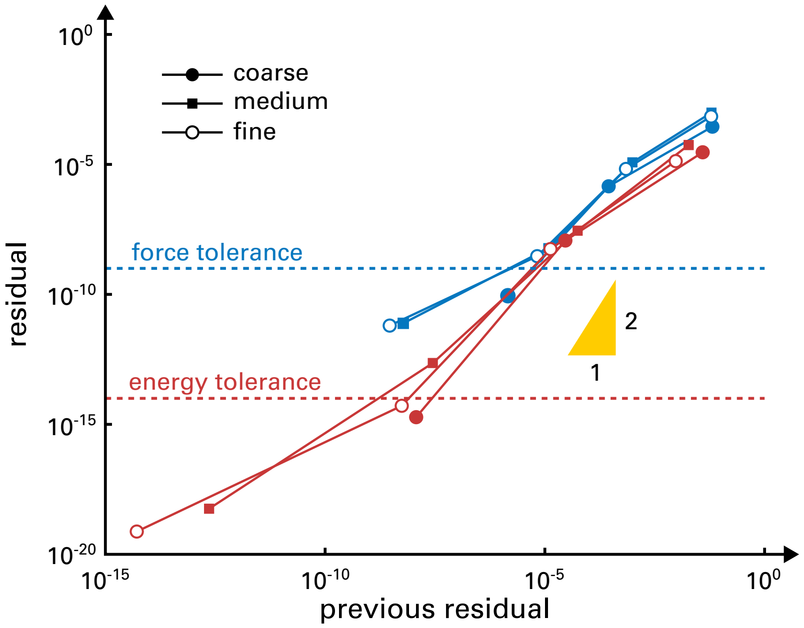

Figure 4.6: Global Newton-Raphson convergence in the final step for each discretisation level, in terms of both the normalised force and energy on a log-log plot. The small step size used means that convergence is achieved relatively quickly.

specification.

Furthermore the micropolar model is characterised by much greater numerical stability and robustness. In the classical examples a large Newton-Raphson convergence criterion of $\bar{f}_{\text{tol}} = 10^{-5}$ is required due to extremely poor convergence behaviour; even then, an adaptive routine is required (despite the small displacement increment of $\frac{0.02\,\text{m}}{200}$ per step) as convergence is frequently unachievable, and in the most refined example the simulation fails just beyond halfway. In other words, the results are both imprecise and exceedingly difficult to obtain (not that they are particularly meaningful anyway), and are therefore practically useless from an engineering perspective. Conversely, the micropolar solver is consistently stable: all three analyses run to completion, with a rapid rate of convergence in every step towards a significantly more precise error tolerance of $\bar{f}_{\text{tol}} = 10^{-9}$. This is reflected in Figure 4.6, which shows the asymptotic convergence of $\bar{f}$ and $\bar{e}$ in the final load step of each micropolar test. The indicated convergence rate becomes very nearly quadratic (before machine precision impedes progress), verifying the derivation and implementation of the algorithmically-consistent tangent.[4,5] While 200 steps are used for consistency with the classical simulations, the stability is such that the analysis requires nowhere near as many to satisfactorily reach completion. In fact, when attempting the example with the

---

[4] Unlike in the MMS verification of Section 3.5.1, unavoidable integration errors here (as well as the numerical accuracy of the constitutive model solution) mean that exactly quadratic asymptotic convergence can never truly be attained.

[5] The small step size used in this study means the local elastoplastic solver converges in just one or two iterations, preventing meaningful conclusions to be drawn.

most refined mesh with just ten load steps, convergence is achieved with no more than nine Newton-Raphson iterations each time (and typically just five or six).

Altogether, the elastoplastic micropolar MPM developed in this thesis appears so far to be superior in terms of accuracy, reliability, efficiency and stability than its classical equivalent when simulating strain localisation. However, it has yet to be tested in anything like a realistic two- or three-dimensional engineering problem. Validation of the derived MPM against more physically-motivated – and particularly *geotechnical* – large-deformation examples forms the remainder of this chapter.

4.5 Numerical examples

Due to the relative simplicity of the constitutive model in terms of its number of physical parameters, especially realistic geotechnical problems are unfortunately beyond the capability of the derived method in its proposed form. The validation problems presented in this section are instead designed to demonstrate key properties of the model, and comparisons with experimental observations are in general only qualitative. However, they highlight the promising potential of the proposed method, and future extensions of this work may indeed result in a predictive framework which provides true, reliable accuracy for realistic strain localisation problems in geomaterials. Unless otherwise stated, the same ghost and Newton-Raphson parameters are used as in the shear layer example ($\gamma_{g1} = \frac{\lambda}{100}$ and $\gamma_{g2} = \frac{\gamma}{100}$, and $\bar{f}_{\text{tol}} = 10^{-9}$, $\bar{e}_{\text{tol}} = 10^{-14}$ and $\bar{p}_{\text{tol}} = 10^{-9}$), and the principle of bounded stiffness is employed throughout.

4.5.1 Biaxial test

When it comes to validation problems involving localisation in geomaterials, the plane strain biaxial test is the quintessential classic. It provided a basis for the first analytical [27] and numerical [135] applications of micropolar theory to the strain localisation issue; correspondingly, no proper validation would be complete without it. The test itself is straightforward, and since the apparatus was standardised in the 1980s [340, 341] it has become a mainstay of experimental granular physics, along with the more routinely used triaxial test. A rectangular prismatic sample of soil or rock, typically twice as tall in the 'axial' direction as it is wide, is constrained against out-of-plane motion, and has loading applied axially by means of rigid platens, and hydrostatically with either a cell pressure or applied vacuum. This allows the sample to deform homogeneously such that shear bands appear to emerge spontaneously, and force and displacement measurements can be converted into material properties such as the apparent cohesion, and friction and dilatancy angles [340]. Typical results for drained analysis of sand are detailed in [29].

There are two different numerical setups to this problem. One is to fix both the top and the base such that the two faces of the specimen retain their alignment throughout the simulation, leading to a symmetrical deformation field and resulting localisation pattern.

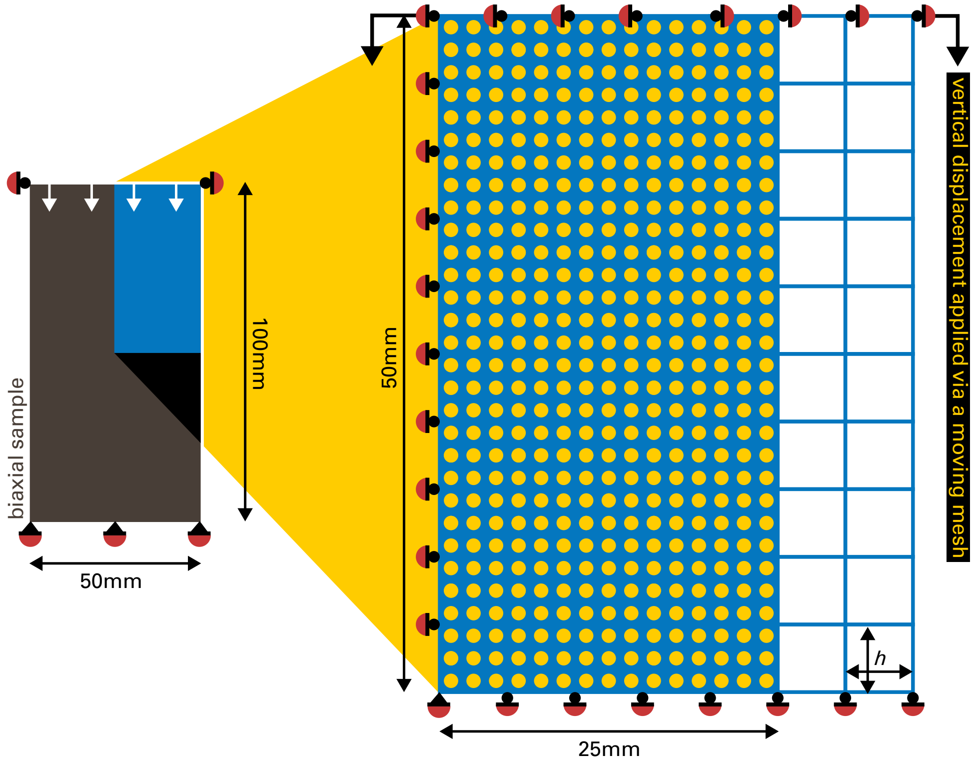

Figure 4.7: Setup of the plane strain biaxial test, showing a representative discretisation of 10×5 cells ($h = 5\,\text{mm}$) occupied by 3^3 material points each.

The other way is to allow one face to translate rigidly, then applying a perturbation in loading or material properties which induces a strongly asymmetric deformation pattern – typically a single diagonal shear band (recall Figure 1.1). While small imperfections in loading conditions mean that the majority of experimental results more closely match the second type, in this work the former will be pursued. This is because the inherent symmetries allow for just a quarter of the domain to be analysed, requiring significantly fewer computational resources to achieve parity in mesh refinement. The particular chosen setup is depicted in Figure 4.7. The top right-hand quadrant of a $100\,\text{mm} \times 50\,\text{mm}$ column of soil is discretised into $\frac{10\,\text{mm}}{h} \times \frac{5\,\text{mm}}{h}$ elements, each h^3 in size and containing 3^3 generalised interpolation material points. Horizontal motion is prevented along the top and left-hand side of the quadrant, while the base is constrained vertically. While rotations should technically be constrained along the symmetry planes, in practice this makes very little difference in this genre of problem [128, 278] and thus they are left free on every face to avoid an overly stiff response. The analysis employs displacement control, applied adaptively to the nodes at the top of the sample by means of a moving mesh (see Section 2.2.4) up to a limit of 10 mm (20% axial strain). The sample is considered weightless, and to avoid a non-conforming Neumann boundary condition no cell pressure is applied either (rendering the problem a *uniaxial* test, strictly). Instead, the material is given a relatively large apparent cohesion of 100 kPa, which has the effect of shifting the Drucker-Prager failure surface in the hydrostatic direction – the same effective result, broadly speaking, as an applied cell pressure. The other material parameters are $\lambda = \mu = 8\,\mathrm{MPa}$, $\kappa = \frac{\mu}{10}$, $\ell_b = \ell^{\mathrm{p}} = 2\,\mathrm{mm}$, $H = 0$, $\phi = 30°$ and $\psi = 10°$ (though this last parameter will be varied later on). If ℓ_b is taken to be the mean particle diameter, these material properties loosely describe a drained, perfectly-plastic coarse-grained sand. Note that no perturbation or imperfection is introduced; localisation follows solely from the way the boundary conditions are applied.

The objective of this numerical example is chiefly to observe the localisation patterns predicted by the proposed method at finite strains, to see if they are broadly consistent with results from experiments as well as previous numerical work. The formulation's mesh objectivity is demonstrated concurrently by conducting analyses at four discretisation levels which are close to the selected internal length scale of $\ell_b = 2\,\mathrm{mm}$. These results are shown in Figure 4.8, where the effect of varying h between $0.625\ell_b$ and $2.5\ell_b$ is reflected in the final distribution of plastic straining at 20% axial strain. The corresponding stress-strain curves are shown in Figure 4.9, using macroscopically-defined quantities: the stress is calculated as the total reaction force at the top divided by the (constant) cross-sectional area; the strain is the axial shortening of the sample divided by its original height. In fact, there is little difference across the four sets of results – particularly between the two where the internal length exceeds the mesh size. In each case a single shear band originating at the bottom left is predicted, which curves diagonally upwards towards the top right. In the complete specimen, this produces an X-shaped localisation pattern as shown in Figure 4.10 – a result that matches empirical observations when sufficient care is taken to ensure symmetrical loading conditions, e.g. by satisfying the van Hove conditions [5]. The thickness of the shear band converges towards a steady value of approximately 21 mm, and accordingly the maximum degree of plastic straining plateaus at approximately $\chi = 1.1$. This is consistent with the idea that the thickness of shear bands corresponds to several multiples of the average grain size. Indeed, the factor quoted in the literature is usually 10-20 [8, 27, 28, 30], which fits with the $\frac{21\,\mathrm{mm}}{2\,\mathrm{mm}} = 10.5$ observed here. This suggests that it is correct to link both ℓ_b and ℓ^{p} to the average particle diameter, at least in the context of this example. However, as stated previously (see the discussion in Section 3.3.7), the exact relationship between the micropolar internal lengths and the microstructures they represent is still unclear. While this result satisfyingly validates the approach, further analysis lies beyond this thesis' scope but nevertheless points towards an interesting avenue for future work. Furthermore the shape of the stress-strain curve broadly matches similar results obtained experimentally [15, 29] and numerically [59, 128]. Initial yielding occurs at a relatively low strain, whereupon the stress peaks before falling to a steady value – the *critical state*, where continuous deformation requires no change in stress input. Unfortunately, the simplicity of the constitutive model mean that further interpretation of this result would result in little insight gained.

The orientation of the shear band, meanwhile, appears to curve from near-horizontal

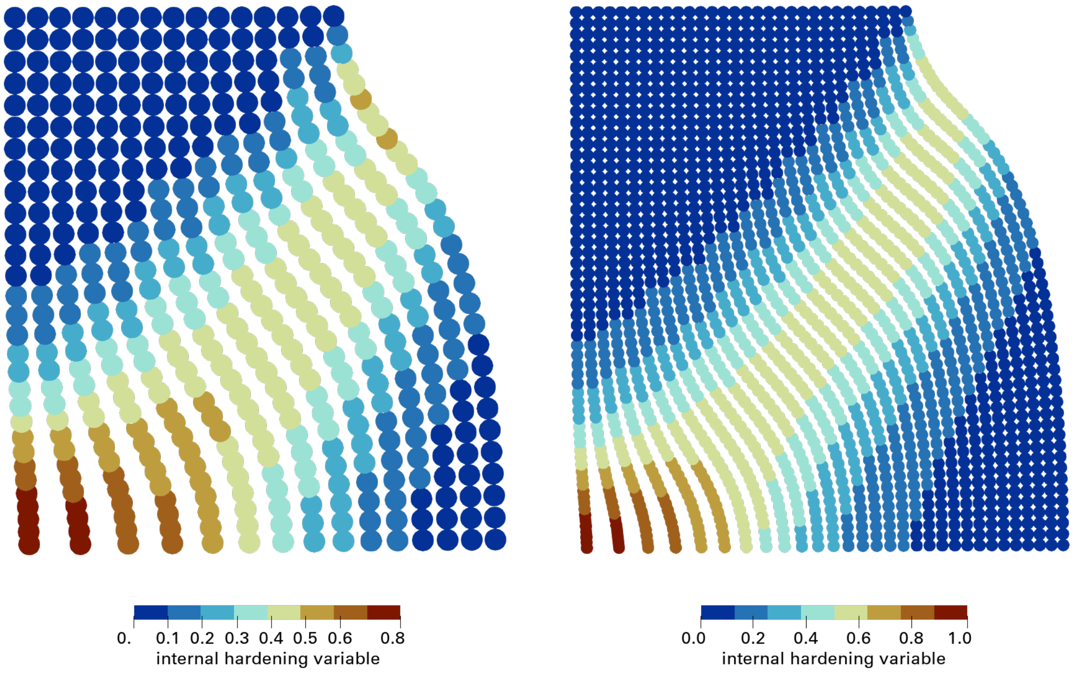

(a) $h = 5\,\mathrm{mm}$ **(b)** $h = 2.5\,\mathrm{mm}$

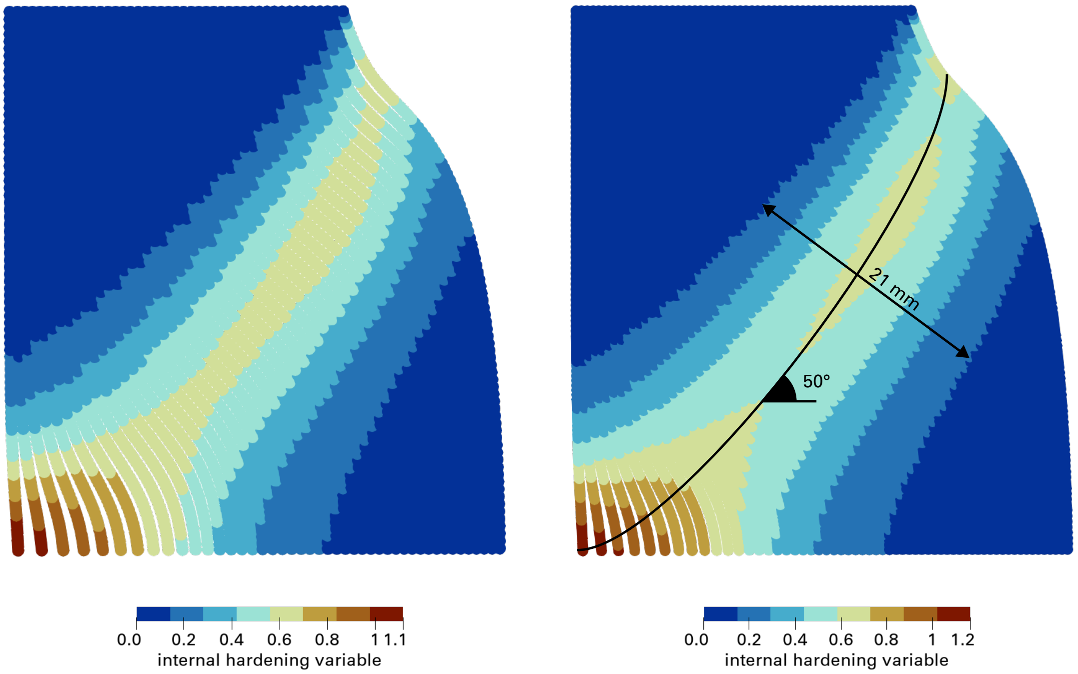

(c) $h = 1.67\,\mathrm{mm}$ **(d)** $h = 1.25\,\mathrm{mm}$

Figure 4.8: Final configuration for each biaxial test with varying mesh refinement, coloured according to the internal hardening variable χ.

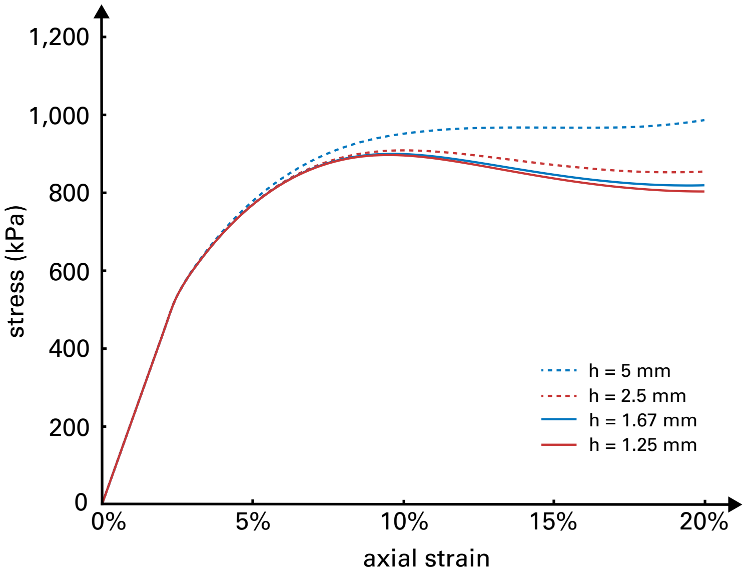

Figure 4.9: Macroscopic stress-strain curves for the biaxial test with varying mesh size.

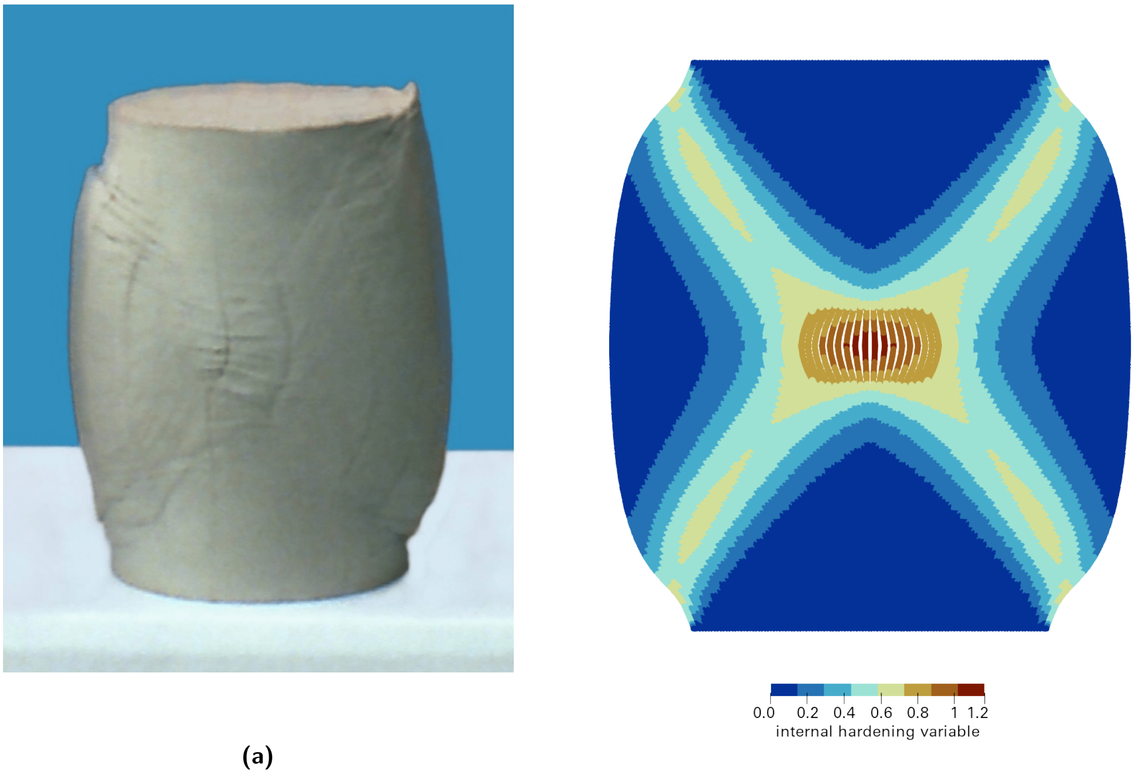

(a)

(b)

Figure 4.10: X-shaped shear bands observed in **(a)** triaxial loading of a cylindrical sample of clay, reproduced from [342], and **(b)** the numerical result for $h = 1.25\,\mathrm{mm}$ (reflected horizontally and vertically), which can be viewed in GIF format here.

at the centre of the sample to near-vertical at the edge. This is interesting because, as far as can be discerned, all prior numerical work on biaxial testing of geomaterials – both micropolar and classical – seems to predict localisation bands which are practically straight. Whether or not this follows from the diminished influence of the mesh in the MPM in comparison with the FEM is unclear, as [59,102,225] all reported rectilinear failure patterns in similar problems. However, while real shear bands might commonly be thought to be flat, the slight curvature present in the results is not necessarily unphysical: empirical evidence of curved bands has been widely recorded [29,343], particularly when rigid platens are used, as is the case here. The specific source, nature and consequences of this apparent curvature are at present unknown, but potentially represent a significant, distinctive feature of the method yet to be exploited.

That said, although the shear band overall resembles an arc, the majority of its path lies close to an angle of precisely 50° to the horizontal. This exactly matches Roscoe's [8] solution,

$$\theta = 45^\circ + \frac{\psi}{2}, \tag{4.88}$$

which was issued as a correction to Coulomb's earlier formula,

$$\theta = 45^\circ + \frac{\phi}{2}. \tag{4.89}$$

In turn, Roscoe's was later challenged by the empirical formula of Arthur et al. [344], which is simply an intermediary line exactly halfway between his and Coulomb's:

$$\theta = 45^\circ + \frac{\phi + \psi}{4}. \tag{4.90}$$

Each has amassed significant experimental evidence, but it is also important to note that real localisation bands do not form at a fixed angle; instead they evolve continuously from before even the peak strength is reached until arriving at the critical state, as the degree of mobilised friction changes [345]. But because precisely matching a specific set of experimental results is not the aim of this example, that the orientation of the predicted shear band is within the 50–60° range predicted by the above equations is a sufficient validation in itself.

To pursue this line of validation further, though, two additional analyses were conducted where the angle of dilatancy was altered to either 0° or 20°, while keeping the element size constant at $h = 2.5\,\mathrm{mm}$. These results are shown in Figure 4.11, and the stress-strain responses in Figure. 4.12. As would be expected, the greater the dilatancy, the more the sample expands laterally. This, in turn, leads to a higher load-bearing capacity, such that the peak strength increases significantly. While the thickness of each predicted shear band does not appear to change greatly, their orientations clearly do. At $\psi = 0^\circ$, the band is shallower than at $\psi = 10^\circ$: practically 45° near its halfway point. At $\psi = 20^\circ$, on the other hand, the band is steep enough to almost reach the top right-hand corner

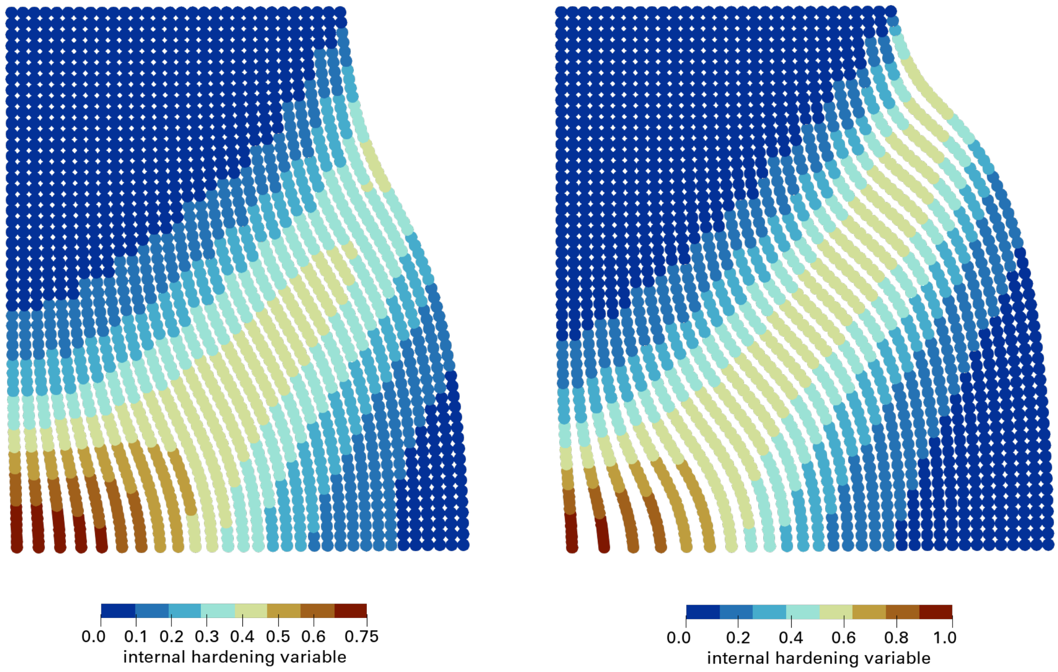

(a) $\psi = 0^\circ$ **(b)** $\psi = 10^\circ$

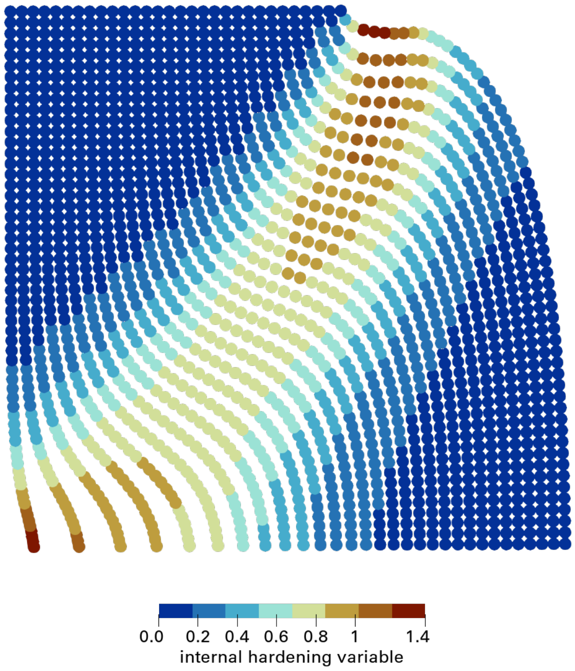

(c) $\psi = 20^\circ$

Figure 4.11: Final configuration for each biaxial test with varying dilatancy angle ψ at fixed $h = 2.5\,\mathrm{mm}$, coloured according to the internal hardening variable χ.

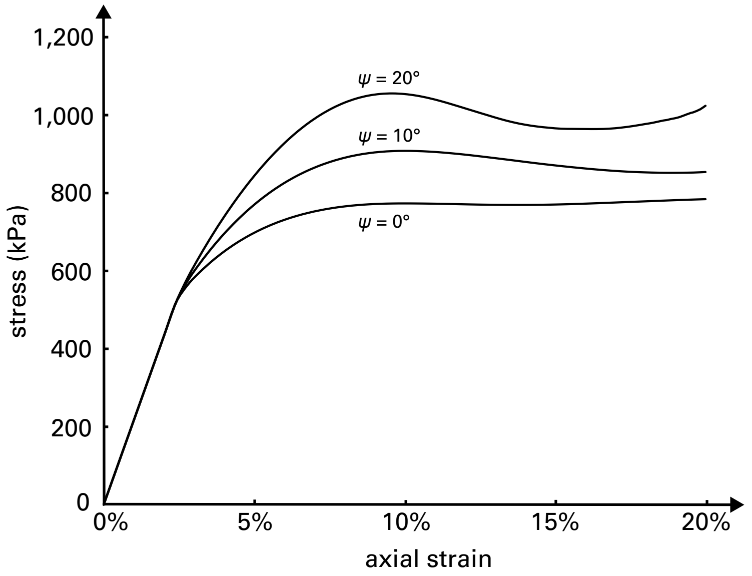

Figure 4.12: Macroscopic stress-strain curves for the biaxial test with varying dilatancy angle.

of the domain, and has an orientation of between 55° and 60° – the angles predicted by Roscoe and Coulomb respectively. The only unexpected outcome appears towards the end of the $\psi = 20°$ stress-strain curve, where instead of descending towards a critical state, the stress begins to increase again. However, this can probably be ascribed to the boundary conditions applied to the top of the domain, which begin to influence the material points at the terminus of the shear band: having deformed so severely, they enter the very top layer of the background grid. This artefact would likely be rectified by employing a different boundary condition application method, or perhaps by separating the sample from the boundary with a rigid topcap, which could be achieved using the methodology described in [346].

The final set of results drawn from this example comprises an examination of the microrotations and wryness which develop in the specimen. Forming the principal distinction between micropolar and classical continua, these quantities hold the regularising power which leads to mesh-objective results. The spatial variation in microrotation and its vertical wryness (i.e. the rate of change in microrotation per metre upwards) across one of the fully-deformed specimens is depicted in Figure 4.13. The microrotation varies smoothly, reaching a peak of $0.68\,\text{rad} \approx 39°$ along the centre of the failure zone. Though grain rotation is a complex phenomenon governed by angularity, void ratio and many more parameters, this result is consistent with the particle rotations observed by Amirrahmat et al. [268] at 19.9% axial strain during triaxial testing of sand, which were in the neighbourhood of 40° inside the shear band. As for the wryness, its variation – while still smooth – is much more severe. This is shown more clearly in Figure 4.14, which plots both quantities through a vertical column of material points located approximately halfway between the left-hand boundary and the edge in the reference configuration. That the wryness is essentially the

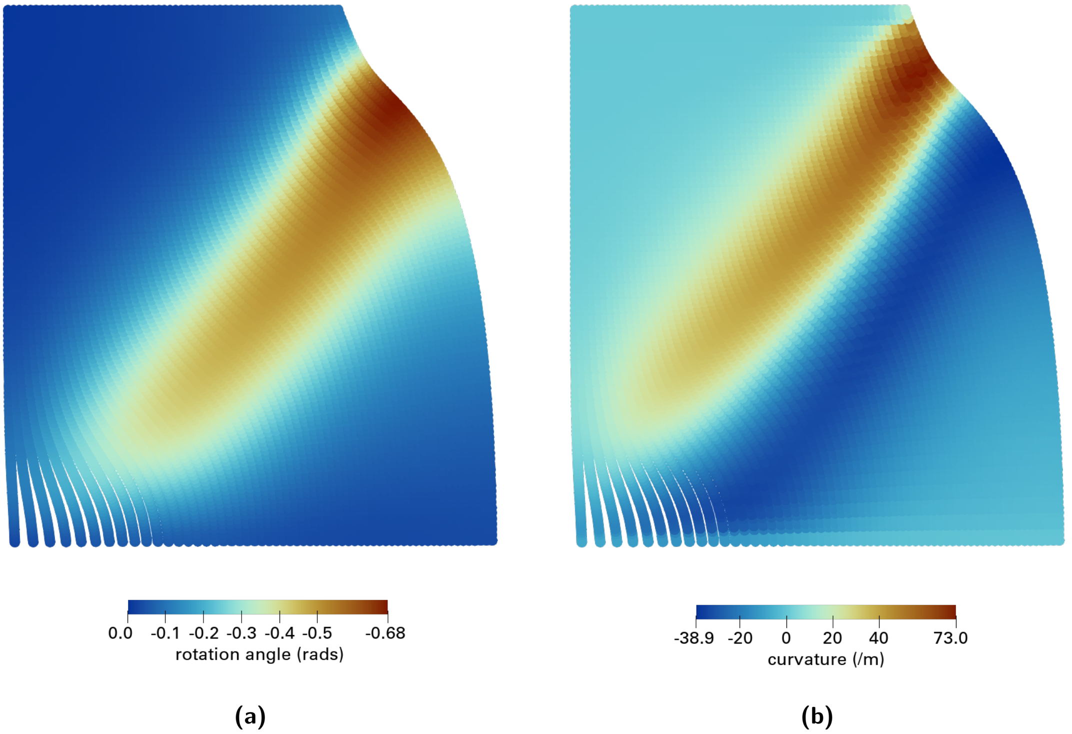

Figure 4.13: Variation in **(a)** in-plane rotation, and **(b)** its total wryness in the vertical direction for $h = 1.25\,\mathrm{mm}$ and $\psi = 10°$.

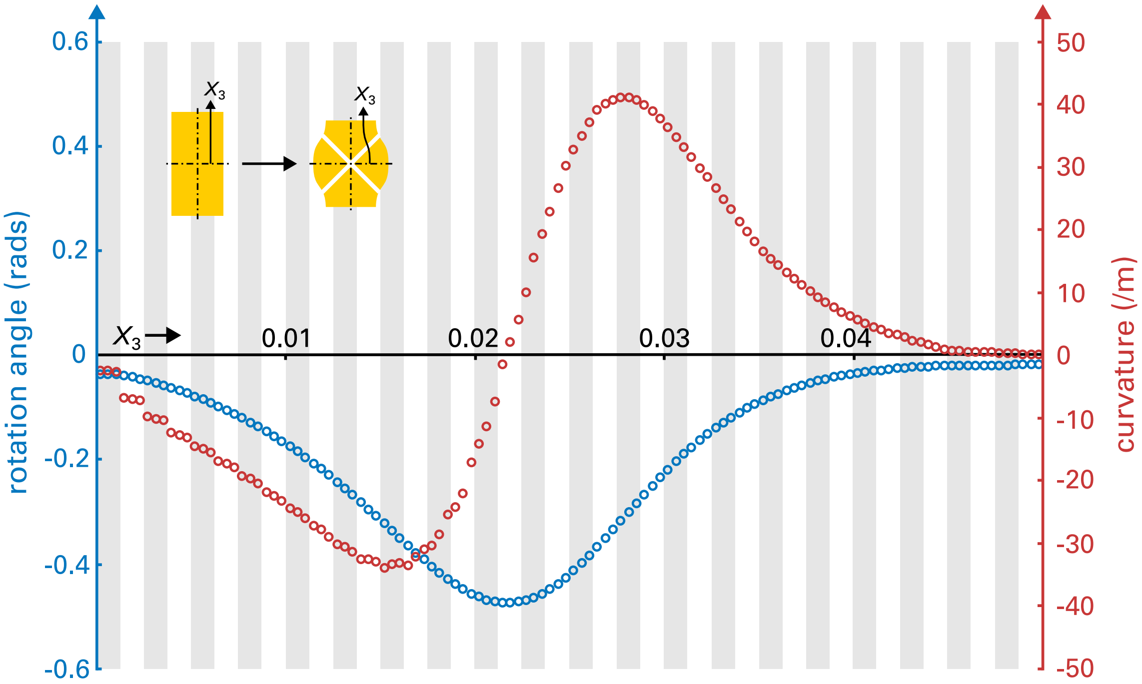

Figure 4.14: Variation in microrotation and its wryness along an originally-vertical line located approximately halfway across the computational domain. Each vertical bar denotes a grid cell.

spatial gradient of the microrotation is clear: the microrotation reaches stationary points where the wryness is approximately zero, and is increasing or decreasing most rapidly when the wryness is respectively at a maximum or minimum. Herein lies the way that the micropolar continuum is able to prevent unphysical, zero-thickness localisation. In regions of the domain where severe rotation gradients emerge, the resultant spikes in wryness act as energetic penalties, and effectively smooth the deformation pattern by a degree determined by the selected internal length scale. In the classical continuum, no such penalty is attached to this higher-order quantity, so there is nothing to prevent the problematic jumps in the gradient of the strain rate which induce discontinuous bifurcation. However, this also highlights a limitation of micropolar theory: regularisation is only possible when rotation gradients emerge – when the structure experiences shearing, in other words. In modes of pure tension or compression, micropolar theory has no special ability, and other methods such as gradient damage [278] or more highly-generalised continuum theories must be used instead (see Section 3.2). In geomaterials, however, concentrated shearing is the predominant failure mechanism across virtually all scales and media [127], and micropolar theory is the natural choice of regularisation technique.

4.5.2 Torsion of microscale cylinders

While not particularly pertinent to geotechnics (or indeed localisation), the torsion experiments performed by Fleck et al. [21] on very thin wires provide a compelling benchmark to validate the model against, particularly as the problem is inherently three-dimensional. In these experiments, five annealed, polycrystalline copper wires of varying diameters were subjected to a monotonic uniaxial torque, and exhibited a pronounced size effect in their yielding and hardening behaviour, as shown in Figure 4.17a. The wire diameters, ranging from 12 to 170 µm, were comparable to the copper grain size, estimated to be between 5 and 25 µm. At smaller scales, the reduced number of grains means that the dislocations produced by torsional straining are less likely to pile up against grain boundaries, avoiding any associated stress concentrations and therefore bringing an effective increase in structural strength. This phenomenon, known as *Hall-Petch strengthening*, cannot be captured by classical plasticity models [168]. The internal lengths of micropolar theory, however, mean that size effects such as this form a natural part of the model's predictive capabilities. The objective of this numerical example is therefore to simulate the torsion of the five wires, and to compare the size effects produced with the experimental results.

The problem is set up as depicted in Figure 4.15. Each wire is simulated as a circular cylinder of diameter and height $2a$, produced computationally by seeding a background grid of $8 \times 8 \times 10$ cells measuring $\frac{a}{2}$ in every dimension with 2^3 generalised interpolation material points each, and removing any whose centroid falls outside the extremities of the cylinder's circular cross section. Roller boundary conditions on its two circular faces prevent the cylinder from deforming in its axial direction (the Poynting effect), and the

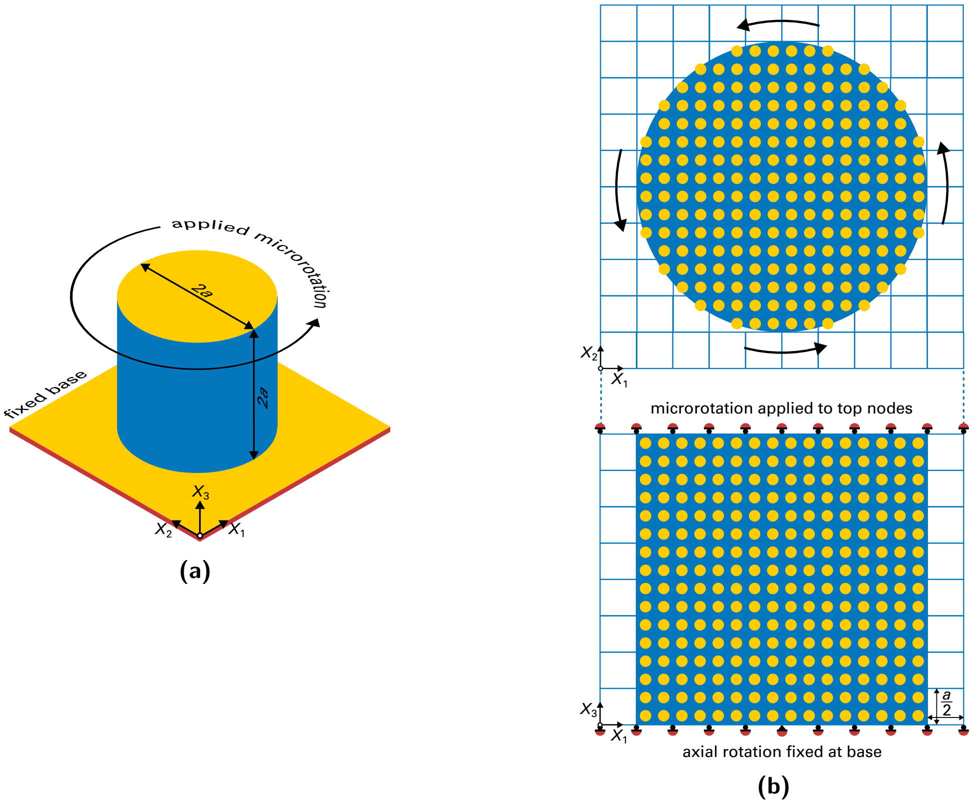

Figure 4.15: **(a)** The setup of the torsion problem and **(b)** its MPM discretisation.

requisite torsion is achieved by applying a 2 rad microrotation evenly across the top face with an adaptive step size, while constraining the axial rotation of the bottom face. A pin at the centre of the base constrains all other translations and microrotations. Some of the elastic parameters are those also selected by Grammenoudis and Tsakmakis [347] to model this particular problem: $\lambda = 69\,\text{GPa}$, $\mu = 46\,\text{GPa}$ and $\kappa = 3\,\text{GPa}$, but the internal length scale is chosen instead to be that proposed originally in [21]: $\ell = 3.7\,\mu\text{m}$. By identifying this with the characteristic length for torsion $\ell_t = \sqrt{\frac{\gamma}{\mu}}$, the principle of bounded stiffness means that $\alpha = -0.419\,38\,\text{N}$, $\gamma = 0.629\,74\,\text{N}$ and $\beta = 0$. Setting $\alpha^{\text{DP}} = \beta^{\text{DP}} = 0$ results in a von Mises yield function and associated flow rule consistent with metal plasticity, parametrised by an initial yield limit $k = 150\,\text{MPa}$ and hardening parameter $H = 75\,\text{MPa}$ with $\ell^{\text{p}} = \ell_t$. Due to the minuscule dimensions of this problem, a smaller energy tolerance than normal of $\bar{e}_{\text{tol}} = 10^{-20}$ is used. An example cylinder is shown in Figure 4.16 in both its reference and final configurations.

Figure 4.17 plots the normalised torque (reaction couple, divided by a^3) against the normalised curvature (angle of twist per length of wire, multiplied by a) which is simply half the applied microrotation, given that each cylinder modelled here is $2a$ in length. The results clearly show the desired size effect: the closer the diameter of the cylinder to the internal length, the greater the developed stiffness, rate of hardening and ultimate torsional capacity. They bear a modest resemblance to the experimental results, especially

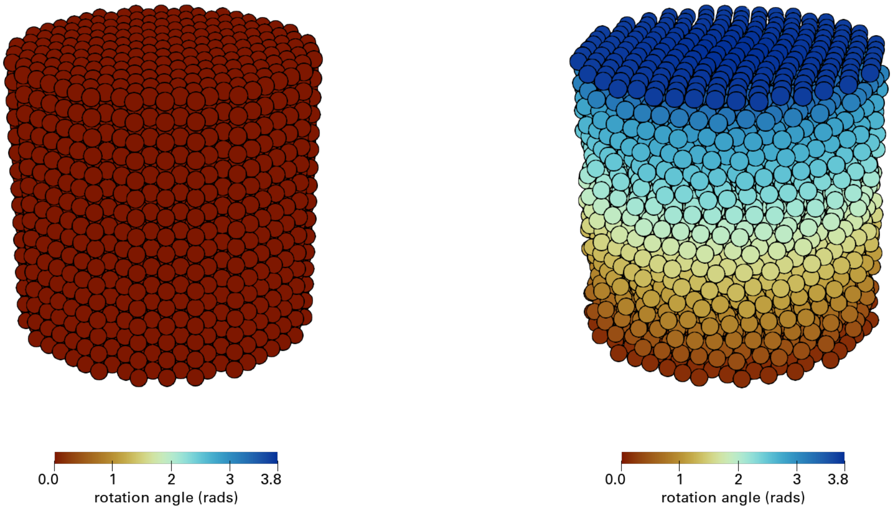

(a) **(b)**

Figure 4.16: The **(a)** undeformed and **(b)** fully deformed 170 µm-diameter cylinder, coloured according to axial rotation angle.

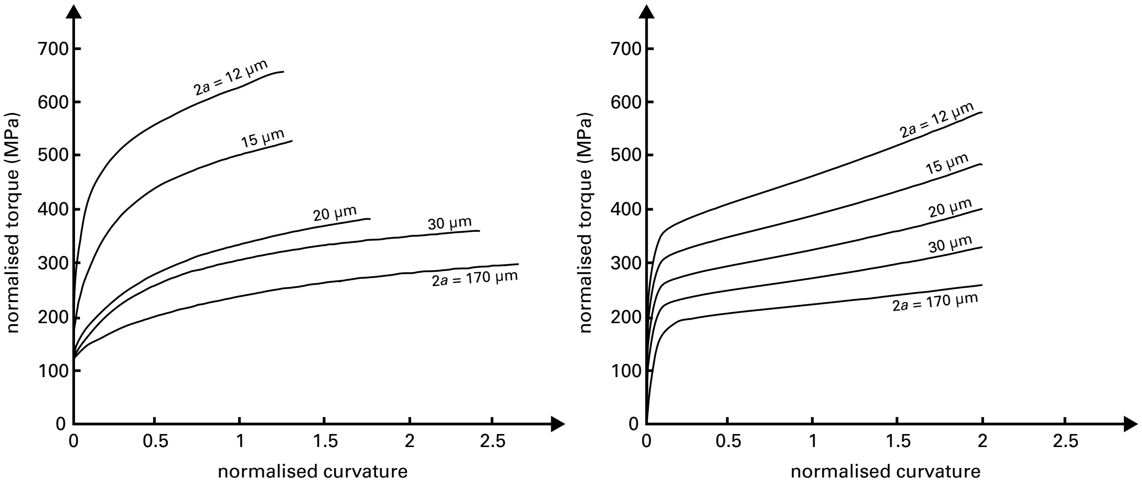

(a) experimental results, adapted from [21, Fig. 6] **(b)** numerical results

Figure 4.17: Normalised torque–curvature graphs for the torsion problem. Without a size dependency every line would be coincident.

for the coarsest three cylinders which demonstrate broadly similar behaviour in both the elastic and plastic regimes. However, the overall shape of the responses seems to differ significantly. This is because the linear, isotropic hardening law used in the computational model is a poor approximation of the real material behaviour, which appears to follow an exponential decay. As such, an impressively close correspondence with experiment is achieved in [347], where a significantly more complex yield function is used in combination with both isotropic and kinematic nonlinear hardening.

The thinnest two specimens give rise to the most obvious disparity between the experimental and numerical results. Upon closer inspection, though, the two experimental curves themselves do not seem particularly consistent with the pattern of the others in its set either, and it may be the case that the apparent discrepancy is due to inconsistencies in experimental procedure, rather than deficiencies in the numerical model. Indeed, the text of [21] reveals that "the larger diameter wires [have] the larger grain sizes." If these are taken to be the three wires for which there is good agreement between results, then attempting to validate the method with the results for $2a = 12\,\mu\text{m}$ and $15\,\mu\text{m}$ would be both futile and pointless anyway. Moreover, it would indicate that the methodology proposed in [347], which assumes a constant (and significantly smaller) characteristic length throughout, is not as rigorous as supposed, suggesting instead that the good agreement between their results and experiment follows from a heuristic tuning of the very large number of material parameters required.

Ultimately, if the two suspect specimens are excluded, then this example shows that the derived method captures size effects ably: the predicted strength and stiffness increase at approximately the appropriate rate as the structural size decreases. This demonstrates the potential of the method to be used in fields outside geomechanics; all that is missing is some further specialisation of the constitutive model towards the particular material of interest. This example also shows that the elastoplastic formulation functions properly in a three-dimensional context. Although the applied rotation is strictly only uniaxial and therefore planar, this only has implications for the kinematic update procedure, which was verified fully in Section 3.5.4. Here it does not limit the scope of the validation of the constitutive model, which operates at a level removed from the kinematics themselves, and is therefore impervious to the dimensionality of the microrotation field.

4.5.3 Column collapse

Traditionally, slope stability problems are extremely challenging to simulate [31]. The pathological problems with strain localisation aside, their inherent severe, concentrated deformations, especially at the toe of the structure, render mesh-based techniques useless (recall Figure 2.1). The final numerical example presented in this thesis, therefore, concerns the collapse of a plane strain column of soil. The purpose is to attempt a true large-deformation problem in a context similar to the types of geotechnical failure event which

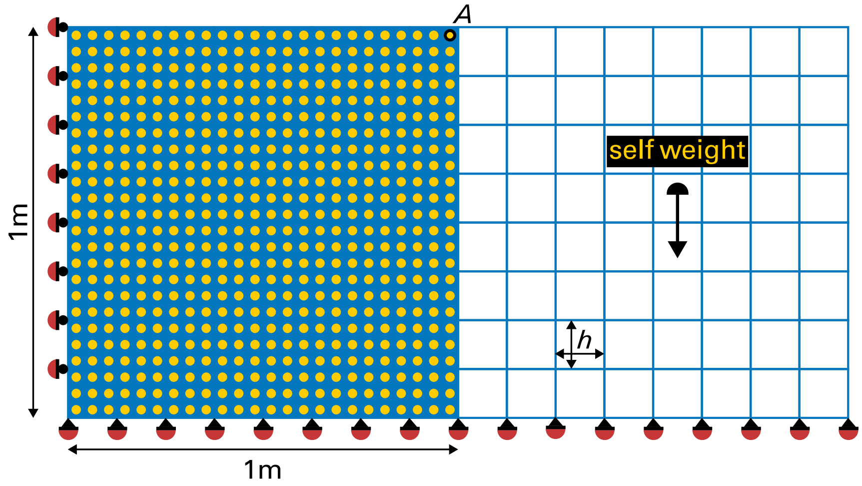

Figure 4.18: Setup of the column collapse problem, showing a discretisation coarser than the one used.

motivate this thesis (and the selection of the MPM): landslides, cuttings and retaining wall failures etc. Therefore it is really more of a qualitative demonstration of the method, rather than a replication of a specific experiment. As depicted in Figure 4.18, the domain consists of a 1 m × 1 m square, constrained horizontally on one side and both horizontally and vertically along its base. It is discretised into 12^2 elements, each measuring $h = 0.0833\,\text{m}$ in every dimension and containing 3^3 generalised interpolation material points. The chosen material properties are as follows: $\lambda = 288.4615\,\text{kPa}$, $\mu = 192.3077\,\text{kPa}$ (corresponding to $E = 500\,\text{kPa}$ and $\nu = 0.3$), $\kappa = \frac{\mu}{8}$, $\ell_b = \ell^{\text{p}} = 0.01\,\text{m}$, $c = 1\,\text{kPa}$, $H = 0$, $\phi = 25°$ and $\psi = 5°$. The global Newton-Raphson tolerances are increased purely for computational expediency to $\bar{f}_{\text{tol}} = 10^{-7}$ and $\bar{e}_{\text{tol}} = 10^{-11}$. The analysis advances by incrementally scaling up the self weight ρg of the structure (applied as a uniformly distributed body force at each material point, where ρ is mass density and g the acceleration due to gravity), using an adaptive routine until the analysis stalls. Again, no imperfection or perturbation is applied.

The displacement (calculated as the L_2-norm of the total translation of material point A shown in Figure 4.18) is plotted against the applied specific weight in Figure 4.19. The geometry of the domain at five specific load steps is also provided in Figure 4.20. Initial yielding (a) begins at $\rho g = 6\,\text{kN}\,\text{m}^{-3}$ following a brief elastic period, with the beginnings of a failure zone nucleating at the stress concentration produced by the boundary conditions at the toe of the column. As the response begins to plateau (b $\rightarrow$ c), the nascent shear band stretches along a well-defined failure plane right through to the top of the domain. Thereafter all further deformation appears to take place exclusively within the localisation zone (d), which shears and dilates severely, ultimately leading to catastrophic collapse of the structure (e). The analysis eventually breaks downs at a specific weight of almost $\rho g = 20\,\text{kN}\,\text{m}^{-3}$ and a settlement in excess of 0.45 m, with an extreme deformation pattern which any mesh-based technique would struggle to cope with without remeshing.

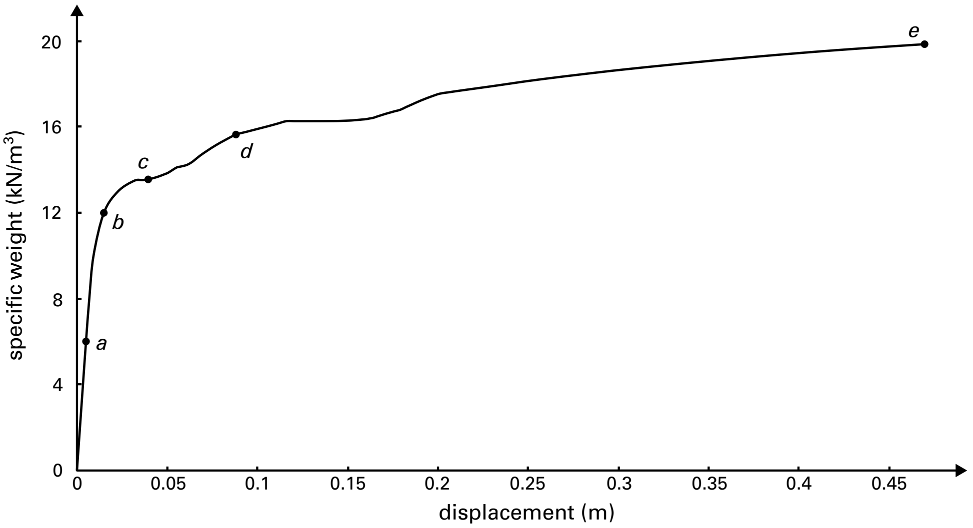

Figure 4.19: Force-displacement curve for the column collapse problem, plotting the specific weight of the material against the displacement at point A. Each annotated point corresponds to a snapshot in Figure 4.20.

An inspection of Figure 4.20 reveals that the shear band in fact changes orientation as the collapse progresses, becoming increasingly steep and leaving behind a ‘wake’ of plastically-deformed material. As with the curved shear bands observed in the biaxial test simulations, this is not a phenomenon which appears to be reproduced elsewhere in the numerical literature. A tentative explanation is as follows. In each load step, the material points are freed from the bias of the previous mesh. Instead, they deform relative to the reset mesh such that a new shear band (at a different orientation) effectively forms each time. Pleasingly, this aligns with empirical evidence which has established that shear bands’ inclinations indeed change as they yield further [345]. This outcome would therefore appear to be a clear strength of the method, as it potentially allows for a more realistic portrayal of geotechnical failure. However, further work is required to understand its true significance more fully.

Although the mesh size used is several times larger than the chosen internal length, the failure pattern is still smooth and continuous, and occupies a region much thicker than a single element width. This indicates that micropolar theory still has some use as a regularisation technique even when coarse discretisations are employed, though the results are not guaranteed to be accurate. Unfortunately, when attempting this problem with a finer mesh resolution, the simulation can barely progress beyond the elastic regime as the global Newton-Raphson search fails to converge as soon as the force-displacement curve begins to plateau, regardless of the adaptive step size. This is likely because the response is more brittle with a finer mesh (as was observed in the previous numerical examples), leading to structural softening which cannot be handled in monotonic load-controlled analyses like this. Instead it would require adoption of an arc-length solution scheme, such as the one developed for the MPM in [348].

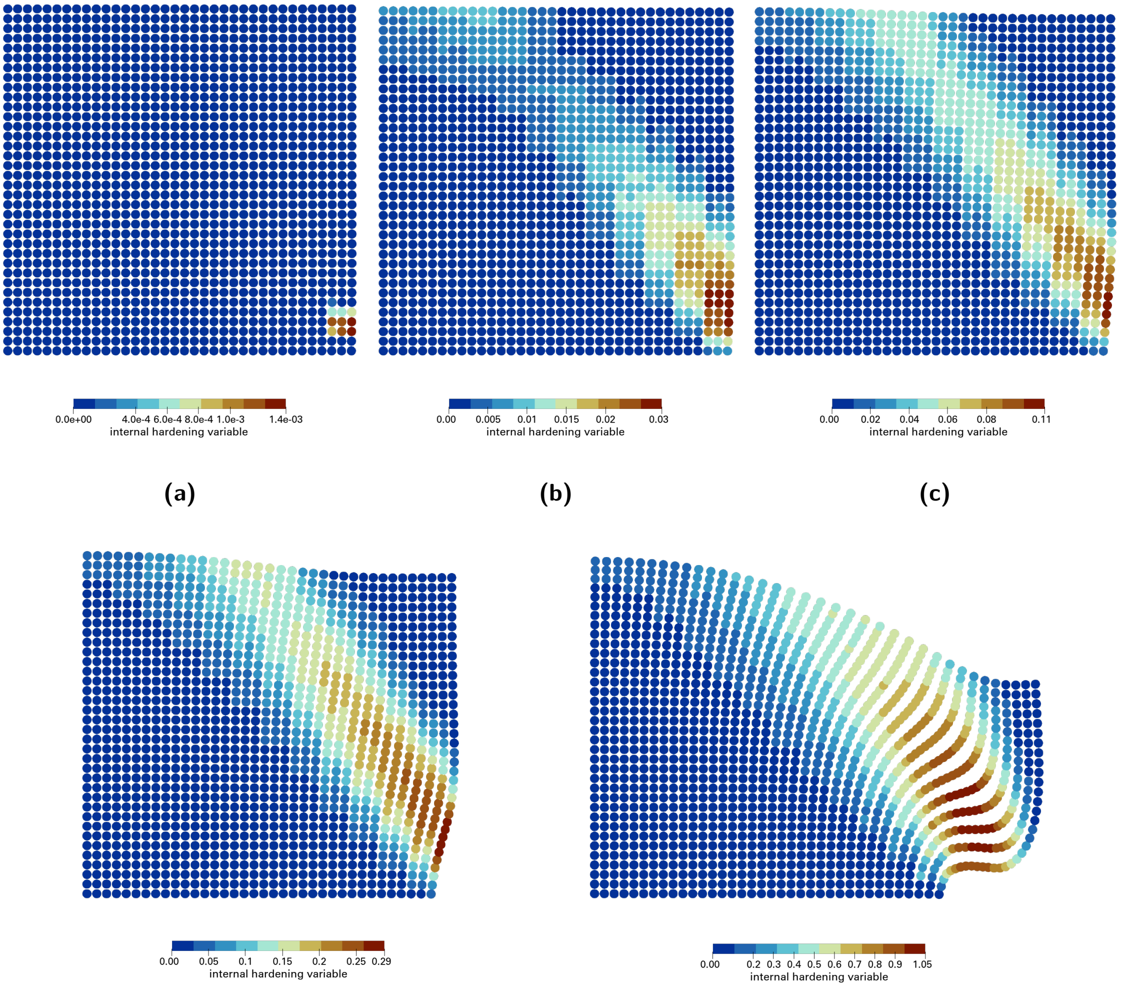

(a) **(b)** **(c)**

(d) **(e)**

Figure 4.20: Progression of the column collapse, coloured according to the internal hardening variable χ. Each figure corresponds to a point shown on Figure 4.19. These results can be viewed in GIF format here.

Alternatively, the failure of these simulations may be indicative of a more fundamental flaw in the methodology. In particular, it is well documented that linear finite element bases struggle to capture modes of localised deformation, and can exhibit shear locking-like behaviour [123]. Indeed, the p-refinement study conducted with a B-spline micropolar MPM in [102] would suggest that classical linear basis functions (i.e. the standard MPM) cannot represent localised shear failure. While the generalised interpolation basis functions employed here have both linear and quadratic sections, at finer levels of discretisation they behave overall more like linear basis functions, as evinced by the convergence study in [129]. Therefore it is possible that beyond a certain mesh resolution threshold, the proposed method simply cannot be used to simulate strain localisation. However, this conclusion would be inconsistent with the results obtained in the preceding numerical examples, in which very obvious shear bands have been successfully simulated across multiple refinement scales. Even in [102], the analysis with standard linear shape functions still ran to completion without suffering numerical breakdown; the response was merely excessively ductile. This particular instability is therefore more likely to have some other explanation – perhaps, as suggested above, simply that the Newton-Raphson solver is encountering an impassable critical point. Equally, it could also be the case that irreconcilable stress states are emerging which lie beyond the apex of the Drucker-Prager cone, or simply that this example requires a higher material point density than 3^3 per cell. Nevertheless, the problem must be thoroughly investigated, understood and overcome before the proposed method can be considered truly robust.

4.6 Remarks

This chapter marks the zenith of this thesis, and sees the development of the final proposed framework for modelling strain localisation in geotechnical structures experiencing large deformations. While the suite of validation problems revealed that the method holds a lot of potential, they also highlighted its key limitations. A particular theme emerged that fundamental non-classical, traditionally challenging phenomena could be captured comfortably (mesh-objective shear bands, size effects, etc.), but close correspondence with real data was invariably eluded. Effectively, this verifies and validates the core elements of the approach, and suggests that extensions of the framework to include more realistic material behaviour would be fruitful.

Particularly remarkable – and novel – is the incidental revelation that the shear bands predicted by the method form at curved, and varying, inclinations. How this relates to real localisation phenomena must be explored in greater depth, but this is nonetheless a promising outcome of this research. However, the instability experienced at certain grid resolutions which was highlighted by the final numerical example must be resolved before the proposed method can be pursued further.

CHAPTER 5

Conclusions

This thesis has been primarily concerned with developing theoretical and numerical models that capture phenomena strongly influenced by microstructural effects. Its central motivation has been the challenge of accurately modelling strain localisation and the catastrophic failures it often precipitates, particularly within geomaterials. While the approach developed in response to this problem has already been verified and validated as part of the main body of work in a relatively insular way, these conclusions relate a broader evaluation of the proposed methods – not only against the criteria and scope set out in Chapter 1, but more widely too.

So has this thesis resolved the modelling problems associated with strain localisation, then? In short, no: there is, of course, still much more work to be done. But that does not make this work in any way a failure, or even a wasted effort; indeed, such a feat would be impossible, and certainly within a single body of work. As an exercise in following one particular approach to localisation in geomechanics it has still borne fruit, and progress, however gradual, is still progress. In fact, this is the basis of almost all modern scientific advancements. The task now at hand is to extract whatever novel developments, findings or insights, however incremental, have emerged from taking this path, and which may be of use or interest to future research efforts or practitioners in this discipline and elsewhere. To that end, the remainder of this chapter is organised according to the two major outcomes from this research: the elastic material point method, and its elastoplastic counterpart. A final, general discussion then draw the thesis to a close.

5.1 Elastic micropolar MPM

Chapter 1 introduces the broader context of this research, while the subsequent chapters explore the analytical and computational barriers which have traditionally impeded the accurate and reliable modelling of localised material failure. It is not until halfway through Chapter 3, when nonlinear micropolar theory and the MPM are selected as a combination worth pursuing, that any novelty emerges. Here, a purely elastic, but geometrically-nonlinear formulation is designed, implemented and tested, with particular attention given to the treatment of microrotations. It is, however, limited in its practical utility: the Saint-Venant-Kirchhoff (StVK) constitutive model, with its linear relationship between stress and strain, "is only of academic interest" in the words of one anonymous reviewer of [112]. Indeed, in its present state, there would not appear to be any scenario to which this framework could be applied for any significant advantage, as reflected by the absence of any identifiable validation problem against which it could be tested. Although the framework can ably predict elastic size effects, the nanoscale applications in which these become apparent (MEMS, wearable electronics, etc.) rarely experience the severe, heterogeneous deformations for which the MPM is uniquely advantageous. As such there is no reason why an equivalent, but more accurate and efficient, FEM could not be used in this context. Nonetheless, as nanotechnology rapidly advances, it is conceivable that future applications, especially involving soft nanomaterials like gels and colloids which are currently under development [349], could benefit from analyses which use a micropolar-based MPM framework.

In developing this formulation, a rotational parametrisation was selected which in truth far exceeds what was really necessary, particularly in geomechanical applications. Though the use of intrinsic microrotation increments (vis-à-vis extrinsic rotations) simplifies the task of consistent linearisation, there is no real benefit to using quaternions here. The attractive continuity they provide at whole revolutions ($\theta \approx 2n\pi$, $\forall\, n \in \mathbb{Z}$) was unlikely to ever be reached in the simulations of geomaterials attempted in this thesis; duly, neither the biaxial test nor the column collapse problem in Chapter 4 generated microrotations in excess of approximately 40°. The other reason often cited in the literature for their use is that quaternions offer an improvement in computation speed [320], as they only require vector arithmetic (recall (3.167)) and thus avoid a (single) multiplication of two 3×3 matrices to update the rotation state. While this might make a difference in explicit analyses – particularly those in computer graphics applications – in implicit analyses the time gained is negligible, especially when a nonlinear constitutive model is used. Therefore, a conceptually much simpler rotational parametrisation employing only intrinsic increments to the microrotation tensor could ultimately have been used to very little detriment. However, developing a framework with greater flexibility than currently required is no bad thing per se, and it is often prudent to be robust against the unexpected. A single material point, say, could have for some unexpected reason exceeded a whole revolution; the resulting artefacts had it done so without a quaternion basis could spoil the entire simulation. A fully-verified, robust three-dimensional rotational capability may also in the future be beneficial in future research directions in as-yet unforeseen ways.

Where this particular method may provide some use, then, might primarily be only as a stepping stone to further developments and more advanced material models. This conclusion should not be particularly surprising or disappointing as, after all, it aligns with the purpose for which the technique was originally conceived. One promising area, for instance, is that of architected metamaterials, which are engineered with distinct structural configurations across multiple scales. Micropolar elasticity inherently captures size-dependent phenomena at the nano- to microscale in materials characterised by cellular, lattice, or foam-like microstructures [193] – indeed, the few available comprehensive sets of micropolar elastic parameters have predominantly been derived for foam-like materials [203]. Coupled with the MPM's capability to handle extreme distortions and self-contact (*densification*, in this context), this combined framework might present potential for simulating the intricate mechanical behaviours underpinning metamaterials' architected properties. Also interesting would be an electromechanical extension of the method, somehow exploiting the connection between micropolar theory and piezoelectricity [206]. Exceedingly little work appears to have taken place so far into modelling the piezoelectric effect with the MPM [350], so this formulation may provide an ideal starting point to explore this area further. However, a worthwhile application would have to be identified first (and potentially this is the factor which accounts for the lack of existing work).

The final observation on this technique relates to its tractability, and an unexpected advantage it possesses. Setting up both torsion problems analysed in this thesis (Sections 3.5.3 and 4.5.2) was remarkably easy, and only required the application of simple boundary conditions in terms of couples or microrotations. Classical, non-polar simulations, on the other hand, require a significantly more complex, configuration-dependent treatment of the boundary to impress a torque or twist. This ability to manipulate micropolar structures to any desired orientation or curvature is the principle which already underpins so-called Cosserat robots [280, 281], but may also be of interest to the computer graphics community, in which the MPM is already widely used. Thus while a purely elastic MPM may be unconvincing within the context of the present work, perhaps it has more value elsewhere.

5.2 Elastoplastic micropolar MPM

The thesis culminated in Chapter 4 with the development of the "advanced computational technique capable of accurately capturing strain localisation in geomaterials," to quote the aim as stated in Chapter 1. Before evaluating its merits, though, it is first useful to revisit why it was deemed necessary to develop this method at all. Classical continuum models inherently fail to predict localised failure accurately, as their outcomes – such as failure load and post-peak response – are heavily influenced by the numerical mesh's resolution and configuration rather than genuine physical processes. Consequently, predictions regarding the timing, extent, or severity of failure are frequently misleading, if not entirely incorrect. Alarmingly, currently available commercial geotechnical software packages do not provide effective solutions to this critical flaw. As a result, geotechnical infrastructure worldwide is often designed and evaluated using analyses that, fundamentally, lack meaningful predictive capability. To more accurately understand, prevent, and mitigate significant geotechnical hazards – such as landslides, fault ruptures, slope failures, and structural collapses – it will thus be essential to adopt modelling approaches more sophisticated than those presently employed.

Could the technique produced and validated in Chapter 4 fulfil this brief? Unlikely, and certainly not in its current form. While it readily captures strain localisation in a manner that appears physically plausible, it does so in a conceptually elaborate way which would discourage most practising geotechnical engineers from applying it. At the same time, it lacks enough ingredients to exhibit realistic material behaviour, rendering it incapable of convincingly replicating standard geotechnical test data. Paradoxically, the method in its proposed form appears to be too complicated to be *useable*, but not complicated enough to be *useful*. As such, the strength of the proposed technique mainly lies in its foundational potential – providing a robust basis from which future refinements and extensions can be made.

In this context, three principal themes were originally identified for the developments of this thesis to address. Namely, the proposed method must (i) be immune to the ill-posedness/mesh-dependency issue, (ii) handle large, complex deformations appropriately, and (iii) be computationally viable for large-scale analyses. Nonlinear micropolar theory was chosen to resolve the first point directly. Indeed, objective solutions were produced by following this approach, as demonstrated in two numerical examples in Chapter 4. However, this outcome is far from novel, and was guaranteed *a priori* from the choice of regularisation technique; had the response instead been mesh-dependent, it would be more indicative of a fault in the implementation than an actual novelty. Similarly, none of the attractive qualities of the approach that follow from employing micropolar theory per se (e.g. grain microrotations, thermodynamic consistency, size effects) can really be claimed as new, or even especially interesting outcomes of this work. On the contrary, they formed the rationale *behind* the selected approach.

What is novel, then, is chiefly the *combination* of micropolar theory with the MPM, which was the chosen response to points (ii) and (iii). Although related studies [102, 233] emerged concurrently, the derived constitutive model is unique, as is the use of an implicit GIMPM and ghost stabilisation. Consequently, this research presents the first instance of an MPM integrated with micropolar regularisation which is explicitly aimed at capturing strain localisation phenomena in soils. The developed numerical framework demonstrates robustness in the presence of finite strains, as clearly evidenced by the numerical examples presented in Chapter 4, successfully avoiding typical instabilities associated with cell-crossing or boundary-induced numerical artefacts. Furthermore the core elements of the formulation (those which distinguish it from conventional and classical approaches) have been verified and validated to a degree that shows that the method, at the very least, holds promise in geomechanics and for modelling size-dependent phenomena. The phenomenology of the model was a critical concern at every stage of its development and, in the opinion of its designer, provides an excellent balance between physical validity, mechanistic and thermodynamical rigour, and simplicity. Indeed, while the model might seem objectively complex, it uses significantly fewer parameters than comparable methods (e.g. [102, 225]) to achieve similar results, and substantial care was taken to minimise those without a compelling physical interpretation. In this sense, the StVK elastic model and its similarly straightforward elastoplastic extension are not necessarily a drawback of the method, but instead present the simplest possible geometrically-exact micropolar continuum which effectively describes localised, pressure-dependent material failure. Consequently, this constitutive framework offers great potential for future research, not necessarily using the MPM, and perhaps even beyond geomechanics.

Another strength of the method lies in its use of implicit time- and stress-integration. The robust Newton-Raphson solvers developed here significantly enhance numerical stability, accuracy, and computational efficiency, even under large deformation conditions. Correspondingly, the comprehensive linearisation details (provided over some thirty pages of appendices) represent a significant output from this research. Perhaps the method's most compelling advantage, though, is the unique way in which the predicted shear bands appear to evolve dynamically through the analysis, following the deformation of the material points. The precise impact of these evolving localisation zones on critical outcomes (such as the global force-displacement response, run-out distances, or post-failure deformation patterns) remains to be fully explored, but their connection to reality initially appears to be corroborated by existing research [345]. Future research in this area promises to enhance the predictive capabilities and clarify the physical realism of micropolar-based MPM models addressing localised failure.

However, several barriers must be overcome to advance the present work towards greater utility, the most obvious being the phenomenological simplicity of the constitutive model which has surfaced throughout the current and previous chapters. To achieve more realistic, more *useful* simulations of geomaterials, a significantly higher degree of nonlinearity must be incorporated into both elastic and elastoplastic formulations. A particularly promising direction involves integrating the recently developed micropolar modified Cam-Clay model by Hofer et al. [351], but the formulation would have to be adapted for geometric nonlinearity first. In classical continuum mechanics, small-strain constitutive models and stress-integration algorithms can be extended to finite strains by employing the Hencky model, which combines Kirchhoff stress with logarithmic strain measures [352]. Finding an analogous approach within the micropolar continuum would be highly beneficial, but the general asymmetries of the stress and deformation tensors make this a challenging, if not impossible task. Alternatively, developing hyperelastic pressure-dependent models similar to those proposed by Houlsby et al. [296] may offer another promising line of enquiry in this direction.

Many of the scenarios for which the developed framework would be most relevant, such as landslides and slope failures, are inherently gravity-driven. As demonstrated in Section 4.5.3, the solution technique adopted in this thesis struggles with force-driven analyses when structural softening occurs, clearly limiting its applicability in such practical cases. To address this significant limitation, adapting an arc-length solver [348] could enhance the method's versatility and robustness, but it may also be the case that a dynamic reformulation would be in general better suited here. This may ultimately be the way this thesis provides most value going forward.

Another notable limitation relates to the connection between the internal length scale and the mesh resolution, particularly concerning the discretisation required to fully exploit its regularising properties. Chapter 4 highlighted that using a mesh coarser than strictly necessary still results in smooth localisation zones but produces a response that is artificially more ductile than realistic, marking a clear drawback of the current method. A promising avenue for future research would be to devise techniques capable of accurately incorporating nonlocal effects at coarser mesh resolutions. For example, directly linking the hardening parameter to element size or developing adaptive meshing strategies that maintain computational efficiency without sacrificing the accuracy of localisation predictions could represent meaningful advancements.

Finally, some concluding remarks on micropolar theory in general. As a continuum approach, it is undoubtedly complicated and intellectually taxing. However, the level of insight it provides about geomaterials is unparalleled among comparable regularisation techniques. What other method directly links failure processes, nonlocally, to rigid rotations of the microstructure, using physically-meaningful material parameters? For this reason, the author believes that the micropolar approach might represent an *optimal* regularisation technique in a geomechanical context, and still holds significant potential. But for micropolar theory to gain more widespread acceptance, far more work must be done first to disseminate its virtues and demystify its complexities. Particularly essential is the derivation and validation of a more rigorous and *manageable* approach to determining its extra material parameters, continuing Vardoulakis' experimental legacy [312]. If these goals are achieved, there is nothing to prevent micropolar theory from being used much more broadly, and even within commercial codes. Only time will tell if the contents of this thesis will contribute.

5.3 How do you solve a problem like *strain localisation*?

It was established early on in this thesis that strain localisation, long a subject of fascination and inquiry, continues to elude simple solutions and complete characterisation. Despite the centuries of research devoted to it, it remains as much a conceptual challenge as a mechanical one. The preceding chapters have responded to this persistent problem from a particular standpoint – one grounded in a kind of mechanistic and mathematical meticulousness. This approach, often labelled *rigour*, favours formal consistency and thoroughness, sometimes at the expense of simplicity or computational convenience, but with an earnest desire to capture some kind of physical truth or realism. It reflects a key paradigm in engineering science: one that has been instrumental in advancing our understanding of complex natural phenomena. But no matter how thermodynamically-consistent a formulations is, what degree of nonlinearity it contains, or how precisely its solutions can be procured, it will always ultimately remain a *model* – a model built from concepts, assumptions and interpretative choices. No model can ever be the reality it attempts to describe, and hence a 'perfect' degree of rigour is illusory. To strive for 'completeness' purely for its own sake is, then, misguided. Likewise, to judge a model solely on how closely it mimics some perceived realism is to misunderstand the purpose of modelling. The value of a model is not absolute but arises in relation to the context of its development and use, and where its limitations are acknowledged transparently. A model that has clearly defined applications and boundaries is far more useful than one which attempts to explain everything.

Such was the premise of this chapter, and indeed the thesis as a whole. The methods developed herein are, in many ways, sophisticated – but they are also necessarily incomplete. And it is precisely *because* they are limited that they have value. Understanding where a model ceases to be valid does not undermine its utility; on the contrary, it makes its utility more meaningful. It more clearly defines its strengths, situates its purpose within its context, and points to clear directions for further development. From this perspective, the idea of a definitive solution to the strain localisation problem becomes not only unrealistic but also undesirable. The question posed by the heading remains entirely rhetorical: can localisation ever truly be solved, or is it, by nature, a phenomenon that must always remain partially beyond reach? Arguably, it is far more useful to us this way – not as a puzzle to be definitively solved, but as a lens through which we can come to a more nuanced engagement with the phenomenon.

This thesis does not claim to have 'solved' strain localisation. Nor does it rest on the fallacy that such a solution is possible. Like all conceptual frameworks, models emerge from human thought, briefly illuminating certain aspects of reality while inevitably leaving others obscured. Recognising this allows for continued progress, not through achieving definitive answers but through deepening our understanding of what makes these questions complex and worthy of continued investigation.

> *All composed things are like a dream,*
> *a phantom, a drop of dew, a flash of lightning.*
> *That is how to meditate on them,*
> *that is how to observe them.*
>
> —Vajracchedikā Prajñāpāramitā Sūtra (*The Diamond that Cuts through Illusion*)

APPENDIX A

Linearisation of the nonlinear elastic problem

In this appendix, the analytical consistent linearisation of the discretised internal force and couple vectors $\boldsymbol{p}^{\text{int}}$ and $\boldsymbol{q}^{\text{int}}$ with respect to incremental translations $\boldsymbol{u}$ and spin microrotations $\boldsymbol{\varphi}$ is presented. Expressions for the consistent tangent $\boldsymbol{K}$ are produced, formed from four subtangents defined

$$\begin{Bmatrix} \delta\boldsymbol{p}^{\text{int}} \\ \delta\boldsymbol{q}^{\text{int}} \end{Bmatrix} = \begin{bmatrix} \boldsymbol{K}^{pu} & \boldsymbol{K}^{p\varphi} \\ \boldsymbol{K}^{qu} & \boldsymbol{K}^{q\varphi} \end{bmatrix} \begin{Bmatrix} \delta\boldsymbol{u} \\ \delta\boldsymbol{\varphi} \end{Bmatrix} , \tag{A.1}$$

which are used in the Newton-Raphson solution of the global boundary-value problem. The linearisation is presented as comprehensively as possible using index notation due to its highly intricate nature. To aid intelligibility, certain conventions are adopted in notating tensor indices, which here are defined according to a three-dimensional Cartesian frame. Namely, lower-case Latin letters are used for spatial quantities, lower-case Greek for material, and upper-case Latin for node numbers. This means, for instance, that u_{Hi} would refer to a translation recorded at node H in coordinate direction i. For greater clarity and to avoid ambiguity, nodal basis functions N are used rather than MPM weighting functions S_{vp} specifically.

A.1 Linearisation of the internal force vector

In index notation, the Galerkin expression for the internal force is

$$p_{Ii}^{\text{int}} = \int_{\Omega} \frac{\partial N_I}{\partial x_r} \sigma_{ir} \, \mathrm{d}\Omega \, , \tag{A.2}$$

but it is more convenient to frame this equation in the reference configuration than to account for the changing domain size. The formula $\mathrm{d}\Omega = J\,\mathrm{d}\Omega_0$ leads to

$$p^{\text{int}}_{Ii} = \int_{\Omega_0} \frac{\partial N_I}{\partial x_r} \tau_{ir}\,\mathrm{d}\Omega_0 \tag{A.3}$$

in terms of Kirchhoff stress $\boldsymbol{\tau} = J\boldsymbol{\sigma}$.

A.1.1 With respect to translations

First, by the linearity of differential operators,

$$\begin{aligned}
\frac{\partial F_{m\theta}}{\partial u_{Jj}} &= \frac{\partial}{\partial u_{Jj}} \left(\frac{\partial x_m}{\partial X_\theta} \right) && \text{(A.4)}\\
&= \frac{\partial}{\partial u_{Jj}} \left(\delta_{m\theta} + \frac{\partial u_m}{\partial X_\theta} \right) && \text{(A.5)}\\
&= \frac{\partial}{\partial X_\theta} \left(\frac{\partial u_m}{\partial u_{Jj}} \right) && \text{(A.6)}\\
&= \frac{\partial}{\partial X_\theta} \left(\frac{\partial}{\partial u_{Jj}} \left(N_H u_{Hm} \right) \right) && \text{(A.7)}\\
&= \frac{\partial}{\partial X_\theta} \left(N_H \delta_{HJ} \delta_{jm} \right) && \text{(A.8)}\\
&= \delta_{jm} \frac{\partial N_J}{\partial X_\theta} = \delta_{jm} \frac{\partial N_J}{\partial x_s} F_{s\theta}. && \text{(A.9)}
\end{aligned}$$

Through the application of the chain rule,

$$\begin{aligned}
K^{pu}_{IiJj} &= \frac{\partial p^{\text{int}}_{Ii}}{\partial u_{Jj}} && \text{(A.10)}\\
&= \int_{\Omega_0} \frac{\partial}{\partial u_{Jj}} \left(\frac{\partial N_I}{\partial x_r} \tau_{ir} \right) \mathrm{d}\Omega_0 && \text{(A.11)}\\
&= \int_{\Omega_0} \frac{\partial}{\partial F_{m\theta}} \left(\frac{\partial N_I}{\partial x_r} \tau_{ir} \right) \frac{\partial F_{m\theta}}{\partial u_{Jj}}\,\mathrm{d}\Omega_0 && \text{(A.12)}\\
&= \int_{\Omega_0} \frac{\partial}{\partial F_{m\theta}} \left(\frac{\partial N_I}{\partial x_r} \tau_{ir} \right) \delta_{jm} \frac{\partial N_J}{\partial x_s} F_{s\theta}\,\mathrm{d}\Omega_0\,. && \text{(A.13)}
\end{aligned}$$

Then by the product rule

$$\frac{\partial}{\partial F_{m\theta}} \left(\frac{\partial N_I}{\partial x_r} \tau_{ir} \right) = \frac{\partial}{\partial F_{m\theta}} \left(\frac{\partial N_I}{\partial x_r} \right) \tau_{ir} + \frac{\partial N_I}{\partial x_r} \frac{\partial \tau_{ir}}{\partial F_{m\theta}} \tag{A.14}$$

where

$$\begin{aligned}
\frac{\partial}{\partial F_{m\theta}} \left(\frac{\partial N_I}{\partial x_r} \right) &= \frac{\partial}{\partial F_{m\theta}} \left(\frac{\partial N_I}{\partial X_\rho} F^{-1}_{\rho r} \right) && \text{(A.15)}\\
&= \frac{\partial N_I}{\partial X_\rho} \frac{\partial F^{-1}_{\rho r}}{\partial F_{m\theta}} && \text{(A.16)}
\end{aligned}$$

$$= -\frac{\partial N_I}{\partial X_\rho} F^{-1}_{\rho m} F^{-1}_{\theta r} \tag{A.17}$$

$$= -\frac{\partial N_I}{\partial x_m} F^{-1}_{\theta r} \tag{A.18}$$

such that (A.14) now becomes

$$\frac{\partial}{\partial F_{m\theta}} \left(\frac{\partial N_I}{\partial x_r} \tau_{ir} \right) = \frac{\partial N_I}{\partial x_r} \frac{\partial \tau_{ir}}{\partial F_{m\theta}} - \frac{\partial N_I}{\partial x_m} \tau_{ir} F^{-1}_{\theta r}. \tag{A.19}$$

Meanwhile, substitution of the Biot stress definition (3.70), constitutive equation (3.122) and strain (3.34) leads to

$$\begin{aligned}
\frac{\partial \tau_{ir}}{\partial F_{m\theta}} &= \frac{\partial}{\partial F_{m\theta}} \left(Q_{i\alpha} B_{\alpha\beta} F_{r\beta} \right) && \text{(A.20)}\\
&= Q_{i\alpha} \left(\frac{\partial B_{\alpha\beta}}{\partial F_{m\theta}} F_{r\beta} + B_{\alpha\beta} \frac{\partial F_{r\beta}}{\partial F_{m\theta}} \right) && \text{(A.21)}\\
&= Q_{i\alpha} \left(\frac{\partial}{\partial F_{m\theta}} (D_{\alpha\beta\gamma\pi} E_{\gamma\pi}) F_{r\beta} + B_{\alpha\beta} \delta_{rm} \delta_{\beta\theta} \right) && \text{(A.22)}\\
&= Q_{i\alpha} \left(\frac{\partial}{\partial F_{m\theta}} (D_{\alpha\beta\gamma\pi} (Q_{i\gamma} F_{i\pi} - \delta_{\gamma\pi})) F_{r\beta} + B_{\alpha\theta} \delta_{rm} \right) && \text{(A.23)}\\
&= Q_{i\alpha} \left(D_{\alpha\beta\gamma\pi} Q_{i\gamma} \frac{\partial F_{i\pi}}{\partial F_{m\theta}} F_{r\beta} + B_{\alpha\theta} \delta_{rm} \right) && \text{(A.24)}\\
&= Q_{i\alpha} \left(D_{\alpha\beta\gamma\pi} Q_{i\gamma} \delta_{im} \delta_{\pi\theta} F_{r\beta} + B_{\alpha\theta} \delta_{rm} \right) && \text{(A.25)}\\
&= Q_{i\alpha} \left(D_{\alpha\beta\gamma\theta} Q_{m\gamma} F_{r\beta} + B_{\alpha\theta} \delta_{rm} \right) && \text{(A.26)}
\end{aligned}$$

which can be substituted into (A.19) for

$$\begin{aligned}
\frac{\partial}{\partial F_{m\theta}} \left(\frac{\partial N_I}{\partial x_r} \tau_{ir} \right) &= \frac{\partial N_I}{\partial x_r} Q_{i\alpha} \left(D_{\alpha\beta\gamma\theta} Q_{m\gamma} F_{r\beta} + B_{\alpha\theta} \delta_{rm} \right) - \frac{\partial N_I}{\partial x_m} \tau_{ir} F^{-1}_{\theta r} && \text{(A.27)}\\
&= \frac{\partial N_I}{\partial x_r} Q_{i\alpha} F_{r\beta} D_{\alpha\beta\gamma\theta} Q_{m\gamma} + \frac{\partial N_I}{\partial x_m} \left(Q_{i\alpha} B_{\alpha\theta} - \tau_{ir} F^{-1}_{\theta r} \right) && \text{(A.28)}\\
&= \frac{\partial N_I}{\partial x_r} Q_{i\alpha} F_{r\beta} D_{\alpha\beta\gamma\theta} Q_{m\gamma} + \frac{\partial N_I}{\partial x_m} \left(Q_{i\alpha} B_{\alpha\theta} - Q_{i\alpha} B_{\alpha\beta} F_{r\beta} F^{-1}_{\theta r} \right) && \text{(A.29)}\\
&= \frac{\partial N_I}{\partial x_r} Q_{i\alpha} F_{r\beta} D_{\alpha\beta\gamma\theta} Q_{m\gamma} + \frac{\partial N_I}{\partial x_m} \left(Q_{i\alpha} B_{\alpha\theta} - Q_{i\alpha} B_{\alpha\theta} \right) && \text{(A.30)}\\
&= \frac{\partial N_I}{\partial x_r} L_{ir\alpha\beta} D_{\alpha\beta\gamma\theta} Q_{m\gamma}. && \text{(A.31)}
\end{aligned}$$

where $L_{ir\alpha\beta} = Q_{i\alpha} F_{r\beta}$ is a fourth-order dyadic stretch tensor. And finally, the expression for tangent stiffness is

$$\begin{aligned}
K^{pu}_{IiJj} &= \int_{\Omega_0} \frac{\partial N_I}{\partial x_r} L_{ir\alpha\beta} D_{\alpha\beta\gamma\theta} Q_{m\gamma} \frac{\partial N_J}{\partial x_s} F_{s\theta} \delta_{jm} \, \mathrm{d}\Omega_0 && \text{(A.32)}\\
&= \int_{\Omega} \frac{\partial N_I}{\partial x_r} J^{-1} L_{ir\alpha\beta} D_{\alpha\beta\gamma\theta} L_{js\gamma\theta} \frac{\partial N_J}{\partial x_s} \, \mathrm{d}\Omega && \text{(A.33)}
\end{aligned}$$

$$= \int_\Omega \frac{\partial N_I}{\partial x_r} (a_1)_{irjs} \frac{\partial N_J}{\partial x_s} \, \mathrm{d}\Omega \tag{A.34}$$

$$= \int_\Omega G_{arIi} (a_1)_{arbs} G_{bsJj} \, \mathrm{d}\Omega \tag{A.35}$$

where

$$(a_1)_{arbs} = J^{-1} L_{ar\alpha\beta} D_{\alpha\beta\gamma\theta} L_{bs\gamma\theta} \tag{A.36}$$

is a tangent modulus and

$$G_{arIi} = \frac{\partial N_I}{\partial x_r} \delta_{ai}. \tag{A.37}$$

A.1.2 With respect to microrotations

The Newton-Raphson algorithm is constructed in terms of intrinsic microrotation vector increments $\delta\boldsymbol{\varphi}$, therefore linearisation occurs with respect to this quantity, not the extrinsic total rotation vector $\boldsymbol{\theta}$. Since microrotations have no effect on volume change (i.e. $\frac{\partial J}{\partial \varphi_s} = 0$), the evolution of the domain size is inconsequential here. Hence,

$$K^{p\varphi}_{IiJj} = \frac{\partial p^{\mathrm{int}}_{Ii}}{\partial \varphi_{Jj}} \tag{A.38}$$

$$= \int_\Omega \frac{\partial}{\partial \varphi_{Jj}} \left(\frac{\partial N_I}{\partial x_r} \sigma_{ir} \right) \mathrm{d}\Omega \tag{A.39}$$

$$= \int_\Omega \frac{\partial}{\partial Q_{m\theta}} \left(\frac{\partial N_I}{\partial x_r} \sigma_{ir} \right) \frac{\partial Q_{m\theta}}{\partial \varphi_{Jj}} \, \mathrm{d}\Omega \tag{A.40}$$

$$= \int_\Omega \frac{\partial N_I}{\partial x_r} \frac{\partial \sigma_{ir}}{\partial Q_{m\theta}} \frac{\partial Q_{m\theta}}{\partial \varphi_s} \frac{\partial \varphi_s}{\partial \varphi_{Jj}} \, \mathrm{d}\Omega \tag{A.41}$$

$$= \int_\Omega \frac{\partial N_I}{\partial x_r} \frac{\partial \sigma_{ir}}{\partial Q_{m\theta}} \frac{\partial Q_{m\theta}}{\partial \varphi_s} \frac{\partial (N_H \varphi_{Hs})}{\partial \varphi_{Jj}} \, \mathrm{d}\Omega \tag{A.42}$$

$$= \int_\Omega \frac{\partial N_I}{\partial x_r} \frac{\partial \sigma_{ir}}{\partial Q_{m\theta}} \frac{\partial Q_{m\theta}}{\partial \varphi_s} \left(N_H \delta_{HJ} \delta_{sj} \right) \mathrm{d}\Omega \tag{A.43}$$

$$= \int_\Omega \frac{\partial N_I}{\partial x_r} \frac{\partial \sigma_{ir}}{\partial Q_{m\theta}} \frac{\partial Q_{m\theta}}{\partial \varphi_j} N_J \, \mathrm{d}\Omega \,. \tag{A.44}$$

Then

$$\frac{\partial \sigma_{ir}}{\partial Q_{m\theta}} = \frac{\partial}{\partial Q_{m\theta}} \left(J^{-1} Q_{i\alpha} B_{\alpha\beta} F_{r\beta} \right) \tag{A.45}$$

$$= J^{-1} \left(\frac{\partial Q_{i\alpha}}{\partial Q_{m\theta}} B_{\alpha\beta} + Q_{i\alpha} \frac{\partial B_{\alpha\beta}}{\partial Q_{m\theta}} \right) F_{r\beta} \tag{A.46}$$

$$= J^{-1} \left(\delta_{im} \delta_{\alpha\theta} B_{\alpha\beta} + Q_{i\alpha} \frac{\partial}{\partial Q_{m\theta}} (D_{\alpha\beta\gamma\pi} E_{\gamma\pi}) \right) F_{r\beta} \tag{A.47}$$

$$= J^{-1} \left(\delta_{im} B_{\theta\beta} + Q_{i\alpha} D_{\alpha\beta\gamma\pi} \frac{\partial}{\partial Q_{m\theta}} (Q_{k\gamma} F_{k\pi} - \delta_{\gamma\pi}) \right) F_{r\beta} \tag{A.48}$$

$$= J^{-1}\left(\delta_{im}B_{\theta\beta} + Q_{i\alpha}D_{\alpha\beta\gamma\pi}\frac{\partial Q_{k\gamma}}{\partial Q_{m\theta}}F_{k\pi}\right)F_{r\beta} \tag{A.49}$$

$$= J^{-1}\left(\delta_{im}B_{\theta\beta} + Q_{i\alpha}D_{\alpha\beta\gamma\pi}\delta_{km}\delta_{\gamma\theta}F_{k\pi}\right)F_{r\beta} \tag{A.50}$$

$$= J^{-1}\delta_{im}B_{\theta\beta}F_{r\beta} + J^{-1}L_{ir\alpha\beta}D_{\alpha\beta\theta\pi}F_{m\pi}. \tag{A.51}$$

The derivative of the microrotation tensor with respect to a superposed microrotation vector increment from the follower axes is obtained as (see 3.4.1)

$$\frac{\partial Q_{m\theta}}{\partial \varphi_j} = e_{mjn}Q_{n\theta} \tag{3.162}$$

which can be multiplied by (A.51) to give

$$\frac{\partial \sigma_{ir}}{\partial Q_{m\theta}}\frac{\partial Q_{m\theta}}{\partial \varphi_j} = (J^{-1}\delta_{im}B_{\theta\beta}F_{r\beta} + J^{-1}L_{ir\alpha\beta}D_{\alpha\beta\theta\pi}F_{m\pi})e_{mjn}Q_{n\theta} \tag{A.52}$$

$$= (J^{-1}\delta_{im}Q_{n\theta}B_{\theta\beta}F_{r\beta} + J^{-1}L_{ir\alpha\beta}D_{\alpha\beta\theta\pi}L_{nm\theta\pi})e_{mjn} \tag{A.53}$$

$$= (\delta_{im}\sigma_{nr} + J^{-1}L_{ir\alpha\beta}D_{\alpha\beta\theta\pi}L_{nm\theta\pi})e_{mjn} \tag{A.54}$$

to be substituted into (A.44) for

$$K^{p\varphi}_{IiJj} = \int_\Omega \frac{\partial N_I}{\partial x_r}\left(J^{-1}L_{ir\alpha\beta}D_{\alpha\beta\theta\pi}L_{nm\theta\pi} + \delta_{im}\sigma_{nr}\right)e_{mjn}N_J\,\mathrm{d}\Omega \tag{A.55}$$

$$= \int_\Omega \frac{\partial N_I}{\partial x_r}(a_2)_{irnm}e_{nmj}N_J\,\mathrm{d}\Omega \tag{A.56}$$

$$= \int_\Omega G_{brIi}(a_2)_{brnm}\check{G}_{nmJj}\,\mathrm{d}\Omega \tag{A.57}$$

where

$$\check{G}_{nmJj} = e_{nmj}N_J. \tag{A.58}$$

Conveniently,

$$(a_2)_{brnm} = (a_1)_{brnm} + \delta_{bm}\sigma_{nr}. \tag{A.59}$$

A.2 Linearisation of the internal couple vector

The Galerkin form of the internal couple is written

$$q^{\text{int}}_{Ii} = \int_\Omega \left(\frac{\partial N_I}{\partial x_r}\mu_{ir} + N_I e_{irn}\sigma_{rn}\right)\mathrm{d}\Omega\,, \tag{A.60}$$

which is equivalent to

$$q^{\text{int}}_{Ii} = \int_{\Omega_0} \left(\frac{\partial N_I}{\partial x_r}\nu_{ir} + N_I e_{irn}\tau_{rn}\right)\mathrm{d}\Omega_0 \tag{A.61}$$

on the reference volume.

A.2.1 With respect to translations

Reusing (A.9), the tangent stiffness is

$$
\begin{aligned}
K^{qu}_{IiJj} &= \frac{\partial q^{\text{int}}_{Ii}}{\partial u_{Jj}} && \text{(A.62)}\\
&= \int_{\Omega_0} \frac{\partial}{\partial u_{Jj}} \left(\frac{\partial N_I}{\partial x_r} \nu_{ir} + N_I e_{irn} \tau_{rn} \right) \mathrm{d}\Omega_0 && \text{(A.63)}\\
&= \int_{\Omega_0} \frac{\partial}{\partial F_{m\theta}} \left(\frac{\partial N_I}{\partial x_r} \nu_{ir} + N_I e_{irn} \tau_{rn} \right) \frac{\partial F_{m\theta}}{\partial u_{Jj}} \,\mathrm{d}\Omega_0 && \text{(A.64)}\\
&= \int_{\Omega_0} \frac{\partial}{\partial F_{m\theta}} \left(\frac{\partial N_I}{\partial x_r} \nu_{ir} + N_I e_{irn} \tau_{rn} \right) \frac{\partial N_J}{\partial x_s} F_{s\theta} \delta_{jm} \,\mathrm{d}\Omega_0 && \text{(A.65)}\\
&= \int_{\Omega_0} \left(\frac{\partial}{\partial F_{j\theta}} \left(\frac{\partial N_I}{\partial x_r} \nu_{ir} \right) + N_I e_{irn} \frac{\partial \tau_{rn}}{\partial F_{j\theta}} \right) \frac{\partial N_J}{\partial x_s} F_{s\theta} \,\mathrm{d}\Omega_0 && \text{(A.66)}
\end{aligned}
$$

where, following (A.19),

$$
\frac{\partial}{\partial F_{j\theta}} \left(\frac{\partial N_I}{\partial x_r} \nu_{ir} \right) = \frac{\partial N_I}{\partial x_r} \frac{\partial \nu_{ir}}{\partial F_{j\theta}} - \frac{\partial N_I}{\partial x_j} \nu_{ir} F^{-1}_{\theta r}. \qquad \text{(A.67)}
$$

Using the definition of Biot couple-stress (3.71),

$$
\begin{aligned}
\frac{\partial \nu_{ir}}{\partial F_{j\theta}} &= \frac{\partial}{\partial F_{j\theta}} (Q_{i\alpha} S_{\alpha\beta} F_{r\beta}) && \text{(A.68)}\\
&= Q_{i\alpha} S_{\alpha\beta} \frac{\partial F_{r\beta}}{\partial F_{j\theta}} && \text{(A.69)}\\
&= Q_{i\alpha} S_{\alpha\beta} \delta_{rj} \delta_{\beta\theta} && \text{(A.70)}\\
&= Q_{i\alpha} S_{\alpha\theta} \delta_{rj} && \text{(A.71)}
\end{aligned}
$$

so that (A.67) becomes

$$
\begin{aligned}
\frac{\partial}{\partial F_{j\theta}} \left(\frac{\partial N_I}{\partial x_r} \nu_{ir} \right) &= \frac{\partial N_I}{\partial x_r} Q_{i\alpha} S_{\alpha\theta} \delta_{rj} - \frac{\partial N_I}{\partial x_j} \nu_{ir} F^{-1}_{\theta r} && \text{(A.72)}\\
&= \frac{\partial N_I}{\partial x_j} \left(Q_{i\alpha} S_{\alpha\theta} - \nu_{ir} F^{-1}_{\theta r} \right) && \text{(A.73)}\\
&= \frac{\partial N_I}{\partial x_j} \left(\nu_{ir} F^{-1}_{\theta r} - \nu_{ir} F^{-1}_{\theta r} \right) && \text{(A.74)}\\
&= 0. && \text{(A.75)}
\end{aligned}
$$

From (A.66), and using (A.26),

$$
\begin{aligned}
N_I e_{irn} \frac{\partial \tau_{rn}}{\partial F_{j\theta}} F_{s\theta} &= N_I e_{irn} \left(Q_{r\alpha} \left(D_{\alpha\beta\gamma\theta} Q_{j\gamma} F_{n\beta} + B_{\alpha\theta} \delta_{nj} \right) \right) F_{s\theta} && \text{(A.76)}\\
&= N_I e_{irn} \left(L_{rn\alpha\beta} D_{\alpha\beta\gamma\theta} L_{js\gamma\theta} + Q_{r\alpha} B_{\alpha\theta} \delta_{nj} F_{s\theta} \right) && \text{(A.77)}\\
&= N_I e_{irn} \left(L_{rn\alpha\beta} D_{\alpha\beta\gamma\theta} L_{js\gamma\theta} + \delta_{nj} \tau_{rs} \right) && \text{(A.78)}
\end{aligned}
$$

and, putting everything together,

$$K^{qu}_{IiJj} = \int_{\Omega_0} \left(N_I e_{irn} \left(L_{rn\alpha\beta} D_{\alpha\beta\gamma\theta} L_{js\gamma\theta} + \delta_{nj}\tau_{rs}\right)\right) \frac{\partial N_J}{\partial x_s}\,\mathrm{d}\Omega_0 \tag{A.79}$$

$$= \int_{\Omega} \left(N_I e_{irn} \left(J^{-1} L_{rn\alpha\beta} D_{\alpha\beta\gamma\theta} L_{js\gamma\theta} + \delta_{nj}\sigma_{rs}\right)\right) \frac{\partial N_J}{\partial x_s}\,\mathrm{d}\Omega \tag{A.80}$$

$$= \int_{\Omega} N_I e_{irn} (a_2)_{jsrn} \frac{\partial N_J}{\partial x_s}\,\mathrm{d}\Omega \tag{A.81}$$

$$= \int_{\Omega} \check{G}_{rnIi} (a_2)_{jsrn} G_{jsJj}\,\mathrm{d}\Omega\,. \tag{A.82}$$

A.2.2 With respect to rotations

The tangent stiffness is

$$K^{q\varphi}_{IiJj} = \frac{\partial q^{\mathrm{int}}_{Ii}}{\partial \varphi_{Jj}} \tag{A.83}$$

$$= \int_{\Omega} \frac{\partial}{\partial \varphi_{Jj}} \left(\frac{\partial N_I}{\partial x_r}\mu_{ir} + N_I e_{irn}\sigma_{rn}\right)\mathrm{d}\Omega \tag{A.84}$$

$$= \int_{\Omega} \left(\frac{\partial N_I}{\partial x_r}\frac{\partial \mu_{ir}}{\partial \varphi_{Jj}} + N_I e_{irn}\frac{\partial \sigma_{rn}}{\partial Q_{m\theta}}\frac{\partial Q_{m\theta}}{\partial \varphi_{Jj}}\right)\mathrm{d}\Omega\,. \tag{A.85}$$

Then,

$$\frac{\partial \mu_{ir}}{\partial \varphi_{Jj}} = \frac{\partial}{\partial \varphi_{Jj}}\left(J^{-1} Q_{i\alpha} S_{\alpha\beta} F_{r\beta}\right) \tag{A.86}$$

$$= J^{-1}\left(\frac{\partial Q_{i\alpha}}{\partial \varphi_{Jj}} S_{\alpha\beta} + Q_{i\alpha}\frac{\partial S_{\alpha\beta}}{\partial \varphi_{Jj}}\right) F_{r\beta} \tag{A.87}$$

where

$$\frac{\partial Q_{i\alpha}}{\partial \varphi_{Jj}} = \frac{\partial Q_{i\alpha}}{\partial \varphi_s}\frac{\partial \varphi_s}{\partial \varphi_{Jj}} \tag{A.88}$$

$$= (e_{isn} Q_{n\alpha})\frac{\partial N_H \varphi_{Hs}}{\partial \varphi_{Jj}} \tag{A.89}$$

$$= Q_{n\alpha} e_{ijn} N_J \tag{A.90}$$

and

$$\frac{\partial S_{\alpha\beta}}{\partial \varphi_{Jj}} = \frac{\partial}{\partial \varphi_{Jj}}\left(\check{D}_{\alpha\beta\gamma\pi}\Gamma_{\gamma\pi}\right) \tag{A.91}$$

$$= \check{D}_{\alpha\beta\gamma\pi}\frac{\partial \Gamma_{\gamma\pi}}{\partial \varphi_{Jj}} \tag{A.92}$$

which are substituted back into (A.87) to give

$$\frac{\partial \mu_{ir}}{\partial \varphi_{Jj}} = J^{-1} \left(Q_{n\alpha} S_{\alpha\beta} e_{ijn} N_J + Q_{i\alpha} \check{D}_{\alpha\beta\gamma\pi} \frac{\partial \Gamma_{\gamma\pi}}{\partial \varphi_{Jj}} \right) F_{r\beta} \tag{A.93}$$

$$= \mu_{nr} e_{ijn} N_J + J^{-1} L_{ir\alpha\beta} \check{D}_{\alpha\beta\gamma\pi} \frac{\partial \Gamma_{\gamma\pi}}{\partial \varphi_{Jj}}. \tag{A.94}$$

A discretisation of the Gateaux derivative of the wryness tensor [292],

$$\delta \Gamma_{\gamma\pi} = Q_{j\gamma} \frac{\partial (\delta \varphi_j)}{\partial X_\pi} \tag{A.95}$$

$$= Q_{j\gamma} \frac{\partial (N_J \delta \varphi_{Jj})}{\partial X_\pi} \tag{A.96}$$

$$= Q_{j\gamma} \frac{\partial N_J}{\partial X_\pi} \delta \varphi_{Jj} \tag{A.97}$$

can be rearranged to yield the straightforward result

$$\frac{\partial \Gamma_{\gamma\pi}}{\partial \varphi_{Jj}} = Q_{j\gamma} \frac{\partial N_J}{\partial X_\pi} = Q_{j\gamma} \frac{\partial N_J}{\partial x_n} F_{n\pi} \tag{A.98}$$

so that (A.94) becomes

$$\frac{\partial \mu_{ij}}{\partial \varphi_{Jj}} = \mu_{nr} \epsilon_{ijn} N_J + J^{-1} L_{ir\alpha\beta} \check{D}_{\alpha\beta\gamma\pi} L_{jn\gamma\pi} \frac{\partial N_J}{\partial x_n}. \tag{A.99}$$

Combining this with result (A.54) and substituting into (A.85) gives

$$\begin{aligned} K^{q\varphi}_{IiJj} = \int_\Omega \Bigg(& N_I \epsilon_{irn} \left(\delta_{rm} \sigma_{sn} + J^{-1} L_{rn\alpha\beta} D_{\alpha\beta\gamma\pi} L_{sm\gamma\pi} \right) \epsilon_{mjs} N_J \\ & + \frac{\partial N_I}{\partial x_r} \left(J^{-1} L_{ir\alpha\beta} \check{D}_{\alpha\beta\gamma\pi} Q_{jn\gamma\pi} \frac{\partial N_J}{\partial x_n} + \mu_{nr} \epsilon_{ijn} N_J \right) \Bigg) \mathrm{d}\Omega \end{aligned} \tag{A.100}$$

$$\begin{aligned} = \int_\Omega & (N_I e_{irn} (a_2)_{rnsm} \epsilon_{smj} N_J \\ & + \frac{\partial N_I}{\partial x_r} \left((a_3)_{irjn} \frac{\partial N_J}{\partial x_n} + (a_4)_{irns} \epsilon_{nsj} N_J \right) \Bigg) \mathrm{d}\Omega \end{aligned} \tag{A.101}$$

$$= \int_\Omega \left(\check{G}_{rnIi} (a_2)_{rnsm} \check{G}_{smJj} + G_{arIi} \left((a_3)_{arbn} G_{bnJj} + (a_4)_{arns} \check{G}_{nsJj} \right) \right) \mathrm{d}\Omega \tag{A.102}$$

where

$$(a_3)_{arbn} = J^{-1} L_{ar\alpha\beta} \check{D}_{\alpha\beta\gamma\theta} L_{bn\gamma\theta} \tag{A.103}$$

$$(a_4)_{arns} = \delta_{as} \mu_{nr}. \tag{A.104}$$

APPENDIX B

Linearisation of the elastoplastic constitutive equations

This appendix details the analytical consistent linearisation of the elastoplastic residuals

$$\boldsymbol{r}^U = \boldsymbol{U}^\mathrm{e} - \boldsymbol{Q}^\mathrm{T} \exp\left(-\Delta\gamma^\mathrm{p} \frac{\partial g}{\partial \boldsymbol{\tau}}\right) (\boldsymbol{F}^\mathrm{e})^\mathrm{tr} \tag{4.57}$$

$$\boldsymbol{r}^\Gamma = \boldsymbol{\Gamma}^\mathrm{e} + \Delta\gamma^\mathrm{p} \boldsymbol{Q}^\mathrm{T} \frac{\partial g}{\partial \boldsymbol{\nu}} \boldsymbol{F} - (\boldsymbol{\Gamma}^\mathrm{e})^\mathrm{tr} \tag{4.58}$$

$$r^\chi = \chi - \widetilde{\chi} - \Delta\gamma^\mathrm{p} \tag{4.59}$$

and yield function

$$f = q + \alpha^\mathrm{DP} p - (k + \Lambda) \tag{4.39}$$

with respect to the elastic stretch $\boldsymbol{U}^\mathrm{e}$, elastic wryness $\boldsymbol{\Gamma}^\mathrm{e}$, internal hardening χ and plastic multiplier $\Delta\gamma^\mathrm{p}$, in order to form the Jacobian C in the nonlinear solution of the local constitutive equations. Note that the total kinematic measures, and the trial and previously converged values, remain constant. As in Appendix A, index notation is used to designate the various configurations in which each tensor quantity is defined. Specifically, lower-case Latin letters are used for spatial quantities, lower-case Greek for material, and overbarred Latin for the plastic intermediary configuration. First, however, the expressions for the plastic flow vectors used are derived for later use.

B.1 Evaluation of the plastic flow vectors

In the adopted non-associated flow rules, plastic flow occurs relative to the plastic potential function

$$g = q + \beta^\mathrm{DP} p - \Lambda \tag{4.40}$$

where, in index notation,

$$q = \sqrt{\frac{3}{2}(s_{ij}s_{ij} + (\ell^{\mathrm{p}})^{-2}\nu_{ij}\nu_{ij})} \tag{B.1}$$

and

$$p = \frac{1}{3}\tau_{ii}. \tag{B.2}$$

The deviatoric symmetrised Kirchhoff stress s_{ij} is defined

$$s_{ij} = \frac{1}{2}(\tau_{ij} + \tau_{ji}) - \frac{1}{3}\delta_{ij}\tau_{kk} \tag{B.3}$$

so that

$$\frac{\partial s_{ab}}{\partial \tau_{ij}} = \frac{1}{2}(\delta_{ai}\delta_{jb} + \delta_{bi}\delta_{ja}) - \frac{1}{3}\delta_{ij}\delta_{ab}. \tag{B.4}$$

Also,

$$\begin{aligned}
\frac{\partial q}{\partial s_{ab}} &= \frac{1}{2}q^{-1} \cdot \frac{\partial}{\partial s_{ab}}\left(\frac{3}{2}(s_{ij}s_{ij} + (\ell^{\mathrm{p}})^{-2}\nu_{ij}\nu_{ij})\right) && \text{(B.5)}\\
&= \frac{1}{2}q^{-1}\left(\frac{3}{2}(\delta_{ia}\delta_{bj}s_{ij} + s_{ij}\delta_{ia}\delta_{bj})\right) && \text{(B.6)}\\
&= \frac{3}{2}q^{-1}s_{ab} && \text{(B.7)}
\end{aligned}$$

and, similarly,

$$\frac{\partial q}{\partial \nu_{ab}} = \frac{3}{2}(\ell^{\mathrm{p}})^{-2}q^{-1}\nu_{ab}. \tag{B.8}$$

Therefore, by the chain rule,

$$\begin{aligned}
\frac{\partial q}{\partial \tau_{ij}} &= \frac{\partial q}{\partial s_{ab}}\frac{\partial s_{ab}}{\partial \tau_{ij}} && \text{(B.9)}\\
&= \frac{3}{2}q^{-1}s_{ab} \cdot \left(\frac{1}{2}(\delta_{ai}\delta_{jb} + \delta_{bi}\delta_{ja}) - \frac{1}{3}\delta_{ij}\delta_{ab}\right) && \text{(B.10)}\\
&= \frac{3}{2}q^{-1}\left(\frac{1}{2}(s_{ij} + s_{ji}) - \frac{1}{3}\delta_{ij}s_{kk}\right) && \text{(B.11)}
\end{aligned}$$

but because s_{ij} is already symmetric and deviatoric (qualities which are idempotent), this reduces to

$$\frac{\partial q}{\partial \tau_{ij}} = \frac{3}{2}q^{-1}s_{ij}. \tag{B.12}$$

Hence,

$$\begin{aligned}
\frac{\partial g}{\partial \tau_{ij}} &= \frac{\partial q}{\partial \tau_{ij}} + \beta^{\mathrm{DP}}\frac{\partial p}{\partial \tau_{ij}} && \text{(B.13)}\\
&= \frac{3}{2}q^{-1}s_{ij} + \frac{1}{3}\beta^{\mathrm{DP}}\delta_{ij} && \text{(B.14)}
\end{aligned}$$

and

$$\frac{\partial g}{\partial \nu_{ab}} = \frac{\partial q}{\partial \nu_{ab}} \tag{B.15}$$

$$= \frac{3}{2}(\ell^{\mathrm{p}})^{-2} q^{-1} \nu_{ab}. \tag{B.16}$$

Trivially,

$$\frac{\partial g}{\partial \Lambda} = -1. \tag{B.17}$$

B.2 Linearisation of the stretch residual

The residual equation is written

$$r^{U}_{\alpha\bar{i}} = U^{\mathrm{e}}_{\alpha\bar{i}} - Q_{i\alpha} \exp\left(-\Delta\gamma^{\mathrm{p}} \frac{\partial g}{\partial \boldsymbol{\tau}}\right)_{ij} (F^{\mathrm{e}})^{\mathrm{tr}}_{j\bar{i}}. \tag{B.18}$$

Here it is convenient to define a quantity $\boldsymbol{\mathcal{E}}$, which is a fourth-order tensor representing the derivative of the exponential part of the residual with respect to its argument, i.e.

$$\mathcal{E}_{ijkl} = \frac{\partial \exp\left(-\Delta\gamma^{\mathrm{p}} \frac{\partial g}{\partial \boldsymbol{\tau}}\right)_{ij}}{\partial \left(-\Delta\gamma^{\mathrm{p}} \frac{\partial g}{\partial \tau_{kl}}\right)}. \tag{B.19}$$

Because the argument

$$-\Delta\gamma^{\mathrm{p}} \frac{\partial g}{\partial \tau_{ij}} = -\Delta\gamma^{\mathrm{p}} \left(\frac{3}{2} q^{-1} s_{ij} + \frac{1}{3}\beta^{\mathrm{DP}} \delta_{ij}\right) \tag{B.20}$$

is symmetric, this quantity can be evaluated computationally according to an implementation described by Miehe [353].

With respect to elastic stretch

The derivative is

$$\frac{\partial r^{U}_{\alpha\bar{i}}}{\partial U^{\mathrm{e}}_{\theta\bar{j}}} = \delta_{\alpha\theta}\delta_{\bar{i}\bar{j}} - Q_{i\alpha}\mathcal{E}_{ijkl} \frac{\partial}{\partial U^{\mathrm{e}}_{\theta\bar{j}}} \left(-\Delta\gamma^{\mathrm{p}} \left(\frac{3}{2} q^{-1} s_{kl} + \frac{1}{3}\beta^{\mathrm{DP}} \delta_{kl}\right)\right) (F^{\mathrm{e}})^{\mathrm{tr}}_{j\bar{i}} \tag{B.21}$$

$$= \delta_{\alpha\theta}\delta_{\bar{i}\bar{j}} + \frac{3\Delta\gamma^{\mathrm{p}}}{2} Q_{i\alpha}\mathcal{E}_{ijkl} \frac{\partial}{\partial U^{\mathrm{e}}_{\theta\bar{j}}} \left(q^{-1} s_{kl}\right) (F^{\mathrm{e}})^{\mathrm{tr}}_{j\bar{i}}. \tag{B.22}$$

Given that the Kirchhoff stress is defined

$$\tau_{ab} = Q_{a\alpha} D_{\alpha\bar{l}\gamma\bar{k}} \left(U^{\mathrm{e}}_{\gamma\bar{k}} - \delta_{\gamma\bar{k}}\right) Q_{b\delta} U^{\mathrm{e}}_{\delta\bar{l}} \tag{B.23}$$

$$= Q_{a\alpha} D_{\alpha\bar{l}\gamma\bar{k}} U^{\mathrm{e}}_{\gamma\bar{k}} Q_{b\delta} U^{\mathrm{e}}_{\delta\bar{l}} - Q_{a\alpha} D_{\alpha\bar{l}\gamma\bar{k}} \delta_{\gamma\bar{k}} Q_{b\delta} U^{\mathrm{e}}_{\delta\bar{l}}, \tag{B.24}$$

its derivative with respect to elastic stretch is

$$
\begin{aligned}
\frac{\partial \tau_{ab}}{\partial U^{e}_{\theta\bar{j}}} &= Q_{a\alpha} D_{\alpha\bar{l}\gamma\bar{k}} \delta_{\gamma\theta} \delta_{\bar{j}\bar{k}} Q_{b\delta} U^{\mathrm{e}}_{\delta\bar{l}} + Q_{a\alpha} D_{\alpha\bar{l}\gamma\bar{k}} U^{\mathrm{e}}_{\gamma\bar{k}} Q_{b\delta} \delta_{\delta\theta} \delta_{\bar{j}\bar{l}} - Q_{a\alpha} D_{\alpha\bar{l}\gamma\bar{k}} \delta_{\gamma\bar{k}} Q_{b\delta} \delta_{\delta\theta} \delta_{\bar{j}\bar{l}} && \text{(B.25)} \\
&= Q_{a\alpha} D_{\alpha\bar{l}\theta\bar{j}} Q_{b\delta} U^{\mathrm{e}}_{\delta\bar{l}} + Q_{a\alpha} D_{\alpha\bar{j}\gamma\bar{k}} U^{\mathrm{e}}_{\gamma\bar{k}} Q_{b\theta} - Q_{a\alpha} D_{\alpha\bar{j}\gamma\bar{k}} \delta_{\gamma\bar{k}} Q_{b\theta} && \text{(B.26)} \\
&= Q_{a\alpha} F^{\mathrm{e}}_{b\bar{l}} D_{\alpha\bar{l}\theta\bar{j}} + Q_{a\alpha} B_{\alpha\bar{j}} Q_{b\theta} && \text{(B.27)} \\
&= L^{\mathrm{e}}_{ab\alpha\bar{l}} D_{\alpha\bar{l}\theta\bar{j}} + Q_{a\alpha} B_{\alpha\bar{j}} Q_{b\theta}, && \text{(B.28)}
\end{aligned}
$$

where $L^{\mathrm{e}}_{ab\alpha\bar{l}} = Q_{a\alpha} F^{\mathrm{e}}_{b\bar{l}}$.Therefore, reusing (B.4),

$$
\begin{aligned}
\frac{\partial s_{kl}}{\partial U^{e}_{\theta\bar{j}}} &= \frac{\partial s_{kl}}{\partial \tau_{ab}} \frac{\partial \tau_{ab}}{\partial U^{e}_{\theta\bar{j}}} && \text{(B.29)} \\
&= \left(\frac{1}{2} (\delta_{ka}\delta_{bl} + \delta_{la}\delta_{bk}) - \frac{1}{3} \delta_{ab}\delta_{kl} \right) \left(L^{\mathrm{e}}_{ab\alpha\bar{l}} D_{\alpha\bar{l}\theta\bar{j}} + Q_{a\alpha} B_{\alpha\bar{j}} Q_{b\theta} \right) && \text{(B.30)} \\
&= \frac{1}{2} \left(Q_{k\alpha} F^{\mathrm{e}}_{l\bar{l}} D_{\alpha\bar{l}\theta\bar{j}} + Q_{k\alpha} B_{\alpha\bar{j}} Q_{l\theta} + Q_{l\alpha} F^{\mathrm{e}}_{k\bar{l}} D_{\alpha\bar{l}\theta\bar{j}} + Q_{l\alpha} B_{\alpha\bar{j}} Q_{k\theta} \right) \\
&\qquad - \frac{1}{3} \delta_{kl} \left(Q_{b\alpha} F^{\mathrm{e}}_{b\bar{l}} D_{\alpha\bar{l}\theta\bar{j}} + Q_{b\alpha} B_{\alpha\bar{j}} Q_{b\theta} \right) && \text{(B.31)} \\
&= \frac{1}{2} \left(Q_{k\alpha} F^{\mathrm{e}}_{l\bar{l}} + Q_{l\alpha} F^{\mathrm{e}}_{k\bar{l}} \right) D_{\alpha\bar{l}\theta\bar{j}} + \frac{1}{2} \left(Q_{k\alpha} B_{\alpha\bar{j}} Q_{l\theta} + Q_{l\alpha} B_{\alpha\bar{j}} Q_{k\theta} \right) \\
&\qquad - \frac{1}{3} \delta_{kl} \left(U^{\mathrm{e}}_{\alpha\bar{l}} D_{\alpha\bar{l}\theta\bar{j}} + \delta_{\alpha\theta} B_{\alpha\bar{j}} \right) && \text{(B.32)} \\
&= \frac{1}{2} \left(Q_{k\alpha} F^{\mathrm{e}}_{l\bar{l}} + Q_{l\alpha} F^{\mathrm{e}}_{k\bar{l}} \right) D_{\alpha\bar{l}\theta\bar{j}} + \frac{1}{2} \left(Q_{k\alpha} B_{\alpha\bar{j}} Q_{l\theta} + Q_{l\alpha} B_{\alpha\bar{j}} Q_{k\theta} \right) \\
&\qquad - \frac{1}{3} \delta_{kl} \left(2B_{\theta\bar{j}} + \delta_{\alpha\bar{l}} D_{\alpha\bar{l}\theta\bar{j}} \right) =: (\mathcal{D}_1)_{kl\theta\bar{j}}. && \text{(B.33)}
\end{aligned}
$$

This means that, from (B.7)

$$
\begin{aligned}
\frac{\partial q}{\partial U^{\mathrm{e}}_{\theta\bar{j}}} &= \frac{\partial q}{\partial s_{kl}} \frac{\partial s_{kl}}{\partial U^{\mathrm{e}}_{kl}} && \text{(B.34)} \\
&= \frac{3}{2} q^{-1} s_{kl} (\mathcal{D}_1)_{kl\theta\bar{j}} =: (\mathcal{D}_2)_{\theta\bar{j}} && \text{(B.35)}
\end{aligned}
$$

so that the quotient rule may be used to give

$$
\begin{aligned}
\frac{\partial}{\partial U^{e}_{\theta\bar{j}}} \left(q^{-1} s_{kl} \right) &= q^{-2} \left(q \frac{\partial s_{kl}}{\partial U^{e}_{\theta\bar{j}}} - \frac{\partial q}{\partial U^{e}_{\theta\bar{j}}} s_{kl} \right) && \text{(B.36)} \\
&= q^{-1} (\mathcal{D}_1)_{kl\theta\bar{j}} - q^{-2} s_{kl} (\mathcal{D}_2)_{\theta\bar{j}}. && \text{(B.37)}
\end{aligned}
$$

Therefore, returning to (B.22),

$$
\begin{aligned}
\frac{\partial r^{U}_{\alpha\bar{i}}}{\partial U^{e}_{\theta\bar{j}}} &= \delta_{\alpha\theta} \delta_{\bar{i}\bar{j}} + \frac{3\Delta\gamma^{\mathrm{p}}}{2} Q_{i\alpha} \mathcal{E}_{ijkl} \left(q^{-1} (\mathcal{D}_1)_{kl\theta\bar{j}} - q^{-2} s_{kl} (\mathcal{D}_2)_{\theta\bar{j}} \right) (F^{\mathrm{e}})^{\mathrm{tr}}_{j\bar{i}} && \text{(B.38)} \\
&= \delta_{\alpha\theta} \delta_{\bar{i}\bar{j}} + \frac{3\Delta\gamma^{\mathrm{p}}}{2q} Q_{i\alpha} (F^{\mathrm{e}})^{\mathrm{tr}}_{j\bar{i}} \mathcal{E}_{ijkl} \left((\mathcal{D}_1)_{kl\theta\bar{j}} - q^{-1} s_{kl} (\mathcal{D}_2)_{\theta\bar{j}} \right) && \text{(B.39)}
\end{aligned}
$$

which is the first component of the Jacobian.

With respect to elastic wryness

Firstly, the Kirchhoff couple-stress is defined

$$\nu_{ab} = Q_{a\alpha}\check{D}_{\alpha\beta\gamma\delta}\Gamma^{\mathrm{e}}_{\gamma\delta}F_{b\beta} \tag{B.40}$$

which means that

$$\begin{aligned} \frac{\partial \nu_{ab}}{\partial \Gamma^{\mathrm{e}}_{\theta\psi}} &= Q_{a\alpha}\check{D}_{\alpha\beta\gamma\delta}\delta_{\gamma\theta}\delta_{\psi\delta}F_{b\beta} &\quad \text{(B.41)}\\ &= Q_{a\alpha}F_{b\beta}\check{D}_{\alpha\beta\theta\psi}. &\quad \text{(B.42)} \end{aligned}$$

Hence, with (B.8),

$$\begin{aligned} \frac{\partial q}{\partial \Gamma^{\mathrm{e}}_{\theta\psi}} &= \frac{\partial q}{\partial \nu_{ab}}\frac{\partial \nu_{ab}}{\partial \Gamma^{\mathrm{e}}_{\theta\psi}} &\quad \text{(B.43)}\\ &= \frac{3}{2}(\ell^{\mathrm{p}})^{-2}q^{-1}\nu_{ab}Q_{a\alpha}F_{b\beta}\check{D}_{\alpha\beta\theta\psi} =: (\mathcal{D}_3)_{\theta\psi} &\quad \text{(B.44)} \end{aligned}$$

so that

$$\begin{aligned} \frac{\partial}{\partial \Gamma^{\mathrm{e}}_{\theta\psi}}\left(q^{-1}s_{kl}\right) &= q^{-2}\left(q\frac{\partial s_{kl}}{\partial \Gamma^{\mathrm{e}}_{\theta\psi}} - s_{kl}\frac{\partial q}{\partial \Gamma^{\mathrm{e}}_{\theta\psi}}\right) &\quad \text{(B.45)}\\ &= -q^{-2}s_{kl}(\mathcal{D}_3)_{\theta\psi} &\quad \text{(B.46)} \end{aligned}$$

The final derivative is therefore

$$\begin{aligned} \frac{\partial r^{U}_{\alpha\bar{i}}}{\partial \Gamma^{\mathrm{e}}_{\theta\psi}} &= \frac{3\Delta\gamma^{\mathrm{p}}}{2}Q_{i\alpha}\mathcal{E}_{ijkl}\frac{\partial}{\partial \Gamma^{\mathrm{e}}_{\theta\psi}}\left(q^{-1}s_{kl}\right)(F^{\mathrm{e}})^{\mathrm{tr}}_{j\bar{i}} &\quad \text{(B.47)}\\ &= \frac{3\Delta\gamma^{\mathrm{p}}}{2q^2}Q_{i\alpha}(F^{\mathrm{e}})^{\mathrm{tr}}_{j\bar{i}}\mathcal{E}_{ijkl}s_{kl}(\mathcal{D}_3)_{\theta\psi}. &\quad \text{(B.48)} \end{aligned}$$

With respect to the plastic multiplier

The derivative is simply

$$\begin{aligned} \frac{\partial r^{U}_{\alpha\bar{i}}}{\partial \Delta\gamma^{\mathrm{p}}} &= -Q_{i\alpha}\mathcal{E}_{ijkl}\frac{\partial}{\partial \Delta\gamma^{\mathrm{p}}}\left(-\Delta\gamma^{\mathrm{p}}\frac{\partial g}{\partial \tau_{kl}}\right)(F^{\mathrm{e}})^{\mathrm{tr}}_{j\bar{i}} &\quad \text{(B.49)}\\ &= Q_{i\alpha}(F^{\mathrm{e}})^{\mathrm{tr}}_{j\bar{i}}\mathcal{E}_{ijkl}\frac{\partial g}{\partial \tau_{kl}}. &\quad \text{(B.50)} \end{aligned}$$

B.3 Linearisation of the wryness residual

The residual is written

$$r^{\Gamma}_{\rho\epsilon} = \Gamma^{\mathrm{e}}_{\rho\epsilon} + \Delta\gamma^{\mathrm{p}} Q_{i\rho} \frac{\partial g}{\partial \nu_{ij}} F_{j\epsilon} - (\Gamma^{\mathrm{e}})^{\mathrm{tr}}_{\rho\epsilon}, \tag{B.51}$$

where

$$\frac{\partial g}{\partial \nu_{ij}} = \frac{3}{2} (\ell^{\mathrm{p}})^{-2} q^{-1} \nu_{ij}, \tag{B.16}$$

so

$$r^{\Gamma}_{\rho\epsilon} = \Gamma^{\mathrm{e}}_{\rho\epsilon} + \frac{3\Delta\gamma^{\mathrm{p}}}{2(\ell^{\mathrm{p}})^2 q} Q_{i\rho} \nu_{ij} F_{j\epsilon} - (\Gamma^{\mathrm{e}})^{\mathrm{tr}}_{\rho\epsilon}. \tag{B.52}$$

With respect to elastic stretch

The residual's only dependency on elastic stretch is provided by q, so

$$\frac{\partial r^{\Gamma}_{\rho\epsilon}}{\partial U^{\mathrm{e}}_{\theta\bar{\jmath}}} = \frac{3\Delta\gamma^{\mathrm{p}}}{2(\ell^{\mathrm{p}})^2} Q_{i\rho} \nu_{ij} F_{j\epsilon} \frac{\partial q^{-1}}{\partial U^{\mathrm{e}}_{\theta\bar{\jmath}}} \tag{B.53}$$

$$= \frac{3\Delta\gamma^{\mathrm{p}}}{2(\ell^{\mathrm{p}})^2 q^2} Q_{i\rho} \nu_{ij} F_{j\epsilon} \frac{\partial q}{\partial U^{\mathrm{e}}_{\theta\bar{\jmath}}} \tag{B.54}$$

$$= \frac{3\Delta\gamma^{\mathrm{p}}}{2(\ell^{\mathrm{p}})^2 q^2} Q_{i\rho} \nu_{ij} F_{j\epsilon} (\mathcal{D}_2)_{\theta\bar{\jmath}} \tag{B.55}$$

$$= \frac{\Delta\gamma^{\mathrm{p}}}{q} Q_{i\rho} \frac{\partial g}{\partial \nu_{ij}} F_{j\epsilon} (\mathcal{D}_2)_{\theta\bar{\jmath}}. \tag{B.56}$$

With respect to elastic wryness

With (B.44),

$$\frac{\partial}{\partial \Gamma^{\mathrm{e}}_{\theta\psi}} \left(q^{-1}\nu_{ij}\right) = q^{-2} \left(q \frac{\partial \nu_{ij}}{\partial \Gamma^{\mathrm{e}}_{\theta\psi}} - \frac{\partial q}{\partial \Gamma^{\mathrm{e}}_{\theta\psi}} \nu_{ij} \right) \tag{B.57}$$

$$= q^{-2} \left(q Q_{i\alpha} F_{j\beta} \check{D}_{\alpha\beta\theta\psi} - \nu_{ij} (\mathcal{D}_3)_{\theta\psi} \right). \tag{B.58}$$

Hence the derivative is

$$\frac{\partial r^{\Gamma}_{\rho\epsilon}}{\partial \Gamma^{\mathrm{e}}_{\theta\psi}} = \delta_{\rho\theta}\delta_{\psi\epsilon} + \frac{3\Delta\gamma^{\mathrm{p}}}{2(\ell^{\mathrm{p}})^2} Q_{i\rho} \frac{\partial}{\partial \Gamma^{\mathrm{e}}_{\theta\psi}} \left(q^{-1}\nu_{ij}\right) F_{j\epsilon} \tag{B.59}$$

$$= \delta_{\rho\theta}\delta_{\psi\epsilon} + \frac{3\Delta\gamma^{\mathrm{p}}}{2(\ell^{\mathrm{p}})^2 q^2} Q_{i\rho} F_{j\epsilon} \left(q Q_{i\alpha} F_{j\beta} \check{D}_{\alpha\beta\theta\psi} - \nu_{ij} (\mathcal{D}_3)_{\theta\psi} \right). \tag{B.60}$$

With respect to the plastic multiplier

$$\frac{\partial r^{\Gamma}_{\rho\epsilon}}{\partial \Delta\gamma^{\mathrm{p}}} = \frac{3}{2(\ell^{\mathrm{p}})^2 q} Q_{i\rho} \nu_{ij} F_{j\epsilon} \tag{B.61}$$

$$= Q_{i\rho} \frac{\partial g}{\partial \nu_{ij}} F_{j\epsilon}. \tag{B.62}$$

B.4 Linearisation of the hardening residual

The residual is

$$r^{\chi} = \chi - \widetilde{\chi} - \Delta\gamma^{\mathrm{p}} \tag{??}$$

Therefore

$$\frac{\partial r^{\chi}}{\partial \chi} = 1 \tag{B.63}$$

and

$$\frac{\partial r^{\chi}}{\partial \Delta\gamma^{\mathrm{p}}} = -1. \tag{B.64}$$

B.5 Linearisation of the yield function

The Drucker-Prager yield function is defined

$$f = q + \alpha^{\mathrm{DP}} p - (k + \Lambda), \tag{4.39}$$

where $\Lambda = H\chi$.

With respect to elastic stretch

Using (B.28),

$$\frac{\partial f}{\partial U^{\mathrm{e}}_{\theta\bar{j}}} = \frac{\partial q}{\partial U^{\mathrm{e}}_{\theta\bar{j}}} + \alpha^{\mathrm{DP}} \frac{\partial \tau_{aa}}{\partial U^{\mathrm{e}}_{\theta\bar{j}}} \tag{B.65}$$

$$= (\mathcal{D}_2)_{\theta\bar{j}} + \alpha^{\mathrm{DP}} \delta_{ab} \frac{\partial \tau_{ab}}{\partial U^{\mathrm{e}}_{\theta\bar{j}}} \tag{B.66}$$

$$= (\mathcal{D}_2)_{\theta\bar{j}} + \alpha^{\mathrm{DP}} \left(Q_{a\alpha} F^{\mathrm{e}}_{a\bar{l}} D_{\alpha\bar{l}\theta\bar{j}} + Q_{a\alpha} B_{\alpha\bar{j}} Q_{a\theta} \right) \tag{B.67}$$

$$= (\mathcal{D}_2)_{\theta\bar{j}} + \alpha^{\mathrm{DP}} \left(U^{\mathrm{e}}_{\alpha\bar{l}} D_{\alpha\bar{l}\theta\bar{j}} + \delta_{\alpha\theta} B_{\alpha\bar{j}} \right) \tag{B.68}$$

$$= (\mathcal{D}_2)_{\theta\bar{j}} + \alpha^{\mathrm{DP}} \left(2B_{\theta\bar{j}} + \delta_{\theta\bar{j}} \right). \tag{B.69}$$

With respect to elastic wryness

From (B.44),

$$\frac{\partial f}{\partial \Gamma^{\mathrm{e}}_{\theta\psi}} = \frac{\partial q}{\partial \Gamma^{\mathrm{e}}_{\theta\psi}} \tag{B.70}$$

$$= (\mathcal{D}_3)_{\theta\psi}. \tag{B.71}$$

With respect to internal hardening

The derivative is

$$\frac{\partial f}{\partial \chi} = \frac{\partial}{\partial \chi}(-\Lambda) \tag{B.72}$$

$$= -H. \tag{B.73}$$

All the residuals $\boldsymbol{r}$ and their linearisations derived above are recalculated and assembled to form the Jacobian $\boldsymbol{C}$ in each iteration of the local Newton-Raphson search. The increments in the four unknowns $\boldsymbol{\mathcal{X}}$ are found by performing

$$\Delta \boldsymbol{\mathcal{X}} = -\boldsymbol{C}^{-1}\boldsymbol{r}. \tag{B.74}$$

APPENDIX C

Derivation of the auxiliary Jacobian

This appendix presents the linearisation of the elastoplastic residuals

$$\boldsymbol{r}^U = \boldsymbol{U}^{\mathrm{e}} - \boldsymbol{Q}^{\mathrm{T}} \exp\left(-\Delta\gamma^{\mathrm{p}} \frac{\partial g}{\partial \boldsymbol{\tau}}\right) (\boldsymbol{F}^{\mathrm{e}})^{\mathrm{tr}} \tag{4.57}$$

$$\boldsymbol{r}^\Gamma = \boldsymbol{\Gamma}^{\mathrm{e}} + \Delta\gamma^{\mathrm{p}} \boldsymbol{Q}^{\mathrm{T}} \frac{\partial g}{\partial \boldsymbol{\nu}} \boldsymbol{F} - (\boldsymbol{\Gamma}^{\mathrm{e}})^{\mathrm{tr}} \tag{4.58}$$

$$r^\chi = \chi - \widetilde{\chi} - \Delta\gamma^{\mathrm{p}} \tag{??}$$

and yield function

$$f = q + \alpha^{\mathrm{DP}} p - (k + \Lambda) \tag{4.39}$$

with respect to the total deformation gradient $\boldsymbol{F}$, microrotation tensor $\boldsymbol{Q}$, trial elastic deformation gradient $(\boldsymbol{F}^{\mathrm{e}})^{\mathrm{tr}}$ and wryness tensor $(\boldsymbol{\Gamma}^{\mathrm{e}})^{\mathrm{tr}}$, and trial internal hardening variable $\widetilde{\chi}$. Together these derivatives make a Jacobian $\boldsymbol{T}$ which is used to produce an algorithmically-consistent linearisation of the plastic return mapping. Therefore all derivatives are taken at *convergence* of the residual equations, i.e. the output variables $\boldsymbol{\mathcal{X}} = \{\boldsymbol{U}^{\mathrm{e}}, \boldsymbol{\Gamma}^{\mathrm{e}}, \chi, \Delta\gamma^{\mathrm{p}}\}$ of the constitutive model are assumed fixed. This derivation makes use of several quantities which were defined in Appendix B, and reuses its notational conventions.

C.1 Linearisation of the stretch residual

In index notation, the residual equation is

$$r^U_{\alpha\bar{i}} = U^{\mathrm{e}}_{\alpha\bar{i}} - Q_{i\alpha} \exp\left(-\Delta\gamma^{\mathrm{p}} \frac{\partial g}{\partial \boldsymbol{\tau}}\right)_{ij} (F^{\mathrm{e}})^{\mathrm{tr}}_{j\bar{i}} \tag{B.18}$$

where

$$\frac{\partial g}{\partial \tau_{ij}} = \frac{3}{2} q^{-1} s_{ij} + \frac{1}{3} \beta^{\mathrm{DP}} \delta_{ij}. \tag{B.14}$$

With respect to the total deformation gradient

Firstly, using (B.8),

$$\begin{aligned}
\frac{\partial q}{\partial F_{m\theta}} &= \frac{\partial q}{\partial \nu_{ab}} \frac{\partial \nu_{ab}}{\partial F_{m\theta}} && \text{(C.1)}\\
&= \frac{3}{2} (\ell^{\mathrm{p}})^{-2} q^{-1} \nu_{ab} \frac{\partial}{\partial F_{m\theta}} \left(Q_{a\pi} \check{D}_{\pi\beta\gamma\delta} \Gamma^{\mathrm{e}}_{\gamma\delta} F_{b\beta} \right) && \text{(C.2)}\\
&= \frac{3}{2} (\ell^{\mathrm{p}})^{-2} q^{-1} \nu_{ab} Q_{a\pi} \check{D}_{\pi\beta\gamma\delta} \Gamma^{\mathrm{e}}_{\gamma\delta} \delta_{bm} \delta_{\theta\beta} && \text{(C.3)}\\
&= \frac{3}{2} (\ell^{\mathrm{p}})^{-2} q^{-1} \nu_{am} Q_{a\pi} S_{\pi\theta}. && \text{(C.4)}
\end{aligned}$$

Then, recalling the definition of $\boldsymbol{\mathcal{E}}$ from (B.19),

$$\begin{aligned}
\frac{\partial r^{U}_{\alpha\bar{i}}}{\partial F_{m\theta}} &= -Q_{i\alpha} \mathcal{E}_{ijkl} \frac{\partial}{\partial F_{m\theta}} \left(-\Delta\gamma^{\mathrm{p}} \left(\frac{3}{2} q^{-1} s_{kl} + \frac{1}{3} \beta^{\mathrm{DP}} \delta_{kl} \right) \right) (F^{\mathrm{e}})^{\mathrm{tr}}_{j\bar{i}} && \text{(C.5)}\\
&= \frac{3\Delta\gamma^{\mathrm{p}}}{2} Q_{i\alpha} \mathcal{E}_{ijkl} s_{kl} \frac{\partial q^{-1}}{\partial F_{m\theta}} (F^{\mathrm{e}})^{\mathrm{tr}}_{j\bar{i}} && \text{(C.6)}\\
&= -\frac{3\Delta\gamma^{\mathrm{p}}}{2q^2} Q_{i\alpha} \mathcal{E}_{ijkl} s_{kl} \frac{\partial q}{\partial F_{m\theta}} (F^{\mathrm{e}})^{\mathrm{tr}}_{j\bar{i}} && \text{(C.7)}\\
&= -\frac{9\Delta\gamma^{\mathrm{p}}}{4(\ell^{\mathrm{p}})^2 q^3} Q_{i\alpha} (F^{\mathrm{e}})^{\mathrm{tr}}_{j\bar{i}} \mathcal{E}_{ijkl} s_{kl} \nu_{am} Q_{a\pi} S_{\pi\theta}. && \text{(C.8)}
\end{aligned}$$

With respect to the microrotation tensor

Given that the elastic stretch is assumed constant, the Biot stress is also fixed. Hence,

$$\begin{aligned}
\frac{\partial \tau_{ij}}{\partial Q_{m\theta}} &= \frac{\partial}{\partial Q_{m\theta}} \left(Q_{i\alpha} B_{\alpha\bar{l}} Q_{j\delta} U^{\mathrm{e}}_{\delta\bar{l}} \right) && \text{(C.9)}\\
&= \delta_{im} \delta_{\theta\alpha} B_{\alpha\bar{l}} Q_{j\delta} U^{\mathrm{e}}_{\delta\bar{l}} + Q_{i\alpha} B_{\alpha\bar{l}} \delta_{jm} \delta_{\theta\delta} U^{\mathrm{e}}_{\delta\bar{l}} && \text{(C.10)}\\
&= \delta_{im} Q_{k\theta} Q_{k\alpha} B_{\alpha\bar{l}} F^{\mathrm{e}}_{j\bar{l}} + Q_{i\alpha} B_{\alpha\bar{l}} \delta_{jm} U^{\mathrm{e}}_{\theta\bar{l}} && \text{(C.11)}\\
&= \delta_{im} Q_{k\theta} \tau_{kj} + Q_{i\alpha} B_{\alpha\bar{l}} \delta_{jm} Q_{k\theta} F^{\mathrm{e}}_{k\bar{l}} && \text{(C.12)}\\
&= \left(\delta_{im} \tau_{kj} + \delta_{jm} \tau_{ik} \right) Q_{k\theta} && \text{(C.13)}
\end{aligned}$$

so that, with (B.4),

$$\begin{aligned}
\frac{\partial s_{ab}}{\partial Q_{m\theta}} &= \frac{\partial s_{ab}}{\partial \tau_{ij}} \frac{\partial \tau_{ij}}{\partial Q_{m\theta}} && \text{(C.14)}\\
&= \left(\frac{1}{2} (\delta_{ai} \delta_{jb} + \delta_{bi} \delta_{ja}) - \frac{1}{3} \delta_{ij} \delta_{ab} \right) \left(\delta_{im} \tau_{kj} + \delta_{jm} \tau_{ik} \right) Q_{k\theta} && \text{(C.15)}
\end{aligned}$$

$$= \left(\frac{1}{2}(\delta_{am}\tau_{kb} + \delta_{bm}\tau_{ak} + \delta_{bm}\tau_{ka} + \delta_{am}\tau_{bk}) - \frac{1}{3}(\delta_{ab}\tau_{km} + \delta_{ab}\tau_{mk})\right) Q_{k\theta} \tag{C.16}$$

$$= \left(\frac{1}{2}\delta_{am}(\tau_{bk} + \tau_{kb}) + \frac{1}{2}\delta_{bm}(\tau_{ak} + \tau_{ka}) - \frac{1}{3}\delta_{ab}(\tau_{km} + \tau_{mk})\right) Q_{k\theta} \tag{C.17}$$

$$:= (\mathcal{D}_4)_{abm\theta}. \tag{C.18}$$

The elastic wryness and, as such, the Biot couple-stress are both fixed, so

$$\frac{\partial \nu_{ab}}{\partial Q_{m\theta}} = \frac{\partial}{\partial Q_{m\theta}}\left(Q_{a\alpha} S_{\alpha\beta} F_{b\beta}\right) \tag{C.19}$$

$$= \delta_{am}\delta_{\theta\alpha} S_{\alpha\beta} F_{b\beta} \tag{C.20}$$

$$= \delta_{am} Q_{k\theta} Q_{k\alpha} S_{\alpha\beta} F_{b\beta} \tag{C.21}$$

$$= \delta_{am}\nu_{kb} Q_{k\theta}. \tag{C.22}$$

Therefore, using (B.7) and (B.8),

$$\frac{\partial q}{\partial Q_{m\theta}} = \frac{\partial q}{\partial s_{ab}}\frac{\partial s_{ab}}{\partial Q_{m\theta}} + \frac{\partial q}{\partial \nu_{ab}}\frac{\partial \nu_{ab}}{\partial Q_{m\theta}} \tag{C.23}$$

$$\begin{aligned} &= \frac{3}{2}q^{-1}s_{ab}\left(\frac{1}{2}\delta_{am}(\tau_{bk} + \tau_{kb}) + \frac{1}{2}\delta_{bm}(\tau_{ak} + \tau_{ka}) - \frac{1}{3}\delta_{ab}(\tau_{km} + \tau_{mk})\right) Q_{k\theta} \\ &\quad + \frac{3}{2}(\ell^{\mathrm{p}})^{-2}q^{-1}\nu_{ab}\delta_{am}\nu_{kb}Q_{k\theta} \end{aligned} \tag{C.24}$$

$$\begin{aligned} &= \frac{3}{2}q^{-1}\left(\frac{1}{2}s_{mb}(\tau_{bk} + \tau_{kb}) + \frac{1}{2}s_{am}(\tau_{ak} + \tau_{ka}) - \frac{1}{3}s_{aa}(\tau_{km} + \tau_{mk})\right) Q_{k\theta} \\ &\quad + \frac{3}{2}(\ell^{\mathrm{p}})^{-2}q^{-1}\nu_{mb}\nu_{kb}Q_{k\theta} \end{aligned} \tag{C.25}$$

but given that s_{ab} is both symmetric and traceless, this becomes

$$\frac{\partial q}{\partial Q_{m\theta}} = \frac{3}{2}q^{-1}\left(s_{mb}(\tau_{bk} + \tau_{kb}) + (\ell^{\mathrm{p}})^{-2}\nu_{mb}\nu_{kb}\right) Q_{k\theta} := (\mathcal{D}_5)_{m\theta}. \tag{C.26}$$

Returning then to the residual,

$$\frac{\partial r^{U}_{\alpha\bar{i}}}{\partial Q_{m\theta}} = \frac{\partial}{\partial Q_{m\theta}}\left(U^{\mathrm{e}}_{\alpha\bar{i}} - Q_{i\alpha}\exp\left(-\Delta\gamma^{\mathrm{p}}\frac{\partial g}{\partial \boldsymbol{\tau}}\right)_{ij}(F^{\mathrm{e}})^{\mathrm{tr}}_{j\bar{i}}\right) \tag{C.27}$$

$$\begin{aligned} &= -\frac{\partial Q_{i\alpha}}{\partial Q_{m\theta}}\exp\left(-\Delta\gamma^{\mathrm{p}}\frac{\partial g}{\partial \boldsymbol{\tau}}\right)_{ij}(F^{\mathrm{e}})^{\mathrm{tr}}_{j\bar{i}} \\ &\quad - Q_{i\alpha}\mathcal{E}_{ijkl}\frac{\partial}{\partial Q_{m\theta}}\left(-\Delta\gamma^{\mathrm{p}}\left(\frac{3}{2}q^{-1}s_{kl} + \frac{1}{3}\beta^{\mathrm{DP}}\delta_{kl}\right)\right)(F^{\mathrm{e}})^{\mathrm{tr}}_{j\bar{i}} \end{aligned} \tag{C.28}$$

$$\begin{aligned} &= \frac{3\Delta\gamma^{\mathrm{p}}}{2q^2}Q_{i\alpha}\mathcal{E}_{ijkl}\left(q\frac{\partial s_{kl}}{\partial Q_{m\theta}} - s_{kl}\frac{\partial q}{\partial Q_{m\theta}}\right)(F^{\mathrm{e}})^{\mathrm{tr}}_{j\bar{i}} \\ &\quad - \delta_{im}\delta_{\theta\alpha}\exp\left(-\Delta\gamma^{\mathrm{p}}\frac{\partial g}{\partial \boldsymbol{\tau}}\right)_{ij}(F^{\mathrm{e}})^{\mathrm{tr}}_{j\bar{i}} \end{aligned} \tag{C.29}$$

$$
\begin{aligned}
&= \frac{3\Delta\gamma^{\mathrm{p}}}{2q^2} Q_{i\alpha} \mathcal{E}_{ijkl} \left(q(\mathcal{D}_4)_{klm\theta} - s_{kl}(\mathcal{D}_5)_{m\theta} \right) (F^{\mathrm{e}})^{\mathrm{tr}}_{j\bar{i}} \\
&\quad - Q_{i\gamma} Q_{m\gamma} \delta_{\theta\alpha} \exp\left(-\Delta\gamma^{\mathrm{p}} \frac{\partial g}{\partial \boldsymbol{\tau}} \right)_{ij} (F^{\mathrm{e}})^{\mathrm{tr}}_{j\bar{i}}
\end{aligned} \tag{C.30}
$$

$$
= \frac{3\Delta\gamma^{\mathrm{p}}}{2q^2} Q_{i\alpha} (F^{\mathrm{e}})^{\mathrm{tr}}_{j\bar{i}} \mathcal{E}_{ijkl} \left(q(\mathcal{D}_4)_{klm\theta} - s_{kl}(\mathcal{D}_5)_{m\theta} \right) - Q_{m\gamma} U^{\mathrm{e}}_{\gamma\bar{i}} \delta_{\theta\alpha} \tag{C.31}
$$

$$
= \frac{3\Delta\gamma^{\mathrm{p}}}{2q^2} Q_{i\alpha} (F^{\mathrm{e}})^{\mathrm{tr}}_{j\bar{i}} \mathcal{E}_{ijkl} \left(q(\mathcal{D}_4)_{klm\theta} - s_{kl}(\mathcal{D}_5)_{m\theta} \right) - F^{\mathrm{e}}_{m\bar{i}} \delta_{\theta\alpha}. \tag{C.32}
$$

With respect to the trial elastic deformation gradient

$$
\frac{\partial r^{U}_{\alpha\bar{i}}}{\partial (F^{\mathrm{e}})^{\mathrm{tr}}_{k\bar{j}}} = -Q_{i\alpha} \exp\left(-\Delta\gamma^{\mathrm{p}} \frac{\partial g}{\partial \boldsymbol{\tau}} \right)_{ij} \delta_{jk} \delta_{\bar{j}\bar{i}} \tag{C.33}
$$

$$
= -Q_{i\alpha} \exp\left(-\Delta\gamma^{\mathrm{p}} \frac{\partial g}{\partial \boldsymbol{\tau}} \right)_{ik} \delta_{\bar{j}\bar{i}}. \tag{C.34}
$$

C.2 Linearisation of the wryness residual

The residual equation is

$$
r^{\Gamma}_{\rho\epsilon} = \Gamma^{\mathrm{e}}_{\rho\epsilon} + \Delta\gamma^{\mathrm{p}} Q_{i\rho} \frac{\partial g}{\partial \nu_{ij}} F_{j\epsilon} - (\Gamma^{\mathrm{e}})^{\mathrm{tr}}_{\rho\epsilon} \tag{B.51}
$$

where

$$
\frac{\partial g}{\partial \nu_{ij}} = \frac{3}{2} (\ell^{\mathrm{p}})^{-2} q^{-1} \nu_{ij} \tag{B.16}
$$

such that

$$
r^{\Gamma}_{\rho\epsilon} = \Gamma^{\mathrm{e}}_{\rho\epsilon} + \frac{3\Delta\gamma^{\mathrm{p}}}{2(\ell^{\mathrm{p}})^2 q} S_{\rho\epsilon} - (\Gamma^{\mathrm{e}})^{\mathrm{tr}}_{\rho\epsilon}. \tag{C.35}
$$

With respect to the total deformation gradient

Using the chain rule and (C.4),

$$
\frac{\partial r^{\Gamma}_{\rho\epsilon}}{\partial F_{m\theta}} = -\frac{3\Delta\gamma^{\mathrm{p}}}{2(\ell^{\mathrm{p}})^2 q^2} S_{\rho\epsilon} \frac{\partial q}{\partial F_{m\theta}} \tag{C.36}
$$

$$
= -\frac{9\Delta\gamma^{\mathrm{p}}}{4(\ell^{\mathrm{p}})^4 q^3} S_{\rho\epsilon} \nu_{am} Q_{a\pi} S_{\pi\theta}. \tag{C.37}
$$

With respect to the microrotation tensor

Via (C.26),

$$
\frac{\partial r^{\Gamma}_{\rho\epsilon}}{\partial Q_{m\theta}} = -\frac{3\Delta\gamma^{\mathrm{p}}}{2(\ell^{\mathrm{p}})^2 q^2} S_{\rho\epsilon} \frac{\partial q}{\partial Q_{m\theta}} \tag{C.38}
$$

$$= -\frac{3\Delta\gamma^{\mathrm{p}}}{2(\ell^{\mathrm{p}})^2 q^2} S_{\rho\epsilon}(\mathcal{D}_5)_{m\theta}. \tag{C.39}$$

With respect to the trial elastic wryness

Simply,

$$\frac{\partial r^{\Gamma}_{\rho\epsilon}}{\partial(\Gamma^{\mathrm{e}})^{\mathrm{tr}}_{\psi\theta}} = -\frac{\partial(\Gamma^{\mathrm{e}})^{\mathrm{tr}}_{\rho\epsilon}}{\partial(\Gamma^{\mathrm{e}})^{\mathrm{tr}}_{\psi\theta}} \tag{C.40}$$

$$= -\delta_{\rho\psi}\delta_{\theta\epsilon}. \tag{C.41}$$

C.3 Linearisation of the hardening residual

The residual is

$$r^{\chi} = \chi - \widetilde{\chi} - \Delta\gamma^{\mathrm{p}} \tag{??}$$

Therefore

$$\frac{\partial r^{\chi}}{\partial\widetilde{\chi}} = -1. \tag{C.42}$$

C.4 Linearisation of the yield function

The yield function is written

$$f = q + \alpha^{\mathrm{DP}} p - (k + \Lambda), \tag{4.39}$$

where $\Lambda = H\chi$.

With respect to the total deformation gradient

From (C.4),

$$\frac{\partial f}{\partial F_{m\theta}} = \frac{\partial q}{\partial F_{m\theta}} \tag{C.43}$$

$$= \frac{3}{2(\ell^{\mathrm{p}})^2 q} \nu_{am} Q_{a\pi} S_{\pi\theta}. \tag{C.44}$$

With respect to the microrotation tensor

From (C.26),

$$\frac{\partial f}{\partial Q_{m\theta}} = \frac{\partial q}{\partial Q_{m\theta}} \tag{C.45}$$

$$= (\mathcal{D}_5)_{m\theta}. \tag{C.46}$$

APPENDIX D

Algorithmically-consistent linearisation of the elastoplastic problem

This appendix fully derives the consistent tangent used in the Newton-Raphson algorithm to solve the global elastoplastic boundary-value problem. It reuses the notational conventions defined previously with respect to tensor indices. First, recall the Jacobian $\boldsymbol{P}$ which represents a linearisation of the elastoplastic return-mapping algorithm at convergence:

$$\boldsymbol{P} = \begin{bmatrix} \frac{\partial \boldsymbol{U}^{\mathrm{e}}}{\partial \boldsymbol{F}} & \frac{\partial \boldsymbol{U}^{\mathrm{e}}}{\partial \boldsymbol{Q}} & \frac{\partial \boldsymbol{U}^{\mathrm{e}}}{\partial (\boldsymbol{F}^{\mathrm{e}})^{\mathrm{tr}}} & \frac{\partial \boldsymbol{U}^{\mathrm{e}}}{\partial (\boldsymbol{\Gamma}^{\mathrm{e}})^{\mathrm{tr}}} & \frac{\partial \boldsymbol{U}^{\mathrm{e}}}{\partial \widetilde{\chi}} \\ \frac{\partial \boldsymbol{\Gamma}^{\mathrm{e}}}{\partial \boldsymbol{F}} & \frac{\partial \boldsymbol{\Gamma}^{\mathrm{e}}}{\partial \boldsymbol{Q}} & \frac{\partial \boldsymbol{\Gamma}^{\mathrm{e}}}{\partial (\boldsymbol{F}^{\mathrm{e}})^{\mathrm{tr}}} & \frac{\partial \boldsymbol{\Gamma}^{\mathrm{e}}}{\partial (\boldsymbol{\Gamma}^{\mathrm{e}})^{\mathrm{tr}}} & \frac{\partial \boldsymbol{\Gamma}^{\mathrm{e}}}{\partial \widetilde{\chi}} \\ \frac{\partial \chi}{\partial \boldsymbol{F}} & \frac{\partial \chi}{\partial \boldsymbol{Q}} & \frac{\partial \chi}{\partial (\boldsymbol{F}^{\mathrm{e}})^{\mathrm{tr}}} & \frac{\partial \chi}{\partial (\boldsymbol{\Gamma}^{\mathrm{e}})^{\mathrm{tr}}} & \frac{\partial \chi}{\partial \widetilde{\chi}} \\ \frac{\partial \Delta\gamma^{\mathrm{p}}}{\partial \boldsymbol{F}} & \frac{\partial \Delta\gamma^{\mathrm{p}}}{\partial \boldsymbol{Q}} & \frac{\partial \Delta\gamma^{\mathrm{p}}}{\partial (\boldsymbol{F}^{\mathrm{e}})^{\mathrm{tr}}} & \frac{\partial \Delta\gamma^{\mathrm{p}}}{\partial (\boldsymbol{\Gamma}^{\mathrm{e}})^{\mathrm{tr}}} & \frac{\partial \Delta\gamma^{\mathrm{p}}}{\partial \widetilde{\chi}} \end{bmatrix}. \tag{4.71}$$

Also recall that the elastic trial deformation gradient $(\boldsymbol{F}^{\mathrm{e}})^{\mathrm{tr}}$ is proposed using

$$(\boldsymbol{F}^{\mathrm{e}})^{\mathrm{tr}} = \Delta \boldsymbol{F} \widetilde{\boldsymbol{F}^{\mathrm{e}}} = \boldsymbol{F} \widetilde{\boldsymbol{F}^{\mathrm{p}}}^{-1} \tag{4.42}$$

and the trial elastic wryness is

$$(\boldsymbol{\Gamma}^{\mathrm{e}})^{\mathrm{tr}} = \boldsymbol{\Gamma} - \widetilde{\boldsymbol{\Gamma}^{\mathrm{p}}}, \tag{4.44}$$

where $\widetilde{(\bullet)}$ denotes a previously-converged value from the last load step.

D.1 Linearisation of the internal force vector

In index notation, the Galerkin expression for internal force is

$$p_{Ii}^{\mathrm{int}} = \int_{\Omega} \frac{\partial N_I}{\partial x_r} \sigma_{ir} \, \mathrm{d}\Omega \tag{A.2}$$

$$= \int_{\Omega_0} \frac{\partial N_I}{\partial x_r} \tau_{ir} \, \mathrm{d}\Omega_0 \,. \tag{A.3}$$

As in Appendix A, the linearisations with respect to translations must use A.3 due to their effect on domain size, whereas the linearisations with respect to microrotations can use A.2 directly.

D.1.1 With respect to translations

The derivative of the elastic stretch $\boldsymbol{U}^{\mathrm{e}}$ with respect to translations now includes an additional dependency via the elastoplastic constitutive model. As such, and reusing (A.9),

$$\frac{\partial U^{\mathrm{e}}_{\psi\bar{b}}}{\partial u_{Jj}} = \frac{\partial U^{\mathrm{e}}_{\psi\bar{b}}}{\partial F_{m\theta}} \frac{\partial F_{m\theta}}{\partial u_{Jj}} + \frac{\partial U^{\mathrm{e}}_{\psi\bar{b}}}{\partial (F^{\mathrm{e}})^{\mathrm{tr}}_{m\bar{i}}} \frac{\partial (F^{\mathrm{e}})^{\mathrm{tr}}_{m\bar{i}}}{\partial u_{Jj}} \tag{D.1}$$

$$= \frac{\partial U^{\mathrm{e}}_{\psi\bar{b}}}{\partial F_{m\theta}} \delta_{jm} F_{s\theta} \frac{\partial N_J}{\partial x_s} + \frac{\partial U^{\mathrm{e}}_{\psi\bar{b}}}{\partial (F^{\mathrm{e}})^{\mathrm{tr}}_{m\bar{i}}} \frac{\partial F_{m\alpha}}{\partial u_{Jj}} (\widetilde{F^{\mathrm{p}}})^{-1}_{\alpha\bar{i}} \tag{D.2}$$

$$= \frac{\partial U^{\mathrm{e}}_{\psi\bar{b}}}{\partial F_{m\theta}} \delta_{jm} F_{s\theta} \frac{\partial N_J}{\partial x_s} + \frac{\partial U^{\mathrm{e}}_{\psi\bar{b}}}{\partial (F^{\mathrm{e}})^{\mathrm{tr}}_{m\bar{i}}} \delta_{jm} F_{s\alpha} \frac{\partial N_J}{\partial x_s} (\widetilde{F^{\mathrm{p}}})^{-1}_{\alpha\bar{i}} \tag{D.3}$$

$$= \frac{\partial U^{\mathrm{e}}_{\psi\bar{b}}}{\partial F_{m\theta}} \delta_{jm} F_{s\theta} \frac{\partial N_J}{\partial x_s} + \frac{\partial U^{\mathrm{e}}_{\psi\bar{b}}}{\partial (F^{\mathrm{e}})^{\mathrm{tr}}_{m\bar{i}}} \delta_{jm} (F^{\mathrm{e}})^{\mathrm{tr}}_{s\bar{i}} \frac{\partial N_J}{\partial x_s} \tag{D.4}$$

$$= \left(\frac{\partial U^{\mathrm{e}}_{\psi\bar{b}}}{\partial F_{m\theta}} F_{s\theta} + \frac{\partial U^{\mathrm{e}}_{\psi\bar{b}}}{\partial (F^{\mathrm{e}})^{\mathrm{tr}}_{m\bar{i}}} (F^{\mathrm{e}})^{\mathrm{tr}}_{s\bar{i}} \right) G_{msJj}, \tag{D.5}$$

where $G_{msJj} = \delta_{jm} \frac{\partial N_J}{\partial x_s}$. From the Kirchhoff stress definition (B.23),

$$\frac{\partial \tau_{ir}}{\partial U^{\mathrm{e}}_{\psi\bar{b}}} = \frac{\partial}{\partial U^{\mathrm{e}}_{\psi\bar{b}}} \left(Q_{i\alpha} D_{\alpha\bar{l}\gamma\bar{k}} E^{\mathrm{e}}_{\gamma\bar{k}} Q_{r\delta} U^{\mathrm{e}}_{\delta\bar{l}} \right) \tag{D.6}$$

$$= Q_{i\alpha} D_{\alpha\bar{l}\gamma\bar{k}} \frac{\partial E^{\mathrm{e}}_{\gamma\bar{k}}}{\partial U^{\mathrm{e}}_{\psi\bar{b}}} Q_{r\delta} U^{\mathrm{e}}_{\delta\bar{l}} + Q_{i\alpha} D_{\alpha\bar{l}\gamma\bar{k}} E^{\mathrm{e}}_{\gamma\bar{k}} Q_{r\delta} \frac{\partial U^{\mathrm{e}}_{\delta\bar{l}}}{\partial U^{\mathrm{e}}_{\psi\bar{b}}} \tag{D.7}$$

$$= Q_{i\alpha} D_{\alpha\bar{l}\gamma\bar{k}} \delta_{\gamma\psi} \delta_{\bar{b}\bar{k}} Q_{r\delta} U^{\mathrm{e}}_{\delta\bar{l}} + Q_{i\alpha} D_{\alpha\bar{l}\gamma\bar{k}} E^{\mathrm{e}}_{\gamma\bar{k}} Q_{r\delta} \delta_{\delta\psi} \delta_{\bar{b}\bar{l}} \tag{D.8}$$

$$= L^{\mathrm{e}}_{ir\alpha\bar{l}} D_{\alpha\bar{l}\psi\bar{b}} + Q_{i\alpha} B_{\alpha\bar{b}} Q_{r\psi} \tag{D.9}$$

so that

$$\frac{\partial \tau_{ir}}{\partial u_{Jj}} = \left(L^{\mathrm{e}}_{ir\alpha\bar{l}} D_{\alpha\bar{l}\psi\bar{b}} + Q_{i\alpha} B_{\alpha\bar{b}} Q_{r\psi} \right) \left(\frac{\partial U^{\mathrm{e}}_{\psi\bar{b}}}{\partial F_{m\theta}} F_{s\theta} + \frac{\partial U^{\mathrm{e}}_{\psi\bar{b}}}{\partial (F^{\mathrm{e}})^{\mathrm{tr}}_{m\bar{i}}} (F^{\mathrm{e}})^{\mathrm{tr}}_{s\bar{i}} \right) G_{msJj}. \tag{D.10}$$

Meanwhile, the tangent stiffness can begin to be constructed by combining (A.18) with (A.9), leading to

$$K^{pu}_{IiJj} = \frac{\partial p^{\mathrm{int}}_{Ii}}{\partial u_{Jj}} \tag{D.11}$$

$$
\begin{aligned}
&= \int_{\Omega_0} \frac{\partial}{\partial u_{Jj}} \left(\frac{\partial N_I}{\partial x_r} \tau_{ir} \right) \mathrm{d}\Omega_0 && \text{(D.12)} \\
&= \int_{\Omega_0} \left(\frac{\partial}{\partial u_{Jj}} \left(\frac{\partial N_I}{\partial x_r} \right) \tau_{ir} + \frac{\partial N_I}{\partial x_r} \frac{\partial \tau_{ir}}{\partial u_{Jj}} \right) \mathrm{d}\Omega_0 && \text{(D.13)} \\
&= \int_{\Omega_0} \left(\frac{\partial N_I}{\partial x_r} \frac{\partial \tau_{ir}}{\partial u_{Jj}} - \frac{\partial N_I}{\partial x_m} \tau_{ir} F^{-1}_{\theta r} F_{s\theta} \delta_{jm} \frac{\partial N_J}{\partial x_s} \right) \mathrm{d}\Omega_0 && \text{(D.14)} \\
&= \int_{\Omega_0} \left(\frac{\partial N_I}{\partial x_r} \frac{\partial \tau_{ir}}{\partial u_{Jj}} - \frac{\partial N_I}{\partial x_j} \tau_{is} \frac{\partial N_J}{\partial x_s} \right) \mathrm{d}\Omega_0 && \text{(D.15)} \\
&= \int_{\Omega_0} \frac{\partial N_I}{\partial x_r} \left(\frac{\partial \tau_{ir}}{\partial u_{Jj}} - \tau_{is} \delta_{jr} \frac{\partial N_J}{\partial x_s} \right) \mathrm{d}\Omega_0 && \text{(D.16)}
\end{aligned}
$$

into which (D.10) may be substituted to give

$$
\begin{aligned}
K^{pu}_{IiJj} &= \int_{\Omega_0} \frac{\partial N_I}{\partial x_r} \Bigg(\left(L^{\mathrm{e}}_{ir\alpha\bar{l}} D_{\alpha\bar{l}\psi\bar{b}} + Q_{i\alpha} B_{\alpha\bar{b}} Q_{r\psi} \right) \Bigg(\frac{\partial U^{\mathrm{e}}_{\psi\bar{b}}}{\partial F_{m\theta}} F_{s\theta} \\
&\qquad + \frac{\partial U^{\mathrm{e}}_{\psi\bar{b}}}{\partial (F^{\mathrm{e}})^{\mathrm{tr}}_{m\bar{i}}} (F^{\mathrm{e}})^{\mathrm{tr}}_{s\bar{i}} \Bigg) G_{msJj} - \tau_{is} \delta_{jr} \frac{\partial N_J}{\partial x_s} \Bigg) \mathrm{d}\Omega_0 && \text{(D.17)} \\
&= \int_{\Omega} G_{arIi} \Bigg(J^{-1} \left(L^{\mathrm{e}}_{ar\alpha\bar{l}} D_{\alpha\bar{l}\psi\bar{b}} + Q_{a\alpha} B_{\alpha\bar{b}} Q_{r\psi} \right) \Bigg(\frac{\partial U^{\mathrm{e}}_{\psi\bar{b}}}{\partial F_{m\theta}} F_{s\theta} \\
&\qquad + \frac{\partial U^{\mathrm{e}}_{\psi\bar{b}}}{\partial (F^{\mathrm{e}})^{\mathrm{tr}}_{m\bar{i}}} (F^{\mathrm{e}})^{\mathrm{tr}}_{s\bar{i}} \Bigg) - \sigma_{as} \delta_{rm} \Bigg) G_{msJj} \, \mathrm{d}\Omega && \text{(D.18)} \\
&= \int_{\Omega} G_{arIi} (a_1)_{arms} G_{msJj} \, \mathrm{d}\Omega && \text{(D.19)}
\end{aligned}
$$

where

$$
(a_1)_{arms} = J^{-1} \left(L^{\mathrm{e}}_{ar\alpha\bar{l}} D_{\alpha\bar{l}\psi\bar{b}} + Q_{a\alpha} B_{\alpha\bar{b}} Q_{r\psi} \right) \left(\frac{\partial U^{\mathrm{e}}_{\psi\bar{b}}}{\partial F_{m\theta}} F_{s\theta} + \frac{\partial U^{\mathrm{e}}_{\psi\bar{b}}}{\partial (F^{\mathrm{e}})^{\mathrm{tr}}_{m\bar{i}}} (F^{\mathrm{e}})^{\mathrm{tr}}_{s\bar{i}} \right) - \sigma_{as} \delta_{rm}. \tag{D.20}
$$

D.1.2 With respect to microrotations

Using (3.162) and (A.98), the derivative of the elastic stretch with respect to a nodal microrotation increment is

$$
\begin{aligned}
\frac{\partial U^{\mathrm{e}}_{\psi\bar{b}}}{\partial \varphi_{Jj}} &= \frac{\partial U^{\mathrm{e}}_{\psi\bar{b}}}{\partial Q_{m\theta}} \frac{\partial Q_{m\theta}}{\partial \varphi_{Jj}} + \frac{\partial U^{\mathrm{e}}_{\psi\bar{b}}}{\partial (\Gamma^{\mathrm{e}})^{\mathrm{tr}}_{\gamma\pi}} \frac{\partial (\Gamma^{\mathrm{e}})^{\mathrm{tr}}_{\gamma\pi}}{\partial \varphi_{Jj}} && \text{(D.21)} \\
&= \frac{\partial U^{\mathrm{e}}_{\psi\bar{b}}}{\partial Q_{m\theta}} e_{mjn} Q_{n\theta} N_J + \frac{\partial U^{\mathrm{e}}_{\psi\bar{b}}}{\partial (\Gamma^{\mathrm{e}})^{\mathrm{tr}}_{\gamma\pi}} \frac{\partial \Gamma_{\gamma\pi}}{\partial \varphi_{Jj}} && \text{(D.22)} \\
&= \frac{\partial U^{\mathrm{e}}_{\psi\bar{b}}}{\partial Q_{m\theta}} e_{mjn} Q_{n\theta} N_J + \frac{\partial U^{\mathrm{e}}_{\psi\bar{b}}}{\partial (\Gamma^{\mathrm{e}})^{\mathrm{tr}}_{\gamma\pi}} Q_{j\gamma} \frac{\partial N_J}{\partial x_s} F_{s\pi} && \text{(D.23)} \\
&= \frac{\partial U^{\mathrm{e}}_{\psi\bar{b}}}{\partial Q_{m\theta}} Q_{n\theta} \check{G}_{nmJj} + \frac{\partial U^{\mathrm{e}}_{\psi\bar{b}}}{\partial (\Gamma^{\mathrm{e}})^{\mathrm{tr}}_{\gamma\pi}} L_{ms\gamma\pi} G_{msJj}, && \text{(D.24)}
\end{aligned}
$$

where $\check{G}_{nmJj} = e_{nmj} N_J$. The derivative of the Kirchhoff stress is

$$\begin{aligned}
\frac{\partial \tau_{ir}}{\partial \varphi_{Jj}} &= \frac{\partial}{\partial \varphi_{Jj}} \left(Q_{i\alpha} D_{\alpha\bar{l}\gamma\bar{k}} E^{\mathrm{e}}_{\gamma\bar{k}} Q_{r\delta} U^{\mathrm{e}}_{\delta\bar{l}} \right) && \text{(D.25)} \\
&= \frac{\partial Q_{i\alpha}}{\partial \varphi_{Jj}} B_{\alpha\bar{l}} F^{\mathrm{e}}_{r\bar{l}} + Q_{i\alpha} D_{\alpha\bar{l}\gamma\bar{k}} \frac{\partial E^{\mathrm{e}}_{\gamma\bar{k}}}{\partial \varphi_{Jj}} F^{\mathrm{e}}_{r\bar{l}} + Q_{i\alpha} B_{\alpha\bar{l}} \frac{\partial Q_{r\delta}}{\partial \varphi_{Jj}} U^{\mathrm{e}}_{\delta\bar{l}} + Q_{i\alpha} B_{\alpha\bar{l}} Q_{r\delta} \frac{\partial U^{\mathrm{e}}_{\delta\bar{l}}}{\partial \varphi_{Jj}} && \text{(D.26)} \\
&= Q_{n\alpha} B_{\alpha\bar{l}} F^{\mathrm{e}}_{r\bar{l}} e_{ijn} N_J + L^{\mathrm{e}}_{ir\alpha\bar{l}} D_{\alpha\bar{l}\gamma\bar{k}} \frac{\partial U^{\mathrm{e}}_{\gamma\bar{k}}}{\partial \varphi_{Jj}} + Q_{i\alpha} B_{\alpha\bar{l}} Q_{n\delta} U^{\mathrm{e}}_{\delta\bar{l}} e_{rjn} N_J + Q_{i\alpha} B_{\alpha\bar{l}} Q_{r\delta} \frac{\partial U^{\mathrm{e}}_{\delta\bar{l}}}{\partial \varphi_{Jj}} && \text{(D.27)} \\
&= \tau_{nr} \check{G}_{niJj} + L^{\mathrm{e}}_{ir\alpha\bar{l}} D_{\alpha\bar{l}\gamma\bar{k}} \frac{\partial U^{\mathrm{e}}_{\gamma\bar{k}}}{\partial \varphi_{Jj}} + \tau_{in} \check{G}_{nrJj} + Q_{i\alpha} B_{\alpha\bar{k}} Q_{r\gamma} \frac{\partial U^{\mathrm{e}}_{\gamma\bar{k}}}{\partial \varphi_{Jj}} && \text{(D.28)}
\end{aligned}$$

which can be combined with (D.24) to give

$$\begin{aligned}
\frac{\partial \tau_{ir}}{\partial \varphi_{Jj}} = &\left(\left(L^{\mathrm{e}}_{ir\alpha\bar{l}} D_{\alpha\bar{l}\gamma\bar{k}} + Q_{i\alpha} B_{\alpha\bar{k}} Q_{r\gamma} \right) \frac{\partial U^{\mathrm{e}}_{\gamma\bar{k}}}{\partial Q_{m\theta}} Q_{n\theta} + \tau_{nr} \delta_{im} + \tau_{in} \delta_{rm} \right) \check{G}_{nmJj} \\
&+ \left(L^{\mathrm{e}}_{ir\alpha\bar{l}} D_{\alpha\bar{l}\gamma\bar{k}} + Q_{i\alpha} B_{\alpha\bar{k}} Q_{r\gamma} \right) \frac{\partial U^{\mathrm{e}}_{\gamma\bar{k}}}{\partial (\Gamma^{\mathrm{e}})^{\mathrm{tr}}_{\theta\pi}} L_{ms\theta\pi} G_{msJj}
\end{aligned} \qquad \text{(D.29)}$$

The tangent stiffness is then

$$\begin{aligned}
K^{p\varphi}_{IiJj} &= \frac{\partial p^{\mathrm{int}}_{Ii}}{\partial \varphi_{Jj}} && \text{(D.30)} \\
&= \int_\Omega \frac{\partial N_I}{\partial x_r} \frac{\partial \sigma_{ir}}{\partial \varphi_{Jj}} \,\mathrm{d}\Omega && \text{(D.31)} \\
&= \int_\Omega \frac{\partial N_I}{\partial x_r} \left(J^{-1} \left(\left(L^{\mathrm{e}}_{ir\alpha\bar{l}} D_{\alpha\bar{l}\gamma\bar{k}} + Q_{i\alpha} B_{\alpha\bar{k}} Q_{r\gamma} \right) \frac{\partial U^{\mathrm{e}}_{\gamma\bar{k}}}{\partial Q_{m\theta}} Q_{n\theta} + \tau_{nr} \delta_{im} + \tau_{in} \delta_{rm} \right) \check{G}_{nmJj} \right. \\
&\qquad \left. + \left(L^{\mathrm{e}}_{ir\alpha\bar{l}} D_{\alpha\bar{l}\gamma\bar{k}} + Q_{i\alpha} B_{\alpha\bar{k}} Q_{r\gamma} \right) \frac{\partial U^{\mathrm{e}}_{\gamma\bar{k}}}{\partial (\Gamma^{\mathrm{e}})^{\mathrm{tr}}_{\theta\pi}} L_{ms\theta\pi} G_{msJj} \right) \mathrm{d}\Omega && \text{(D.32)} \\
&= \int_\Omega G_{arIi} \left((a_2)_{arnm} \check{G}_{nmJj} + (a_3)_{arms} G_{msJj} \right) \mathrm{d}\Omega && \text{(D.33)}
\end{aligned}$$

where

$$(a_2)_{arnm} = J^{-1} \left(L^{\mathrm{e}}_{ar\alpha\bar{l}} D_{\alpha\bar{l}\gamma\bar{k}} + Q_{a\alpha} B_{\alpha\bar{k}} Q_{r\gamma} \right) \frac{\partial U^{\mathrm{e}}_{\gamma\bar{k}}}{\partial Q_{m\theta}} Q_{n\theta} + \sigma_{nr} \delta_{am} + \sigma_{an} \delta_{rm} \qquad \text{(D.34)}$$

and

$$(a_3)_{arms} = J^{-1} \left(L^{\mathrm{e}}_{ar\alpha\bar{l}} D_{\alpha\bar{l}\gamma\bar{k}} + Q_{a\alpha} B_{\alpha\bar{k}} Q_{r\gamma} \right) \frac{\partial U^{\mathrm{e}}_{\gamma\bar{k}}}{\partial (\Gamma^{\mathrm{e}})^{\mathrm{tr}}_{\theta\pi}} L_{ms\theta\pi}. \qquad \text{(D.35)}$$

D.2 Linearisation of the internal couple vector

The internal couple vector is written

$$q_{Ii}^{\mathrm{int}} = \int_{\Omega} \left(\frac{\partial N_I}{\partial x_r} \mu_{ir} + N_I e_{irn} \sigma_{rn} \right) \mathrm{d}\Omega \tag{A.60}$$

$$= \int_{\Omega_0} \left(\frac{\partial N_I}{\partial x_r} \nu_{ir} + N_I e_{irn} \tau_{rn} \right) \mathrm{d}\Omega_0 \,. \tag{A.61}$$

D.2.1 With respect to translations

Following a similar pattern to the elastic stretch, the elastic wryness tensor now depends on translations via the deformation gradient and elastic trial deformation gradient, i.e.

$$\frac{\partial \Gamma^{\mathrm{e}}_{\gamma\delta}}{\partial u_{Jj}} = \frac{\partial \Gamma^{\mathrm{e}}_{\gamma\delta}}{\partial F_{m\theta}} \frac{\partial F_{m\theta}}{\partial u_{Jj}} + \frac{\partial \Gamma^{\mathrm{e}}_{\gamma\delta}}{\partial (F^{\mathrm{e}})^{\mathrm{tr}}_{m\bar{i}}} \frac{\partial (F^{\mathrm{e}})^{\mathrm{tr}}_{m\bar{i}}}{\partial u_{Jj}} \tag{D.36}$$

$$= \left(\frac{\partial \Gamma^{\mathrm{e}}_{\gamma\delta}}{\partial F_{m\theta}} F_{s\theta} + \frac{\partial \Gamma^{\mathrm{e}}_{\gamma\delta}}{\partial (F^{\mathrm{e}})^{\mathrm{tr}}_{m\bar{i}}} (F^{\mathrm{e}})^{\mathrm{tr}}_{s\bar{i}} \right) G_{msJj}, \tag{D.37}$$

cf. (D.5). Moving onto the Kirchhoff couple-stress, and using (A.9),

$$\frac{\partial \nu_{ir}}{\partial u_{Jj}} = \frac{\partial}{\partial u_{Jj}} \left(Q_{i\alpha} \check{D}_{\alpha\beta\gamma\delta} \Gamma^{\mathrm{e}}_{\gamma\delta} F_{r\beta} \right) \tag{D.38}$$

$$= Q_{i\alpha} \check{D}_{\alpha\beta\gamma\delta} \left(\frac{\partial \Gamma^{\mathrm{e}}_{\gamma\delta}}{\partial u_{Jj}} F_{r\beta} + \Gamma^{\mathrm{e}}_{\gamma\delta} \frac{\partial F_{r\beta}}{\partial u_{Jj}} \right) \tag{D.39}$$

$$= L_{ir\alpha\beta} \check{D}_{\alpha\beta\gamma\delta} \frac{\partial \Gamma^{\mathrm{e}}_{\gamma\delta}}{\partial u_{Jj}} + Q_{i\alpha} S_{\alpha\beta} \delta_{jr} F_{s\beta} \frac{\partial N_J}{\partial x_s} \tag{D.40}$$

$$= L_{ir\alpha\beta} \check{D}_{\alpha\beta\gamma\delta} \frac{\partial \Gamma^{\mathrm{e}}_{\gamma\delta}}{\partial u_{Jj}} + \nu_{is} G_{rsJj}, \tag{D.41}$$

into which may be substituted (D.37) to give

$$\frac{\partial \nu_{ir}}{\partial u_{Jj}} = \left(L_{ir\alpha\beta} \check{D}_{\alpha\beta\gamma\delta} \left(\frac{\partial \Gamma^{\mathrm{e}}_{\gamma\delta}}{\partial F_{m\theta}} F_{s\theta} + \frac{\partial \Gamma^{\mathrm{e}}_{\gamma\delta}}{\partial (F^{\mathrm{e}})^{\mathrm{tr}}_{m\bar{i}}} (F^{\mathrm{e}})^{\mathrm{tr}}_{s\bar{i}} \right) + \nu_{is} \delta_{mr} \right) G_{msJj}. \tag{D.42}$$

Adapting (D.16), the tangent stiffness is then

$$K^{qu}_{IiJj} = \frac{\partial q^{\mathrm{int}}_{Ii}}{\partial u_{Jj}} \tag{D.43}$$

$$= \int_{\Omega_0} \frac{\partial}{\partial u_{Jj}} \left(\frac{\partial N_I}{\partial x_r} \nu_{ir} + N_I e_{irn} \tau_{rn} \right) \mathrm{d}\Omega_0 \tag{D.44}$$

$$= \int_{\Omega_0} \left(\frac{\partial}{\partial u_{Jj}} \left(\frac{\partial N_I}{\partial x_r} \right) \nu_{ir} + \frac{\partial N_I}{\partial x_r} \frac{\partial \nu_{ir}}{\partial u_{Jj}} + N_I e_{irn} \frac{\partial \tau_{rn}}{\partial u_{Jj}} \right) \mathrm{d}\Omega_0 \tag{D.45}$$

$$= \int_{\Omega_0} \left(\frac{\partial N_I}{\partial x_r} \left(\frac{\partial \nu_{ir}}{\partial u_{Jj}} - \nu_{is} \delta_{jr} \frac{\partial N_J}{\partial x_s} \right) + N_I e_{irn} \frac{\partial \tau_{rn}}{\partial u_{Jj}} \right) \mathrm{d}\Omega_0 \,, \tag{D.46}$$

and substitution of (D.42) and (D.10) leads to

$$\begin{aligned} K^{qu}_{IiJj} &= \int_{\Omega_0} \left(\frac{\partial N_I}{\partial x_r} L_{ir\alpha\beta} \check{D}_{\alpha\beta\gamma\delta} \left(\frac{\partial \Gamma^{\mathrm{e}}_{\gamma\delta}}{\partial F_{m\theta}} F_{s\theta} + \frac{\partial \Gamma^{\mathrm{e}}_{\gamma\delta}}{\partial (F^{\mathrm{e}})^{\mathrm{tr}}_{m\bar{\imath}}} (F^{\mathrm{e}})^{\mathrm{tr}}_{s\bar{\imath}} \right) G_{msJj} \right. \\ &\qquad \left. + N_I e_{irn} \left(L^{\mathrm{e}}_{rn\alpha\bar{l}} D_{\alpha\bar{l}\psi\bar{b}} + Q_{r\alpha} B_{\alpha\bar{b}} Q_{n\psi} \right) \left(\frac{\partial U^{\mathrm{e}}_{\psi\bar{b}}}{\partial F_{m\theta}} F_{s\theta} + \frac{\partial U^{\mathrm{e}}_{\psi\bar{b}}}{\partial (F^{\mathrm{e}})^{\mathrm{tr}}_{m\bar{\imath}}} (F^{\mathrm{e}})^{\mathrm{tr}}_{s\bar{\imath}} \right) G_{msJj} \right) \mathrm{d}\Omega_0 \end{aligned} \tag{D.47}$$

$$= \int_{\Omega} \left(G_{arIi} (a_4)_{arms} + \check{G}_{rnIi} (a_5)_{rnms} \right) G_{msJj} \, \mathrm{d}\Omega \,, \tag{D.48}$$

where

$$(a_4)_{arms} = J^{-1} L_{ar\alpha\beta} \check{D}_{\alpha\beta\gamma\delta} \left(\frac{\partial \Gamma^{\mathrm{e}}_{\gamma\delta}}{\partial F_{m\theta}} F_{s\theta} + \frac{\partial \Gamma^{\mathrm{e}}_{\gamma\delta}}{\partial (F^{\mathrm{e}})^{\mathrm{tr}}_{m\bar{\imath}}} (F^{\mathrm{e}})^{\mathrm{tr}}_{s\bar{\imath}} \right) \tag{D.49}$$

and

$$(a_5)_{rnms} = (a_1)_{rnms} + \sigma_{rs} \delta_{nm}. \tag{D.50}$$

D.2.2 With respect to microrotations

Beginning with a linearisation of the elastic wryness tensor,

$$\begin{aligned} \frac{\partial \Gamma^{\mathrm{e}}_{\gamma\delta}}{\partial \varphi_{Jj}} &= \frac{\partial \Gamma^{\mathrm{e}}_{\gamma\delta}}{\partial Q_{m\theta}} \frac{\partial Q_{m\theta}}{\partial \varphi_{Jj}} + \frac{\partial \Gamma^{\mathrm{e}}_{\gamma\delta}}{\partial (\Gamma^{\mathrm{e}})^{\mathrm{tr}}_{\psi\pi}} \frac{\partial (\Gamma^{\mathrm{e}})^{\mathrm{tr}}_{\psi\pi}}{\partial \varphi_{Jj}} && \text{(D.51)} \\ &= \frac{\partial \Gamma^{\mathrm{e}}_{\gamma\delta}}{\partial Q_{m\theta}} Q_{n\theta} \check{G}_{nmJj} + \frac{\partial \Gamma^{\mathrm{e}}_{\gamma\delta}}{\partial (\Gamma^{\mathrm{e}})^{\mathrm{tr}}_{\psi\pi}} L_{ms\psi\pi} G_{msJj} && \text{(D.52)} \end{aligned}$$

following (D.24). Considering the Kirchhoff couple-stress next,

$$\begin{aligned} \frac{\partial \nu_{ir}}{\partial \varphi_{Jj}} &= \frac{\partial}{\partial \varphi_{Jj}} \left(Q_{i\alpha} \check{D}_{\alpha\beta\gamma\delta} \Gamma^{\mathrm{e}}_{\gamma\delta} F_{r\beta} \right) && \text{(D.53)} \\ &= \frac{\partial Q_{i\alpha}}{\partial \varphi_{Jj}} \check{D}_{\alpha\beta\gamma\delta} \Gamma^{\mathrm{e}}_{\gamma\delta} F_{r\beta} + Q_{i\alpha} \check{D}_{\alpha\beta\gamma\delta} \frac{\partial \Gamma^{\mathrm{e}}_{\gamma\delta}}{\partial \varphi_{Jj}} F_{r\beta} && \text{(D.54)} \\ &= Q_{n\alpha} e_{ijn} N_J S_{\alpha\beta} F_{r\beta} + L_{ir\alpha\beta} \check{D}_{\alpha\beta\gamma\delta} \frac{\partial \Gamma^{\mathrm{e}}_{\gamma\delta}}{\partial \varphi_{Jj}} && \text{(D.55)} \\ &= \nu_{nr} \check{G}_{niJj} + L_{ir\alpha\beta} \check{D}_{\alpha\beta\gamma\delta} \frac{\partial \Gamma^{\mathrm{e}}_{\gamma\delta}}{\partial \varphi_{Jj}} && \text{(D.56)} \end{aligned}$$

which, using (D.52), becomes

$$\frac{\partial \nu_{ir}}{\partial \varphi_{Jj}} = L_{ir\alpha\beta} \check{D}_{\alpha\beta\gamma\delta} \frac{\partial \Gamma^{\mathrm{e}}_{\gamma\delta}}{\partial (\Gamma^{\mathrm{e}})^{\mathrm{tr}}_{\psi\pi}} L_{ms\psi\pi} G_{msJj} + \left(L_{ir\alpha\beta} \check{D}_{\alpha\beta\gamma\delta} \frac{\partial \Gamma^{\mathrm{e}}_{\gamma\delta}}{\partial Q_{m\theta}} Q_{n\theta} + \nu_{nr} \delta_{im} \right) \check{G}_{nmJj}. \tag{D.57}$$

Therefore, with (D.29), the tangent stiffness is

$$
\begin{aligned}
K^{q\varphi}_{IiJj} &= \frac{\partial q^{\text{int}}_{Ii}}{\partial \varphi_{Jj}} && \text{(D.58)}\\
&= \int_\Omega \left(\frac{\partial N_I}{\partial x_r} \frac{\partial \mu_{ir}}{\partial \varphi_{Jj}} + N_I e_{irn} \frac{\partial \sigma_{rn}}{\partial \varphi_{Jj}} \right) \mathrm{d}\Omega && \text{(D.59)}\\
&= \int_\Omega J^{-1} \Bigg(\frac{\partial N_I}{\partial x_r} \Bigg(L_{ir\alpha\beta} \check{D}_{\alpha\beta\gamma\delta} \frac{\partial \Gamma^{\mathrm{e}}_{\gamma\delta}}{\partial (\Gamma^{\mathrm{e}})^{\mathrm{tr}}_{\psi\pi}} L_{ms\psi\pi} G_{msJj} \\
&\qquad + \left(L_{ir\alpha\beta} \check{D}_{\alpha\beta\gamma\delta} \frac{\partial \Gamma^{\mathrm{e}}_{\gamma\delta}}{\partial Q_{m\theta}} Q_{n\theta} + \nu_{nr} \delta_{im} \right) \check{G}_{nmJj} \Bigg) \\
&\qquad + N_I e_{irn} \Bigg(\Bigg(\left(L^{\mathrm{e}}_{ir\alpha\bar{l}} D_{\alpha\bar{l}\gamma\bar{k}} + Q_{i\alpha} B_{\alpha\bar{k}} Q_{r\gamma} \right) \frac{\partial U^{\mathrm{e}}_{\gamma\bar{k}}}{\partial Q_{m\theta}} Q_{n\theta} + \tau_{nr} \delta_{im} + \tau_{in} \delta_{rm} \Bigg) \check{G}_{nmJj} \\
&\qquad + \left(L^{\mathrm{e}}_{ir\alpha\bar{l}} D_{\alpha\bar{l}\gamma\bar{k}} + Q_{i\alpha} B_{\alpha\bar{k}} Q_{r\gamma} \right) \frac{\partial U^{\mathrm{e}}_{\gamma\bar{k}}}{\partial (\Gamma^{\mathrm{e}})^{\mathrm{tr}}_{\theta\pi}} L_{ms\theta\pi} G_{msJj} \Bigg) \Bigg) \mathrm{d}\Omega \\
& && \text{(D.60)}\\
&= \int_\Omega \big(G_{arIi} ((a_6)_{arms} G_{msJj} + (a_7)_{arnm} \check{G}_{nmJj}) \\
&\qquad + \check{G}_{nmJj} ((a_3)_{arms} G_{msJj} + (a_2)_{arnm} \check{G}_{nmJj}) \big) \mathrm{d}\Omega\,, && \text{(D.61)}
\end{aligned}
$$

where

$$(a_6)_{arms} = J^{-1} L_{ar\alpha\beta} \check{D}_{\alpha\beta\gamma\delta} \frac{\partial \Gamma^{\mathrm{e}}_{\gamma\delta}}{\partial (\Gamma^{\mathrm{e}})^{\mathrm{tr}}_{\psi\pi}} L_{ms\psi\pi} \tag{D.62}$$

and

$$(a_7)_{arnm} = J^{-1} L_{ar\alpha\beta} \check{D}_{\alpha\beta\gamma\delta} \frac{\partial \Gamma^{\mathrm{e}}_{\gamma\delta}}{\partial Q_{m\theta}} Q_{n\theta} + \mu_{nr} \delta_{am}. \tag{D.63}$$

D.3 In the elastic case

If it transpires that the trial stress state is contained within the yield surface (i.e. $f < 0$), then the elastic trial state is accepted without calling the return mapping algorithm. Therefore to use the expressions for the tangent stiffness as laid out above, an elastic variant of $\boldsymbol{P}$ must be computed. This section derives only the eight components of $\boldsymbol{P}$ which are actually used in the formulation. Here the elastic stretch $\boldsymbol{U}^{\mathrm{e}}$ equals its elastic trial, defined

$$\boldsymbol{U}^{\mathrm{e}} = \boldsymbol{Q}^{\mathrm{T}} (\boldsymbol{F}^{\mathrm{e}})^{\mathrm{tr}}. \tag{D.64}$$

Therefore

$$\frac{\partial U^{\mathrm{e}}_{\psi\bar{b}}}{\partial F_{m\theta}} = 0, \tag{D.65}$$

as the constitutive model assumes that $(\boldsymbol{F}^{\mathrm{e}})^{\mathrm{tr}}$ and $\boldsymbol{F}$ are independent input variables, but

$$\frac{\partial U^{\mathrm{e}}_{\psi\bar{b}}}{\partial Q_{m\theta}} = \frac{\partial Q_{i\psi}}{\partial Q_{m\theta}}(F^{\mathrm{e}})^{\mathrm{tr}}_{i\bar{b}} \tag{D.66}$$

$$= \delta_{im}\delta_{\theta\psi}(F^{\mathrm{e}})^{\mathrm{tr}}_{i\bar{b}} \tag{D.67}$$

$$= \delta_{\theta\psi}(F^{\mathrm{e}})^{\mathrm{tr}}_{m\bar{b}}, \tag{D.68}$$

$$\frac{\partial U^{\mathrm{e}}_{\psi\bar{b}}}{\partial (F^{\mathrm{e}})^{\mathrm{tr}}_{m\bar{i}}} = Q_{i\psi}\frac{\partial (F^{\mathrm{e}})^{\mathrm{tr}}_{i\bar{b}}}{\partial (F^{\mathrm{e}})^{\mathrm{tr}}_{m\bar{i}}} \tag{D.69}$$

$$= Q_{i\psi}\delta_{im}\delta_{\bar{i}\bar{b}} \tag{D.70}$$

$$= Q_{m\psi}\delta_{\bar{i}\bar{b}} \tag{D.71}$$

and

$$\frac{\partial U^{\mathrm{e}}_{\psi\bar{b}}}{\partial (\Gamma^{\mathrm{e}})^{\mathrm{tr}}_{\gamma\pi}} = 0. \tag{D.72}$$

The elastic wryness tensor also assumes its elastic trial state, i.e. $\boldsymbol{\Gamma}^{\mathrm{e}} = (\boldsymbol{\Gamma}^{\mathrm{e}})^{\mathrm{tr}}$, so

$$\frac{\partial \Gamma^{\mathrm{e}}_{\gamma\delta}}{\partial F_{m\theta}} = \frac{\partial \Gamma^{\mathrm{e}}_{\gamma\delta}}{\partial Q_{m\theta}} = 0 \tag{D.73}$$

and

$$\frac{\partial \Gamma^{\mathrm{e}}_{\gamma\delta}}{\partial (F^{\mathrm{e}})^{\mathrm{tr}}_{m\bar{i}}} = 0, \tag{D.74}$$

while

$$\frac{\partial \Gamma^{\mathrm{e}}_{\gamma\delta}}{\partial (\Gamma^{\mathrm{e}})^{\mathrm{tr}}_{\psi\pi}} = \delta_{\gamma\psi}\delta_{\pi\delta}. \tag{D.75}$$

References

[1] H. Tresca, “On further applications of the flow of solids,” *Journal of the Franklin Institute*, vol. 106, pp. 326–334, Nov. 1878.

[2] C.-A. de Coulomb, “Essai sur une Application des Règles de Maximis et Minimis à quelques Problèmes de Statique, relatifs à l’Architecture,” *Mémoires de l’Académie des Sciences*, 1776. (In French).

[3] J. Salençon, “About Tresca’s Memoirs on the fluidity of solids (1864–1870),” *Comptes Rendus. Mécanique*, vol. 349, pp. 1–7, Feb. 2021.

[4] S. P. Timothy, “The structure of adiabatic shear bands in metals: A critical review,” *Acta Metallurgica*, vol. 35, pp. 301–306, Feb. 1987.

[5] D. Bigoni, *Nonlinear Solid Mechanics: Bifurcation Theory and Material Instability.* Cambridge: Cambridge University Press, 2012.

[6] F. Barras and N. Brantut, “Shear localisation controls the dynamics of earthquakes,” *Nature Communications*, vol. 16, p. 711, Jan. 2025. Publisher: Nature Publishing Group.

[7] B. Wang and Z. Liu, “Investigations on the chip formation mechanism and shear localization sensitivity of high-speed machining Ti6Al4V,” *The International Journal of Advanced Manufacturing Technology*, vol. 75, pp. 1065–1076, Nov. 2014.

[8] K. H. Roscoe, “The Influence of Strains in Soil Mechanics,” *Géotechnique*, vol. 20, pp. 129–170, June 1970.

[9] K. Soga, E. Alonso, A. Yerro, K. Kumar, and S. Bandara, “Trends in large-deformation analysis of landslide mass movements with particular emphasis on the material point method,” *Géotechnique*, vol. 66, pp. 248–273, Mar. 2016. Publisher: ICE Publishing.

[10] J. Knappett and R. F. Craig, *Craig’s Soil Mechanics.* Boca Raton: CRC Press, 9th edition ed., Oct. 2019.

[11] M. Hatherly and A. Malin, “Shear bands in deformed metals,” *Scripta Metallurgica*, vol. 18, no. 5, pp. 449–454, 1984.

[12] Q. Wei, D. Jia, K. Ramesh, and E. Ma, “Evolution and microstructure of shear bands in nanostructured Fe,” *Applied Physics Letters*, vol. 81, no. 7, pp. 1240–1242, 2002.

[13] I. Vardoulakis, “SECTION 11.4 - Behavior of Granular Materials,” in *Handbook of Materials Behavior Models* (J. Lemaitre, ed.), pp. 1093–1106, Burlington: Academic Press, Jan. 2001.

[14] A. Fall, F. Bertrand, G. Ovarlez, and D. Bonn, “Yield stress and shear banding in granular suspensions,” *Physical Review Letters*, vol. 103, no. 17, 2009.

[15] J. Desrues and E. Andò, “Strain localisation in granular media,” *Comptes Rendus Physique*, vol. 16, no. 1, pp. 26–36, 2015.

[16] P. Møller, S. Rodts, M. Michels, and D. Bonn, “Shear banding and yield stress in soft glassy materials,” *Physical Review E - Statistical, Nonlinear, and Soft Matter Physics*, vol. 77, no. 4, 2008.

[17] A. L. Greer, Y. Q. Cheng, and E. Ma, “Shear bands in metallic glasses,” *Materials Science and Engineering: R: Reports*, vol. 74, pp. 71–132, Apr. 2013.

[18] N. Golding, E. Schulson, and C. Renshaw, “Shear faulting and localized heating in ice: The influence of confinement,” *Acta Materialia*, vol. 58, no. 15, pp. 5043–5056, 2010.

[19] S. Bair and C. McCabe, “A study of mechanical shear bands in liquids at high pressure,” *Tribology International*, vol. 37, no. 10, pp. 783–789, 2004.

[20] J. Sulem and I. G. Vardoulakis, *Bifurcation Analysis in Geomechanics.* London: CRC Press, 1995.

[21] N. A. Fleck, G. M. Muller, M. F. Ashby, and J. W. Hutchinson, “Strain gradient plasticity: Theory and experiment,” *Acta Metallurgica et Materialia*, vol. 42, no. 2, pp. 475–487, 1994.

[22] J. Bodig and B. A. Jayne, *Mechanics of Wood and Wood Composites.* Van Nostrand Reinhold, 1982.

[23] P. N. Mollema and M. A. Antonellini, “Compaction bands: a structural analog for anti-mode I cracks in aeolian sandstone,” *Tectonophysics*, vol. 267, pp. 209–228, Dec. 1996.

[24] N. J. Price, *Analysis of geological structures.* Cambridge: Univ. P., 1990.

[25] X. Du Bernard, P. Eichhubl, and A. Aydin, “Dilation bands: A new form of localized failure in granular media,” *Geophysical Research Letters*, vol. 29, no. 24, pp. 29–1–29–4, 2002.

[26] F. Nicot, X. Wang, A. Wautier, R. Wan, and F. Darve, “Shear banding as a dissipative structure from a thermodynamic viewpoint,” *Journal of the Mechanics and Physics of Solids*, vol. 179, p. 105394, Oct. 2023.

[27] H.-B. Mühlhaus and I. Vardoulakis, “The thickness of shear bands in granular materials,” *Géotechnique*, vol. 37, no. 3, pp. 271–283, 1987.

[28] G. Viggiani, M. Küntz, and J. Desrues, "An experimental investigation of the relationships between grain size distribution and shear banding in sand," in *Continuous and Discontinuous Modelling of Cohesive-Frictional Materials* (P. A. Vermeer, H. J. Herrmann, S. Luding, W. Ehlers, S. Diebels, and E. Ramm, eds.), pp. 111–127, Berlin, Heidelberg: Springer, 2001.

[29] J. Desrues and G. Viggiani, "Strain localization in sand: an overview of the experimental results obtained in Grenoble using stereophotogrammetry," *International Journal for Numerical and Analytical Methods in Geomechanics*, vol. 28, no. 4, pp. 279–321, 2004.

[30] H. Rattez, Y. Shi, A. Sac-Morane, T. Klaeyle, B. Mielniczuk, and M. Veveakis, "Effect of grain size distribution on the shear band thickness evolution in sand," *Géotechnique*, vol. 72, pp. 350–363, Apr. 2022.

[31] F. Ceccato, A. Yerro, and G. Di Carluccio, "Simulating landslides with the material point method: Best practices, potentialities, and challenges," *Engineering Geology*, vol. 338, p. 107614, Aug. 2024.

[32] A. Weidner and H. Biermann, "Review on Strain Localization Phenomena Studied by High-Resolution Digital Image Correlation," *Advanced Engineering Materials*, vol. 23, no. 4, p. 2001409, 2021.

[33] Q. T. Phan, H. H. Bui, G. D. Nguyen, and F. Nicot, "Strain localization in the standard triaxial tests of granular materials: Insights into meso- and macro-scale behaviours," *International Journal for Numerical and Analytical Methods in Geomechanics*, vol. 48, no. 5, pp. 1345–1371, 2024.

[34] D. Kuriki, F. Briffod, T. Shiraiwa, and M. Enoki, "Multimodal deep learning framework to predict strain localization of Mg/LPSO two-phase alloys," *Acta Materialia*, vol. 281, p. 120398, Dec. 2024.

[35] W. Muhammad, A. P. Brahme, O. Ibragimova, J. Kang, and K. Inal, "A machine learning framework to predict local strain distribution and the evolution of plastic anisotropy & fracture in additively manufactured alloys," *International Journal of Plasticity*, vol. 136, p. 102867, Jan. 2021.

[36] Z. Cheng, J. Wang, and W. Xiong, "A machine learning-based strategy for experimentally estimating force chains of granular materials using X-ray micro-tomography," *Géotechnique*, vol. 74, pp. 1291–1303, Nov. 2024. Publisher: ICE Publishing.

[37] M. Miot, N. Deng, A. Wautier, F. Nicot, and R. Wan, "Stress transmission in granular materials versus epidemic spreading in human societies," in *ASCE Engineering Mechanics Institute 2024 International Conference* (C. Hellmich, B. Pichler, and S. Scheiner, eds.), (TU Wien, Vienna, Austria), Sept. 2024.

[38] N. Deng, M. Miot, A. Wautier, F. Nicot, and R. Wan, "A granular view of modelling a pandemic using the Discrete Element Method," in *ASCE Engineering Mechanics Institute 2024 International Conference* (C. Hellmich, B. Pichler, and S. Scheiner, eds.), (TU Wien, Vienna, Austria), Sept. 2024.

[39] U. S. Dixit, M. Hazarika, and J. P. Davim, “History of Mechanics,” in *A Brief History of Mechanical Engineering* (U. S. Dixit, M. Hazarika, and J. P. Davim, eds.), pp. 47–72, Cham: Springer International Publishing, 2017.

[40] W. Noll, “Purpose, Method, and Program of Nonlinear Continuum Mechanics,” in *An Idiot’s Fugitive Essays on Science: Methods, Criticism, Training, Circumstances* (C. Truesdell, ed.), pp. 49–68, New York, NY: Springer, 1984.

[41] T. Belytschko, W. K. Liu, B. Moran, and K. Elkhodary, *Nonlinear finite elements for continua and structures.* John Wiley & Sons, 2 ed., 2014.

[42] S. Patankar, *Numerical Heat Transfer and Fluid Flow.* Boca Raton: CRC Press, Oct. 2018.

[43] C. E. Augarde, S. J. Lee, and D. Loukidis, “Numerical modelling of large deformation problems in geotechnical engineering: A state-of-the-art review,” *Soils and Foundations*, vol. 61, pp. 1718–1735, Dec. 2021.

[44] F. Ceccato, *Study of large deformation geomechanical problem with the Material Point Method.* Doctoral Thesis, University of Padova, Sept. 2015.

[45] D. J. Benson, “An efficient, accurate, simple ALE method for nonlinear finite element programs,” *Computer Methods in Applied Mechanics and Engineering*, vol. 72, pp. 305–350, Mar. 1989.

[46] S. Li and W. K. Liu, “Meshfree and particle methods and their applications,” *Applied Mechanics Reviews*, vol. 55, pp. 1–34, Jan. 2002.

[47] W. F. Noh, “CEL: A time-dependent, two-space-dimensional, coupled Eulerian-Lagrange code,” tech. rep., Lawrence Livermore National Lab.(LLNL), Livermore, CA (United States), 1963.

[48] D. J. Benson, “Computational methods in Lagrangian and Eulerian hydrocodes,” *Computer Methods in Applied Mechanics and Engineering*, vol. 99, pp. 235–394, Sept. 1992.

[49] Dassault Systèmes, “Abaqus/CAE User’s Manual (6.11),” 2011.

[50] J. O. Hallquist, ed., *LS-DYNA: theory manual.* Livermore, Calif: Livermore Software Technology Corp, 2006.

[51] N. Matos, M. Gomes, and V. Infante, “Numerical modelling of soft body impacts: A review,” *Engineering Failure Analysis*, vol. 153, p. 107595, Nov. 2023.

[52] L. Zhang, Z. Cai, L. Wang, R. Zhang, and H. Liu, “Coupled Eulerian-Lagrangian finite element method for simulating soil-tool interaction,” *Biosystems Engineering*, vol. 175, pp. 96–105, Nov. 2018.

[53] R. A. Gingold and J. J. Monaghan, “Smoothed particle hydrodynamics: theory and application to non-spherical stars,” *Monthly Notices of the Royal Astronomical Society*, vol. 181, pp. 375–389, Dec. 1977.

[54] L. B. Lucy, “A numerical approach to the testing of the fission hypothesis,” *Astronomical Journal, vol. 82, Dec. 1977, p. 1013-1024.*, vol. 82, pp. 1013–1024, 1977.

[55] C. Augarde and C. Heaney, “The use of meshless methods in geotechnics,” *Computational Geomechanics, COMGEO I - Proceedings of the 1st International Symposium on Computational Geomechanics*, Jan. 2009.

[56] J. J. Monaghan, “Smoothed particle hydrodynamics,” *Reports on Progress in Physics*, vol. 68, p. 1703, July 2005.

[57] S. Zhao, H. H. Bui, V. Lemiale, and G. D. Nguyen, “SPH Simulation of Strain Localisation in Geomaterials Using a Visco-Plastic Constitutive Model,” in *Poromechanics VI*, pp. 1876–1883, American Society of Civil Engineers, July 2017.

[58] J. Pamin, H. Askes, and R. de Borst, “Two gradient plasticity theories discretized with the element-free Galerkin method,” *Computer Methods in Applied Mechanics and Engineering*, vol. 192, pp. 2377–2403, May 2003.

[59] C. Zhu, C. Peng, and W. Wu, “Applications of micropolar SPH in geomechanics,” *Acta Geotechnica*, vol. 16, pp. 2355–2369, Aug. 2021.

[60] Z. Ullah, W. M. Coombs, and C. E. Augarde, “An adaptive finite element/meshless coupled method based on local maximum entropy shape functions for linear and nonlinear problems,” *Computer Methods in Applied Mechanics and Engineering*, vol. 267, pp. 111–132, Dec. 2013.

[61] T. Belytschko, Y. Y. Lu, and L. Gu, “Element-free Galerkin methods,” *International Journal for Numerical Methods in Engineering*, vol. 37, no. 2, pp. 229–256, 1994.

[62] B. Chen and S. Coppieters, “Meshfree Digital Image Correlation Using Element Free Galerkin Method: Theory, Algorithm and Validation,” *Experimental Mechanics*, vol. 63, pp. 517–528, Mar. 2023.

[63] F. Asadi-Mehregan, P. Assari, and M. Dehghan, “The numerical solution of a mathematical model of the Covid-19 pandemic utilizing a meshless local discrete Galerkin method,” *Engineering with Computers*, vol. 39, pp. 3327–3351, Oct. 2023.

[64] S. N. Atluri and T. Zhu, “A new Meshless Local Petrov-Galerkin (MLPG) approach in computational mechanics,” *Computational Mechanics*, vol. 22, pp. 117–127, Aug. 1998.

[65] C. Heaney, C. Augarde, and A. Deeks, “Modelling Elasto-Plasticity Using the Hybrid MLPG Method,” *Computer Modeling in Engineering & Sciences*, vol. 56, no. 2, pp. 153–178, 2010. Publisher: Tech Science Press.

[66] S. N. Atluri, *The Meshless Method (MLPG) for Domain and BIE Discretizations*. Forsyth, Ga: Tech Science Press, July 2004.

[67] L. Monforte, M. Arroyo, J. M. Carbonell, and A. Gens, “Numerical simulation of undrained insertion problems in geotechnical engineering with the Particle Finite Element Method (PFEM),” *Computers and Geotechnics*, vol. 82, pp. 144–156, 2017. Publisher: Elsevier.

[68] J. M. Carbonell, L. Monforte, M. O. Ciantia, M. Arroyo, and A. Gens, “Geotechnical particle finite element method for modeling of soil-structure interaction under large deformation conditions,” *Journal of Rock Mechanics and Geotechnical Engineering*, vol. 14, pp. 967–983, June 2022.

[69] M. Cremonesi, A. Franci, S. Idelsohn, and E. Oñate, "A State of the Art Review of the Particle Finite Element Method (PFEM)," *Archives of Computational Methods in Engineering*, vol. 27, pp. 1709–1735, Nov. 2020.

[70] P. A. Cundall and O. D. L. Strack, "A discrete numerical model for granular assemblies," *Géotechnique*, vol. 29, pp. 47–65, Mar. 1979. Publisher: ICE Publishing.

[71] C. O'Sullivan, "Particle-Based Discrete Element Modeling: Geomechanics Perspective," *International Journal of Geomechanics*, vol. 11, pp. 449–464, Dec. 2011. Publisher: American Society of Civil Engineers.

[72] G. R. McDowell and O. Harireche, "Discrete element modelling of soil particle fracture," *Géotechnique*, vol. 52, pp. 131–135, Mar. 2002. Publisher: ICE Publishing.

[73] D. O. Potyondy and P. A. Cundall, "A bonded-particle model for rock," *International Journal of Rock Mechanics and Mining Sciences*, vol. 41, pp. 1329–1364, Dec. 2004.

[74] P. A. Langston, R. Masling, and B. N. Asmar, "Crowd dynamics discrete element multi-circle model," *Safety Science*, vol. 44, pp. 395–417, June 2006.

[75] J. Bruchmüller, B. G. M. van Wachem, S. Gu, and K. H. Luo, "Heat and Mass Transfer of Drying Particles in a Fluidized Bed," in *2010 14th International Heat Transfer Conference, Volume 4*, (Washington DC, USA), pp. 289–295, American Society of Mechanical Engineers Digital Collection, Mar. 2011.

[76] R. Kawamoto, E. Andò, G. Viggiani, and J. E. Andrade, "Level set discrete element method for three-dimensional computations with triaxial case study," *Journal of the Mechanics and Physics of Solids*, vol. 91, pp. 1–13, June 2016.

[77] S. Liu, F. Chen, W. Ge, and P. Ricoux, "NURBS-based DEM for non-spherical particles," *Particuology*, vol. 49, pp. 65–76, Apr. 2020.

[78] D. Wolpert and W. Macready, "No free lunch theorems for optimization," *IEEE Transactions on Evolutionary Computation*, vol. 1, pp. 67–82, Apr. 1997. Conference Name: IEEE Transactions on Evolutionary Computation.

[79] A. de Vaucorbeil, V. P. Nguyen, S. Sinaie, and J. Y. Wu, "Chapter Two - Material point method after 25 years: Theory, implementation, and applications," in *Advances in Applied Mechanics* (S. P. A. Bordas and D. S. Balint, eds.), vol. 53, pp. 185–398, Elsevier, Jan. 2020.

[80] W. T. Sołowski, M. Berzins, W. M. Coombs, J. E. Guilkey, M. Möller, Q. A. Tran, T. Adibaskoro, S. Seyedan, R. Tielen, and K. Soga, "Material point method: Overview and challenges ahead," in *Advances in Applied Mechanics* (S. P. A. Bordas and D. S. Balint, eds.), vol. 54, pp. 113–204, Elsevier, Jan. 2021.

[81] V. P. Nguyen, A. D. Vaucorbeil, and S. Bordas, *The Material Point Method: Theory, Implementations and Applications.* Scientific Computation, Cham: Springer International Publishing, 2023.

[82] M. W. Evans and F. H. Harlow, "The particle-in-cell method for hydrodynamic calculations," Tech. Rep. LA-2139, Los Alamos Scientific Lab., N. Mex., June 1957.

[83] F. H. Harlow, “Hydrodynamic Problems Involving Large Fluid Distortions,” *J. ACM*, vol. 4, pp. 137–142, Apr. 1957.

[84] F. H. Harlow, D. O. Dickman, J. Harris, and R. E. Martin, “Two-dimensional hydrodynamic calculations,” Tech. Rep. LA-2301, Los Alamos National Lab. (LANL), Los Alamos, NM (United States), Apr. 1959.

[85] F. H. Harlow, “The particle-in-cell computing method for fluid dynamics,” *Methods Comput. Phys.*, vol. 3, pp. 319–343, 1964.

[86] J. Brackbill, D. Kothe, and H. Ruppel, “FLIP: A Low-Dissipation, Particle-in-Cell Method for Fluid Flow,” *Computer Physics Communications*, vol. 48, pp. 25–38, Jan. 1988.

[87] T. Tajima, J. N. Leboeuf, and J. M. Dawson, “A magnetohydrodynamic particle code with force free electrons for fluid simulations,” *Journal of Computational Physics*, vol. 38, pp. 237–250, Nov. 1980.

[88] J. U. Brackbill, “FLIP MHD: A particle-in-cell method for magnetohydrodynamics,” *Journal of Computational Physics*, vol. 96, pp. 163–192, Sept. 1991.

[89] D. Sulsky, Z. Chen, and H. L. Schreyer, “A particle method for history-dependent materials,” *Computer Methods in Applied Mechanics and Engineering*, vol. 118, no. 1-2, pp. 179–196, 1994. Publisher: Elsevier.

[90] D. Sulsky, S.-J. Zhou, and H. L. Schreyer, “Application of a particle-in-cell method to solid mechanics,” *Computer Physics Communications*, vol. 87, pp. 236–252, May 1995.

[91] J. Nairn, “Material Point Method Calculations with Explicit Cracks,” *CMES - Computer Modeling in Engineering and Sciences*, vol. 4, Dec. 2003.

[92] G. Pretti, *Continuum mechanics and implicit material point method to underpin the modelling of drag anchors for cable risk assessment.* Doctoral Thesis, Durham University, 2024.

[93] N. D. Gavin, *Case in Points: Developing a Patient-specific Model of the Human Left Ventricle using the Material Point Method.* Doctoral Thesis, Durham University, 2024.

[94] A. Stomakhin, C. Schroeder, L. Chai, J. Teran, and A. Selle, “A material point method for snow simulation,” *ACM Transactions on Graphics*, vol. 32, no. 4, pp. 1–10, 2013. Publisher: ACM New York, NY, USA.

[95] G. Klar, T. Gast, A. Pradhana, C. Fu, C. Schroeder, C. Jiang, and J. Teran, “Drucker-Prager elastoplasticity for sand animation,” *ACM Transactions on Graphics*, vol. 35, pp. 1–12, July 2016.

[96] J. Gaume and A. M. Puzrin, “Mechanisms of slab avalanche release and impact in the Dyatlov Pass incident in 1959,” *Communications Earth & Environment*, vol. 2, no. 1, pp. 1–11, 2021. Publisher: Nature Publishing Group.

[97] J. E. Guilkey and J. A. Weiss, “Implicit time integration for the material point method: Quantitative and algorithmic comparisons with the finite element method,” *International Journal for Numerical Methods in Engineering*, vol. 57, no. 9, pp. 1323–1338, 2003. Publisher: Wiley Online Library.

[98] S. G. Bardenhagen, “Energy Conservation Error in the Material Point Method for Solid Mechanics,” *Journal of Computational Physics*, vol. 180, pp. 383–403, July 2002.

[99] N. M. Newmark, “A Method of Computation for Structural Dynamics,” *Journal of the Engineering Mechanics Division*, vol. 85, pp. 67–94, July 1959. Publisher: American Society of Civil Engineers.

[100] D. Sulsky and A. Kaul, “Implicit dynamics in the material-point method,” *Computer Methods in Applied Mechanics and Engineering*, vol. 193, pp. 1137–1170, Mar. 2004.

[101] J. Yu, J. Zhao, W. Liang, and S. Zhao, “A semi-implicit material point method for coupled thermo-hydro-mechanical simulation of saturated porous media in large deformation,” *Computer Methods in Applied Mechanics and Engineering*, vol. 418, p. 116462, Jan. 2024.

[102] M. Neuner, A. Dummer, S. Abrari Vajari, P. Gamnitzer, H. Gimperlein, C. Linder, and G. Hofstetter, “A B-spline based gradient-enhanced micropolar implicit material point method for large localized inelastic deformations,” *Computer Methods in Applied Mechanics and Engineering*, vol. 431, p. 117291, Nov. 2024.

[103] S. G. Bardenhagen and E. M. Kober, “The generalized interpolation material point method,” *Computer Modeling in Engineering and Sciences*, vol. 5, no. 6, pp. 477–496, 2004. Publisher: Tech Science Press.

[104] A. Sadeghirad, R. M. Brannon, and J. Burghardt, “A convected particle domain interpolation technique to extend applicability of the material point method for problems involving massive deformations,” *International Journal for Numerical Methods in Engineering*, vol. 86, no. 12, pp. 1435–1456, 2011.

[105] A. Sadeghirad, R. Brannon, and J. Guilkey, “Second-order convected particle domain interpolation (CPDI2) with enrichment for weak discontinuities at material interfaces,” *International Journal for Numerical Methods in Engineering*, vol. 95, no. 11, pp. 928–952, 2013.

[106] L. Wang, W. M. Coombs, C. E. Augarde, M. Cortis, T. J. Charlton, M. J. Brown, J. Knappett, A. Brennan, C. Davidson, D. Richards, and A. Blake, “On the use of domain-based material point methods for problems involving large distortion,” *Computer Methods in Applied Mechanics and Engineering*, vol. 355, pp. 1003–1025, Oct. 2019.

[107] M. Steffen, R. M. Kirby, and M. Berzins, “Analysis and reduction of quadrature errors in the material point method (MPM),” *International Journal for Numerical Methods in Engineering*, vol. 76, no. 6, pp. 922–948, 2008.

[108] M. Steffen, P. C. Wallstedt, J. E. Guilkey, R. M. Kirby, and M. Berzins, “Examination and Analysis of Implementation Choices within the Material Point Method (MPM),”

Computer Modeling in Engineering & Sciences, vol. 31, no. 2, pp. 107–128, 2008. Publisher: Tech Science Press.

[109] Y. Yamaguchi, S. Moriguchi, and K. Terada, "Extended B-spline-based implicit material point method," *International Journal for Numerical Methods in Engineering*, vol. 122, no. 7, pp. 1746–1769, 2021.

[110] T. J. Charlton, W. M. Coombs, and C. E. Augarde, "iGIMP: An implicit generalised interpolation material point method for large deformations," *Computers & Structures*, vol. 190, pp. 108–125, 2017. Publisher: Elsevier.

[111] W. M. Coombs, "Ghost stabilisation of the material point method for stable quasi-static and dynamic analysis of large deformation problems," *International Journal for Numerical Methods in Engineering*, vol. 124, no. 21, pp. 4841–4875, 2023.

[112] T. J. O'Hare, P. A. Gourgiotis, W. M. Coombs, and C. E. Augarde, "An implicit Material Point Method for micropolar solids undergoing large deformations," *Computer Methods in Applied Mechanics and Engineering*, vol. 419, p. 116668, Feb. 2024.

[113] L. Beuth, *Formulation and application of a quasi-static material point method.* Doctoral Thesis, University of Stuttgart, 2012.

[114] L. Wang, W. M. Coombs, C. E. Augarde, M. Brown, J. Knappett, A. Brennan, D. Richards, and A. Blake, "Modelling Screwpile Installation Using the MPM," *Procedia Engineering*, vol. 175, pp. 124–132, Jan. 2017.

[115] M. Cortis, W. Coombs, C. Augarde, M. Brown, A. Brennan, and S. Robinson, "Imposition of essential boundary conditions in the material point method," *International Journal for Numerical Methods in Engineering*, vol. 113, no. 1, pp. 130–152, 2018.

[116] Y. Bing, M. Cortis, T. J. Charlton, W. M. Coombs, and C. E. Augarde, "B-spline based boundary conditions in the material point method," *Computers & Structures*, vol. 212, pp. 257–274, 2019. Publisher: Elsevier.

[117] Y. Liang, J. Given, and K. Soga, "The imposition of nonconforming Neumann boundary condition in the material point method without boundary representation," *Computer Methods in Applied Mechanics and Engineering*, vol. 404, p. 115785, Feb. 2023.

[118] G. Remmerswaal, P. J. Vardon, and M. A. Hicks, "Inhomogeneous Neumann boundary conditions for MPM and GIMP," *Computers and Geotechnics*, vol. 173, p. 106494, Sept. 2024.

[119] B. Chandra, V. Singer, T. Teschemacher, R. Wüchner, and A. Larese, "Nonconforming Dirichlet boundary conditions in implicit material point method by means of penalty augmentation," *Acta Geotechnica*, vol. 16, pp. 2315–2335, Aug. 2021.

[120] V. Singer, T. Teschemacher, A. Larese, R. Wüchner, and K.-U. Bletzinger, "Lagrange multiplier imposition of non-conforming essential boundary conditions in implicit material point method," *Computational Mechanics*, vol. 73, pp. 1311–1333, June 2024.

[121] C. Liu and W. Sun, “ILS-MPM: An implicit level-set-based material point method for frictional particulate contact mechanics of deformable particles,” *Computer Methods in Applied Mechanics and Engineering*, vol. 369, p. 113168, Sept. 2020.

[122] E. Burman, “Ghost penalty,” *Comptes Rendus. Mathématique*, vol. 348, no. 21-22, pp. 1217–1220, 2010.

[123] A. Nacar, A. Needleman, and M. Ortiz, “A finite element method for analyzing localization in rate dependent solids at finite strains,” *Computer Methods in Applied Mechanics and Engineering*, vol. 73, pp. 235–258, Aug. 1989.

[124] E. A. de Souza Neto, D. Peric, and D. R. Owen, *Computational methods for plasticity: theory and applications.* John Wiley & Sons, 2011.

[125] E. A. de Souza Neto, D. Perić, M. Dutko, and D. R. J. Owen, “Design of simple low order finite elements for large strain analysis of nearly incompressible solids,” *International Journal of Solids and Structures*, vol. 33, pp. 3277–3296, Aug. 1996.

[126] W. M. Coombs, T. J. Charlton, M. Cortis, and C. E. Augarde, “Overcoming volumetric locking in material point methods,” *Computer Methods in Applied Mechanics and Engineering*, vol. 333, pp. 1–21, 2018. Publisher: Elsevier.

[127] P. A. Vermeer, “Non-Associated Plasticity for Soils, Concrete and Rock,” in *Physics of Dry Granular Media* (H. J. Herrmann, J.-P. Hovi, and S. Luding, eds.), pp. 163–196, Dordrecht: Springer Netherlands, 1998.

[128] R. de Borst, S. A. Sabet, and T. Hageman, “Non-associated Cosserat plasticity,” *International Journal of Mechanical Sciences*, vol. 230, p. 107535, 2022. Publisher: Elsevier.

[129] W. M. Coombs and C. E. Augarde, “AMPLE: A Material Point Learning Environment,” *Advances in Engineering Software*, vol. 139, p. 102748, Jan. 2020.

[130] E. H. Lee and D. T. Liu, “Finite-Strain Elastic—Plastic Theory with Application to Plane-Wave Analysis,” *Journal of Applied Physics*, vol. 38, pp. 19–27, Jan. 1967.

[131] E. H. Lee, “Elastic-Plastic Deformation at Finite Strains,” *Journal of Applied Mechanics*, vol. 36, pp. 1–6, Mar. 1969.

[132] W. M. Coombs, C. E. Augarde, A. J. Brennan, M. J. Brown, T. J. Charlton, J. A. Knappett, Y. G. Motlagh, and L. Wang, “On Lagrangian mechanics and the implicit material point method for large deformation elasto-plasticity,” *Computer Methods in Applied Mechanics and Engineering*, vol. 358, p. 112622, 2020.

[133] T. J. Charlton, *An implicit generalised interpolation material point method for large deformation and gradient elasto-plasticity.* Doctoral Thesis, Durham University, 2018.

[134] W. M. Coombs, *Finite deformation of particulate geomaterials: frictional and anisotropic Critical State elasto-plasticity.* Doctoral Thesis, Durham University, 2011.

[135] R. de Borst, “Simulation of strain localization: A reappraisal of the Cosserat continuum,” *Engineering Computations*, vol. 8, pp. 317–332, 1991.

[136] T. Hageman, S. A. Sabet, and R. de Borst, “Convergence in non-associated plasticity and fracture propagation for standard, rate-dependent, and Cosserat continua,” *International Journal for Numerical Methods in Engineering*, vol. 122, no. 3, pp. 777–795, 2021.

[137] J. W. Rudnicki and J. R. Rice, “Conditions for the localization of deformation in pressure-sensitive dilatant materials,” *Journal of the Mechanics and Physics of Solids*, vol. 23, pp. 371–394, Dec. 1975.

[138] S. A. Sabet and R. de Borst, “Structural softening, mesh dependence, and regularisation in non-associated plastic flow,” *International Journal for Numerical and Analytical Methods in Geomechanics*, vol. 43, no. 13, pp. 2170–2183, 2019.

[139] R. de Borst, M. Crisfield, J. Remmers, and C. Verhoosel, *Nonlinear finite element analysis of solids and structures.* Wiley series in computational mechanics, Chichester, West Sussex, United Kingdom: Wiley, 2nd ed. ed., 2012.

[140] A. Zervos, I. Vardoulakis, M. Jean, and P. Lerat, “Numerical investigation of granular interfaces kinematics,” *Mechanics of Cohesive-frictional Materials*, vol. 5, no. 4, pp. 305–324, 2000.

[141] J. Liu, F. Nicot, and W. Zhou, “Sustainability of internal structures during shear band forming in 2D granular materials,” *Powder Technology*, vol. 338, pp. 458–470, Oct. 2018.

[142] R. de Borst, “Numerical modelling of bifurcation and localisation in cohesive-frictional materials,” *Pure and Applied Geophysics*, vol. 137, pp. 367–390, Dec. 1991.

[143] R. de Borst, L. Sluys, H. Mühlhaus, and J. Pamin, “Fundamental issues in finite element analyses of localization of deformation,” *Engineering Computations*, vol. 10, pp. 99–121, Feb. 1993.

[144] R. Hill, “Acceleration waves in solids,” *Journal of the Mechanics and Physics of Solids*, vol. 10, pp. 1–16, Jan. 1962.

[145] D. C. Erlich, D. R. Curran, and L. Seaman, “Further Development of a Computational Shear Band Model.:,” tech. rep., Defense Technical Information Center, Fort Belvoir, VA, Mar. 1980.

[146] P. Hofer, M. Neuner, P. Gamnitzer, and G. Hofstetter, “Revisiting strain localization analysis for elastoplastic constitutive models in geomechanics,” *International Journal for Numerical Methods in Engineering*, vol. n/a, no. n/a, p. e7579, 2024.

[147] D. C. Drucker, “A Definition of Stable Inelastic Material,” *Journal of Applied Mechanics*, vol. 26, pp. 101–106, Mar. 1959.

[148] R. Hill, “A general theory of uniqueness and stability in elastic-plastic solids,” *Journal of the Mechanics and Physics of Solids*, vol. 6, pp. 236–249, May 1958.

[149] T. B. Stoughton and J. W. Yoon, “Review of Drucker’s postulate and the issue of plastic stability in metal forming,” *International Journal of Plasticity*, vol. 22, pp. 391–433, Mar. 2006.

[150] O. C. Zienkiewicz, C. Humpheson, and R. W. Lewis, “Associated and non-associated visco-plasticity and plasticity in soil mechanics,” *Géotechnique*, vol. 25, pp. 671–689, Dec. 1975. Publisher: ICE Publishing.

[151] A. Needleman and M. Ortiz, “Effect of boundaries and interfaces on shear-band localization,” *International Journal of Solids and Structures*, vol. 28, pp. 859–877, Jan. 1991.

[152] A. Benallal and R. Billardon, “Hierarchy of Localization Phenomena Inside, at the Boundaries and Interfaces of Solids,” in *Anisotropy and Localization of Plastic Deformation* (J.-P. Boehler and A. S. Khan, eds.), (Dordrecht), pp. 39–42, Springer Netherlands, 1991.

[153] J. E. Marsden and T. J. R. Hughes, *Mathematical Foundations of Elasticity.* Courier Corporation, Jan. 1994. Google-Books-ID: RjzhDL5rLSoC.

[154] Z. P. Bažant and F.-B. Lin, “Non-local yield limit degradation,” *International Journal for Numerical Methods in Engineering*, vol. 26, no. 8, pp. 1805–1823, 1988.

[155] S. Forest, “Micromorphic Approach for Gradient Elasticity, Viscoplasticity, and Damage,” *Journal of Engineering Mechanics*, vol. 135, pp. 117–131, Mar. 2009. Publisher: American Society of Civil Engineers.

[156] G. Pijaudier-Cabot and F. Dufour, “Non local damage model: Boundary and evolving boundary effects,” *European Journal of Environmental and Civil Engineering*, vol. 14, pp. 729–749, June 2010.

[157] M. Jirásek and S. Rolshoven, “Comparison of integral-type nonlocal plasticity models for strain-softening materials,” *International Journal of Engineering Science*, vol. 41, pp. 1553–1602, Aug. 2003.

[158] E. C. Aifantis, “The physics of plastic deformation,” *International Journal of Plasticity*, vol. 3, pp. 211–247, Jan. 1987.

[159] M. Jirásek and S. Rolshoven, “Localization properties of strain-softening gradient plasticity models. Part I: Strain-gradient theories,” *International Journal of Solids and Structures*, vol. 46, pp. 2225–2238, June 2009.

[160] L. Anand, O. Aslan, and S. A. Chester, “A large-deformation gradient theory for elastic–plastic materials: Strain softening and regularization of shear bands,” *International Journal of Plasticity*, vol. 30-31, pp. 116–143, Mar. 2012.

[161] N. A. Fleck and J. W. Hutchinson, “A reformulation of strain gradient plasticity,” *Journal of the Mechanics and Physics of Solids*, vol. 49, pp. 2245–2271, Oct. 2001.

[162] H. Askes and M. A. Gutiérrez, “Implicit gradient elasticity,” *International Journal for Numerical Methods in Engineering*, vol. 67, no. 3, pp. 400–416, 2006.

[163] M. E. Gurtin and L. Anand, “Thermodynamics applied to gradient theories involving the accumulated plastic strain: The theories of Aifantis and Fleck and Hutchinson and their generalization,” *Journal of the Mechanics and Physics of Solids*, vol. 57, pp. 405–421, Mar. 2009.

[164] S. Forest, “Continuum thermomechanics of nonlinear micromorphic, strain and stress gradient media,” *Philosophical Transactions of the Royal Society A: Mathematical, Physical and Engineering Sciences*, vol. 378, p. 20190169, Mar. 2020. Publisher: Royal Society.

[165] R. de Borst and H.-B. Mühlhaus, “Gradient-dependent plasticity: Formulation and algorithmic aspects,” *International Journal for Numerical Methods in Engineering*, vol. 35, no. 3, pp. 521–539, 1992.

[166] A. Rodríguez-Ferran, T. Bennett, H. Askes, and E. Tamayo-Mas, “A general framework for softening regularisation based on gradient elasticity,” *International Journal of Solids and Structures*, vol. 48, pp. 1382–1394, May 2011.

[167] M. A. Mánica, A. Gens, J. Vaunat, and D. F. Ruiz, “Nonlocal plasticity modelling of strain localisation in stiff clays,” *Computers and Geotechnics*, vol. 103, pp. 138–150, Nov. 2018.

[168] E. Arzt, “Size effects in materials due to microstructural and dimensional constraints: a comparative review,” *Acta materialia*, vol. 46, no. 16, pp. 5611–5626, 1998. Publisher: Elsevier.

[169] L. An, D. Zhang, L. Zhang, and G. Feng, “Effect of nanoparticle size on the mechanical properties of nanoparticle assemblies,” *Nanoscale*, vol. 11, no. 19, pp. 9563–9573, 2019. Publisher: Royal Society of Chemistry.

[170] J. S. Stölken and A. G. Evans, “A microbend test method for measuring the plasticity length scale,” *Acta Materialia*, vol. 46, no. 14, pp. 5109–5115, 1998. Publisher: Elsevier BV.

[171] S. C. Cowin, “Stress functions for Cosserat elasticity,” *International Journal of Solids and Structures*, vol. 6, no. 4, pp. 389–398, 1970.

[172] W. Voigt, *Theoretische Studien über die Elasticitätsverhältnisse der Krystalle.* Abhandlungen der Königlichen Gesellschaft der Wissenschaften in Göttingen, Dieterichsche Verlags-Buchhandlung, 1887. (In German).

[173] R. A. Toupin, “Elastic materials with couple-stresses,” *Archive for Rational Mechanics and Analysis*, vol. 11, no. 1, pp. 385–414, 1962. Publisher: Springer Verlag.

[174] R. D. Mindlin and H. F. Tiersten, “Effects of couple-stresses in linear elasticity,” *Archive for Rational Mechanics and Analysis*, vol. 11, pp. 415–448, Jan. 1962.

[175] R. D. Mindlin, “Influence of couple-stresses on stress concentrations,” tech. rep., Columbia Univ., New York, USA, 1962.

[176] R. D. Mindlin, “Micro-structure in linear elasticity,” *Archive for Rational Mechanics and Analysis*, vol. 16, no. 1, pp. 51–78, 1964.

[177] R. D. Mindlin, “Second gradient of strain and surface-tension in linear elasticity,” *International Journal of Solids and Structures*, vol. 1, pp. 417–438, Nov. 1965.

[178] W. T. Koiter, “Couple Stresses in the Theory of Elasticity, I and II,” in *Proceedings Series B*, vol. 67, (Koninklijke Nederlandse Akademie van Wetenschappen), pp. 17–44, 1964.

[179] G. Hamel, *Elementare mechanik, ein lehrbuch enthaltend: eine begründung der allgemeinen mechanik; die mechanik der systeme starrer körper: die synthetischen und die elemente der analytischen methoden, sowie eine einführung in die prizipien der mechanik deformierbarer system.* B.G. Teubner, 1912. (In German).

[180] H. Schaefer, "The Cosserat Continuum," tech. rep., Gamm Meeting, Zürich, Switzerland, Mar. 1967. Translated from the original German by D. H. Delphenich.

[181] J. P. Bardet and I. Vardoulakis, "The asymmetry of stress in granular media," *International Journal of Solids and Structures*, vol. 38, pp. 353–367, Jan. 2001.

[182] F. Froiio, G. Tomassetti, and I. Vardoulakis, "Mechanics of granular materials: The discrete and the continuum descriptions juxtaposed," *International Journal of Solids and Structures*, vol. 43, pp. 7684–7720, Dec. 2006.

[183] S.-A. Papanicolopulos and E. Veveakis, "Sliding and rolling dissipation in Cosserat plasticity," *Granular Matter*, vol. 13, pp. 197–204, June 2011.

[184] I. Vardoulakis, *Cosserat Continuum Mechanics: With Applications to Granular Media.* Lecture Notes in Applied and Computational Mechanics, Springer International Publishing, 2018.

[185] R. P. Figueiredo, E. D. A. Vargas, and A. Moraes, "Analysis of bookshelf mechanisms using the mechanics of Cosserat generalized continua," *Journal of Structural Geology*, vol. 26, pp. 1931–1943, Oct. 2004.

[186] C. Atkinson and F. G. Leppington, "The effect of couple stresses on the tip of a crack," *International Journal of Solids and Structures*, vol. 13, pp. 1103–1122, Jan. 1977.

[187] P. A. Gourgiotis, T. Zisis, A. E. Giannakopoulos, and H. G. Georgiadis, "The Hertz contact problem in couple-stress elasticity," *International Journal of Solids and Structures*, vol. 168, pp. 228–237, Aug. 2019.

[188] J. T. Oden, D. M. Rigsby, and D. Cornett, "On the numerical solution of a class of problems in a linear first strain–gradient theory of elasticity," *International Journal for Numerical Methods in Engineering*, vol. 2, pp. 159–174, Apr. 1970. Publisher: John Wiley & Sons, Ltd.

[189] G. Hattori, J. Trevelyan, and P. A. Gourgiotis, "An isogeometric boundary element formulation for stress concentration problems in couple stress elasticity," *Computer Methods in Applied Mechanics and Engineering*, vol. 407, p. 115932, 2023. Publisher: Elsevier.

[190] M. Ristinmaa and M. Vecchi, "Use of couple-stress theory in elasto-plasticity," *Computer Methods in Applied Mechanics and Engineering*, vol. 136, pp. 205–224, Sept. 1996.

[191] P. A. Gourgiotis and D. Bigoni, "Stress channelling in extreme couple-stress materials Part I: Strong ellipticity, wave propagation, ellipticity, and discontinuity relations," *Journal of the Mechanics and Physics of Solids*, vol. 88, pp. 150–168, Mar. 2016.

[192] P. A. Gourgiotis and D. Bigoni, "Stress channelling in extreme couple-stress materials Part II: Localized folding vs faulting of a continuum in single and cross geometries," *Journal of the Mechanics and Physics of Solids*, vol. 88, pp. 169–185, Mar. 2016.

[193] I. Jasiuk and M. Ostoja-Starzewski, "From lattices and composites to micropolar continua: Analysis of materials with complex microstructure," in *Micromechanics and Nanoscale Effects: MEMS, Multi-Scale Materials and Micro-Flows* (V. M. Harik and L.-S. Luo, eds.), pp. 175–212, Netherlands: Kluwer Academic Publishers, 2004. Section: 7.

[194] E. Cosserat and F. Cosserat, *Théorie des corps déformables*. Paris: A. Hermann et fils, 1909. (In French).

[195] H. B. Mühlhaus, "Application of Cosserat theory in numerical solutions of limit load problems," *Archive of Applied Mechanics*, vol. 59, pp. 124–137, Mar. 1989. Publisher: Springer ADS Bibcode: 1989AAM....59..124M.

[196] R. de Borst and L. Sluys, "Localisation in a Cosserat continuum under static and dynamic loading conditions," *Computer Methods in Applied Mechanics and Engineering*, vol. 90, no. 1-3, pp. 805–827, 1991. Publisher: Elsevier.

[197] P. Neff, "A finite-strain elastic–plastic Cosserat theory for polycrystals with grain rotations," *International Journal of Engineering Science*, vol. 44, no. 8-9, pp. 574–594, 2006. Publisher: Elsevier.

[198] R. Lakes, "Experimental methods for study of Cosserat elastic solids and other generalized elastic continua," *Continuum models for materials with microstructure*, vol. 70, pp. 1–25, 1995. Publisher: Wiley New York.

[199] R. Lakes, "On the torsional properties of single osteons," *Journal of Biomechanics*, vol. 28, pp. 1409–1410, Nov. 1995.

[200] R. Lakes, "Physical meaning of elastic constants in Cosserat, void, and microstretch elasticity," *Journal of Mechanics of Materials and Structures*, vol. 11, no. 3, pp. 217–229, 2016. Publisher: Mathematical Sciences Publishers.

[201] Y. Solyaev, S. Lurie, E. Barchiesi, and L. Placidi, "On the dependence of standard and gradient elastic material constants on a field of defects," *Mathematics and Mechanics of Solids*, vol. 25, pp. 35–45, Jan. 2020. Publisher: SAGE Publications Ltd STM.

[202] S. Hassanpour and G. R. Heppler, "Step-by-Step Simplification of the Micropolar Elasticity Theory to the Couple-Stress and Classical Elasticity Theories," in *ASME 2014 International Mechanical Engineering Congress and Exposition*, vol. 9, American Society of Mechanical Engineers Digital Collection, Mar. 2015.

[203] S. Hassanpour and G. R. Heppler, "Micropolar elasticity theory: a survey of linear isotropic equations, representative notations, and experimental investigations," *Mathematics and Mechanics of Solids*, vol. 22, no. 2, pp. 224–242, 2017. Publisher: SAGE Publications Sage UK: London, England.

[204] A. Dietsche, P. Steinmann, and K. Willam, "Micropolar elastoplasticity and its role in localization," *International Journal of Plasticity*, vol. 9, no. 7, pp. 813–831, 1993.

[205] V. A. Eremeyev, L. P. Lebedev, and H. Altenbach, *Foundations of Micropolar Mechanics*. SpringerBriefs in Applied Sciences and Technology, Berlin, Heidelberg: Springer, 2013.

[206] A. C. Eringen, *Microcontinuum field theories*. Springer Science & Business Media, 2012.

[207] Y. Chen, J. D. Lee, and A. Eskandarian, "Atomistic viewpoint of the applicability of microcontinuum theories," *International Journal of Solids and Structures*, vol. 41, pp. 2085–2097, Apr. 2004.

[208] S. Forest and R. Sievert, "Nonlinear microstrain theories," *International Journal of Solids and Structures*, vol. 43, pp. 7224–7245, Nov. 2006.

[209] C. Sansour, "A unified concept of elastic-viscoplastic Cosserat and micromorphic continua," *Le Journal de Physique IV*, vol. 08, pp. Pr8–348, Nov. 1998. Publisher: EDP Sciences.

[210] R. A. Regueiro, "On finite strain micromorphic elastoplasticity," *International Journal of Solids and Structures*, vol. 47, pp. 786–800, Mar. 2010.

[211] C. Sansour, S. Skatulla, and H. Zbib, "A formulation for the micromorphic continuum at finite inelastic strains," *International Journal of Solids and Structures*, vol. 47, pp. 1546–1554, June 2010.

[212] S. Forest, "Nonlinear regularization operators as derived from the micromorphic approach to gradient elasticity, viscoplasticity and damage," *Proceedings of the Royal Society A: Mathematical, Physical and Engineering Sciences*, vol. 472, p. 20150755, Apr. 2016. Publisher: Royal Society.

[213] K. Saanouni and M. Hamed, "Micromorphic approach for finite gradient-elastoplasticity fully coupled with ductile damage: Formulation and computational aspects," *International Journal of Solids and Structures*, vol. 50, pp. 2289–2309, July 2013.

[214] A. Needleman, "Material rate dependence and mesh sensitivity in localization problems," *Computer Methods in Applied Mechanics and Engineering*, vol. 67, pp. 69–85, Mar. 1988.

[215] B. Loret and J. H. Prevost, "Dynamic strain localization in elasto-(visco-)plastic solids, Part 1. General formulation and one-dimensional examples," *Computer Methods in Applied Mechanics and Engineering*, vol. 83, pp. 247–273, Nov. 1990.

[216] L. J. Sluys and R. de Borst, "Wave propagation and localization in a rate-dependent cracked medium—model formulation and one-dimensional examples," *International Journal of Solids and Structures*, vol. 29, pp. 2945–2958, Jan. 1992.

[217] R. de Borst and T. Duretz, "On viscoplastic regularisation of strain-softening rocks and soils," *International Journal for Numerical and Analytical Methods in Geomechanics*, vol. 44, no. 6, pp. 890–903, 2020.

[218] A. Stathas and I. Stefanou, "The role of viscous regularization in dynamical problems, strain localization and mesh dependency," *Computer Methods in Applied Mechanics and Engineering*, vol. 388, p. 114185, Jan. 2022.

[219] P. Perzyna, “The constitutive equations for rate sensitive plastic materials,” *Quarterly of Applied Mathematics*, vol. 20, no. 4, pp. 321–332, 1963.

[220] J. Burghardt, R. Brannon, and J. Guilkey, “A nonlocal plasticity formulation for the material point method,” *Computer Methods in Applied Mechanics and Engineering*, vol. 225-228, pp. 55–64, 2012.

[221] M. Goodarzi and M. Rouainia, “Modelling Slope Failure Using a Quasi-static MPM with a Non-local Strain Softening Approach,” *Procedia Engineering*, vol. 175, pp. 220–225, 2017.

[222] T. J. Charlton, W. M. Coombs, and C. E. Augarde, “Gradient Elasto-plasticity with the Generalised Interpolation Material Point Method,” *Procedia Engineering*, vol. 175, pp. 110–115, Jan. 2017.

[223] C. Liu and W. Sun, “Shift boundary material point method: an image-to-simulation workflow for solids of complex geometries undergoing large deformation,” *Computational Particle Mechanics*, vol. 7, pp. 291–308, Mar. 2020.

[224] A. de Vaucorbeil, V. P. Nguyen, and T. K. Mandal, “Mesh objective simulations of large strain ductile fracture: A new nonlocal Johnson-Cook damage formulation for the Total Lagrangian Material Point Method,” *Computer Methods in Applied Mechanics and Engineering*, vol. 389, p. 114388, Feb. 2022.

[225] J. L. González Acosta, M. A. Mánica, P. J. Vardon, M. A. Hicks, and A. Gens, “A nonlocal material point method for the simulation of large deformation problems in brittle soils,” *Computers and Geotechnics*, vol. 172, p. 106424, Aug. 2024.

[226] D. Ram, T. Gast, C. Jiang, C. Schroeder, A. Stomakhin, J. Teran, and P. Kavehpour, “A material point method for viscoelastic fluids, foams and sponges,” in *Proceedings of the 14th ACM SIGGRAPH / Eurographics Symposium on Computer Animation*, SCA ’15, (New York, NY, USA), pp. 157–163, Association for Computing Machinery, Aug. 2015.

[227] P. A. Gordon, F. Liu, H. A. Meier, R. Panchadhara, and V. Srivastava, “A material point method for simulation of viscoelastic flows,” *Computational Particle Mechanics*, vol. 6, pp. 311–325, July 2019.

[228] H. Su, T. Xue, C. Han, C. Jiang, and M. Aanjaneya, “A unified second-order accurate in time MPM formulation for simulating viscoelastic liquids with phase change,” *ACM Trans. Graph.*, vol. 40, pp. 119:1–119:18, July 2021.

[229] Z. Więckowski, “The material point method in large strain engineering problems,” *Computer Methods in Applied Mechanics and Engineering*, vol. 193, pp. 4417–4438, Oct. 2004.

[230] Y. Fang, M. Li, M. Gao, and C. Jiang, “Silly rubber: an implicit material point method for simulating non-equilibrated viscoelastic and elastoplastic solids,” *ACM Trans. Graph.*, vol. 38, pp. 118:1–118:13, July 2019.

[231] R. Ma, W. Sun, C. R. Picu, and T. Sewell, “Domain partitioning material point method for simulating shock in polycrystalline energetic materials,” *Computer Methods in Applied Mechanics and Engineering*, vol. 404, p. 115815, Feb. 2023.

[232] Z. Tu, C. Li, Z. Zhao, L. Liu, C. Wang, C. Wang, and H. Qin, “A Unified MPM Framework Supporting Phase-field Models and Elastic-viscoplastic Phase Transition,” *ACM Trans. Graph.*, vol. 43, pp. 19:1–19:19, Jan. 2024.

[233] R. Ma and W. Sun, “A finite micro-rotation material point method for micropolar solid and fluid dynamics with three-dimensional evolving contacts and free surfaces,” *Computer Methods in Applied Mechanics and Engineering*, vol. 391, p. 114540, 2022. Publisher: Elsevier.

[234] T. J. O’Hare, P. A. Gourgiotis, W. M. Coombs, and C. E. Augarde, “A geometrically-exact Finite Element Method for micropolar continua with finite deformations,” in *UKACM Proceedings 2023*, (University of Warwick, Coventry), UKACM, 2023.

[235] T. J. O’Hare, P. A. Gourgiotis, W. M. Coombs, and C. E. Augarde, “Simulation of strain localisation with an elastoplastic micropolar material point method,” in *UKACM Proceedings 2024*, (Durham University, UK), pp. 141–144, Apr. 2024.

[236] J.-F. Pommaret, “François Cosserat et le secret de la théorie mathématique de l’élasticité,” *Annales des Ponts et Chaussées*, vol. 82, pp. 59–66, 1997. (In French).

[237] K. Chatzis and M. Brocato, “Les frères Cosserat : brève introduction à leur vie et à leurs travaux en mécanique,” in *Théorie des corps déformables*, pp. iii–xlv, Hermann, 2009. (In French).

[238] P. Duhem, “Le potentiel thermodynamique et la pression hydrostatique,” *Annales scientifiques de l’École Normale Supérieure*, vol. 3, no. 10, 1893.

[239] E. Cosserat and F. Cosserat, “Sur la théorie de l’élasticité. Premier mémoire,” *Annales de la faculté des sciences de Toulouse Mathématiques*, vol. 10, no. 3-4, pp. 1–116, 1896. (In French).

[240] E. Cosserat and F. Cosserat, “Note sur la théorie de l’action euclidienne,” in *Traité de la mécanique rationelle* (P. Appell, ed.), vol. 3, pp. 557–629, Paris: Gauthier-Villars, 2 ed., 1909. (In French).

[241] J. Sudria, *L’Action euclidienne de déformation et de mouvement.* Mémorial des sciences physiques, Paris: Gauthier - Villars, 1935.

[242] S. P. Timoshenko, “LXVI. On the correction for shear of the differential equation for transverse vibrations of prismatic bars,” *The London, Edinburgh, and Dublin Philosophical Magazine and Journal of Science*, May 1921. Publisher: Taylor & Francis Group.

[243] J. L. Ericksen and C. Truesdell, “Exact theory of stress and strain in rods and shells,” *Archive for Rational Mechanics and Analysis*, vol. 1, pp. 295–323, Jan. 1957.

[244] A. C. Eringen, “Linear Theory of Micropolar Elasticity,” *Journal of Mathematics and Mechanics*, vol. 15, no. 6, pp. 909–923, 1966. Publisher: Indiana University Mathematics Department.

[245] A. C. Eringen, “Theory of micropolar elasticity,” tech. rep., Princeton University, June 1967.

[246] A. C. Eringen, “Mechanics of Micromorphic Continua,” in *Mechanics of Generalized Continua* (E. Kröner, ed.), (Berlin, Heidelberg), pp. 18–35, Springer Berlin Heidelberg, 1968.

[247] A. C. Eringen, “Continuum physics. Volume 4: Polar and nonlocal field theories,” *New York*, 1976.

[248] C. B. Kafadar and A. C. Eringen, “Micropolar media—I the classical theory,” *International Journal of Engineering Science*, vol. 9, pp. 271–305, Mar. 1971.

[249] R. D. Mindlin, “Stress functions for a Cosserat continuum,” *International Journal of Solids and Structures*, vol. 1, no. 3, pp. 265–271, 1965.

[250] H. Neuber, “On the general solution of linear-elastic problems in isotropic and anisotropic Cosserat continua,” in *Applied Mechanics* (H. Görtler, ed.), (Berlin, Heidelberg), pp. 153–158, Springer Berlin Heidelberg, 1966.

[251] W. Nowacki, “Couple-Stresses in the Theory of Thermoelasticity,” in *Irreversible Aspects of Continuum Mechanics and Transfer of Physical Characteristics in Moving Fluids* (H. Parkus and L. I. Sedov, eds.), (Vienna), pp. 259–278, Springer, 1968.

[252] H. Schaefer, “Versuch einer Elastizitätstheorie des zweidimensionalen ebenen Cosserat-Kontinuums,” in *Miszellaneen der Angewandten Mechanik* (M. Schäfer, ed.), Berlin: Akademie Verlag, 1962.

[253] R. A. Toupin, “Theories of elasticity with couple-stress,” *Archive for Rational Mechanics and Analysis*, vol. 17, no. 2, pp. 85–112, 1964.

[254] C. Truesdell and R. Toupin, “The Classical Field Theories,” in *Principles of Classical Mechanics and Field Theory / Prinzipien der Klassischen Mechanik und Feldtheorie* (S. Flügge, ed.), pp. 226–858, Berlin, Heidelberg: Springer, 1960.

[255] C. Truesdell and W. Noll, “The Non-Linear Field Theories of Mechanics,” in *The Non-Linear Field Theories of Mechanics* (C. Truesdell, W. Noll, and S. S. Antman, eds.), pp. 1–579, Berlin, Heidelberg: Springer, 2004.

[256] N. Sachio, R. Benedict, and R. Lakes, “Finite element method for orthotropic micropolar elasticity,” *International Journal of Engineering Science*, vol. 22, pp. 319–330, Jan. 1984.

[257] E. Providas and M. A. Kattis, “Finite element method in plane Cosserat elasticity,” *Computers & Structures*, vol. 80, no. 27, pp. 2059–2069, 2002.

[258] F.-Y. Huang and L. Keo-Zoo, “Torsional analysis of micropolar elasticity using the finite element method,” *International Journal of Engineering Science*, vol. 32, no. 2, pp. 347–358, 1994. Publisher: Elsevier.

[259] S. Nakamura and R. Lakes, “Finite element analysis of Saint-Venant end effects in micropolar elastic solids,” *Engineering Computations*, vol. 12, no. 6, pp. 571–587, 1995. Publisher: MCB UP Ltd.

[260] F.-Y. Huang, B.-H. Yan, J.-L. Yan, and D.-U. Yang, “Bending analysis of micropolar elastic beam using a 3-D finite element method,” *International Journal of Engineering Science*, vol. 38, no. 3, pp. 275–286, 2000. Publisher: Elsevier.

[261] L. Li and S. Xie, "Finite element method for linear micropolar elasticity and numerical study of some scale effects phenomena in MEMS," *International Journal of Mechanical Sciences*, vol. 46, pp. 1571–1587, Nov. 2004.

[262] H. Zhang, H. Wang, and G. Liu, "Quadrilateral isoparametric finite elements for plane elastic Cosserat bodies," *Acta Mechanica Sinica*, vol. 21, no. 4, pp. 388–394, 2005. Publisher: Springer.

[263] A. Khoei, S. Yadegari, and S. Biabanaki, "3D finite element modeling of shear band localization via the micro-polar Cosserat continuum theory," *Computational Materials Science*, vol. 49, no. 4, pp. 720–733, 2010. Publisher: Elsevier.

[264] M. I. Alsaleh, G. Z. Voyiadjis, and K. A. Alshibli, "Modelling strain localization in granular materials using micropolar theory: mathematical formulations," *International Journal for Numerical and Analytical Methods in Geomechanics*, vol. 30, no. 15, pp. 1501–1524, 2006.

[265] K. A. Alshibli, M. I. Alsaleh, and G. Z. Voyiadjis, "Modelling strain localization in granular materials using micropolar theory: numerical implementation and verification," *International Journal for Numerical and Analytical Methods in Geomechanics*, vol. 30, no. 15, pp. 1525–1544, 2006.

[266] J. Tang, X. Chen, L. Cui, and Z. Liu, "Strain localization of Mohr-Coulomb soils with non-associated plasticity based on micropolar continuum theory," *Journal of Rock Mechanics and Geotechnical Engineering*, 2023.

[267] J. Wan, W. Qu, and X. Chu, "Operator-derived micropolar peridynamics," *Theoretical and Applied Fracture Mechanics*, p. 104806, Jan. 2025.

[268] S. Amirrahmat, A. M. Druckrey, K. A. Alshibli, and R. I. Al-Raoush, "Micro Shear Bands: Precursor for Strain Localization in Sheared Granular Materials," *Journal of Geotechnical and Geoenvironmental Engineering*, vol. 145, p. 04018104, Feb. 2019. Publisher: American Society of Civil Engineers.

[269] P. Steinmann, "A micropolar theory of finite deformation and finite rotation multiplicative elastoplasticity," *International Journal of Solids and Structures*, vol. 31, no. 8, pp. 1063–1084, 1994.

[270] C. Sansour, "A theory of the elastic-viscoplastic Cosserat continuum," *Archives of Mechanics*, vol. 50, pp. 577–597, Jan. 1998. Number: 3.

[271] P. Grammenoudis and C. Tsakmakis, "Finite element implementation of large deformation micropolar plasticity exhibiting isotropic and kinematic hardening effects," *International Journal for Numerical Methods in Engineering*, vol. 62, no. 12, pp. 1691–1720, 2005. Publisher: Wiley Online Library.

[272] S. Bauer, M. Schäfer, P. Grammenoudis, and C. Tsakmakis, "Three-dimensional finite elements for large deformation micropolar elasticity," *Computer Methods in Applied Mechanics and Engineering*, vol. 199, no. 41-44, pp. 2643–2654, 2010. Publisher: Elsevier.

[273] S. Ramezani, R. Naghdabadi, and S. Sohrabpour, "Constitutive equations for micropolar hyper-elastic materials," *International Journal of Solids and Structures*, vol. 46, pp. 2765–2773, July 2009.

[274] S. Bauer, W. G. Dettmer, D. Perić, and M. Schäfer, "Micropolar hyperelasticity: constitutive model, consistent linearization and simulation of 3D scale effects," *Computational Mechanics*, vol. 50, pp. 383–396, Oct. 2012.

[275] S. Bauer, W. G. Dettmer, D. Perić, and M. Schäfer, "Micropolar hyper-elastoplasticity: constitutive model, consistent linearization, and simulation of 3D scale effects," *International Journal for Numerical Methods in Engineering*, vol. 91, no. 1, pp. 39–66, 2012.

[276] S. G. Erdelj, G. Jelenić, and A. Ibrahimbegović, "Geometrically non-linear 3D finite-element analysis of micropolar continuum," *International Journal of Solids and Structures*, vol. 202, pp. 745–764, 2020. Publisher: Elsevier.

[277] M. Neuner, P. Gamnitzer, and G. Hofstetter, "A 3D gradient-enhanced micropolar damage-plasticity approach for modeling quasi-brittle failure of cohesive-frictional materials," *Computers & Structures*, vol. 239, p. 106332, Oct. 2020.

[278] M. Neuner, R. A. Regueiro, and C. Linder, "A unified finite strain gradient-enhanced micropolar continuum approach for modeling quasi-brittle failure of cohesive-frictional materials," *International Journal of Solids and Structures*, vol. 254-255, p. 111841, Nov. 2022.

[279] R. S. Lakes, "Size effects and micromechanics of a porous solid," *Journal of Materials Science*, vol. 18, no. 9, pp. 2572 – 2580, 1983.

[280] F. Renda, F. Boyer, J. Dias, and L. Seneviratne, "Discrete Cosserat Approach for Multisection Soft Manipulator Dynamics," *IEEE Transactions on Robotics*, vol. 34, pp. 1518–1533, Dec. 2018. Conference Name: IEEE Transactions on Robotics.

[281] J. Till, V. Aloi, and C. Rucker, "Real-time dynamics of soft and continuum robots based on Cosserat rod models," *The International Journal of Robotics Research*, vol. 38, pp. 723–746, May 2019. Publisher: SAGE Publications Ltd STM.

[282] D. W. Condiff and J. S. Dahler, "Fluid Mechanical Aspects of Antisymmetric Stress," *The Physics of Fluids*, vol. 7, pp. 842–854, June 1964.

[283] A. C. Eringen, "Simple microfluids," *International Journal of Engineering Science*, vol. 2, pp. 205–217, May 1964.

[284] N. Alkmim, P. Gamnitzer, M. Neuner, and G. Hofstetter, "Block preconditioning strategies for generalized continuum models with micropolar and nonlocal damage formulations," *International Journal for Numerical and Analytical Methods in Geomechanics*, vol. 48, pp. 1879–1906, May 2024.

[285] R. C. McAvoy, "Consistent linearization of micromorphic continuum theories," *Mathematics and Mechanics of Solids*, p. 10812865241280280, Nov. 2024. Publisher: SAGE Publications Ltd STM.

[286] A. Dummer, M. Neuner, P. Gamnitzer, and G. Hofstetter, "Robust and efficient implementation of finite strain generalized continuum models for material failure: Analytical, numerical, and automatic differentiation with hyper-dual numbers," *Computer Methods in Applied Mechanics and Engineering*, vol. 426, p. 116987, 2024. Publisher: Elsevier.

[287] L. Euler, “Découverte d’un nouveau principe de mécanique,” *Mémoires de l’académie des sciences de Berlin*, pp. 185–217, 1752.

[288] J. Argyris, “An excursion into large rotations,” *Computer Methods in Applied Mechanics and Engineering*, vol. 32, no. 1, pp. 85–155, 1982.

[289] R. Brannon, *Rotation, Reflection, and Frame Changes: Orthogonal tensors in computational engineering mechanics.* IOP Publishing, 2018. Publication Title: Orthogonal tensors in computational engineering mechanics.

[290] B. C. Hall, *Lie Groups, Lie Algebras, and Representations: An Elementary Introduction*, vol. 222 of *Graduate Texts in Mathematics.* Cham: Springer International Publishing, 2015.

[291] W. Pietraszkiewicz and V. Eremeyev, “On natural strain measures of the non-linear micropolar continuum,” *International Journal of Solids and Structures*, vol. 46, no. 3-4, pp. 774–787, 2009. Publisher: Elsevier.

[292] C. Sansour and W. Wagner, “Multiplicative updating of the rotation tensor in the finite element analysis of rods and shells – a path independent approach,” *Computational Mechanics*, vol. 31, pp. 153–162, 2003. Publisher: Springer.

[293] S. Ramezani and R. Naghdabadi, “Energy pairs in the micropolar continuum,” *International Journal of Solids and Structures*, vol. 44, pp. 4810–4818, July 2007.

[294] S. Grbčić, *Linked interpolation and strain invariance in finite-element modelling of micropolar continuum.* Doctoral Thesis, University of Rijeka, 2018.

[295] B. D. Coleman and W. Noll, “The thermodynamics of elastic materials with heat conduction and viscosity,” *Archive for Rational Mechanics and Analysis*, vol. 13, pp. 167–178, Dec. 1963.

[296] G. T. Houlsby, A. Amorosi, and E. Rojas, “Elastic moduli of soils dependent on pressure: a hyperelastic formulation,” *Géotechnique*, vol. 55, pp. 383–392, June 2005. Publisher: ICE Publishing.

[297] K. B. Sautter, M. Meßmer, T. Teschemacher, and K.-U. Bletzinger, “Limitations of the St. Venant–Kirchhoff material model in large strain regimes,” *International Journal of Non-Linear Mechanics*, vol. 147, p. 104207, Dec. 2022.

[298] J. F. Nye, *Physical properties of crystals: their representation by tensors and matrices.* Oxford: Clarendon Press, 1957.

[299] J. Jeong and P. Neff, “Existence, Uniqueness and Stability in Linear Cosserat Elasticity for Weakest Curvature Conditions,” *Mathematics and Mechanics of Solids*, vol. 15, pp. 78–95, Jan. 2010. Publisher: SAGE Publications Ltd STM.

[300] P. Neff, “Cosserat.” https://www.uni-due.de/mathematik/ag_neff/neff_cosserat [Accessed: 03/12/2024].

[301] P. Neff, “The Cosserat couple modulus for continuous solids is zero viz the linearized Cauchy-stress tensor is symmetric,” *ZAMM - Journal of Applied Mathematics and Mechanics / Zeitschrift für Angewandte Mathematik und Mechanik*, vol. 86, no. 11, pp. 892–912, 2006.

[302] S. C. Cowin, “An incorrect inequality in micropolar elasticity theory,” *Zeitschrift für angewandte Mathematik und Physik ZAMP*, vol. 21, pp. 494–497, May 1970.

[303] C. S. Chang and M. Lun, “Elastic material constants for isotropic granular solids with particle rotation,” *International Journal of Solids and Structures*, vol. 29, pp. 1001–1018, Jan. 1992.

[304] R. D. Gauthier and W. E. Jahsman, “A Quest for Micropolar Elastic Constants,” *Journal of Applied Mechanics*, vol. 42, pp. 369–374, June 1975.

[305] R. D. Gauthier, “Experimental investigations on micropolar media,” in *Mechanics of Micropolar Media*, pp. 395–463, WORLD SCIENTIFIC, Jan. 1982.

[306] H. C. Park and R. S. Lakes, “Torsion of a micropolar elastic prism of square cross-section,” *International Journal of Solids and Structures*, vol. 23, pp. 485–503, Jan. 1987.

[307] W. B. Anderson and R. S. Lakes, “Size effects due to Cosserat elasticity and surface damage in closed-cell polymethacrylimide foam,” *Journal of Materials Science*, vol. 29, pp. 6413–6419, Dec. 1994.

[308] N. Auffray, R. Bouchet, and Y. Brechet, “Strain gradient elastic homogenization of bidimensional cellular media,” *International Journal of Solids and Structures*, vol. 47, no. 13, pp. 1698–1710, 2010. Publisher: Elsevier.

[309] D. Bigoni and W. J. Drugan, “Analytical derivation of Cosserat moduli via homogenization of heterogeneous elastic materials,” *Journal of Applied Mechanics*, vol. 74, no. 4, pp. 741–753, 2007.

[310] G. Rizzi, F. Dal Corso, D. Veber, and D. Bigoni, “Identification of second-gradient elastic materials from planar hexagonal lattices. Part II: Mechanical characteristics and model validation,” *International Journal of Solids and Structures*, vol. 176, pp. 19–35, 2019. Publisher: Elsevier.

[311] T. Duretz, L. Räss, R. de Borst, and T. Hageman, “A Comparison of Plasticity Regularization Approaches for Geodynamic Modeling,” *Geochemistry, Geophysics, Geosystems*, vol. 24, no. 7, p. e2022GC010675, 2023.

[312] E. Papamichos, “Professor Ioannis Vardoulakis (1949–2009),” *International Journal for Numerical and Analytical Methods in Geomechanics*, vol. 34, no. 5, pp. 441–445, 2010.

[313] P. Neff, J. Jeong, I. Münch, and H. Ramézani, “Linear Cosserat Elasticity, Conformal Curvature and Bounded Stiffness,” in *Mechanics of Generalized Continua* (G. A. Maugin and A. V. Metrikine, eds.), vol. 21, pp. 55–63, New York, NY: Springer New York, 2010. Series Title: Advances in Mechanics and Mathematics.

[314] P. Neff, J. Jeong, and A. Fischle, “Stable identification of linear isotropic Cosserat parameters: bounded stiffness in bending and torsion implies conformal invariance of curvature,” *Acta Mechanica*, vol. 211, pp. 237–249, May 2010.

[315] P. Renteln, *Manifolds, Tensors, and Forms: An Introduction for Mathematicians and Physicists.* Cambridge University Press, Nov. 2013. Google-Books-ID: uJWGAgAAQBAJ.

[316] G. Jelenić and M. A. Crisfield, “Geometrically exact 3D beam theory: implementation of a strain-invariant finite element for statics and dynamics,” *Computer Methods in Applied Mechanics and Engineering*, vol. 171, no. 1, pp. 141–171, 1999.

[317] G. A. Holzapfel, *Nonlinear Solid Mechanics: A Continuum Approach for Engineering.* Wiley, Apr. 2000.

[318] A. Ibrahimbegović, “On the choice of finite rotation parameters,” *Computer Methods in Applied Mechanics and Engineering*, vol. 149, no. 1, pp. 49–71, 1997.

[319] I. Romero, “The interpolation of rotations and its application to finite element models of geometrically exact rods,” *Computational Mechanics*, vol. 34, pp. 121–133, July 2004.

[320] K. Shoemake, “Animating rotation with quaternion curves,” in *Proceedings of the 12th Annual Conference on Computer Graphics and Interactive Techniques*, pp. 245–254, 1985.

[321] J. Blow, “Understanding Slerp, Then Not Using It,” Feb. 2004. http://number-none.com/product/Understanding%20Slerp,%20Then%20Not%20Using%20It/ [Accessed: 11 December 2024].

[322] C. L. Bottasso and M. Borri, “Integrating finite rotations,” *Computer Methods in Applied Mechanics and Engineering*, vol. 164, pp. 307–331, Oct. 1998.

[323] A. Ibrahimbegović and I. Kožar, “Non-linear Wilson’s brick element for finite elastic deformations of three-dimensional solids,” *Communications in Numerical Methods in Engineering*, vol. 11, pp. 655–664, 1995.

[324] A. Ibrahimbegović, F. Frey, and I. Kožar, “Computational aspects of vector-like parametrization of three-dimensional finite rotations,” *International Journal for Numerical Methods in Engineering*, vol. 38, no. 21, pp. 3653–3673, 1995. Publisher: Wiley Online Library.

[325] R. A. Spurrier, “Comment on ” Singularity-Free Extraction of a Quaternion from a Direction-Cosine Matrix”,” *Journal of Spacecraft and Rockets*, vol. 15, pp. 255–255, July 1978. Publisher: American Institute of Aeronautics and Astronautics.

[326] B. W. Boehm, *Software Engineering Economics.* Englewood Cliffs, NJ: Prentice Hall, 1st edition ed., Oct. 1981.

[327] P. J. Roache, *Verification and validation in computational science and engineering.* Albuquerque, N.M: Hermosa Publishers, 1998.

[328] W. L. Oberkampf and C. J. Roy, *Verification and Validation in Scientific Computing.* Cambridge: Cambridge University Press, 2010.

[329] S. Timoshenko and J. N. Goodier, *Theory of Elasticity.* McGraw-Hill, 1969.

[330] C. E. Augarde and A. J. Deeks, “The use of Timoshenko’s exact solution for a cantilever beam in adaptive analysis,” *Finite Elements in Analysis and Design*, vol. 44, pp. 595–601, June 2008.

[331] G. Jelenić, “Pure bending in non-linear micropolar elasticity,” *International Journal of Mechanics and Materials in Design*, vol. 18, no. 1, pp. 243–265, 2022. Publisher: Springer.

[332] K.-J. Bathe and S. Bolourchi, “Large displacement analysis of three-dimensional beam structures,” *International Journal for Numerical Methods in Engineering*, vol. 14, no. 7, pp. 961–986, 1979. Publisher: Wiley Online Library.

[333] H. Lippmann, “Cosserat Plasticity and Plastic Spin,” *Applied Mechanics Reviews*, vol. 48, pp. 753–762, Nov. 1995.

[334] K. C. Bennett, R. A. Regueiro, and R. I. Borja, “Finite strain elastoplasticity considering the Eshelby stress for materials undergoing plastic volume change,” *International Journal of Plasticity*, vol. 77, pp. 214–245, Feb. 2016.

[335] H. Lippmann, “Eine Cosserat-Theorie des plastischen Fließens,” *Acta Mechanica*, vol. 8, pp. 255–284, Sept. 1969. (In German).

[336] D. Besdo, “Ein Beitrag zur nichtlinearen Theorie des Cosserat-Kontinuums,” *Acta Mechanica*, vol. 20, pp. 105–131, Mar. 1974. (In German).

[337] R. de Borst, “A generalisation of J2-flow theory for polar continua,” *Computer Methods in Applied Mechanics and Engineering*, vol. 103, pp. 347–362, 1993.

[338] A. Panteghini and R. Lagioia, “A micropolar isotropic plasticity formulation for non-associated flow rule and softening featuring multiple classical yield criteria,” *International Journal for Numerical and Analytical Methods in Geomechanics*, vol. 46, no. 4, pp. 674–696, 2022.

[339] C. Tamagnini, R. Castellanza, and R. Nova, “A Generalized Backward Euler algorithm for the numerical integration of an isotropic hardening elastoplastic model for mechanical and chemical degradation of bonded geomaterials,” *International Journal for Numerical and Analytical Methods in Geomechanics*, vol. 26, no. 10, pp. 963–1004, 2002.

[340] I. Vardoulakis and M. Goldscheider, “Biaxial Apparatus for Testing Shear Bands in Soils,” in *Proceedings, 10th ICSMFE*, vol. 4/61, (Stockholm), pp. 819–824, Blakema, 1981.

[341] A. Drescher, I. Vardoulakis, and C. Han, “A Biaxial Apparatus for Testing Soils,” *Geotechnical Testing Journal*, vol. 13, pp. 226–234, Sept. 1990.

[342] SSMG-ITALY, “X-shaped shear bands in clay,” 2010.

[343] M. Oda and H. Kazama, “Microstructure of shear bands and its relation to the mechanisms of dilatancy and failure of dense granular soils,” *Géotechnique*, vol. 48, pp. 465–481, Aug. 1998. Publisher: ICE Publishing.

[344] J. R. F. Arthur, T. Dunstan, Q. a. J. L. Al-Ani, and A. Assadi, “Plastic deformation and failure in granular media,” *Géotechnique*, vol. 27, pp. 53–74, Mar. 1977. Publisher: ICE Publishing.

[345] P. A. Vermeer, “The orientation of shear bands in biaxial tests,” *Géotechnique*, vol. 40, pp. 223–236, June 1990. Publisher: ICE Publishing.

[346] R. E. Bird, G. Pretti, W. M. Coombs, C. E. Augarde, Y. U. Sharif, M. J. Brown, G. Carter, C. Macdonald, and K. Johnson, “An implicit material point-to-rigid body contact approach for large deformation soil–structure interaction,” *Computers and Geotechnics*, vol. 174, p. 106646, Oct. 2024.

[347] P. Grammenoudis and C. Tsakmakis, “Predictions of microtorsional experiments by micropolar plasticity,” *Proceedings of the Royal Society A: Mathematical, Physical and Engineering Sciences*, Jan. 2005. Publisher: The Royal Society.

[348] N. D. Gavin, G. Pretti, W. M. Coombs, J. C. Brigham, and C. E. Augarde, “On the implementation of a material point-based arc-length method,” *International Journal for Numerical Methods in Engineering*, vol. 125, no. 9, p. e7438, 2024.

[349] S. Dua, H. Ahmed, and N. Arfin, “Soft Nanomaterials and Their Applications,” in *Nanomaterials: The Building Blocks of Modern Technology: Synthesis, Properties and Applications* (T. Khan, M. Jawaid, K. A. Ahmad, and B. Singh, eds.), pp. 27–68, Singapore: Springer Nature, 2023.

[350] A. K. Chaurasia and G. D. Seidel, “Modeling Nanocomposite Piezoresistive Response With Electromechanical Cohesive Zone Material Point Method,” in *Conference Proceedings: Smart Materials, Adaptive Structures and Intelligent Systems*, American Society of Mechanical Engineers Digital Collection, Nov. 2016.

[351] P. Hofer, M. Neuner, and G. Hofstetter, “Localized Deformation Analysis of a 3D Micropolar Modified Cam-Clay Model,” *International Journal for Numerical and Analytical Methods in Geomechanics*, vol. 49, no. 5, pp. 1544–1562, 2025.

[352] J. C. Simo, “Algorithms for static and dynamic multiplicative plasticity that preserve the classical return mapping schemes of the infinitesimal theory,” *Computer Methods in Applied Mechanics and Engineering*, vol. 99, pp. 61–112, Aug. 1992.

[353] C. Miehe, “Comparison of two algorithms for the computation of fourth-order isotropic tensor functions,” *Computers & Structures*, vol. 66, pp. 37–43, Jan. 1998.